Characterising nanoparticles in complex biological media

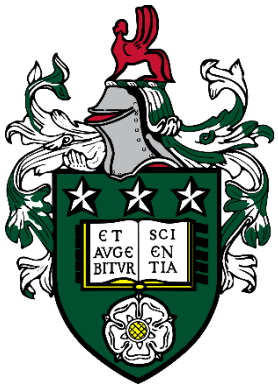

Martha Alice Ilett

School of Chemical and Process Engineering

University of Leeds

Thesis submitted in accordance with the requirements for the degree of

Doctor of Philosophy

April 2020

The candidate confirms that the work submitted is her own, except where work which has formed part of jointly authored publications has been included. The contribution of the candidate and the other authors to this work has been explicitly indicated below. The candidate confirms that appropriate credit has been given within the thesis where reference has been made to the work of others.

The work in **Chapter 4** of this thesis has been published in the following journal:

M Ilett, A Brown, R Brydson and N Hondow, Cryo-analytical STEM of frozen, aqueous dispersions of nanoparticles, Micron, 2019, DOI: 10.1016/j.micron.2019.01.013

The candidate carried out all experimental work, data analysis and writing. All authors contributed to writing the final manuscript

The work in **Chapter 5** of this thesis has been published in the following journals:

M Ilett, F Bamiduro, O Matar, A Brown, R Brydson and N Hondow, Cryo-STEM-EDX spectroscopy for the characterisation of nanoparticles in cell culture media, Journal of Physics conference series, 2017

The candidate carried out all experimental work and data analysis. The manuscript was written by the candidate and A Brown, R Brydson and N Hondow.

M Ilett, J Wills, P Rees, S Sharma, S Micklethwaite, A Brown, R Brydson and N Hondow, Application of automated electron microscopy imaging and machine learning to characterise and quantify nanoparticle dispersion in aqueous media, Journal of Microscopy, 2019, DOI: 10.1111/jmi.12853

The candidate carried out all automated image analysis, validation and optimisation. J Wills and P Rees designed the automated analysis workflow. S Micklethwaite designed the automated imaging workflow. S Sharma prepared the iron oxide nanoparticle dispersions. The manuscript was written by M Ilett with contribution from N Hondow, A Brown, R Brydson, J Wills and P Rees.

M Ilett, F Bamiduro, S Sanchez-Segado, R Brydson, A Brown and N Hondow, Nanoparticle corona artefacts derived from specimen preparation of particle suspensions, Scientific Reports, 2020, DOI: 10.1038/s41598-020-62253-y

The candidate carried out the majority of the experimental work and data analysis. O Matar synthesised the barium titanate nanoparticles and S Sanchez-Segado carried out the thermodynamic modelling. The manuscript was written by M Ilett with contribution from A Brown, R Brydson and N Hondow.

Acknowledgements

Firstly, I would like to thank Dr Nicole Hondow for her generous support, guidance and enthusiasm throughout the course of my PhD. Nicole has been ever approachable and has made my PhD a thoroughly enjoyable experience and for that I am extremely grateful – thank you. My sincere thanks also to Dr Andy Brown and Professor Rik Brydson for their invaluable help and scientific input.

I would like to thank and acknowledge Dr John Wills and Professor Paul Rees for their collaboration in the work presented in Chapter 5 using automated image analysis. I also had the opportunity to visit the In Vitro Toxicology Group at the University of Swansea under the guidance of Dr Steve Evans and would like to thank the whole group for this valuable experience, with specific thanks to Steve for providing the genotoxicity and cytotoxicity data presented in Chapter 6. I also acknowledge and thank Dr Sergio Sanchez-Segado for carrying out the thermodynamic modelling presented in Chapter 5.

Thank you to all the LEMAS staff for their support with the electron microscopes, and particular thanks to Stuart Micklethwaite for collecting the Helios FIB-SEM data presented in Chapters 5 and 6.

I acknowledge and thank the EPRSC for funding this PhD.

Finally, thanks to my parents, sisters and brother-in-law for their continued interest and support in all I do, and to Matt for everything.

Abstract

Progress in the application of nanotechnology within medicine has been limited in part due to the difficulties in understanding and predicting the behaviour of nanoparticles in complex biological media. How nanoparticles disperse in biological media and the interactions that occur at the bio-nano interface dramatically influence their subsequent biological function. Techniques to measure and monitor these behaviours are usually bulk techniques, however these can be limited by the more complex nature of biological environments which routinely contain a number of bio-macromolecules e.g. vitamins, proteins and salts. As such, high spatial resolution analysis through electron microscopy has been investigated as an alternative to more accurately characterise nanoparticles in biological fluids. However, electron microscopy itself can be limited by the ultra-high vacuum requirements which mean samples must be dried before analysis. This necessitates the development of *in situ* techniques in order to characterise nanoparticle suspensions in the representative, native hydrated state.

Using cryogenic transmission electron microscopy (cryo-TEM) a sample can be analysed in the frozen, hydrated state. However, typically this is limited to imaging alone. In this thesis, the use of analytical scanning TEM (STEM) to characterise nanoparticle dispersions captured in a layer of vitreous ice is demonstrated using both STEM energy dispersive X-ray spectroscopy and electron energy loss spectroscopy under cryogenic conditions. A noticeable difference in damage to the surrounding vitreous ice was observed between conventional TEM (CTEM) and STEM where damage occurred at much higher electron fluences in STEM (<2000 $e^-/Å^2$) compared to CTEM (<100 $e^-/Å^2$). Applying these techniques to characterise nanoparticles dispersed in cell culture media showed that incorrect specimen preparation or analysis where a significant raise in pH level is caused can induce an artefactual, nanoscale, calcium phosphate-rich, amorphous coating on nanoparticles dispersed in cell culture media. Recommendations to prevent this are given which will prevent any specimen preparation artefacts that could drive alterations in the *in vivo* or *in vitro* function of nanoparticles.

For nanoparticle dispersion analysis automated electron microscopy imaging and analysis of plunge frozen vacuum dried nanoparticle suspensions was shown to be a viable alternative to dynamic light scattering for quantification of nanoparticle agglomerates in biological dispersants. Using two simple freeware codes, CellProfiler and Ilastik automated image analysis was achieved and validated for both monodisperse and agglomerated nanoparticle systems.

Finally, cellular uptake studies assessed the biological effect of two gold nanoparticles coating with PEG and either terminated with a positive NH_2 or neutral OMe group, on blood cells. No significant differences in cell uptake, geno- and cyto- toxicity or immune response was observed for the two nanoparticle types. Protein corona analysis by sodium dodecylsulfate - polyacrylamide gel electrophoresis indicated a comparable hard corona composition for both particles. Preliminary work identified annular bright field-STEM as a potential pathway to image the protein corona. This characterisation indicated possible inter-particle variation in the presence of a corona around particles within an individual suspension.

Overall, the results reported show *in situ* cryo-analytical S/TEM is a powerful tool to characterise nanoparticle dispersions in complex biological media in order to further the understanding of complex bio-nano interactions and nanoparticle dispersion behaviour that ultimately control biological function.

Table of Contents

1. INTRODUCTION 1

1.1 Nanoparticle dispersion 2

1.2 Bio-nano interface 4

1.3 Nanoparticle characterisation in biological media 4

1.4 *In situ* TEM 6

2. LITERATURE REVIEW 8

2.1 Nanotechnology for medical applications 9

2.2 Bio-nano interactions 12

2.2.1 Nanoparticle dispersion 12

2.2.2 The protein corona 19

2.3 Characterising the bio-nano interface 21

2.3.1 TEM for nanoparticle dispersion analysis 23

2.3.2 Analytical-TEM 24

2.3.3 EM limitations 25

2.3.4 In situ TEM 28

2.3.5 Limitations of cryo-EM 29

2.3.6 Cryo-analytical S/TEM 34

2.4 Project Aim 37

2.5 Objectives 37

3. MATERIALS AND METHODS 39

3.1 Nanoparticle synthesis 39

3.2 Nanoparticle suspensions 41

3.2.1 Model nanoparticle suspensions 42

3.2.2 Nanoparticle dispersions in biological media 43

3.3 Electron microscopy 44

3.3.1 Electron beam 46

3.3.2 Electron scattering 46

3.3.3 Lens aberrations 48

3.3.4 Transmission electron microscopy 50

3.3.5 Scanning transmission electron microscopy 54

3.3.6 Analytical-STEM 55

3.3.7 Automated STEM imaging 58
3.3.8 Negative staining 58
3.4 *In situ* electron microscopy 59
3.4.1 Cryogenic-TEM 60
3.4.2 Liquid cell-TEM 61
3.4.3 Electron flux and fluence calculations 63
3.5 Bulk analysis 64
3.5.1 Dynamic light scattering 64
3.5.2 Zeta potential 66
3.6 Gold nanoparticle cell-uptake studies 68
3.6.1 Protein corona analysis 68
3.6.2 Cell uptake studies 70
3.7 Data analysis 76
4. DEVELOPMENT OF CRYOGENIC ANALYTICAL STEM TECHNIQUES 77
4.1 Nanoparticle dispersion characterisation 78
4.1.1 Phase contrast Cryo-TEM 78
4.1.2 Cryo-STEM-EDX 79
4.1.3 Cryo-STEM-EELS 83
4.2 TEM v STEM under cryogenic conditions 87
4.3 Optimising STEM conditions 93
4.3.1 Ice thickness sample variation 93
4.3.2 Influence of probe current on damage rate 94
4.3.3 Influence of pixel size on damage rate 96
4.4 CTEM conditions 97
4.5 Liquid cell TEM 102
5. CHARACTERISATION OF NANOPARTICLES IN COMPLEX BIOLOGICAL MEDIA VIA *IN SITU* AND AUTOMATED STEM TECHNIQUES 108
5.1 Nanoparticles dispersed in cell culture media 109
5.1.1 Interactions at the bio-nano interface 109
5.1.2 Drop cast v cryo analytical STEM 112
5.1.3 Sample preparation artefacts 113
5.1.4 What form of calcium phosphate? 120
5.1.5 Recommendations for sample preparation without artefact inducement 122

5.2 Nanoparticle dispersion states 124
5.2.1 Nanoparticles in lysosomal buffers 124
5.2.2 Nanoparticles in simulated body fluid 128
5.2.3 Automated imaging set-up 131
5.2.4 Automated image analysis design 133
5.2.5 Validation 140
5.2.6 Validating native state representative sample preparation techniques 143
5.2.7 Validating the applicability to more complex systems 146
5.2.8 Application in real systems 150
6. CELLULAR UPTAKE OF NANOPARTICLES AND INVESTIGATION OF THE PROTEIN CORONA 154
6.1 Exposing cells to gold nanoparticles 155
6.1.1 Cellular uptake 156
6.1.2 Genotoxicity and Cytotoxicity 162
6.1.3 Inflammation 166
6.2 Protein corona investigations 168
6.2.1 SDS-PAGE 168
6.2.2 Imaging the protein corona 171
7. CONCLUSIONS AND FUTURE WORK 184
7.1 Summary of findings 184
7.2 Final conclusions 188
7.3 Further work 189
REFERENCES 191

List of Tables

Table 1: The main constituents in DMEM and RPMI supplemented with 10% FBS [37]. 43

Table 2: Reagents used in preparation of SBF. Reagents added in the order shown in table. 44

Table 3: Protocol for preparing stacking and resolving gels for SDS-PAGE analysis of protein corona 70

Table 4: Protocol for fixing and developing protein corona gels for protein analysis. 70

Table 5: Staining process for resin embedding cell sections 75

Table 6: EDX and EELS quantification of the Ca to P ratio of standards; tribasic calcium phosphate and hydroxyapatite. Errors were calculated as the standard deviation of n>3 measurements. 121

Table 7: Ca to P ratios obtained through EDX and EELS quantification. There was some suggestion that there could be a degree of difference in the composition of the coating between two different media, although this was not significant. Errors are given as the standard deviation of n>3 measurements. 121

Table 8: Thermodynamic modelling carried out using HSC Chemistry (v 5.1) software. Highlighted in red are the three most likely forms of calcium phosphate precipitate to form from a system modelled on the ions present in CCM. 122

List of Figures

Figure 1: A schematic illustrating the possible dispersion states of nanoparticles in suspension. Colloidally stable nanoparticles remain monodispersed (A). Alternatively, nanoparticles can dissolve in suspension and/or transform into agglomerates or aggregates (B). Some nanoparticles can fall out of suspension entirely and sediment (C). Adapted from [5]. 3

Figure 2: DLS analysis of cell culture media with 10% fetal bovine serum supplement (red) alongside a suspension of 9 nm CeO_2 nanoparticles in cell culture media with 10% fetal bovine serum (5 μg/mL). The scattering signal from serum proteins is at ~7 nm and cannot be distinguished from that of the 9 nm nanoparticles by DLS analysis alone. 5

Figure 3: An illustration of the application and current goals of nanotechnology in medicine. Research has shown a range of nanostructures and devices have potential in diagnostics, theranostics and therapeutics. Reproduced from [11]. 9

Figure 4: A schematic of a nanoparticle with multiple design features for targeted drug delivery. Reproduced from [29] 11

Figure 5: A schematic showing the impact of ionic strength on effective electrostatic forces between suspended particles as a function of distance and ionic strength. At low ionic strength (blue) repulsive coulombic forces dominate. Increasing the ionic strength reduces the repulsive potential barrier (green line). Further increasing the ionic strength in line with that predicted for a physiological buffer system leads to a significant decrease in repulsive interaction potential, and the repulsive energy barrier preventing particle agglomeration is lost. Reproduced from [32]. 13

Figure 6: TiO_2 nanoparticle agglomerate size as measured by high throughput DLS in a range of different CCM. Agglomerate size increased in CCM and with increasing TiO_2 nanoparticle concentration. The different CCMs used were; Bronchial Epithelial Growth Medium (BEGM), Dulbecco's Modified Eagle's Medium (DMEM), Luria Bertani Broth (LB), Tryptic Soy Broth (TSB), Synthetic Defined medium (SD), Yeast Extract Peptone Dextrose medium (YPD). Reproduced from [34]. 15

Figure 7: A schematic illustrating electrostatic (A) and steric (B) dispersion stabilisation. In biological media the distance the electrical double layer extends away from the particle surface is reduced preventing effective electrostatic stabilisation, whilst steric stabilisation by polymer addition for example can enhance colloidal stability. Adapted from [50]. 17

Figure 8: A simplified schematic of the main process of endocytosis, the method through which nanoparticles can be taken up into a cell. Adapted from [52]. 18

Figure 9: A schematic of the protein corona that forms around nanoparticles exposed to protein containing biological media. Reproduced from [7]. 19

Figure 10: HAADF-STEM and STEM-EDX analysis of CuO nanoparticles suspended in CCCM. A 'nano-bio-complex' composed of K^+, Ca^{2+}, Na^+, P^{4-}, Cl^- was said to form around the nanoparticles during incubation in CCCM. (a) Dark-field TEM image; (b) EDX O K map, (C) EDX Zn Kα map, (d) Ca Kα map, (e) EDX Na Kα map, (f) EDX K Kα map, (g) EDX P Kα map, (h) EDX Cl Kα map. (i) A simple model of the CuO bio-complex. Reproduced from [78]. 25

Figure 11: (A) A schematic showing how nanoparticles can move on a TEM support grid during droplet drying in air due to the 'coffee-ring' effect. (B-E) Four HAADF-STEM images of a dispersion of silica nanoparticles (100 nm spheres) in water drop cast onto a TEM grid and dried in air. DLS analysis of the suspension showed the nanoparticles were monodispersed. Drying artefacts occurred during TEM sample preparation such that large agglomerates formed (C) and evidence of the coffee-ring effect was seen (A, C). (D) Indicates an area of the grid where drying artefacts probably did not occur and presents evidence of a monodispersed suspension. The white scale bar indicates a distance of 5 µm. 27

Figure 12: (1) Images and corresponding diffraction patterns of three forms of ice taken at the same magnification; (A) Hexagonal ice; (B) Cubic ice and (C) vitreous ice. Reproduced from [107]. (2) Images of highly diffracting hexagonal ice; (A) Hexagonal ice (white arrow) alongside goethite crystallites (black arrows) and (B) hexagonal ice (white arrow) with spheroid frost (black arrow). Reproduced from [106]. 30

Figure 13: An illustration of the main reactions that occur during the three stages of water radiolysis. Upon beam irradiation immediate formation of ionised and excited water molecules occurs (physical stage), these species then undergo a series of reactions (physico-chemical stage) to produce highly reactive damage species which can then go on to react with each other and any molecules captured in vitreous ice/water (chemical stage). Reproduced from [110]. 32

Figure 14: Two cryo-TEM images identifying some common technique artefacts. (A) shows cubic ice (black arrow) and spheroid frost (white arrow). (B) shows bubbling of the vitreous ice which occurs preferentially first at the contact point between the vitreous ice and the carbon film (white arrow). 33

Figure 15: Cryo-EELS (low loss) spectra from pure amorphous ice (blue), pure polydimethyl siloxane (PDMS) (green) and methyl acrylate-methyl methacrylate-vinyl acetate (copolymer) (red). Spatial elemental mapping is also shown for the corresponding spectra signal indicating the copolymer is trapped within the PDMS over 10s of nm. Reproduced from [116]. 35

Figure 16: (A) An electron transparent cryo-FIB lift out lamellae of a liquid electrolyte illustrating the solid-liquid interfaces found in lithium-metal batteries. (B) HAADF cryo-STEM imaging reveals information regarding the size of the solid-electrolyte interphase (SEI). (C) Cryo-STEM-EELS elemental mapping indicates the SEI layer and the dendrite are oxygen rich. Scale bars 1 µm (A) and 300 nm (B, C). Adapted from [119]. 36

Figure 17: Characterisation of synthesised barium titanate by XRD indicated successful synthesis of cubic barium titanate had been carried out. 41

Figure 18: A schematic illustrating the Airy disc phenomenon of diffraction-limited resolution for incoherent illumination. The Rayleigh criterion states that the minimum resolution is the point at which the minimum first diffraction of one disc overlaps with the maximum of another. Adapted from [134]. 45

Figure 19: A schematic showing the different types of electron scattering that can occur in TEM (and SEM) imaging. Reproduced from [135]. 48

Figure 20: A schematic showing two common lens aberrations in TEM, spherical and chromatic aberrations. Spherical aberrations (top) cause electron waves to be bent more at the periphery of the lens. Chromatic aberrations (bottom) relate to the variation in bending of electrons due to differences in energy whereby lower energy electrons are bent to a larger extent. 50

Figure 21: A schematic of a TEM using a twin objective system operating in the BF mode with a parallel beam of illumination. 51

Figure 22: Examples of the three imaging contrast techniques in TEM. (A) A mixture of ZnO, Fe_2O_3 and CeO_2 nanoparticles illustrating mass thickness contrast such that the ceria nanoparticle agglomerates indicated by the black arrows appear darker in comparison to zinc oxide and iron oxide. (B) Diffraction contrast indicated by the variation in contrast between $BaTiO_3$ nanoparticles due to different orientations of the crystals on the support film. (C) Lattice image of TiO_2 orientated along the [111] anatase plane (taken by Dr A. Brown). 53

Figure 23: A schematic of a STEM detector for HAADF and ADF imaging. Adapted from [135]. 54

Figure 24: A schematic showing the electron-electron interactions that occur between the electron beam and the electron shell around atoms of the sample in EM imaging. These inelastic interactions cause inner-shell electron excitation, this in turn results in subsequent outer-shell electron relaxation and the release of detectable X-rays. 55

Figure 25: A HAADF STEM image and an EDX spectrum taken from the image area of a specimen prepared from a suspension of ZnO, Fe_2O_3, and CeO_2 nanoparticles dispersed in water. 56

Figure 26: A schematic of an EELS detector system, indicating the prism through which the transmitted beam is bent, multipole optics and the CCD. 57

Figure 27: Two EELS spectra obtained from a sample prepared from a $BaTiO_3$ nanoparticle dispersion, showing an example of a zero loss peak, plasmon peak and core loss edge (Ti $L_{2,3}$) (inset). 58

Figure 28: Two samples negatively stained, (A) Fe_3O_4 nanoparticles coated with PEG and (B) Fe_3O_4 nanoparticles uncoated. Negative staining provides contrast for the polymer coating around the nanoparticles in (A) which is otherwise not visible in untreated grids. 59

Figure 29: A schematic of a static liquid cell (K-Kit) showing the silicon nitride membrane window, micro-channel and glued ends. 63

Figure 30: The process of preparing, loading and sealing the K-kit static liquid cell. The liquid sample was loaded via capillary action for one minute before sealing the ends of the channel with epoxy glue and mounting the window onto a custom designed copper TEM grid. Reproduced from [151]. 63

Figure 31: A schematic of a Zetasizer used to carry out DLS measurements to obtain size distributions of particles in suspension. 66

Figure 32: A schematic illustrating the double layer theory of charged nanoparticles in suspension. The Stern layer forms of strongly bound ions around the nanoparticle and then a diffuse layer forms made up of more weakly associated ions. The Zeta potential is the electrostatic potential at the edge of the diffuse layer. 67

Figure 33: Taken from [159] this figure shows the different types of cells to be counted when carrying out the CBMN assay. (a) mono-nucleated cell, (b) bi-nucleated cell, (c) multi-nucleated cell, (d) early necrotic cell, (e) late apoptotic cell, (f) bi-nucleated cell containing a Mn, (g) Bi-nucleated cell containing a NPB and (h) bi-nucleated cell containing NBUDs. 72

Figure 34: Cryo-CTEM images of a model nanoparticle dispersion in water containing ZnO, Fe_2O_3, CeO_2 and Au-Ag core-shell nanoparticles, captured in vitreous ice. FFTs (B) and (D) were obtained from the boxed regions in (A) and (C) respectively and show the diffraction spots identified. The spots in FFT (B) correspond to the (111) (red), (002) (blue) and (022) (yellow) lattice planes of ceria and the (201) (green) lattice plane in Fe_2O_3. The FFT in (D) could be assigned to Fe_2O_3 (e.g. (201) green and (211) red) or either Fe_2O_3 or ZnO (e.g. Fe_2O_3 (311) or ZnO (101) (blue) and Fe_2O_3 (410) or ZnO (102) (yellow)). Reproduced from Ilett *et al.* [120]. 79

Figure 35: Cryo-STEM-EDX analysis of a model nanoparticle system collected using a 100 pA probe current for 472 s (1300 $e^-/Å^2$) and showing the presence of CeO_2, Fe_2O_3, ZnO and Au-Ag core-shell nanoparticles. (A) HAADF STEM image showing the area used for EDX analysis. Elemental X-ray mapping of (B) Fe Kα; (C) Zn Kα and (D) Ce Lα is shown alongside the EDX spectrum (E) from the whole image area in (A). Combined EDX maps of Fe Kα (red), Zn Kα (blue), Ce Lα (yellow) and C Kα (green) are shown in (F). To confirm the presence of Ag-Au nanoparticles a second cryo-EDX dataset was collected from the blue boxed region in (A); (G) HAADF STEM image; (H) Ag L (orange) and Au Mα (white) EDX maps and (I) EDX spectrum from the area. The Mα Au signal was used rather than the Lα to avoid the interference of the Zn Kβ signal. Reproduced from Ilett *et al.* [120]. 82

Figure 36: EEL spectra showing the absolute intensity of the carbon *K*-edge (from the TEM support film) collected at four different camera lengths without background subtraction after a 6 s (A) and 10 s (B) exposure. The signal to background ratio (Si:B) was calculated for each camera length from the C K edge by dividing the peak maxima (signal) by the peak minima (background) and the values are shown in (C). These did not vary significantly between the four camera lengths but did improve with increased exposure time. 84

Figure 37: Cryo-STEM-EELS of a model nanoparticle suspension containing ZnO, Fe_2O_3, CeO_2 and Au-Ag core-shell nanoparticles. The Cryo-HAADF STEM image corresponds to the area analysed. The background subtracted cryo-EEL spectrum was obtained using a 0.25 eV/ch dispersion, 2.5 mm entrance aperture, 660 eV HL drift tube with a 60 s exposure and 5 µs dwell time at 225kx magnification. The total electron fluence was 2000 $e^-/Å^2$. The Fe $L_{2,3}$ white line edge at 708 eV confirmed the presence of Fe_2O_3 nanoparticles, the Ce $M_{4,5}$ edges at 883–901 eV confirmed the presence of CeO_2 nanoparticles and the Zn L_3 edge at 1020 eV confirmed the presence of ZnO nanoparticles. No Au or Ag edges were obtained. Reproduced from Ilett *et al.* [120]. 85

Figure 38: EELS-SI using dynamic mapping of a model nanoparticle suspension containing ZnO, Fe_2O_3, CeO_2 and Au-Ag core-shell nanoparticles. Signals for Fe ($L_{2,3}$) (blue), Zn (L_3) (green) and Ce ($M_{4,5}$) (red) were all detected. High speed settings were used in order to obtain the required spatial information whilst limiting the total electron fluence to 2500 $e^-/Å^2$ 87

Figure 39: Qualitative assessment of the damage to the vitreous ice after exposure to increasing electron fluence in CTEM and STEM. For CTEM, some damage was seen as bubbles forming in the region of the carbon film after 100 $e^-/Å^2$ (A), whilst more significant damage to the ice was observed after 400 $e^-/Å^2$ (B). In comparison HAADF STEM images taken before (fluence 300 $e^-/Å^2$) (C) and after (D) exposing the sample to a further fluence of 1000 $e^-/Å^2$ showed some destruction to the ice (inset in (D) altering the contrast shows more clearly the bubbling observed in the vitreous ice indicated by the white arrow). Higher total accumulated fluences could be used in HAADF STEM with (E and F) showing images before and after exposure to 4000 $e^-/Å^2$. After exposure to 8000 $e^-/Å^2$ (H) damage and movement of nanoparticles was observed. Adapted from Ilett *et al*. [120]. 89

Figure 40: (A) A schematic (Egerton, 2019) postulating the relationship between dose rate and damage rate. The diffusion limited damage in ice corresponds to a power law relationship with exponent <1, between damage rate and dose rate (red curve in schematic). This suggests that lower flux CTEM operates at the linear portion of this curve. In comparison STEM operates at a higher flux per pixel i.e. probe flux (Fp), and hence damage per unit fluence is lower. (B) A schematic (not to scale) showing the estimated beam broadening that will occur in STEM through 100 nm of vitreous ice, and the calculated minimum delocalised damage region (shown in orange) around the probe. (C) An alternative view of (B) showing multiple pixels with the STEM probe size and estimated delocalised damage areas (d) illustrated. Reducing the pixel size would result in the delocalised damage extending beyond the imaging pixel and oversampling would occur. Reproduced from Ilett *et al.* [120]. 92

Figure 41: Percentage decrease in ice thickness as a function of the total electron fluence for two varying original ice thicknesses; a 540 nm 'thick' sample (red, circle) and a 220 nm 'thin' sample (black, square). A significant difference was seen in the damage rate, with the thinner sample damaging more quickly ($p<0.05$). However, expressing these measurements per unit volume of irradiated ice rather than per unit area suggests similar damage rates overall. Errors are reported as the standard deviation from n=3 measurements and the linear fit is pinned through (0,0). 94

Figure 42: Percentage decrease in ice thickness as a function of total electron fluence for three different probe currents; 60 pA (black, square), 100 pA (red, circle) and 280 pA (green, triangle). The damage rate was relatively similar for each probe current within error. However, a statistically significant difference was observed between 60 pA and 280 pA ($p<0.05$). The errors are given as the standard deviation of n=3 measurements and the linear fit is pinned to (0,0) 95

Figure 43: Percentage decrease in ice thickness as a function of total electron fluence for three different pixel sizes; 0.1 nm (black, square), 1 nm (red, circle) and 10 nm (blue, triangle). A log-log plot was used to obtain a linear fit, indicating a power law relationship between ice damage and electron fluence. Greater damage was observed when using smaller pixel sizes. Data is plotted as the mean of n=3 experiments. 97

Figure 44: Cryo-CTEM images indicating bubbling in vitreous ice as a function of electron fluence. Damage occurred preferentially at the site of the carbon film indicated by the black boxes at 500 $e^-/Å^2$. Further damage is seen within the holes after exposure to 2000 $e^-/Å^2$ indicated by the white boxes. Scale bar indicates 1000 nm. 100

Figure 45: Three datasets showing the variation in crystallisation in cryo-CTEM. (A) Cryo-TEM image showing clear crystallisation occurred from a region of amorphous vitreous ice after exposure to 4500 $e^-/Å^2$. (B) Further evidence of ice crystallisation in a region with some degree of original crystallinity; brighter diffraction spots were observed after exposure to 3000 $e^-/Å^2$. The diffraction pattern suggested cubic ice formed with the (111) (red), (220) (blue), (311) (green) and (400) (white) lattice planes identified. (C) A final dataset showing no evidence of crystallisation of the vitreous ice after exposure to 3000 $e^-/Å^2$. For all datasets a 50 $e^-/Å^2$.s probe flux was used..... 101

Figure 46: STEM-EDX of a model nanoparticle suspension containing ZnO, Fe_2O_3, CeO_2 and Au-Ag core-shell nanoparticles, in a static liquid cell. (A) A HAADF STEM image of the model nanoparticle suspension from which the corresponding EDX maps and spectrum were obtained. From the EDX spectrum (B) mapping of Ce L_α (C), Fe K_α (D) and Zn L_α (E) X-rays is shown. A combined elemental map is provided in (F)..... 103

Figure 47: Evidence of nanoparticle dissolution in the static liquid cell. HAADF STEM images of the model multi-type nanoparticle suspension in liquid taken after exposure to an initial electron fluence of 30 $e^-/Å^2$ (A) and after exposure to a further 300 $e^-/Å^2$ (B). Examples of the dissolution of ZnO nanoparticles is indicated by the circled regions..... 104

Figure 48: HAADF STEM images of Fe_3O_4-PEG nanoparticles dispersed in water and loaded in a static liquid cell. There was evidence of significant dissolution of the nanoparticles after exposure to increasing total electron fluence. No movement of the nanoparticles was observed suggesting the nanoparticles were adhered to the upper and/or lower silicon nitride window surfaces..... 105

Figure 49: TEM images of six nanoparticle systems dispersed in CCM prepared by drop-casting and air drying. (A) Au-PSS, (B) $BaTiO_3$, (C) ZnO, (D) TiO_2, (E) Fe_2O_3 and (F) $BaTiO_3$-PLL. Each system showed a coating formed around the nanoparticle after suspending in cell culture. (G) Table indicating the variation in zeta potential of the different nanoparticles (all measurements taken in water). EDX analysis of the coating around TiO_2 (H) indicated several elements were present in the coating (Na, P, Ca, Cl and Mg). Reproduced from Ilett *et al.* [90]..... 111

Figure 50: A comparison between $BaTiO_3$-PLL nanoparticles dispersed in CCCM and characterised after drop cast preparation (A) or under cryo conditions (B). Drying artefacts were seen to occur using conventional drop cast techniques where a number of elements spatially resolved to the position of the coating. However when characterising the system in the frozen hydrated state only Ca and P spatially resolved to the position of the coating and the other components of the media were present only in solution. EDX maps were obtained from signals for Ba Lα (red), Ti Kα (blue), Ca Kα (yellow), P

Kα (green), Cl Kα (turquoise), Na Kα (orange), K Kα (purple) and Mg Kα (pink). Adapted from Ilett *et al.* [90]. 113

Figure 51: pH (dashed line) and temperature (solid line) measurements of CCM either bath sonicated, incubated in a water bath at 40°C or incubated at room temperature in atmospheric CO_2 levels. For bath sonication, measurements were taken over a period of 3 h; whilst for incubation at 40°C in a water bath and at room temperature, measurements were taken over a period of 24 h. The increase in pH of the CCM was much quicker when at the elevated temperatures of the water bath and bath sonicator reaching >8 after 3 h. In comparison the increase in pH at room temperature was much slower, only reaching ~8 after 24 h incubation. Reproduced from Ilett *et al.* [90]. 114

Figure 52: $BaTiO_3$ nanoparticles dispersed in CCM and incubated at room temperature for 3 h. No calcium phosphate coating was observed which confirmed that pH and temperature were the critical factors in coating formation. Reproduced from Ilett *et al.* [90]. 115

Figure 53: Three ZnO nanoparticles of different shape and size dispersed in CCCM and drop cast onto a TEM grid and dried. The DLS plot in (D) indicates the increase in size where the blue line corresponds to the particles imaged in (C), the red line to the particles imaged in (B) and the black line to the particles imaged in (A). The hydrodynamic radii were 295 ± 11 nm, 615 ± 36 nm and 1281 ± 141 nm with the range given as the standard deviation of n=3 measurements. The calcium phosphorus rich coating established on all three nanoparticles confirming that coating formation was independent of size and shape. Reproduced from Ilett *et al.* [90]..... 116

Figure 54: Ionic equilibrium data for DMEM at 25°C obtained from HYDRA-MEDUSA software. Precipitation of Ca by phosphate is predicted to occur at pH 6.5 but this does not consider the organic species present in the media (vitamins, amino acids and proteins) which can delay precipitation. . 119

Figure 55: Cryo-analytical-STEM characterisation of $BaTiO_3$-PLL nanoparticles in CCCM prepared without artificial adjustments to pH or temperature. EDX analysis indicates following the recommended sample preparation prevents the formation of the calcium and phosphorus rich coating. The combined elemental map in (B) maps the X-ray signals of Ba (red), Ti (blue), Na (green) and Cl (yellow) of the HAADF STEM image (A) and the spectra in (C) is from the whole image area. Reproduced from Ilett *et al.* [90]. 124

Figure 56: DLS plots for Au-NH_2 nanoparticles dispersed in different media over time. The nanoparticles were dispersed at 100 µg/mL in four different media; (A) H_2O, (B) CCCM, (C) lysosomal buffer pH 4.5 and (D) lysosomal buffer pH 5.5. Nanoparticle agglomeration was only observed after 72 h in both lysosomal buffers. Legend in (A) applies to all plots. 126

Figure 57: Dispersion states of Fe_3O_4 (A), Fe_3O_4-COOH (B) and Fe_3O_4-PEG (C) nanoparticles dispersed in lysosomal buffers at pH 7, pH 5.5 and pH 4.5. Significant agglomeration and colloidal instability was observed for Fe_3O_4-COOH nanoparticles in low pH buffers. The legend in (A) applies to all plots.... 127

Figure 58: DLS plots of Au-NH_2 (A) and Au-OMe (B) nanoparticles dispersed in H_2O (black) and SBF (red). No change in dispersion state was seen for either nanoparticles when dispersed in the higher ionic strength SBF. 129

Figure 59: DLS measurement of SiO_2 (100 nm) nanoparticles dispersed in either water (red), SBF (green) or CCCM (blue). Significant agglomeration was observed when dispersed in SBF, compared to no agglomeration when dispersed in water or CCCM. 129

Figure 60: Two DLS plots comparing the size distribution seen when measuring blank CCCM or CCCM with 9 nm ceria nanoparticles dispersed at 5.27 µg/mL. The nanoparticle signal is indistinguishable from the BSA signal in blank CCCM..... 131

Figure 61: A schematic illustrating the automated imaging process. A 200 mesh TEM support grid with a continuous carbon support film was used. (A) A TEM support grid indicating the large area imaged for SiO_2 nanoparticles. (B) A TEM support grid showing multiple regions imaged for smaller particles. (C) An example of a small 14 x 14 image array, the region outlined in orange (top left) indicates one individual image of 30 µm width. Reproduced from Ilett *et al.* [190]. 133

Figure 62: Automated thresholding of HAADF-STEM images taken from samples prepared from nanoparticle suspensions in water and CCCM. (A) Original HAADF STEM image of SiO_2 in water, and (B) after applying simple binary thresholding that indicated successful segmentation of the agglomerates could be achieved. In comparison the original image of Fe_2O_3 nanoparticles suspended in CCCM (C) and after applying simple thresholding (D) that indicated thresholding could not separate salts (solid arrows) from nanoparticles (dashed arrows). 134

Figure 63: The input modules used for both CellProfiler pipelines in the automated image analysis are given alongside each step in the two CellProfiler pipelines for image illumination correction (pipeline 1) and agglomerate identification and measurement (pipeline 2)..... 135

Figure 64: The workflow of the first pipeline used in CellProfiler to correct the illumination of each image. A manual threshold strategy was applied and pixels below the threshold were set to zero (A), the illumination function was then calculated (B) before applying this to each original thresholded image (C). 136

Figure 65: Automated segmentation using ilastik pixel classification. A small subset of test images were used to train the software. (A) Manual labelling of agglomerates in yellow and the background in blue. (B) Using the 'live update' function the predicted identification of agglomerates and background was demonstrated. (C) Once correct segmentation was achieved a probability map for each image was exported..... 138

Figure 66: CellProfiler – pipline two outputs. (A) Primary objects were identified and any agglomerates touching the outer border of the image were disregarded. (B) Each object was marked by overlaying outlines on each primary object. 139

Figure 67: Every identified agglomerate was numbered on each image and size and shape information was exported as an excel spreadsheet for each numbered object. 140

Figure 68: A DLS plot for monodispersed SiO_2 in water (100 µg/mL). Z average was 122 ± 6 nm and the PDI was 0.2..... 142

Figure 69: (A) Dark field STEM image of silica nanoparticles dispersed in water with manual identification of each nanoparticle agglomerate. This was compared to the machine segmentation of the same STEM image (B). The insets in both STEM images show an enlarged region (white box) indicating more clearly a specific nanoparticle agglomerate. The white scale bar indicates a distance of 5 µm. (D) Example of the focal halo that can erroneously be included in image segmentation in an exported probability image from ilastik, (and has been eliminated by an erosion step in the processing) (C) shows the same area of the original, image (the white scale bars represent a distance of 200 nm). (E) A comparison between the Feret diameter measured manually and by machine analysis is shown

using a box and whisker plot, presenting the interquartile range (the box), the median (-) the mean (▫) and the overall range of the data. There was no significant difference between the two datasets ($p>0.05$). (F) A summary of the measurement data of the Feret diameters shown in the box and whisker plot indicating that there was good agreement between the manual and machine learning approaches. The standard error of the mean is reported for uncertainty values. Reproduced from Ilett *et al.* [190]. 142

Figure 70: Log size distributions of a monodisperse (A) and agglomerated (B) system of SiO_2 nanoparticles in water. Automated size analysis was carried out on large data sets of samples prepared by plunge freezing vacuum drying (PFVD), controlled sublimation (PFS), plunge freezing followed by freeze drying (PFFD) and drop casting followed by air drying (DC). DLS data is plotted alongside for comparison. All data was normalised to the most frequent size to remove any bias from larger datasets. (C) Examples of HAADF STEM images from each data set indicated that larger agglomerates were observed in the agglomerated system. 145

Figure 71: DLS plots of Fe_2O_3 nanoparticles suspended in CCM with (red) and without (black) the addition of FBS. Agglomeration was reduced with the addition of 10% FBS. Errors taken as standard deviation of n=3 measurements. 147

Figure 72: Dark field STEM images from TEM grids prepared from iron oxide nanoparticles dispersed in CCM with 0% (A) and 10% (B) FBS. Successful segmentation of nanoparticles from salts (indicated by the white arrows in (A)) was achieved and the white scale bar indicates 5 µm. Number distributions of agglomerate size for EM data analysis by machine learning (red) and for DLS analysis (black) are shown for both systems; 0% FBS (C) and 10% FBS (D). Table (E) presents the mean values from DLS and EM data analysis for both samples calculated using both a number and volume distribution. A larger degree of agglomeration with complex shapes was seen in the 0% FBS suspension. Good agreement between EM and DLS analysis was seen for the 10% FBS sample, but there was some discrepancy in the 0% FBS sample that may be attributed to overweighting of larger agglomerates in DLS scattering analysis. This was reduced when volume averaged diameters were compared. Reproduced from Ilett *et al.* [190]. 148

Figure 73: Automated EM analysis (AA) of (A) Fe_3O_4-PEG and (B) Fe_3O_4-COOH nanoparticles dispersed in water and CCCM at a concentration of 100 µg/mL. By automated EM imaging and analysis, no difference was observed between the dispersion state of the nanoparticles, despite the DLS analysis suggesting otherwise. DLS can be influenced by components inherently present in the media which could have led to the discrepancies seen. 151

Figure 74: Mean agglomerate sizes for Fe_3O_4-PEG and Fe_3O_4-COOH nanoparticles dispersed in water and CCCM at 50 µg/mL. DLS data (blue) is compared to automated EM analysis (red). Discrepancies within DLS data for Fe_3O_4-PEG dispersions in CCCM and DI H_2O were removed when automated EM analysis was used. Standard error mean was used as the plotted error. 152

Figure 75: S/TEM imaging and analysis of thin sections prepared from cells treated with Au-NH_2 nanoparticles at 50 µg/mL. (A) A TEM image indicating the presence of two nanoparticles within a cell (black arrows). The inset presents a high magnification image of one of the particles. (B) A HAADF STEM image of the same cell section providing better contrast of the detail within the cell, the lower nanoparticle is encased within a vesicle (inset). The large white circles (white arrow) are lipid droplets which bind the osmium fixative strongly. (C) A higher magnification HAADF STEM image of the two

nanoparticles from which EDX analysis was carried out. The X-ray intensity map of the Au Mα signal in red (D) and the EDX spectrum (E) both confirmed the particles were indeed gold nanoparticles.157

Figure 76: S/TEM imaging and analysis of cellular thin sections prepared from cells treated with 50 µg/mL Au-OMe nanoparticles. (A) A TEM image indicating the presence of Au-OMe nanoparticles within a cell (black arrows). (B) A HAADF STEM image of the same cell section providing better contrast of the detail within the cell. The large white circles (white arrow) are lipid droplets that bind the osmium fixative strongly. (C) A higher magnification HAADF STEM image of two of the nanoparticles analysed by EDX spectroscopy. The X-ray intensity map of the Au Mα signal in red (D) and the EDX spectrum (E) clearly indicated the particles to be gold. 158

Figure 77: DLS intensity plots of Au-NH_2 and Au-OMe nanoparticles dispersed in CCCM at 10 µg/mL and 50 µg/mL. The scattering peak at ~9 nm is due to the horse serum albumin present in the growth supplement added to the CCM for cell culture. 159

Figure 78: 3D reconstructions produced using Imaris software from image datasets obtained by slice and view imaging of two cells treated with 50 µg/mL Au-NH_2 nanoparticles. The reconstructions illustrate the range of nanoparticle uptake between cells, with (A) showing a cell containing 183 nanoparticles and (C) a cell containing 22 nanoparticles. Images (B) and (D) have been automatically (contrast) thresholded using Imaris software to segment the nanoparticles in green from the components of the cell in red. 161

Figure 79: (A) A 3D reconstruction of a whole cell treated with 50 µg/mL Au-OMe nanoparticles produced in Imaris software from image datasets obtained by slice and view imaging. (B) Contrast thresholding was carried out using Imaris software to segment the nanoparticles in green from other cell components in red to count a total of 140 nanoparticles inside the cell. 162

Figure 80: Optical light microscope images of TK6 cells exposed to 1 µg/mL Au-NH_2 nanoparticles for 24 h. (A) shows either bi-nucleated cells which indicate healthy cell division, or mono-nucleated and multi-nucleated cells which can be markers of cell cytotoxicity. (B) shows a bi-nucleated cell containing two micro-nuclei, micro-nuclei are markers of genotoxicity. 163

Figure 81: Cell survival and micronucleus presence within bi-nucleated cells for TK6 cells exposed to Au-NH_2. Some degree of toxicity was observed after treatment with nanoparticles (LH y-axis). A significant increase in DNA damage was seen with increasing dose (RH y-axis), where %Bi/Mn is the percent frequency of micronuclei in bi-nucleated cells. Errors are given as the standard deviation of n=3 measurements, with significance obtained by a paired t-test where, * = $p<0.05$. 164

Figure 82: Cell survival and micronuclei presence within bi-nucleated cells for TK6 cells exposed to Au-OMe. No significant cytotoxicity was observed at any dose (LH y-axis), whilst an increase in chromosomal damage was seen with increasing dose (RH y-axis), where %Bi/Mn is the percent frequency of micronuclei in bi-nucleated cells. Errors are given as the standard deviation of n=3 measurements, and statistical significance obtained by a paired t-test, where * = $p<0.05$. 165

Figure 83: IL-6 ELISA for TK6 cells treated with either Au-NH_2 or Au-OMe nanoparticles. Neither particle type caused any immunogenic response as no significant IL-6 expression was seen at any particle concentration. 167

Figure 84: SDS-PAGE of the hard corona (HC) and soft corona around Au-OMe (A) and Au- NH_2 (B) nanoparticles. For soft corona analysis three washes were analysed; wash 1 (W1), wash 2 (W2) and

wash 3 (W3). The procedure was repeated three times and in each case the results of each gel were reproducible. A Bio-rad precision plus protein dual colour reference ladder was used for the protein mass analysis (left hand channel, units are in kDa). 170

Figure 85: Negatively stained TEM grids of Fe_3O_4 nanoparticles either; (A) uncoated or (B) coated with PEG, and dispersed in water. Negative staining of drop-cast grids with 1% uranyl acetate was carried out for 45 s. 172

Figure 86: Negatively stained TEM grids of SiO_2 nanoparticles dispersed in CCCM. Negative staining was carried out for 45 s using 1% Agar scientific, non-radioactive alternative stain. 173

Figure 87: ABF-STEM imaging of a plunge frozen and vacuum dried suspension of Fe_3O_4-PEG nanoparticles in water on a silicon nitride support film. The PEG coating around the Fe_3O_4 nanoparticles was resolved using an annular collection angle of 5 to 30.9 mrad. 174

Figure 88: EDX analysis of Fe_3O_4-PEG nanoparticles. (A) HAADF-STEM image of two nanoparticles which does not show an obvious coating around the particles as compared to the ABF-STEM images in Figure 87. EDX mapping of the (B) Fe Kα and (C) C Kα signals observed in the EDX spectrum (E) indicated a carbon rich coating around the nanoparticles. These false colour maps are combined in (D). The total accumulated electron fluence for the EDX map was 19 x 10^4 $e^-/Å^2$. 175

Figure 89: EDX analysis of Au-NH_2 nanoparticles in CCCM plunge frozen and vacuum dried on a SiN_x grid. (A) HAADF-STEM image of the area scanned for EDX analysis. EDX mapping of C Kα X-ray (C) showed a C rich accumulation around the nanoparticles, themselves mapped using the Au Lα X-ray signal (B). A combined EDX map (D) indicated this coating did not extend very far beyond the nanoparticles. The coating could be due to either the PEG coating, the formation of a protein corona or a combination of both. The total accumulated electron fluence of the EDX scan was 24 x 10^3 $e^-/Å^2$. 176

Figure 90: TEM images of Au-NH_2 nanoparticles after incubating in PBS + 15 nm Au-BSA (10%). Variable results were seen with the position and number of 15 nm Au-BSA marker particles around the Au-NH_2 nanoparticles (30 nm) variable. 177

Figure 91: STEM-EDX dataset of Au-NH_2 nanoparticles (30 nm) dispersed in PBS with 10% BSA-Au (15 nm). (A) HAADF STEM image, the larger particles are the Au-NH_2 nanoparticles with the smaller particle the Au-BSA. X-ray maps were obtained for (B) Au Lα X-rays, (C) C Kα X-rays, and (D) O Kα X-rays and the Au and C X-ray maps combined in (E). The EDX spectrum is shown in (F). The total accumulated electron fluence for the EDX scan was 15 x 10^4 $e^-/Å^2$. 178

Figure 92: ABF-STEM imaging (A-D) and TEM imaging (E-F) of Au labelled BSA. The Au nanoparticles were found to predominantly associate with salts (white arrows) that had formed in the suspension. A diffuse layer was seen around some Au nanoparticles (C) (dashed line indicating part of the diffuse layer), though this was not seen around every particle imaged (D). The TEM images showed contamination occurred on the sample (layer seen to accumulate around the salts) and there was not always a visible gap between the Au nanoparticle and salt (F). 180

Figure 93: TEM images of the protein corona around un-functionalized PS nanoparticles. (A) The hard and soft corona after incubation of un-functionalized PS nanoparticles in human serum and (B) after centrifugation and removal of the supernatant, but before washing steps. (C) A tomogram slice of an area such as (B), scale bar: 100 nm. The hard corona is shown after the 1st wash (D), the 2nd wash (E)

and the 3rd wash (F). An electron tomogram slice of the area presented in (F) is shown in (G) alongside a superimposed 3D reconstruction. Reproduced from [254]. 181

Abbreviations

DLS	Dynamic light scattering
TEM	Transmission electron microscopy
EDX	Energy dispersive X-ray
EELS	Electron energy loss spectroscopy
STEM	Scanning transmission electron microscopy
Cryo-TEM	Cryogenic transmission electron microscopy
LCTEM	Liquid cell transmission electron microscopy
MRI	Magnetic resonance imaging
EPR	Enhanced permeability and retention
DLVO	Derjaguin-Landau-Verwey-Overbeek
CCM	Cell culture media
FBS	Fetal bovine serum
CCCM	Complete cell culture media
PAA	Polyacrylic acid
PEG	Polyethylene glycol
ROS	Reactive oxygen species
PS	Polystyrene
PAGE	Polyacrylamide gel electrophoresis
SDS	Sodium dodecyl sulfate
DCS	Differential centrifugation sedimentation
NTA	Nanoparticle tracking analysis
EM	Electron microscopy
BSA	Bovine serum albumin
PDMS	Polydimethyl siloxane
HAADF	High angle annular dark field
FIB-SEM	Focused ion beam - scanning electron microscopy
DI	De-ionised
XRD	X-ray diffraction
FTir	Fourier transform infrared
PSS	Polystyrene sulfate
DMEM	Dulbecco's Modified Eagle media

RPMI	Roswell Park Memorial Institute
PBS	Phosphate buffered saline
SBF	Simulated body fluid
SEM	Scanning electron microscope
FEG	Field emission gun
CTEM	Conventional transmission electron microscopy
BF	Bright field
DF	Dark field
HRTEM	High resolution transmission electron microscopy
CCD	Charge-coupled device
ADF	Annular dark field
ZLP	Zero loss peak
ELNES	Electron loss near edge structure
SI	Spectral imaging
HS	Horse serum
CBMN	Cytokinesis-block micronucleus assay
ELISA	Enzyme linked immunosorbent assay
RPD	Relative population doubling
FFT	Fast Fourier Transform
HA	Hydroxyapatite
PDI	Polydispersity index
ABF	Annular bright field

Chapter 1

1. INTRODUCTION

A nanoparticle is commonly defined as any particle that has length of 1-100 nm in at least one dimension [1]. Therefore, any particle that falls within this definition can be assigned as a nanomaterial including organic, non-organic and metallic material. In the last 20 years there has been a rapid increase in research and application of nanomaterials within a number of industries. One such application is in medicine where nanotechnology has shown promise in therapeutics and diagnostics. This field of science is referred to as nanomedicine and is a relatively new area of research having only been established in the early 1990s [2]. Today there are numerous publications concerning nanomedicine and the possible application of nanotechnology to a range of diagnostic and therapeutic uses including cancers, tissue engineering and medical imaging [3, 4]. However, widespread successful clinical application has still not been achieved. This is in part due to concerns about the possible toxicity of nanomaterials upon entry into the body. Therefore, a fundamental understanding of the behaviour of nanomaterials when they come into contact with biological systems and fluids is essential to further progress the application of nanotechnology in medicine and address concerns about

(nano)toxicity. Two main ways in which the behaviour of nanoparticles suspended in a fluid *in vivo* and *in vitro* can be influenced is through changes to the dispersion state or through interactions at the surface or bio-nano interface that result in the formation of coatings around nanoparticles.

1.1 Nanoparticle dispersion

The dispersion state of a nanoparticle refers to how it disperses in suspension. For example, nanoparticles can remain mono-dispersed which defines a system where they exist as single, stable colloid particles in suspension (Figure 1(A)). Alternatively nanoparticles can dissolve or transform into agglomerates or aggregates when dispersed in certain media which means they exist as a collection of loosely or physically bound particles respectively (Figure 1(B)). Finally, nanoparticles or agglomerates/aggregates may float or fall out of a suspension entirely, the latter being known as sedimentation (Figure 1(C)).

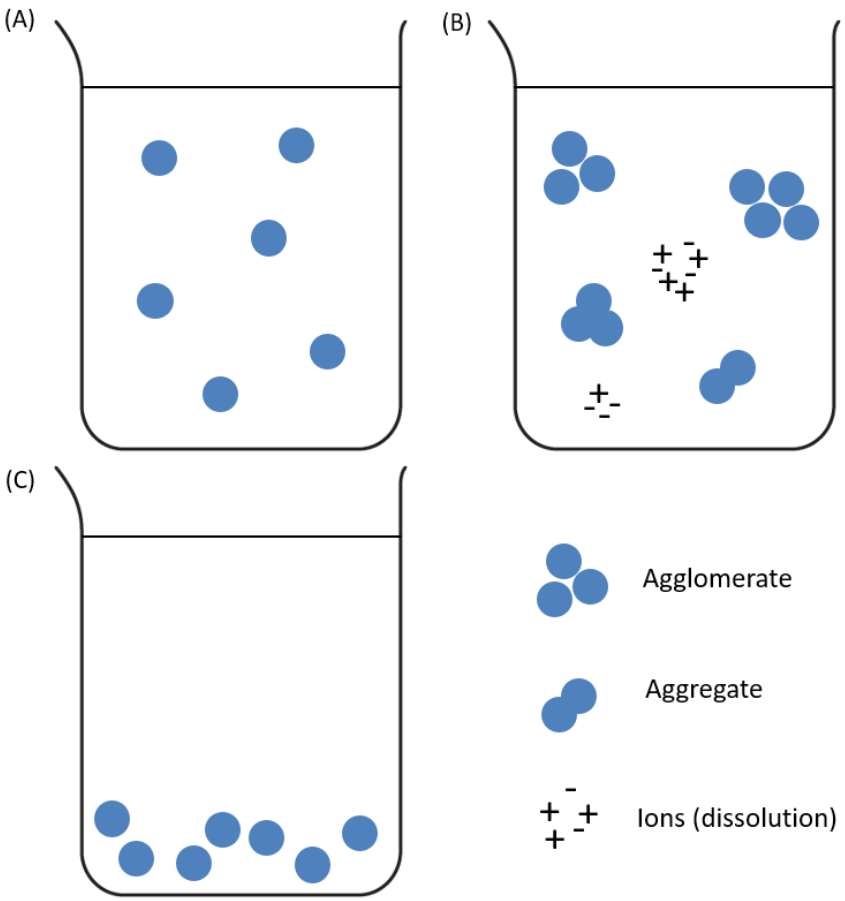

Figure 1: A schematic illustrating the possible dispersion states of nanoparticles in suspension. Colloidally stable nanoparticles remain monodispersed (A). Alternatively, nanoparticles can dissolve in suspension and/or transform into agglomerates or aggregates (B). Some nanoparticles can fall out of suspension entirely and sediment (C). Adapted from [5].

To investigate the therapeutic potential or potential toxicity of specific nanoparticles, target cells must be treated with these nanoparticles through both *in vivo* (in live models) and/or *in vitro* (in isolated tissue or cells) studies. In order to do this, nanoparticles must be dispersed within appropriate biological media prior to cell treatment. Consequently, the dispersion state of nanoparticles within this media can significantly affect biological function. For example, if a system became agglomerated then the effective size of particles that might interact with a cell would increase, and this can alter the overall cell uptake and response [6]. In addition, should an intended dose defined by particle number be used, then this will effectively be reduced upon nanoparticle agglomeration. As a result it is vital to be able to accurately characterise the dispersion state of nanoparticles in biological fluids relevant to

those routinely used in *in vitro* and *in vivo* models. Understanding dispersion will enable comparisons between the efficacy and/or toxicity of different nanoparticles of different size, morphology and composition.

1.2 Bio-nano interface

The bio-nano interface defines the boundary between a nanoparticle's surface and the biological environments it encounters. Interactions that occur at this interface can significantly change the 'biological identity' of a nanoparticle as proteins and other biomolecules can adsorb onto its surface [7]. Since proteins are widely distributed within any biological system these are the most abundant biomacromolecules that bind to a nanoparticle surface and this nanoparticle-protein interaction is often defined as a protein corona [8]. Since the protein corona becomes the outermost surface of a nanoparticle it is a significant factor in determining cellular interactions. Therefore, in similarity to monitoring nanoparticle dispersion state, understanding the specific interactions that occur at the bio-nano interface is necessary to predict and assess the efficacy and toxicity of nanoparticles for therapeutic treatments.

1.3 Nanoparticle characterisation in biological media

It is clear that in order to further the application of nanomaterials in medicine and to understand fully the toxicological implications of nanomaterials, the ability to accurately characterise nanoparticles dispersed in complex biological media is fundamental.

Characterising and understanding the interactions and dispersion state of particles in simple systems such as water can be achieved relatively easily through bulk analysis techniques. For example, dynamic light scattering (DLS) is routinely used for size distribution analysis of nanoparticle dispersions. However, biological fluids are complex systems containing multiple bio-macromolecules in suspension including vitamins, amino acids and proteins. DLS can often be confounded by an inability to distinguish between nanoparticles and these other components in more complex biological media (Figure 2). In addition, studies of the protein corona have largely been carried out using bulk

electrophoresis techniques for protein analysis. However, since the protein corona is a dynamic layer the differences between corona around different particles in suspension is not identified through these bulk techniques. Therefore, the development of alternative characterisation techniques becomes necessary.

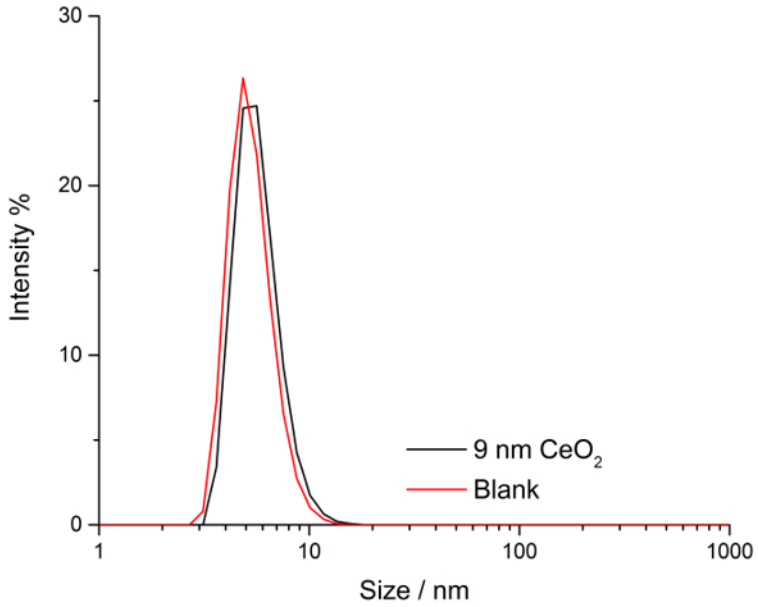

Figure 2: DLS analysis of cell culture media with 10% fetal bovine serum supplement (red) alongside a suspension of 9 nm CeO_2 nanoparticles in cell culture media with 10% fetal bovine serum (5 µg/mL). The scattering signal from serum proteins is at ~7 nm and cannot be distinguished from that of the 9 nm nanoparticles by DLS analysis alone.

One such analytical alternative is transmission electron microscopy (TEM). TEM is a leading technique for nanoparticle characterisation due to its high spatial resolution enabling size, shape and crystallinity information to be obtained. In addition, analytical TEM through energy dispersive X-ray (EDX) spectroscopy and electron energy loss spectroscopy (EELS) can provide elemental analysis of specimens down to the sub nanoparticle level. Such high spatial resolution with the addition of spatially resolved elemental analysis by scanning TEM (STEM) provides a technique that can probe interactions at the solid-liquid interface and accurately identify the primary particle size and/or agglomerate size of dispersed nanoparticles. However, in order to image a specimen in this way by

S/TEM, it must be subject to very high vacuum environments and as such samples are ordinarily dried prior to imaging. For dry samples this does not pose a problem, yet when aiming to investigate the state of nanomaterials in liquid suspension, drying removes the particles from the native state and the original form is lost. Indeed, the process of drying a sample in air can lead to artefacts where nanoparticle dispersion can rearrange on a TEM support grid whilst drying. Resulting images and any elemental analysis are no longer representative of the hydrated suspension. Such drying artefacts make accurate characterisation of dispersed nanoparticles difficult and, as a consequence, *in situ* techniques have been developed which allow TEM analysis of specimens in or close to the hydrated state, despite the vacuum requirements of TEM.

1.4 *In situ* TEM

Two *in situ* TEM techniques are cryogenic (cryo) TEM and liquid cell (LC)TEM. LCTEM permits a liquid to be encased within a specially designed TEM holder allowing direct imaging of a sample in solution. There has been huge interest in this technique, and it is a rapidly developing field of research within materials science. However, with increased use and knowledge it has become clear that there are significant interactions that can occur between a sample and the electron beam. These beam-sample interactions complicate analysis where nanoparticle dissolution, transformation and/or movement away from the original dispersion can be induced [9].

In comparison, cryo-TEM has been developed and used for much longer, traditionally within the life sciences but its use in materials research is now becoming more prevalent [10]. A sample is prepared such that it is captured within a layer of vitreous ice without significant movement or rearrangement of the original nanoparticles in a dispersion. This frozen sample can then be transferred into the TEM allowing a sample to be imaged in the frozen hydrated state – a far more accurate representation of a nanoparticle dispersion compared to a dried sample. The additional benefits of using cryo techniques within material science research is the potential to carry out elemental analysis by EDX and EELS on these frozen samples. This latter type of analysis is still in its infancy yet the development

of these *in situ* cryo analytical TEM techniques for nanoparticle characterisation in biological media will enable a more comprehensive understanding of the bio-nano interface.

Summary

Overall, it has been established that it is the bio-nano interactions and dispersion behaviour of nanoparticles in biological environments that can define their biological function. As such the following chapter looks at past and present literature relating to these areas of interest. In addition important literature focusing on conventional and *in situ* analytical TEM for nanoparticle characterisation is reviewed. Finally, areas for further development in this field will be identified enabling the aims and objectives of this study to be listed ahead of reporting on experimental methods and results.

Chapter 2

2. LITERATURE REVIEW

An evaluation of past and current literature surrounding the dispersion of nanoparticles both in simple media (e.g. water) and complex biological fluids has been presented, alongside important literature referencing the widely studied protein corona formation around nanoparticles in biological environments. Publications demonstrating the use of TEM as a powerful technique for nanoparticle characterisation when dispersed in these challenging environments are presented together with limitations of this technique. Such limitations can often be overcome by the use of *in situ* techniques and work referring to LCTEM and cryo-TEM has been identified. Finally, recent publications that utilise cryo-analytical S/TEM have been reviewed and indicate this technique could be very beneficial in developing accurate techniques for characterising nanoparticles dispersed in more complex biological environments.

2.1 Nanotechnology for medical applications

Among the many applications of nanotechnology, there is a lot of research into the potential for use in medicine for diagnosis, prevention, monitoring and treatment of disease (Figure 3). Nanoparticles have been shown to have significant potential within the field of medicine due to unique properties comparative to the corresponding bulk material. Tuning the size, shape, surface and core properties have all been shown to have a fundamental effect on biological function.

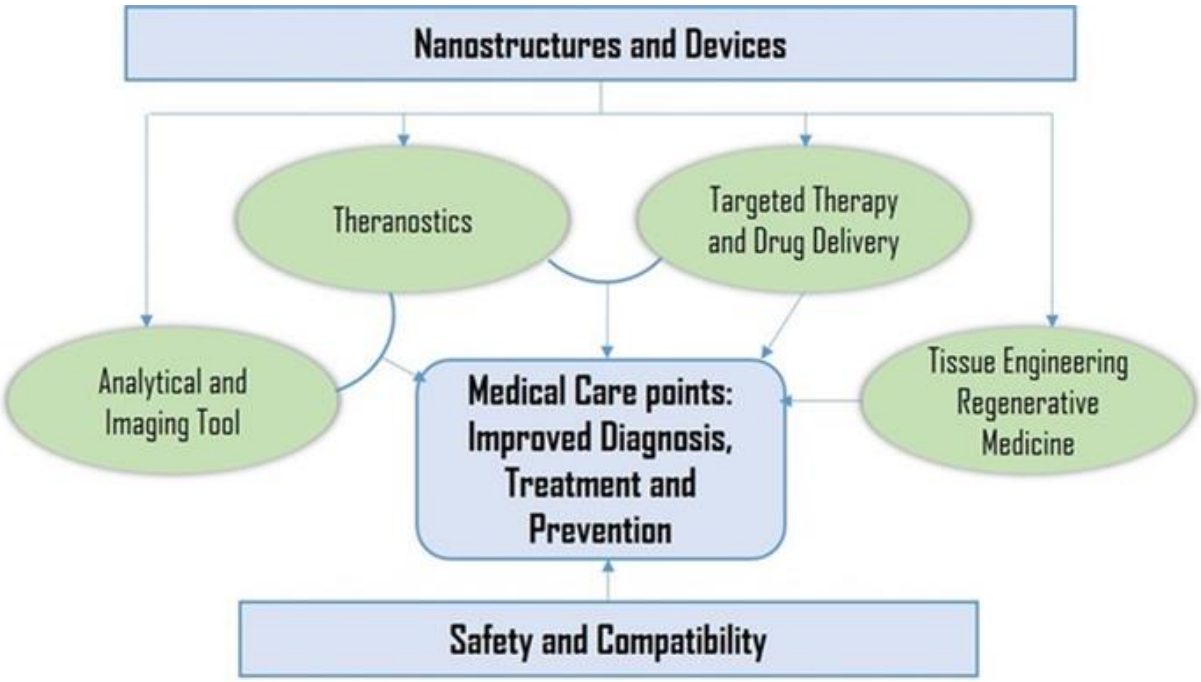

Figure 3: An illustration of the application and current goals of nanotechnology in medicine. Research has shown a range of nanostructures and devices have potential in diagnostics, theranostics and therapeutics. Reproduced from [11].

Nanomaterials can be used to enhance contrast for medical imaging which in turn facilitates early diagnosis and can be used to monitor pathological processes and therapeutic effects [12]. Supraparamagnetic iron oxide nanoparticles (SPIONs) are routinely cited as effective contrast enhancing agents in magnetic resonance imaging (MRI) [13]. The high magnetic strength, extended time of contrast improvement and relatively low cytotoxicity are all factors contributing to the efficiency within MRI [13]. There are now some SPION based products approved for clinical use (e.g. Feridex®, Combidex®, Resovist®) which are formed of an inorganic iron oxide core, coated with a

hydrophilic polymer to extend circulation time and improve bio-compatibility [14]. Gold nanoparticles have also been investigated significantly for application in medical imaging due to their biocompatibility and relatively low toxicity [3, 15-19]. They have been used as contrast agents to detect tumours in mice [3], to detect head and neck cancer *in vitro* using standard clinical, computer-tomography scanning [20], and to selectively target squamous cell carcinoma using gold nanorods conjugated with antibodies [16]. Furthermore, gold nanoparticles exhibit surface plasmon resonance of light at visible wavelengths which makes them ideal candidates for use as optical biosensors [17]. The change in surface plasmon resonance with molecular adsorption or size has been utilised in the detection of human immunodeficiency virus [18] and DNA gene identification [19].

Beyond diagnostics there is clear evidence of potential for therapeutic efficacy of nanomaterials within medicine. This is most often through drug delivery where a drug is encapsulated within or attached to a nanoparticle. These nanoparticles are then either specifically designed to target a certain tissue [21] or in the case of some cancer therapy, can selectively target tumours due to the permeability and retention (EPR) effect [22]. The EPR effect describes a process where the enlarged pore size of blood vessels within a tumour compared to healthy tissues allows nanomaterials to pass easily into the tumour from the blood stream. This, in combination with a loss of lymphatic drainage, results in the selective accumulation of nanoparticles in tumours [23]. The nanoscale particles used in drug delivery are usually small enough that uptake into target cells is relatively easy [4] and in some cases have the ability to cross the blood brain barrier [24]. Polymeric nanoparticles have seen a significant interest for drug delivery since easy manipulation of the surface can allow specific, targeted delivery and also controlled release of the drug. Such 'biopolymers' allow active components, proteins, peptides and genes to be released within a target tissue (Figure 4) [25]. Inorganic metallic nanoparticles have also been shown to have application in drug delivery, for example, relatively inert and biocompatible gold and silver plus zinc oxide, barium titanate and iron oxide nanoparticles, however there are some concerns about the possible toxicity of these nanoparticles [26]. Nonetheless drug delivery systems

utilising nanotechnology have been introduced clinically for the treatment of cancers (Doxil®) [27] and for therapeutic delivery of peptides and other small molecules (Estrasorb®) [28].

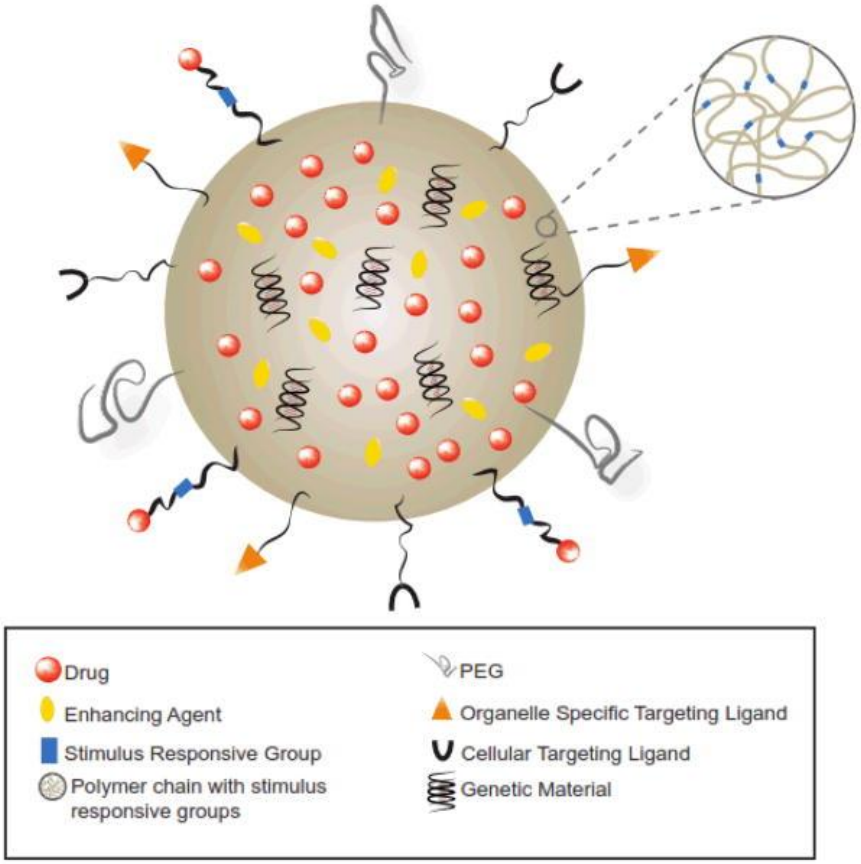

Figure 4: A schematic of a nanoparticle with multiple design features for targeted drug delivery. Reproduced from [29].

However, despite research into the application of nanomaterials in medicine rapidly increasing over the last 20 years, where just 3 papers were cited on Web of Science in 2000 containing the word nanomedicine compared to 1,906 in 2019, progress in clinical application continues to lag behind, with only 50 nanodrugs being used commercially to date [30]. Nanomedicinal studies require nanoparticles to be dispersed in biological fluid prior to use but exactly how nanoparticles interact with this biological fluid is still not properly understood and it is this uncertainty that has prevented, in part, the wholesale clinical application of promising nanomedicines. Interactions occurring at the solid-liquid interface between nanoparticles and biological media can define the *in vivo* and *in vitro*

behaviour of nanoparticles which ultimately determines and allows predictions to be made about potential efficacy and/or toxicity.

2.2 Bio-nano interactions

The interactions that occur at the solid (particle)-liquid (media) interface are often colloquially termed bio-nano interactions [31]. Such bio-nano interactions can define the colloidal stability of nanoparticles within biological media and/or the formation of any coatings around the nanoparticles that alter biological identity. The difficulties in understanding and predicting these interactions stems from the complexity of biological environments. In simple systems where nanoparticles are dispersed in water, theoretical models can be used to accurately predict for example, colloidal stability. However, this is not the case for biological systems, where higher ionic strength and the additional presence of large bio-macromolecules such as proteins can contribute to and complicate the behaviour of nanoparticles dispersed in biological media.

2.2.1 Nanoparticle dispersion

For nanoparticle cell uptake studies either *in vivo* or *in vitro*, nanoparticles must be dispersed in biological media. How nanoparticles disperse in this media, as mono-dispersed, agglomerated or aggregated species or even dissolved or chemically transformed species, can dramatically alter the resulting biological function. It is the nanoparticle-nanoparticle interactions that define dispersion of a system and this is often described using Derjaguin-Landau-Verwey-Overbeek (DLVO) theory. Both short range van der Waal attractive and coulombic repulsive forces exist between particles, the strengths of which define how colloidally stable they are as a dispersion, where colloidal stability is defined as a monodispersion and occurs when repulsive forces dominate. In a simple system such as water which has low ionic strength, colloidal stability of nanoparticles can be predicted relatively easily by the surface potential of the particles; where a surface zeta potential of >+30 mV or <-30 mV usually defines a colloidally stable system. However, these predictions do not hold for nanoparticles dispersed in biological media. Here the greater ionic strength of the media can reduce the electrostatic double

layer of ions around a particle which in turn can reduce the barrier to aggregation and agglomeration and hence alter the dispersion in biological media compared to water [32] (Figure 5). This phenomenon is referred to as the screening effect and is accepted to occur in all high ionic strength media [33].

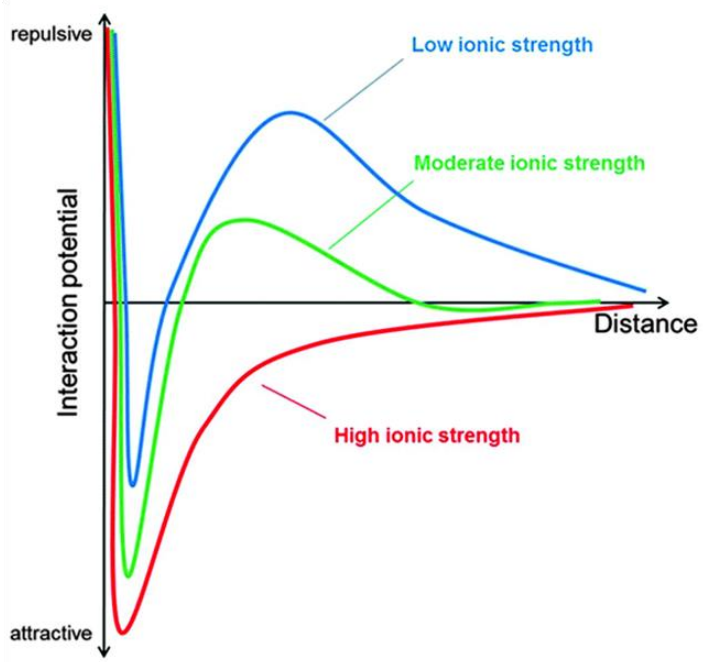

Figure 5: A schematic showing the impact of ionic strength on effective electrostatic forces between suspended particles as a function of distance and ionic strength. At low ionic strength (blue) repulsive coulombic forces dominate. Increasing the ionic strength reduces the repulsive potential barrier (green line). Further increasing the ionic strength in line with that predicted for a physiological buffer system leads to a significant decrease in repulsive interaction potential, and the repulsive energy barrier preventing particle agglomeration is lost. Reproduced from [32].

Nel *et al.* [31] stated the dynamic inhomogeneity of biological media can prevent models like DLVO theory from providing meaningful predictions of nanoparticle colloidal behaviour. For much nanoparticle research in nanomedicine and nanotoxicology nanoparticles are routinely dispersed in cell culture media (CCM). This is an aqueous biological media containing a range of salts, vitamins and

amino acids and when used for cell culture is usually supplemented with a growth factor containing proteins, for example fetal bovine serum (FBS), henceforth CCM supplemented with FBS is referred to as complete cell culture media (CCCM).

Significant work has been carried out looking at the dispersion of different nanoparticles in CCM and CCCM [34-37]. Ji *et al.* [34] measured the dispersion of TiO_2 nanoparticles in a range of biological media using high throughput DLS and identified that, whilst in water the nanoparticles remained colloidally stable with a zeta potential of 30.2 mV, when dispersed in CCM a much poorer dispersion state was observed (Figure 6). Furthermore, they identified that not only does the dispersion change dependent upon the biological media, in CCM the agglomerate size increased with increasing nanoparticle concentration whereas in water the agglomerate size remained fairly stable across a concentration range from 2 µg/mL to 100 µg/mL. Such variations across concentration are significant when cellular dose-response studies encompass a range of concentration treatments. In such instances the average effective nanoparticle or agglomerate size presented to a cell would not then be the same for each dose which could lead to misinterpretation of results showing variations in, for example, cell uptake across concentrations.

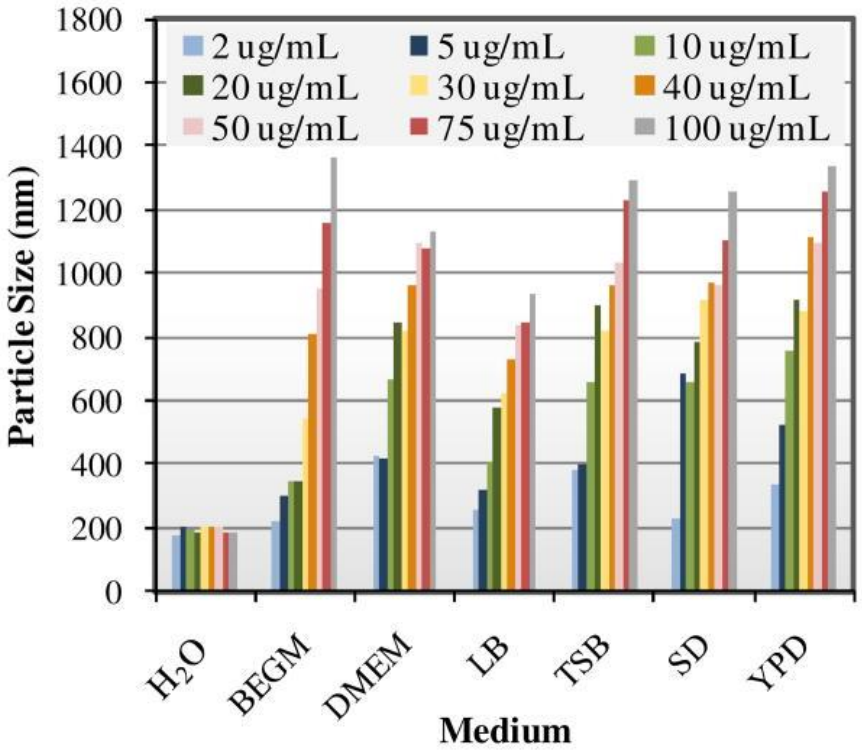

Figure 6: TiO_2 nanoparticle agglomerate size as measured by high throughput DLS in a range of different CCM. Agglomerate size increased in CCM and with increasing TiO_2 nanoparticle concentration. The different CCMs used were; Bronchial Epithelial Growth Medium (BEGM), Dulbecco's Modified Eagle's Medium (DMEM), Luria Bertani Broth (LB), Tryptic Soy Broth (TSB), Synthetic Defined medium (SD), Yeast Extract Peptone Dextrose medium (YPD). Reproduced from [34].

Further work published by Strojan et al. [35] showed, in agreement with Ji *et al.,* that there can be extreme variation in the dispersion state of nanoparticles in different biological media. They dispersed Polyacrylic acid (PAA) coated cobalt ferrite nanoparticles and silica nanoparticles in a range of media including DI water, PBS, NaCl and CCM and, whilst for PAA-cobalt ferrite nanoparticles there was no obvious difference in dispersion between the media, significant agglomeration of the silica nanoparticles was observed in all media. This suggests that not only the suspension media, but also the nanoparticle properties dictate dispersion. Furthermore, agglomeration of the silica nanoparticles was reduced (except in water) when 10% FBS was added. FBS is a protein containing supplement, thus

suggesting that a colloidally stabilising interaction between the proteins and silica nanoparticles occurred, something that is further discussed in section 2.2.2.

Understanding the dispersion of nanoparticles in biological media is paramount to understand and optimise nanomedicinal studies. Halamoda-Kenzaoui *et al.* [38] identified a demonstrable difference in cell uptake dependent upon the agglomeration state of silica nanoparticles. They observed that in the case of 80 nm silica nanoparticles there was greater cell uptake of agglomerated particles (hydrodynamic diameter ~130 nm) compared to single particles. This was most likely driven by an effective increased dose when agglomeration occurred. Further evidence that agglomeration affects cellular uptake was shown by Albanese *et al.* [6] where they indicated a 25% decrease in cellular uptake of aggregated gold nanoparticles compared to monodispersed gold nanoparticles. In addition since it is widely accepted that the size of nanoparticles can greatly influence the efficacy and/or toxicity of nanoparticles [39] then should nanoparticles become agglomerated during *in vivo* or *in vitro* investigation it would follow that their efficacy and toxicity will no longer represent that of the single particle. This could be further complicated since Oberdoster *et al.* [40] have shown that surface area can greatly effect nanotoxicity as well. These studies indicate the importance of preliminary work to fully understand the dispersion of nanoparticles in the biological media in which they will be dispersed for further biological *in vitro* or *in vivo* studies in order to prevent misrepresentation of results.

Current research is looking at the potential of nanoparticle surface modification to enhance and control dispersion in biological fluids. In simple systems (e.g. water) electrostatic stabilisation can improve colloidal stability. However, in the case of biological media where the electrostatic double layer is compressed by the higher ionic strength environments, electrostatic stabilisation rarely improves colloidal stability [41, 42]. In comparison steric stabilisation, where agglomeration of particles is reduced by the introduction of a physical barrier can have some impact within biological environments. This is traditionally performed by coating a nanoparticle surface with a polymer, in addition to which the hydrophilic nature of a polymer chain end can further improve colloidal stability

through the introduction of short-range repulsive hydration forces [37]. One of the most common polymers used to improve colloidal stability in biological systems is polyethylene glycol (PEG), largely due to its high hydrophilic nature which has been shown to permit notable long-term stability in high ionic strength media [43-45]. Other polymers can also be used for colloidal stabilisation [46, 47], however PEG benefits from the ability to easily adapt the termination functional group which can in turn aid in design for effective medicinal use in for example drug delivery [48]. However, incomplete coverage of the nanoparticle or the occurrence of bridging between particles during the coating process can in some instances induce nanoparticle agglomeration, so effective coating techniques must be used [49].

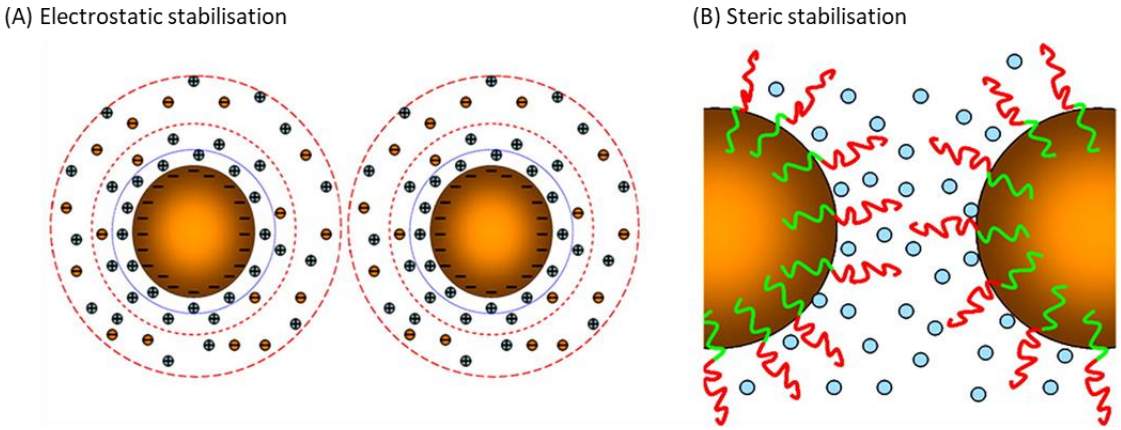

Figure 7: A schematic illustrating electrostatic (A) and steric (B) dispersion stabilisation. In biological media the distance the electrical double layer extends away from the particle surface is reduced preventing effective electrostatic stabilisation, whilst steric stabilisation by polymer addition for example can enhance colloidal stability. Adapted from [50].

Not only is an understanding of the dispersion of nanoparticles in extracellular environments necessary, but complex intracellular environments can also be expected to lead to changes in dispersion. The vast proportion of nanoparticles are taken up into most cells via endocytosis, a broad term describing the process of a cell encapsulating a nanoparticle within a membrane adapted vesicle inside the cell (Figure 8). These vesicles, either endosomes or lysosomes, are at a pH much lower than physiological pH of the cell cytoplasm. As a nanoparticle passes down the endo-lysosomal pathway it

moves from environments of pH 7 (extracellular) to pH 5.5 (early endosomes) and pH 4.5 (lysosomes). To date such investigation of dispersion in buffers to mimic these vesicle environments is limited, yet in cell section imaging nanoparticles can appear as clusters within intracellular vesicles which suggests possible agglomeration. However, whether this occurred prior to cell uptake or is due to cells actively packing nanoparticles together during the formation of lysosomes by amalgamating endosomes, cannot easily be concluded. More extensive research has looked at how the low pH environments can promote nanoparticle dissolution in some cases [51]. Such dissolution, where it occurs, is largely linked with nanoparticle toxicity due to dissolved ions causing the production of reactive oxygen species (ROS) which are detrimental to a number of cell functions. This is another indication of the need to characterise nanoparticles in a range of appropriate biological environments.

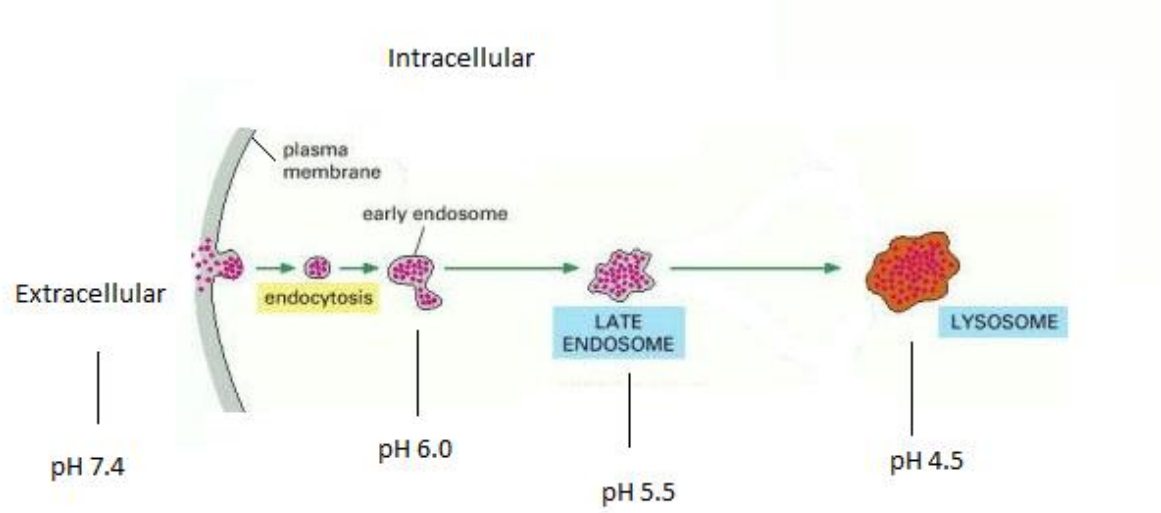

Figure 8: A simplified schematic of the main process of endocytosis, the method through which nanoparticles can be taken up into a cell. Adapted from [52].

Ultimately, there is a clear indication that preliminary dispersion studies of nanoparticles of interest in appropriate biological media prior to or alongside any *in vivo* or *in vitro* studies are necessary. However, the aim must be to enable modelling and accurate predictions of all nanoparticle behaviour in dynamic inhomogeneous biological environments to further progress the clinical application of nanoparticles for medical advancements [37].

2.2.2 The protein corona

Beyond just the dispersion of nanoparticles in biological media, understanding the physical interactions and changes that occur at the surface of a suspended nanoparticle is also important. The high surface potential of many nanoparticles favours interaction with biomacromolecules [53, 54] which leads to the adsorption of proteins immediately upon dispersion in protein containing media. This leads to the formation of a protein corona, a protein layer encapsulating a suspended nanoparticle (Figure 9). The protein corona consists of two layers known as the hard corona and the soft corona. The hard corona refers to tightly bound proteins of high affinity to a nanoparticle surface and the soft corona consists of more loosely bound low affinity proteins [55]. It has been described as a dynamic layer where proteins in the soft corona can bind and unbind depending on their respective affinity for a nanoparticle surface (Figure 9) [8]. Such surface modification upon contact with biological media can dramatically alter the biological identity of nanoparticles and hence change biological function. Yet predicting the dynamic composition of the protein corona is difficult when as many as 3,700 proteins have been identified in blood plasma alone [56].

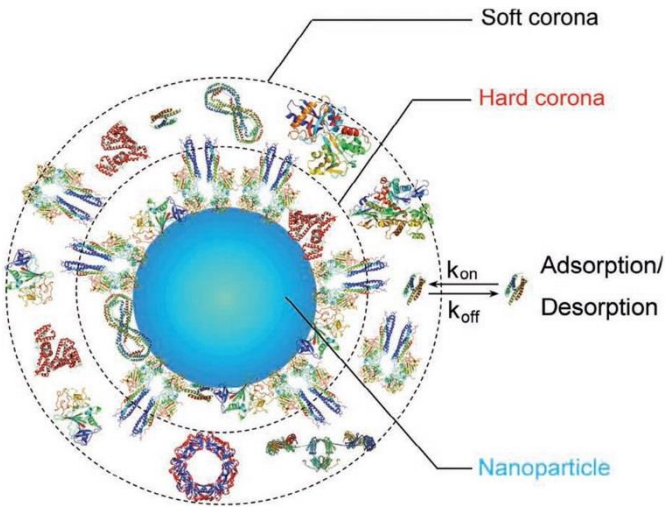

Figure 9: A schematic of the protein corona that forms around nanoparticles exposed to protein containing biological media. Reproduced from [7].

It is widely accepted that the surface curvature of nanoparticles affects protein binding such that it differs to binding on a corresponding bulk material that is relatively flat [57], therefore the size of a

nanoparticle influences the composition of the protein corona that forms [58]. Additionally the surface properties and shape of nanoparticles strongly influence protein absorption. Lundqvist *et al.* [55] determined that size and surface charge of nanoparticles can alter the composition of the protein corona. They identified a degree of difference in the proteins present in corona around polystyrene (PS) nanoparticles with primary particle sizes of 50 or 100 nm by 1D-polyacrylamide gel electrophoresis (PAGE) and mass spectrometry. In addition significant variation in the composition of the protein corona was identified between PS nanoparticles with a positive, neutral or negative surface potential indicating that nanoparticle surface properties play an important if not critical role in determining protein corona formation rather than the inherent core properties of the nanoparticles. Indeed, it has been shown that the hydrophobic or hydrophilic nature of a nanoparticle surface can determine the extent of conformational change (usually irreversible) that proteins undergo on surface contact, where Monopoli *et al.* [59] showed conformational changes in insulin were greater upon absorption to hydrophobic surfaces. Garcia-Álvarez *et al.* [60] showed that nanoparticle shape can also affect the protein corona, and moreover carried out analysis on *in vivo* models which indicated some degree of difference to *in vitro* studies. Therefore, they suggested that *in vivo* conditions should be used more routinely to try and broaden the current understanding of potential medicinal use of nanoparticles.

The presence and composition of a protein corona can greatly influence biological behaviour. For example, Lesniak *et al.* [61] demonstrated that significant differences in nanoparticle cell uptake correlated to differences in protein corona composition. They showed this through the use of fluorescently labelled PS nanoparticles and found that cell uptake of 40 nm PS-COOH nanoparticles was higher when incubation prior to cell treatment was serum free (i.e. without the presence of proteins) than compared to cell uptake of nanoparticles incubated in protein containing serum (i.e. with an established protein corona). Further to this Cheng *et al.* [62] demonstrated that cell uptake was reduced for 50 nm gold nanoparticles with a protein corona compared to nanoparticles without. However, this reduction in cell uptake was not observed for smaller 5 nm and 20 nm nanoparticles

with a protein corona. This suggested that it is not only the presence or otherwise of the protein corona that can dictate cell uptake but also potentially its size/shape and/or composition.

Due to the significant biological impact of the protein corona recent research has looked at employing nanoparticles designed to specifically reduce protein interactions. PEGylation of nanoparticles can deter protein adsorption and lead to extended circulation of particles in the body [63]. However care must be taken where in some cases proteins can competitively exchange with stabilising surfactants and/or enhance agglomeration [37]. Furthermore, Oh *et al.* claimed that such methods do not overcome the necessity to add further ligands to enhance delivery specificity which themselves promote protein corona formation [64]. Instead they suggested that pre-coating nanoparticles with supramolecular proteins can deter the formation of an unknown protein corona, and allows targeting toward specific tissues, etc. Such pre coating with protein is sometimes referred to as 'stealth coating' and has shown promise in optimising nanoparticle design to regulate cellular interaction [65], improve drug delivery [66] and increase circulation time [67].

Overall the protein corona is a well-established interaction that occurs at the solid-liquid interface between nanomaterials and protein containing biological media and hence understanding and predicting these interactions should lead to improvements in the design and application of nanoparticles in medicine. Consequently, identifying potential techniques to accurately characterise these interactions is necessary.

2.3 Characterising the bio-nano interface

Considering the evidence that interactions at the bio-nano interface can drive changes that alter the biological function of nanoparticles, carrying out accurate and thorough characterisation of these interactions is important. The majority of the literature cited so far refers to work carried out using bulk techniques either for dispersion analysis or protein corona analysis [68]. In the case of dispersion analysis, DLS is the most common (bulk) technique used. It is a simple light scattering technique that provides statistically relevant data, yet, it can be complicated by the presence of biological

macromolecules in biological environments (see Chapter 5) where data collected becomes harder to interpret as the technique cannot distinguish between nanoparticles and other inherent components present in the media. Similarly, sodium dodecyl sulfate (SDS)-PAGE is the technique predominantly used for protein corona analysis and is a bulk technique that identifies proteins present within a solution according to molecular weight. When coupled with mass spectrometry, SDS-PAGE can give a precise indication of which proteins are binding with a high or low affinity to certain nanoparticle surfaces. However, the assumption is that the proteins identified are present around every particle in suspension in the same quantity. Whether this is actually the case or not cannot be categorically determined by this technique alone.

Such complications when using bulk techniques to investigate the bio-nano interface lead to the requirement for alternative characterisation methods to be used alongside these traditional techniques. Differential centrifugal sedimentation (DCS) is one such alternative and can be used for size distribution analysis. The technique fractionates particles according to their mass where the sedimentation time of particles is measured under the influence of a centrifugal force. Assuming spherical particles of a known density, the hydrodynamic diameter can be calculated from the sedimentation time using the Stokes-Einstein equation (see Chapter 3 section 3.5). DCS typically detects particles >20 nm and can be useful for detecting larger agglomerates up to 10 µm in diameter [69]. A second alternative is nanoparticle tracking analysis (NTA), a hybrid technique that combines the use of a laser beam and an optical microscope [70]. A nanoparticle suspension is illuminated by a laser, and particles in the path of the laser beam scatter light. This scattered light is then detected using a camera attached to the optical microscope which collects short videos of the particles moving due to Brownian motion. Using tracking software individual particles are analysed to determine the hydrodynamic size, again using the Stokes-Einstein equation. The benefit of NTA is that each measurement is carried out on a particle-by-particle basis greatly improving size distribution resolution and allowing accurate identification of any inter-particle variation and the separation of potentially confounding components within biological media from the nanoparticle signal. In addition,

nanoparticle concentration can also be approximated using this technique. However, typically only particles of 30-600 nm can be resolved, smaller particles (<30 nm) can only be detected if they possess a high refractive index (e.g. Gold or silver) [69]. NTA is still a relatively new technique, but has been validated as a viable alternative to DLS [71]. An example of its use for nanoparticle analysis is in investigating the concentration and size of nanoparticles retained in the lungs of workers routinely exposed to soapstone or quartz dust [72].

Despite both DCS and NTA having improved size resolution in comparison to bulk measurement approaches, they are largely limited to >20 nm nanoparticles. Consequently, using high spatial resolution electron microscopy (EM) to carry out highly accurate analysis of nanoparticles in complex biological media is beneficial. TEM can provide detailed information regarding the shape and primary particle size (to resolutions significantly lower than 20 nm) of individual nanoparticles and has the additional benefit of spectroscopic analysis capabilities where spectroscopic analysis through EDX spectroscopy and EELS can provide elemental information regarding the nanoparticles and the bio-nano interface.

2.3.1 TEM for nanoparticle dispersion analysis

EM can be useful when obtaining size distributions of nanoparticles. Inter-laboratory work has been carried out with the aim of producing standardised approaches for this [73] and comparison between DLS and TEM size distribution characterisation has shown TEM to be more accurate, especially when multi-sized particles are present in a sample [74]. This would suggest that nanoparticle dispersion analysis by TEM rather than DLS will have advantages for more complex biological suspensions which typically contain a number of differing sized components. However, significant statistical relevance of size analysis using TEM can be difficult to obtain without collecting and analysing a vast number of images which is very time inefficient. Consequently, automated image analysis is often utilised to obtained size distributions more readily. This can be done relatively easily by simple thresholding software such as ImageJ, however in cases where nanoparticles are overlapping or where

segmentation from non-nanoparticle species within the suspension is difficult more advance methods are required. These are now being implemented, with Oktay and Gurses [75] reporting a deep learning approach that allowed the detection, sizes and number of particles in an image to be quantified. However, applying these manual, semi-automated and fully automated TEM size distribution techniques has yet to be used routinely to investigate the dispersion of nanoparticles within biological fluids. It is likely that such approaches will provide more accurate information of nanoparticle dispersion in biological media than corresponding bulk DLS measurements in some cases at least.

2.3.2 Analytical-TEM

For investigation of interactions occurring at the bio-nano interface analytical-TEM can be very powerful. Both EDX spectroscopy and EELS take advantage of inelastic scattering of electrons as they interact with the sample. As the incident beam comes into contact with the specimen electron-electron interactions occur such that core electrons are displaced from atoms within the sample. In the case of EDX analysis a resulting X-ray of characteristic energy is released and can be detected when outer shell electrons relax to fill these vacant holes. For EELS it is the energy loss of the incident electron that provides the energy for the ionisation of sample atoms that can be measured. In both cases the quantised nature of electron energy shells within elements leads to characteristic energies of released X-rays and electron energy losses which are detected and used to confirm the presence of specific elements in a sample. Further, the use of STEM, where a focused electron beam is rastered across the sample, allows elemental mapping to be carried out which provides information regarding the positions of elements within a sample potentially down to the atomic scale.

EDX analysis has been used to identify silver nanoparticles in an *in vitro* human gastrointestinal digestion model [76], and to ascertain the uptake of TiO_2 nanoparticles in an *in vivo* rat skin model [77]. In addition, Xu *et al.* [78] suggested the formation of a 'nano-bio-complex' around CuO nanoparticles separate to the protein corona by EDX elemental mapping (Figure 10) and further characterisation of interactions occurring at the bio-nano interface were identified by Ribeiro *et al.*

[79], where a coating rich in calcium and phosphorus was demonstrated to form around the TiO_2 nanoparticles dispersed in CCCM.

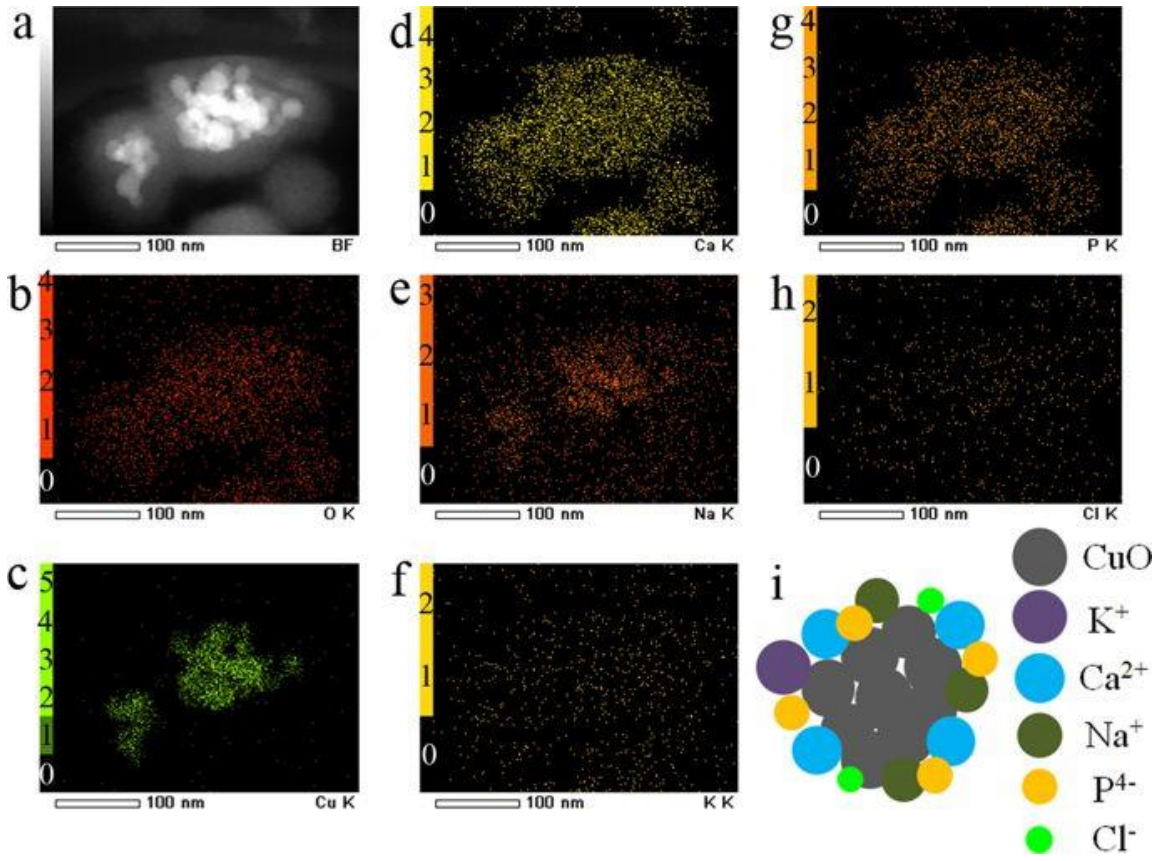

Figure 10: HAADF-STEM and STEM-EDX analysis of CuO nanoparticles suspended in CCCM. A 'nano-bio-complex' composed of K^+, Ca^{2+}, Na^+, P^{4-}, Cl^- was said to form around the nanoparticles during incubation in CCCM. (a) Dark-field TEM image; (b) EDX O K map, (C) EDX Zn Kα map, (d) Ca Kα map, (e) EDX Na Kα map, (f) EDX K Kα map, (g) EDX P Kα map, (h) EDX Cl Kα map. (i) A simple model of the CuO bio-complex. Reproduced from [78].

2.3.3 EM limitations

Characterisation by EM does have limitations; as already mentioned in reference to nanoparticle dispersion analysis by EM, ensuring that there remains statistical relevance to the data is difficult and can be extremely time consuming. In addition TEM analysis is carried out in a high vacuum environment, such that specimens are dried before imaging. This means the samples are no longer suspended in biological media which can remove and/or change any bio-nano interactions.

Furthermore, the most common method of nanoparticle sample preparation is to place a drop of suspension on a TEM grid and leave this to dry in air ('drop cast'). Such sample preparation is known to cause drying artefacts due to surface de-wetting [80] and the 'coffee-ring' effect [81]. Specifically, as a droplet dries on a solid platform capillary action within the droplet can cause the artefactual movement of particles toward the three phase interface i.e. the outer region of the droplet (Figure 11). This induced movement of particles often results in the formation of larger nanoparticle agglomerates/aggregates than are really present in suspension (Figure 11(C)) [82, 83]. Considering these drawbacks of TEM techniques, the development of *in situ* TEM methods has been established which permit the native state characterisation of nanoparticles in solution.

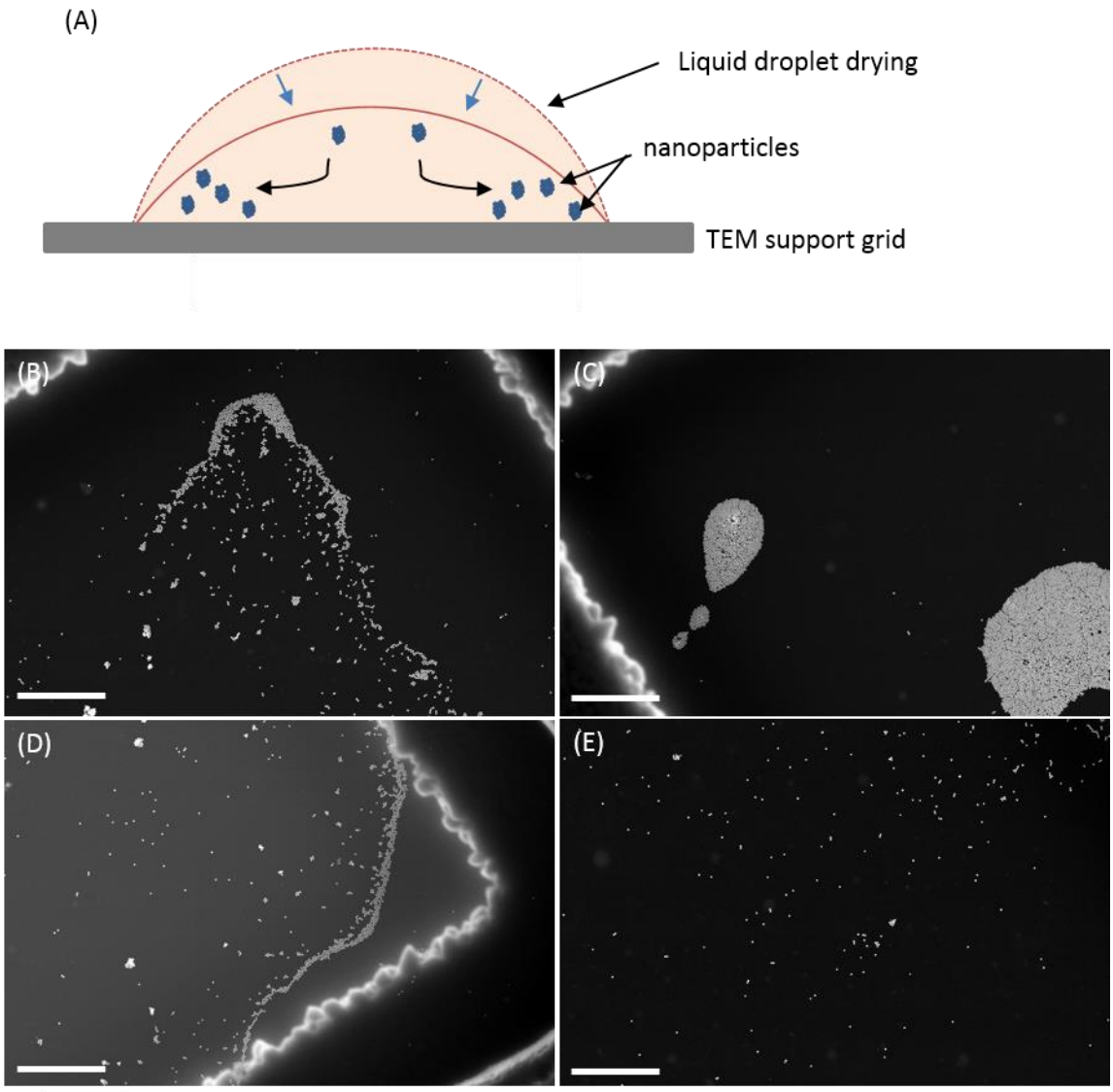

Figure 11: (A) A schematic showing how nanoparticles can move on a TEM support grid during droplet drying in air due to the 'coffee-ring' effect. (B-E) Four HAADF-STEM images of a dispersion of silica nanoparticles (100 nm spheres) in water drop cast onto a TEM grid and dried in air. DLS analysis of the suspension showed the nanoparticles were monodispersed. Drying artefacts occurred during TEM sample preparation such that large agglomerates formed (C) and evidence of the coffee-ring effect was seen (A, C). (D) Indicates an area of the grid where drying artefacts probably did not occur and presents evidence of a monodispersed suspension. The white scale bar indicates a distance of 5 µm.

2.3.4 In situ TEM

Cryo-TEM and LCTEM are two advanced *in situ* TEM techniques that can remove drying artefacts associated with conventional drop-cast TEM and allow characterisation of nanoparticles in the hydrated state. Of the two, LCTEM allows direct observation of a liquid sample without any pre-specimen preparation processes [84]. The technique has application in both life science and materials science research and has been used to, for example, image biological cells [85] monitor crystallisation [86] and examine nanoparticle growth [87]. However, extensive interactions can occur between the electron beam and the liquid sample [88]. These interactions can dramatically alter the chemistry of the liquid sample, producing highly reactive radiolytic products that can alter pH and interact with molecules in the sample. Such beam induced changes can be utilised for the analysis of dynamic process [89] but are detrimental to the investigation of nanoparticle dispersion, where White *et al.* [9] showed that nanoparticle clusters in liquid can break apart after just seconds of beam irradiation due to alterations in nanoparticle surface charge caused by radiolysis products. Furthermore, biological environments are sensitive to changes in pH which can induce precipitation of some salts out of solution [90], and induce the dissolution of some nanoparticles and/or changes in oxidation states [91]. Such incidences remove a particle suspension from the native state and characterisation is no longer representative.

Cryo-TEM provides an alternative approach for *in situ* native state characterisation of nanoparticle suspensions. By rapidly plunge freezing a blotted drop of suspension in liquid ethane a suspension can be captured in a layer of vitreous ice without any redistribution of the nanomaterials within the suspension [92]. Vitreous ice is amorphous and therefore electron transparent and maintaining the sample below -165^{o}C during imaging allows the specimen to be imaged in this frozen hydrated state. Cryo-TEM became prominent in the early 1980s where it was first used to image viruses [93, 94] and is now extensively used in structural biology for single particle reconstruction of viruses and protein complexes. It has since been used to image a wide range of nanomaterials, both lipid based [95] and polymeric nanoparticles [96, 97] along with some metal nanoparticles [98] and is now becoming more

prominent within materials science [10]. A special edition on 'Cryogenic Electron Microscopy in Materials Science' was published in the MRS Bulletin (December 2019) giving an insight into the widening application of cryo-EM in research outside the life sciences. Specifically the publications referenced the use of cryo-EM for specimen preparation, soft materials characterisation, nanomaterials characterisation, and examining the solid-liquid interface [99-101]. Previous work by Hondow *et al.* [102] looked at the agglomerate size of polymer-coated CdTe/ZnS quantum dots measured by DLS, TEM of dried samples and TEM of plunge frozen samples in both water and biological media. Plunge frozen samples were more representative of the dispersion state measured in water by DLS, with a narrower size distribution compared to drop-cast prepared samples. Furthermore, only TEM of plunge frozen samples could provide quantitative analysis of the particle dispersion in biological media due to the confounding signals present in DLS plots from bovine serum albumin (BSA) present in the biological dispersant media. However, the effect of blotting during the plunge freezing process can reduce 3D information [103]. Patterson *et al.* [104] demonstrated the application of cryo-TEM in studying macromolecular assembly processes in solution through nanoparticle nucleation and growth. Specifically they observed that the formation of calcium phosphate occurs through a number of phases with the ultimate crystal formation controlled by kinetic barriers and structural rearrangements. Mirabello *et al.* [105] used cryo-TEM to study the mechanism of formation of magnetite Fe_3O_4 nanoparticle aggregates that have shown use in cancer therapy. By preparing cryo-samples at different time points in the reaction they identified that magnetite crystallisation occurred through a multistep process.

2.3.5 Limitations of cryo-EM

As with all techniques there are certain limitations of cryo-TEM. Three main issues were identified by Burrows *et al.* [106] in their review of cryo-TEM of aqueous suspensions of nanoscale objects. These were; firstly, during sample preparation it is unlikely that perfect vitreous ice will be formed over the entire grid. If a sample is not sufficiently rapidly frozen this can result in the formation of crystalline hexagonal ice (Figure 12). This hexagonal ice has high diffraction contrast and can therefore obscure

features of interest. In addition if a sample is not maintained at a temperature <-165°C during imaging then this can lead to the formation of cubic ice. This crystallisation can also lead to movement of nanoparticles and solutes such that the native state of the suspension is no longer captured.

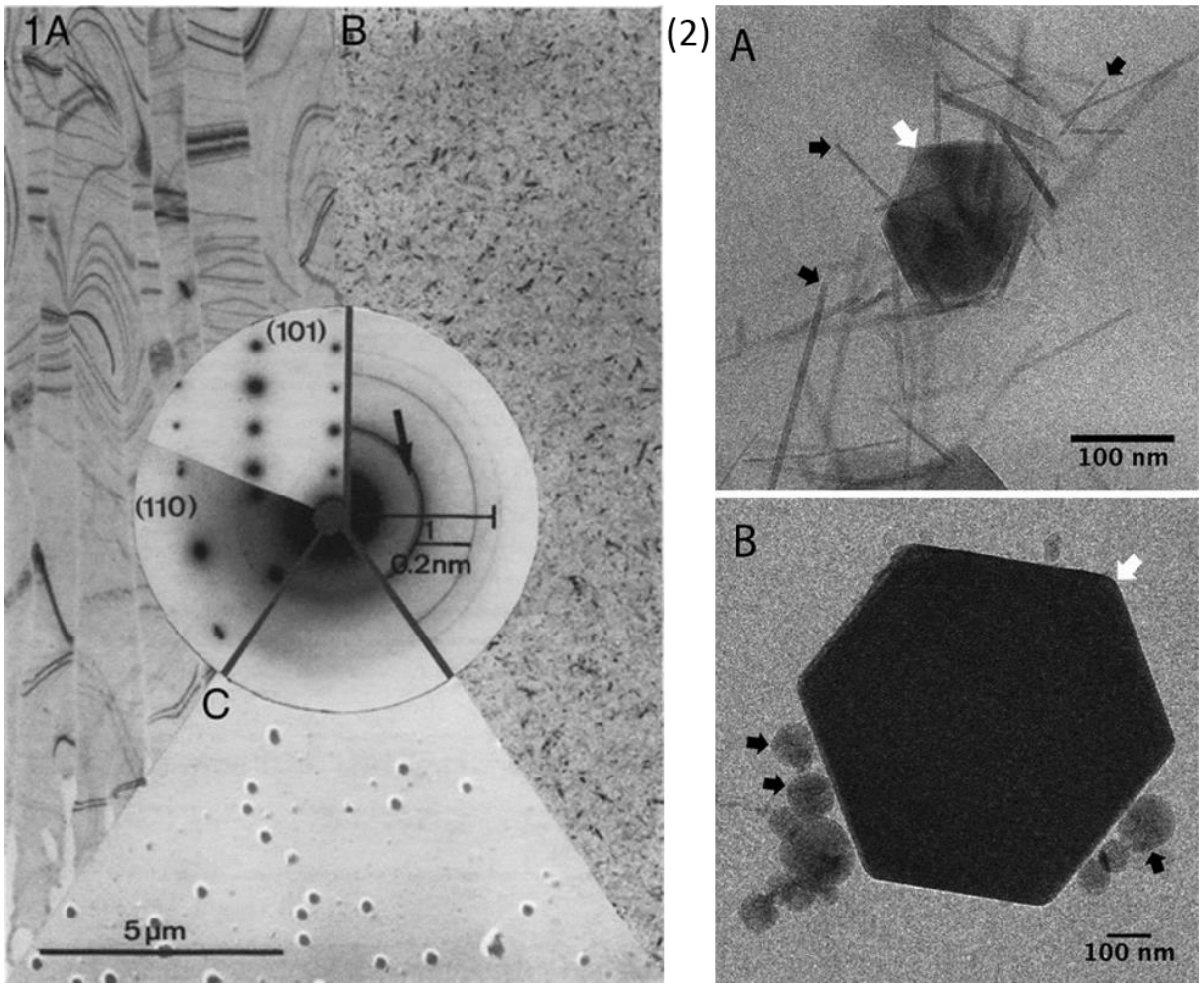

Figure 12: (1) Images and corresponding diffraction patterns of three forms of ice taken at the same magnification; (A) Hexagonal ice; (B) Cubic ice and (C) vitreous ice. Reproduced from [107]. (2) Images of highly diffracting hexagonal ice; (A) Hexagonal ice (white arrow) alongside goethite crystallites (black arrows) and (B) hexagonal ice (white arrow) with spheroid frost (black arrow). Reproduced from [106].

Secondly the condensing of water vapour from the atmosphere during sample preparation can lead to the formation of frost on the sample (Figure 12(2B) and Figure 14(A)), this tends to be small in shape and could easily be mistaken for a nano-feature of interest.

Finally, beam induced artefacts can still occur during cryo-TEM, despite it having been shown to reduce rates of beam damage of beam sensitive materials [108, 109]. This is primarily through the process of water radiolysis. Le Caer [110] defined this process as having three main stages; the physical stage, the physico-chemical stage and the chemical stage and the reactions occurring at each of these stages are summarised in Figure 13. Upon beam irradiation immediate formation of ionised (H_2O^+) and excited (H_2O^*) water molecules occurs (after ~1 fs). Numerous reactions then occur to form the highly reactive primary products during the physico-chemical stage (after ~10^{-15} – 10^{-12} s). These then undergo further reactions on a slower timescale (10^{-12} – 10^{-6} s) to form additional damage products during the chemical stage. These damage products can diffuse in solution and react with each other and surrounding molecules in solution. It is generally considered that it is this latter stage that is slowed or suppressed in frozen samples. There is currently also ongoing discussion surrounding whether cryo-STEM might have benefits over conventional cryo-TEM in preventing or delaying some beam damage and Russo and Egerton [111] postulated STEM could find use in biological fields where samples tend to be more beam sensitive.

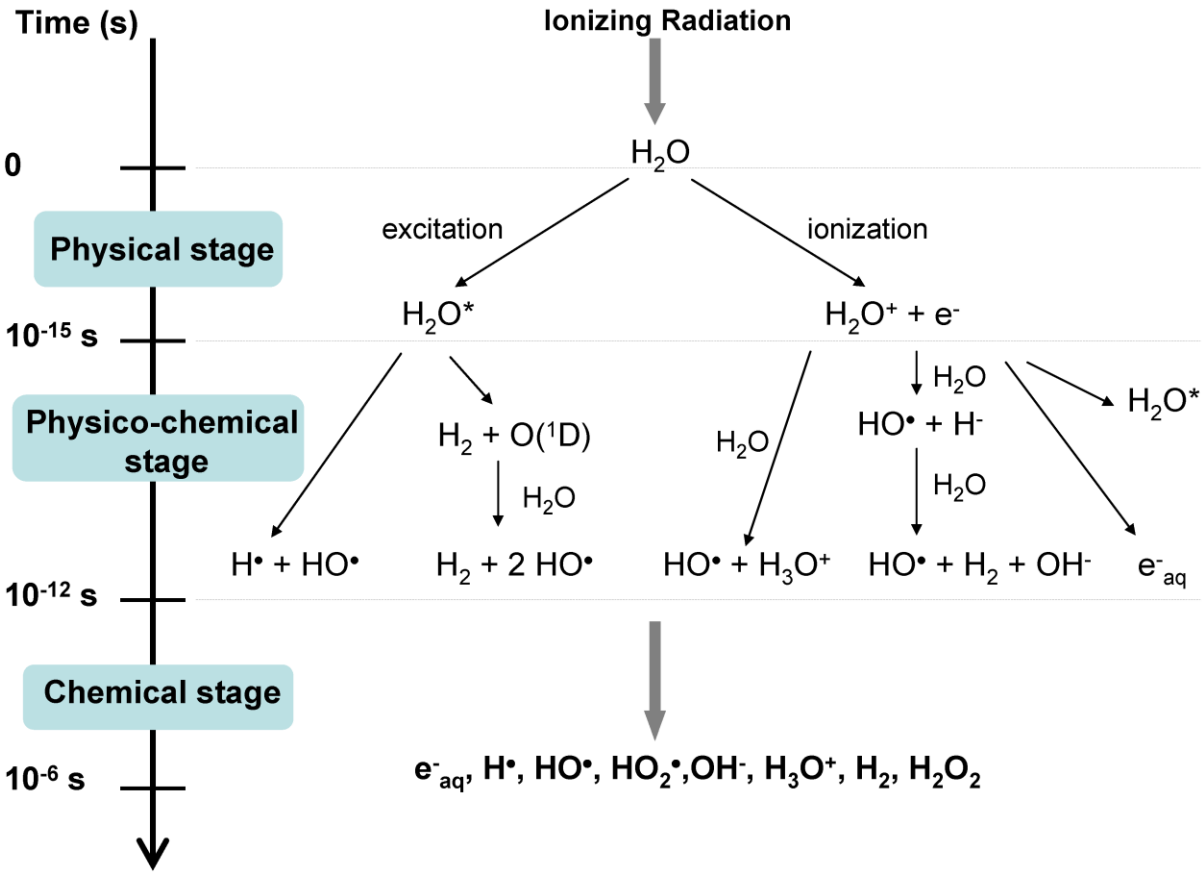

Figure 13: An illustration of the main reactions that occur during the three stages of water radiolysis. Upon beam irradiation immediate formation of ionised and excited water molecules occurs (physical stage), these species then undergo a series of reactions (physico-chemical stage) to produce highly reactive damage species which can then go on to react with each other and any molecules captured in vitreous ice/water (chemical stage). Reproduced from [110].

Evidence of beam induced damage to vitreous ice in cryo-TEM is usually through the formation of bubbles due to the volatile nature of some of the damage products (e.g. H_2) in vacuum conditions (Figure 14 (B)). Furthermore, crystallisation can occur under the electron beam producing hexagonal or cubic ice and once nucleated this can continue to grow under electron beam irradiation. Both these phenomena will induce a rearrangement of nanoparticles within the vitreous ice away from the native state.

Nevertheless, it is thought the lower temperatures in cryo-EM can reduce the reaction rates of these radiolytic processes and the slower diffusion rates of damage products in ice compared to aqueous

liquid can limit the damage to a vitreous sample. Ultimately beam induced damage in cryo-EM could be reduced in comparison to LCTEM.

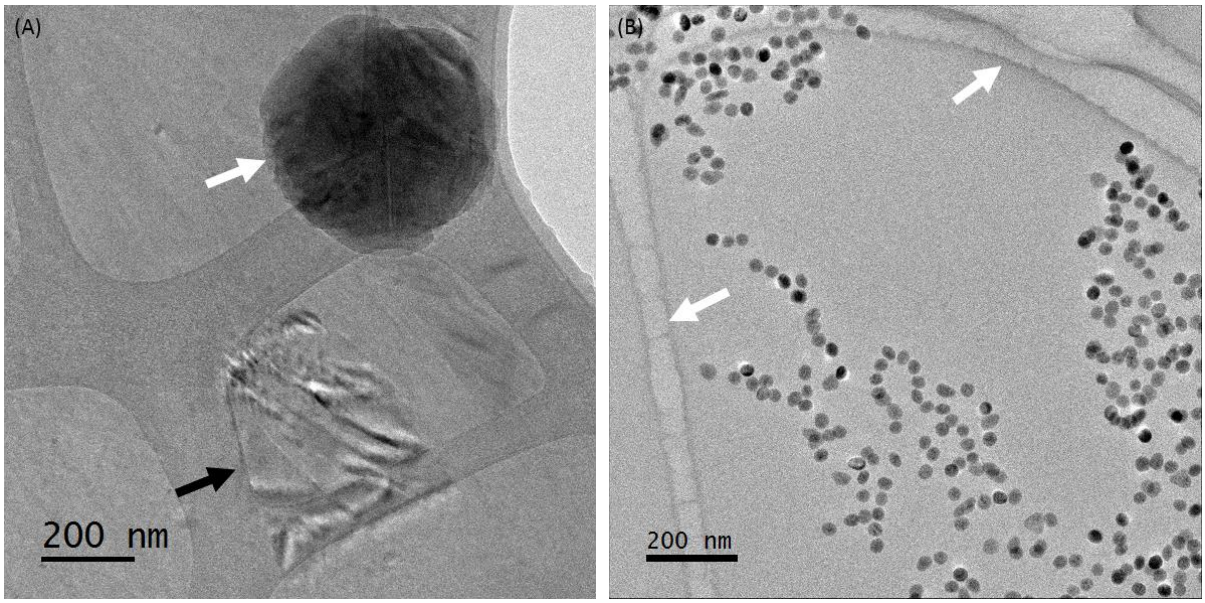

Figure 14: Two cryo-TEM images identifying some common technique artefacts. (A) shows cubic ice (black arrow) and spheroid frost (white arrow). (B) shows bubbling of the vitreous ice which occurs preferentially first at the contact point between the vitreous ice and the carbon film (white arrow).

Despite these limitations cryo-TEM remains a powerful tool in imaging biological soft matter systems on the nanometre and angstrom scale. Although beam-sample interactions do occur these are not as complicated and are currently better understood than those occurring in LCTEM. The technique is becoming increasingly used in the field of materials science where there are opportunities to apply spectroscopic techniques (EDX and EELS) to frozen samples. This would allow the investigation of the bio-nano interface of nanoparticles in the frozen hydrated state. However, the larger electron fluences (see Chapter 3 – 3.4.3 for definitions of electron flux and fluence) that are often required to obtain EELS and/or EDX data of appropriate signal to noise mean preservation of the vitreous ice can be difficult. Nevertheless recent research has demonstrated that cryo-analytical S/TEM techniques are possible.

2.3.6 Cryo-analytical S/TEM

The earliest reference to cryo-analytical S/TEM was by Oleshko *et al.* in 1998 [112, 113] where they used cryo-EELS and cryo-EDX to characterise composite (AgBr,I) tabular microcrystals of photographic emulsions. This was very early work and the suggestion was that in cryo environments a scan time of 3 h was required to obtain meaningful data. No reference is given to electron fluence or dose, but it would be predicted that significant damage to the sample would occur after 3 h electron beam irradiation. More recently, Tester *et al.* [114] used cryo-STEM-EDX to look at the formation of amorphous calcium carbonate encapsulated within a liposome. Electron dense areas were observed in cryo-TEM within the liposomes and upon applying cryo-STEM-EDX these were confirmed to be calcium rich, whilst evidence of calcium outside of the vesicles was not seen. It was predicted that further study would achieve accurate characterisation of any phase transformations in the nucleation and growth of calcium carbonate.

Quantitative information regarding electron dose or fluence was not included in papers until Wolf *et al.'s* [115] work on detecting phosphorus in vitrified bacteria. Here they used STEM-EDX to identify regions within vitrified bacteria that were rich in phosphorus, suggesting these regions were polyphosphate bodies which are common dense granules present in cell cytoplasm involved in storage or regulation. To do this they used an electron flux of 16 x 10^4 $e^-/Å^2.s$ at 200 kV yet the specific total electron fluence was not provided and there was clear evidence of damage to the vitrified cell after carrying out EDX spectroscopy. Nonetheless, the authors noted this but suggested the induced damage was not detrimental to their results.

Work has also been published which utilised cryo-EELS. Kim *et al.* [116] studied the interface between polydimethyl siloxane (PDMS) and a copolymer within a "lobed" particle. They achieved a 10 nm spatial resolution using a 12 $e^-/Å^2$ electron fluence to carry out STEM-EELS, identifying that the copolymer is trapped in the PDMS over tens of nm. This indicated that the interface was far more diffuse than was observed and predicted by the high angle annular dark field (HAADF) cryo-STEM

image alone (Figure 15). Further work by Yakovlev *et al.* [117] looked at trying to optimise experimental conditions to improve resolution. The main limiting factor of low loss EELS is that any beam interactions that lead to changes in the chemical properties of a sample, will likely be detected in the low loss EEL spectra before any obvious indication of mass loss. They concluded that improvements in reference damage spectra can allow electron fluences of 10^3 $e^-/Å^2$ at 200 kV to be used even when damage may start to occur at 10 $e^-/Å^2$.

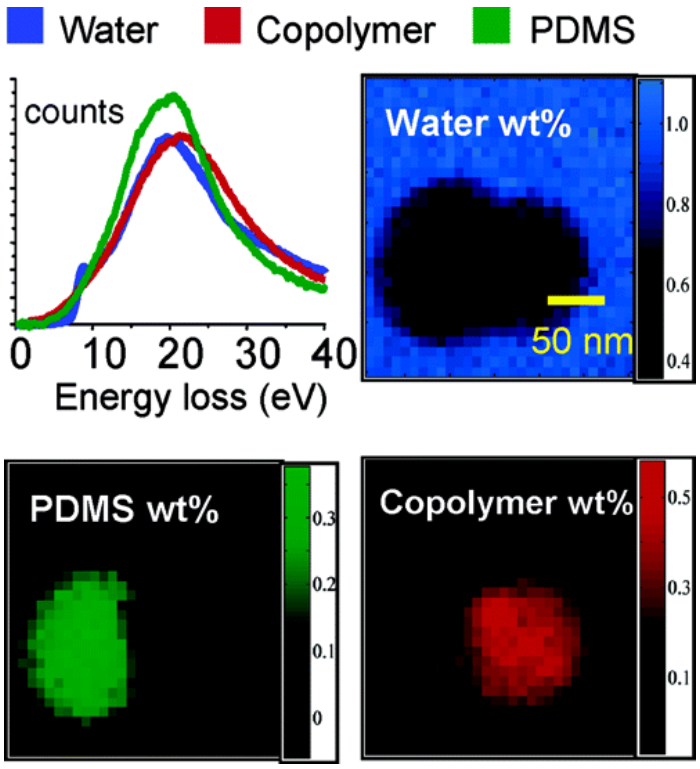

Figure 15: Cryo-EELS (low loss) spectra from pure amorphous ice (blue), pure polydimethyl siloxane (PDMS) (green) and methyl acrylate-methyl methacrylate-vinyl acetate (copolymer) (red). Spatial elemental mapping is also shown for the corresponding spectra signal indicating the copolymer is trapped within the PDMS over 10s of nm. Reproduced from [116].

Recent work by Leijten *et al.* [118] demonstrated advances in using low dose cryo-STEM to look at water and oxygen uptake in beam sensitive materials using electron fluences of 405 $e^-/Å^2$ at 200 kV. More advanced techniques have been used by Zachman *et al.* [119] to prepare ultrathin cryo samples

using cryo-focused ion beam-scanning electron microscopy (FIB-SEM) lift out, a process through which an electron transparent lamellae is first produced using cryo-FIB-SEM, and is then transferred into the TEM whilst maintaining cryo temperatures. Such thin samples can enhance contrast and in addition using a direct electron detector cryo-STEM-EELS was carried out on these lamellae which allowed high spatial resolution mapping of a few nanometres on the positions of low molecular weight carbon, oxygen and fluorine (Figure 16).

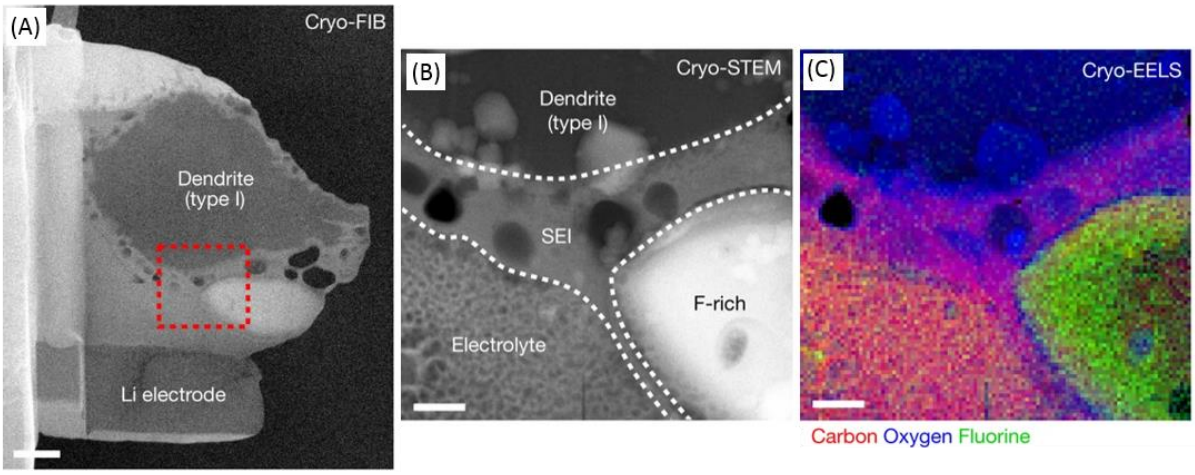

Figure 16: (A) An electron transparent cryo-FIB lift out lamellae of a liquid electrolyte illustrating the solid-liquid interfaces found in lithium-metal batteries. (B) HAADF cryo-STEM imaging reveals information regarding the size of the solid-electrolyte interphase (SEI). (C) Cryo-STEM-EELS elemental mapping indicates the SEI layer and the dendrite are oxygen rich. Scale bars 1 µm (A) and 300 nm (B, C). Adapted from [119].

Ultimately there remains relatively few publications regarding high resolution spectral imaging of cryo samples and fewer still regarding its applications to nanomedicinal or nanotoxicological studies. However, every indication is that it has the capacity to be a powerful technique for characterising materials on the nano scale in the hydrated state. Therefore, a significant aim of this PhD is to develop these methods and the first results are now published in [120].

2.4 Project Aim

It is clear that progress in nanomedicine and understanding the toxicological impact of nanotechnology is dependent upon a better understanding of the behaviour of nanomaterials when dispersed in biological media. Therefore the aim of this project was to develop *in situ* analytical S/TEM techniques to appropriately characterise nanoparticle suspensions in complex biological liquids.

2.5 Objectives

- To develop cryo-TEM in order to successfully carry out EDX and EELS on frozen hydrated aqueous samples without significant damage to the matrix ice.
- To identify and characterise the bio-nano interface of suspended nanoparticles by *in situ* cryo-analytical EM.
- To develop EM techniques which allow the investigation of the dispersion of a number of nanoparticle types in common biological media and compare this to measurements from conventional bulk DLS.
- To assess the impact of changes to the bio-nano interface of surface modified gold nanoparticles on cellular uptake, genotoxicity and cytotoxicity following exposure to cells *in vitro*.

Summary

This chapter has introduced the main literature relating to this PhD project. Identifying the necessity of understanding the behaviour of nanoparticles in biological fluids, either defined as the effect on dispersion, or by interactions that can occur at a nanoparticle's surface. The review has identified that understanding these interactions and dispersion could be advanced by implementing EM techniques. However, this can be limited by the vacuum requirements of EM which require a sample to be dried. Consequently, *in situ* techniques that allow imaging and analysis of hydrated samples are necessary and these are now increasingly being applied within materials science.

The following chapters report on: the materials and methods used for the study (Chapter 3); the experimental results relating to: the development of cryo-analytical STEM techniques (Chapter 4), the application of these techniques alongside automated EM imaging and analysis for the characterisation of nanoparticles in biological media (Chapter 5) and the cellular uptake and effect of surface modified gold nanoparticles and the influence of the protein corona (Chapter 6); and finally the overall conclusions of this PhD alongside suggestions of future work (Chapter 7).

Chapter 3

3. MATERIALS AND METHODS

This chapter provides a detailed report concerning the materials and methodology used for the research undertaken in this project. Thorough procedures are provided for nanoparticle synthesis and suspension preparation, alongside a discussion of a range of characterisation techniques providing both a background to the technique and information regarding how it was applied to the work carried out in this project.

3.1 Nanoparticle synthesis

Barium titanate ($BaTiO_3$) nanoparticles were synthesised via a hydrothermal method [121, 122]. A 1:1 molar ratio of barium to titanium was used with 19.75 g barium hydroxide octahydrate (Lot# MKBR6309V Sigma Aldrich), 5 g titanium (IV) oxide (Lot# MKB58073V Sigma Aldrich, nanopowder 21 nm particle size) and 6.6 g potassium hydroxide (Lot# BCBN9179V Sigma Aldrich) added to a Teflon cup with 40 mL de-ionised (DI) water. The Teflon cup was then encased in a hydrothermal reactor and placed in a furnace and maintained at 150^{o}C for 72 h during which time barium titanate nanoparticles formed. Once cool, the nanoparticles were washed in dilute acetic acid (3 x) and then DI water (1 x)

by centrifuging at 6000 rpm for 5 mins before removing the supernatant and re-dispersing in the appropriate wash solution. Once washed the nanoparticles were completely dried overnight in an oven. Particles of 140 ± 23 nm in diameter were obtained with a square projected shape in 2D.

Zinc oxide (ZnO) nanoparticles were also synthesised via a hydrothermal method [123] and three different shaped particles were synthesised: rods (ZnO-A), platelets (ZnO-B) and ellipses (ZnO-C). For all nanoparticles, 3.75 g zinc acetate dehydrate (Lot# MKBJ7078V Sigma Aldrich) was dissolved in 50 mL DI water and 50 mL 0.2 M sodium hydroxide (NaOH) (Fisher Scientific Lot# 1335727) was added dropwise to this. In order to synthesise the three different shapes the pH of the solution after the addition of the NaOH was adjusted using NaOH pellets (Reidel-de Haen, Lot# 60100) as follows: ZnO-A reached pH 9.43 (desired 9), ZnO-B reached pH 11.08 (desired 11) and ZnO-C reached pH 12.9 (desired 13). The solution was placed in a hydrothermal reactor and kept at 120^{o}C for 12 h. After hydrothermal synthesis the nanoparticles were washed in water (3 x) and ethanol (1 x) with 3 min centrifugation at 4500 rpm between washes. The nanoparticles were finally re-dispersed in ethanol and dried completely overnight in an oven at 60^{o}C. The Feret diameter, which is the distance between two parallel tangential lines on an object, was measured for each shape: ZnO-A 1500 ± 100 nm, ZnO-B 700 ± 30 nm and ZnO-C 300 ± 10 nm.

The synthesised nanoparticles were characterised using X-ray diffraction (XRD) and Fourier Transform infrared (FTir) spectroscopy. The two instruments used were a Bruker D8 advanced XRD and a Thermo iS10 FTir. Characterisation confirmed correct synthesis of the desired nanoparticles (Figure 17).

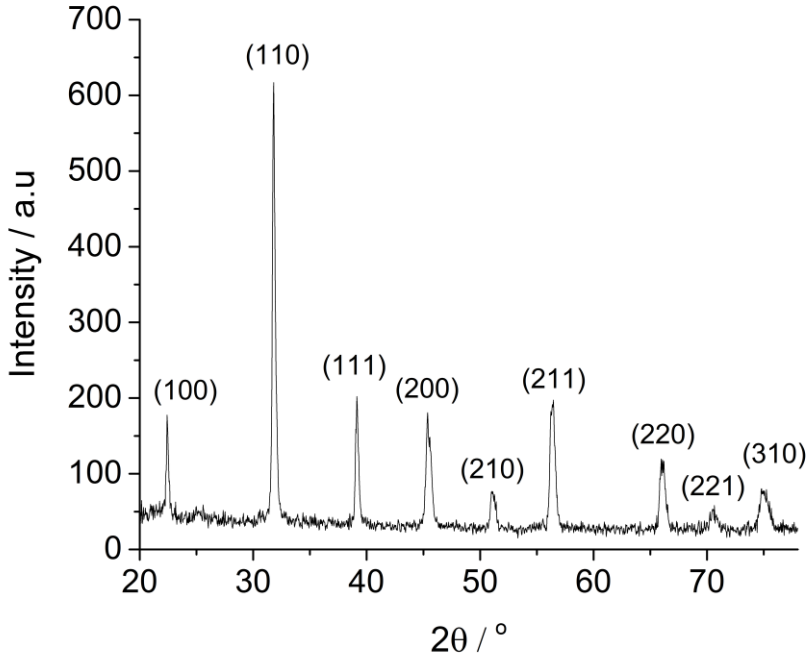

Figure 17: Characterisation of synthesised barium titanate by XRD indicated successful synthesis of cubic barium titanate had been carried out.

3.2 Nanoparticle suspensions

The focus of this project was to characterise nanoparticles when dispersed in complex biological suspensions. Throughout the course of the project a range of different nanoparticle systems were used. These were: the synthesised $BaTiO_3$ and ZnO detailed in section 3.1, gold nanorods coated with polystyrene sulfate (Au-PSS), kindly donated by Lucien Roach and synthesised and coated via the protocols in [124, 125], and commercially sourced: Fe_2O_3 (primary particle size 40 nm; Fluka Chemika, Lot 40095/1 22/00), Fe_3O_4 either uncoated (primary particle size 30 nm; 5 mg/mL in H_2O; Lot# MKCC8126) or coated with PEG (Primary particle size 30 nm; 1 mg/mL in H_2O; Lot# MKBZ0374V) or carboxylic acid (COOH) (primary particle size 30 nm, Sigma Aldrich; 5 mg/mL in H_2O; Lot# MKCD1194), SiO_2 (nanospheres 100 nm primary particle size; AngstromSphere Fiber Optic centre), Au coated with PEG (molecular weight (MW) 5000) and either amine-functionalised (primary particle size 30 nm; Sigma Aldrich; 2.46 mg/mL; Lot# MKBX4831V) or methyl-terminated (primary particle size 30 nm; Sigma Aldrich; 2.46 mg/mL; Lot# MKBZ8832V), CeO_2 (primary particle size 10 nm; Joint Research

Centre, NM-211), ZnO (primary particle size 20-60 nm; Nanotek, ZH1 121 W), and core-shell gold-silver (primary particle size 20 nm; Sigma Aldrich; Lot# MKB19138V).

The rationale behind choosing these different nanoparticle types stemmed largely from their links to possible applications within nanomedicine. $BaTiO_3$ nanoparticles have been identified as potential biomarkers [126] and both Fe_2O_3/Fe_3O_4 and Au nanoparticles have been studied extensively for applications in medical imaging [3, 14]. In addition, ZnO and CeO_2 nanoparticles have been studied not only in terms of potential use in medicine but also with regards to their potential toxicity [127]. This primarily stems from the electrochemical properties of these nanoparticles causing them to undergo dissolution within certain biological environments [128, 129]. This dissolution is a common mechanism of nanotoxicity where heavy metal ions can cause the formation of ROS within cells driving cytotoxicity (cell death) [130]. Consequently, understanding the behaviour of all these nanoparticles within different biological media is important in order to advance the safety and efficacy of these nanoparticles within medicine.

For initial method development simple model nanoparticle dispersions were used whereby nanoparticle systems were dispersed in DI water. More complex systems of nanoparticles dispersed in biological media (such as CCM) were then used to apply these developed methods in order to carry out important characterisation of nanoparticles in complex matrices.

3.2.1 Model nanoparticle suspensions

A model system of four nanoparticles dispersed in water was prepared with the following commercially sourced constituents: 50 µg/ml iron (III) oxide, 100 µg/ml cerium dioxide, 50 µg/ml zinc oxide and 20 µg/ml gold-silver core-shell nanoparticles in DI water. This system was used for the majority of the work reported in Chapter 4. A second model system of silica nanoparticles dispersed in DI water at 100 µg/mL was used for development and validation of an automated imaging and analysis protocol detailed in Chapter 5.2.

3.2.2 Nanoparticle dispersions in biological media

To understand the behaviour of nanoparticles in biological fluids a number of different nanoparticle systems were dispersed in a range of different biological media. Two common CCM were used, Dulbecco's Modified Eagle media (DMEM) (Thermo Fisher Scientific – Life Technologies) and Roswell Park Memorial Institute (RPMI) 1640 (Thermo Fisher Scientific – Life Technologies), these were usually supplemented with 10% FBS (Sigma Aldrich) and 5% penicillin-streptomycin (Sigma Aldrich) (Table 1).

Table 1: The main constituents in DMEM and RPMI supplemented with 10% FBS [37].

Classification	Components details		DMEM + 10% FBS	RPMI + 10% FBS
Amino acids	Total	(mM)	10.65	6.44
Vitamins	Total	(mM)	0.15	0.24
Cations	Sodium Na^+	(mM)	155.31	124.27
	Potassium K^+	(mM)	5.33	5.33
	Calcium Ca^{2+}	(mM)	1.80	0.42
	Magnesium Mg^{2+}	(mM)	0.81	0.41
	Iron Fe^{3+}	(mM)	0.25	n/a
Anions	Chloride Cl^-	(mM)	117.47	100.16
	Bicarbonate HCO^{3-}	(mM)	44.05	23.81
	Sulfate SO^{4-}	(mM)	0.81	0.41
	Nitrate NO^{3-}	(mM)	0.74	0.85
	Phosphate PO_4^{3-}	(mM)	0.92	5.63
Proteins	Total	(g/L)	3.00-4.50	3.00-4.50
	Serum albumin	(mM)	0.05	0.05
	α-Globulins	(g/L)	0.30	0.30
	β-Globulins	(g/L)	0.27	0.27
	γ-Globulins	(g/L)	0.07	0.07
	IgG	(mM)	$3.56 \times 10^{-0.05}$	$3.56 \times 10^{-0.05}$

In addition, two lysosomal buffers were used for nanoparticle dispersion analysis prepared as described by Soenen *et al.* [51] by making a 2 M sodium citrate solution in phosphate-buffered saline (PBS) and diluting in CCM in a 1:1 ratio. The pH was then adjusted to 5.5 and 4.5 using 1 M HCl to mimic the pH found in late endosomes and lysosomes respectively [131].

Simulated body fluid (SBF) was also used as a nanoparticle suspension media and prepared following the protocol outlined by Kokubo *et al.* [132]. For the preparation of 100 mL SBF, 70 mL ultra-pure DI water was placed in a water bath and heated to 36.5±1.5°C. Reagents 1-8 (Table 2) were then dissolved in the order presented ensuring the prior reagent was fully dissolved before adding the next. Once all

the reagents were dissolved the solution was made up to 90 mL with DI water. Whilst maintaining a temperature of 35-38°C, tris-hydroxymethyl aminomethane (Tris) was added slowly to increase the pH of the solution to 7.3±0.05, at which point the temperature was maintained at 36.5±0.5°C and further Tris added to bring the pH to 7.45±0.01. The pH was then lowered to 7.42±0.01 using 1 M HCl. The remaining tris was added alternately with 1 M HCl ensuring the pH remained between 7.42-7.45 at all times. Once all the tris was dissolved the temperature was adjusted to 36.5±0.2°C and the pH adjusted to 7.4 using 1 M HCl. The solution was then poured into a 100 mL volumetric flask and made up to the mark. Once cooled to 20°C the volume of the solution was topped up to the mark if it had reduced whilst cooling.

Table 2: Reagents used in preparation of SBF. Reagents added in the order shown in table.

Order	Reagent	Amount
1	Sodium chloride	0.8035 g
2	Sodium hydrogen carbonate	0.0355 g
3	Potassium chloride	0.0225 g
4	di-potassium hydrogen phosphate trihydrate	0.0231 g
5	Magnesium chloride hexahydrate	0.0311 g
6	1 M Hydrochloric acid	3.9 mL
7	Calcium chloride	0.0292 g
8	Sodium sulfate	0.0072 g
9	Tris-hydroxymethyl aminomethane	0.6118 g
10	1 M Hydrochloric acid	0-0.5 mL

3.3 Electron microscopy

The electron microscope was invented in 1931 by Ernst Ruska [133] alongside Max Knoll and provides the ideal capabilities to carry out high spatial resolution imaging and characterisation of nanoparticles. There are two fundamental types of electron microscope; the TEM which can provide projected internal structure information and the scanning electron microscope (SEM) which can provide surface morphological information. In contrast to optical microscopy, electron microscopy utilises a beam of high energy electrons. Since energy (E) is proportional to inverse wavelength (λ) the wavelength of

electrons is much smaller than the wavelength of lower energy light. It is this small wavelength that enables very high resolving power within the electron microscope.

Assuming a perfect lens system, the minimum resolving distance of a TEM can be defined using the Rayleigh criterion. A single point source is imaged as a series of rings known as Airy discs rather than a single point due to diffraction occurring at the outermost edges of a lens. If the discs from two point sources overlap then they cannot be distinguished and are not resolvable. The Rayleigh criterion defines the minimum resolution limit of a microscope as the point at which the first diffraction minimum of one point source overlaps with the maximum intensity diffraction disc of a second (Figure 18) [134].

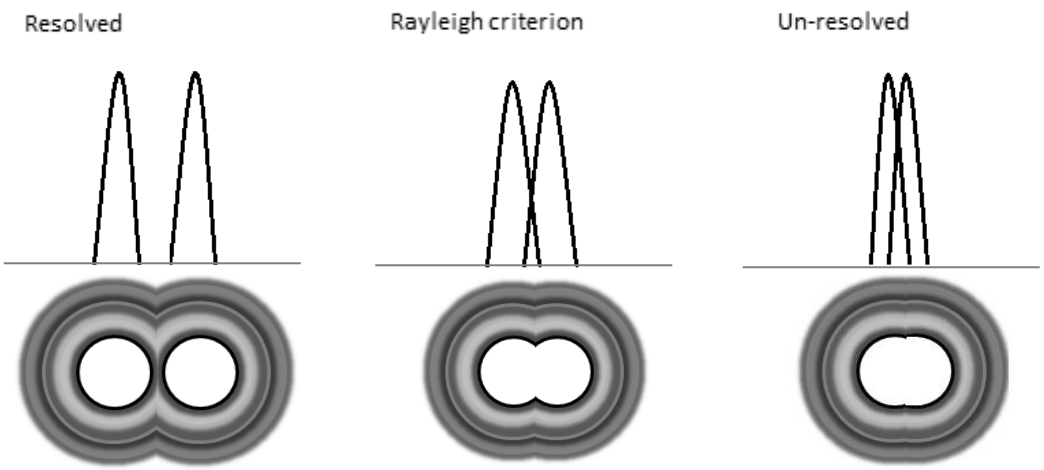

Figure 18: A schematic illustrating the Airy disc phenomenon of diffraction-limited resolution for incoherent illumination. The Rayleigh criterion states that the minimum resolution is the point at which the minimum first diffraction of one disc overlaps with the maximum of another. Adapted from [134].

However, the Rayleigh criterion applies only to incoherent illumination, yet high resolution TEM utilises coherent illumination. Here the resolution limit can be more appropriately defined by the Abbe formula (Eq. 3.1), where d is resolution and NA the numerical aperture. The NA equates to nsinα, where n is the refractive index and α is the collection semi-angle of the lens. Using this approximation for resolution clearly indicates that shorter wavelength electrons (~ 0.001 – 0.01 nm) compared to

light (green light – 400 nm) will have a far greater resolving power. Nevertheless the high resolving power of EM is at the expense of using a very high energy beam which can cause significant damage to specimens.

$$\mathbf{d} = \frac{\boldsymbol{\lambda}}{\mathbf{2NA}} \qquad \textbf{(3.1)}$$

3.3.1 Electron beam

The electron microscope requires an electron source to create a beam of electrons. There are three common sources, tungsten or lanthanum hexaboride (LaB_6) filaments or a field emission gun (FEG). A heated tungsten or LaB_6 electron gun are both thermionic and work by passing a current through the filament by applying a high voltage which causes electrons to be released. In modern TEMs the LaB_6 gun is the only thermionic gun used since it requires a much lower energy to instigate the release of electrons. Comparatively a FEG operates by having two anodes positioned below a negative FEG tip. The first anode has a voltage applied that is sufficient to extract electrons from the FEG tip and the second anode accelerates these electrons down the column [135]. There are two types of FEG, either cold FEGs or Schottky FEGs. Cold FEGs operate at ambient temperatures and therefore require ultra-high vacuum to maintain a pristine tip. In comparison Schottky FEGs are thermally assisted FEGs which allow electron emission in poorer vacuum conditions and treatment of the tip with ZrO_2 can improve the emission characteristics. Both cold and Schottky FEGs are advantageous over other electron guns since they are brighter and have smaller energy distributions which improves resolution. Of the two, cold FEGs have a smaller energy spread of electrons but the requirement for ultra-high vacuum can be expensive and require skilled users whereas Schottky FEGs have a larger energy spread but typically the beam is more stable over time. The microscopes used for the work presented in this thesis were all fitted with Schottky FEGs.

3.3.2 Electron scattering

Fundamental to the operation of the electron microscope is the interaction between the electron beam and the atoms of the sample being imaged. The interactions between the electron beam and

the electron cloud and/or nuclei of the sample atoms results in electron scattering which is the prerequisite for any imaging, diffraction or spectroscopic analysis that can be carried out using EM (Figure 19). There are two types of scattering; elastic or inelastic and these refer to scattering that is either accompanied by no loss of energy (elastic) or accompanied by some measurable amount of energy loss (inelastic) [135]. Scattering can further be defined by being either coherent or incoherent. Coherently scattered electrons remain in phase whilst incoherently scattered electrons have no phase relationship. Elastic scattering in transmission is dominated by low angle forward scattering events caused by Coulombic interactions between the electron beam and the atoms in the sample. It is important in providing image contrast (referred to as diffraction contrast) and also in diffraction analysis. Typically, if a specimen is very thin then low angle elastic scattering is coherent and this can lead to phase contrast in the image where diffracted and undiffracted electrons interfere in the image plane. Inelastic scattering refers to electron-electron interactions and is usually incoherent. The electron beam interacts with the electron cloud around the atomic nuclei of the sample causing excitation of electrons to higher energy levels and possible ionisation of atoms. The subsequent relaxation of electrons in higher energy shells to fill vacant ground state holes results in X-ray emission. This inelastic scattering can be utilised for spectroscopic analysis (see section 3.3.5). Alternatively, Auger electrons can be emitted in place of X-rays, these tend to have very low energies so are generally emitted from the surface of a specimen and are typically favoured only in the lighter elements with small binding energies.

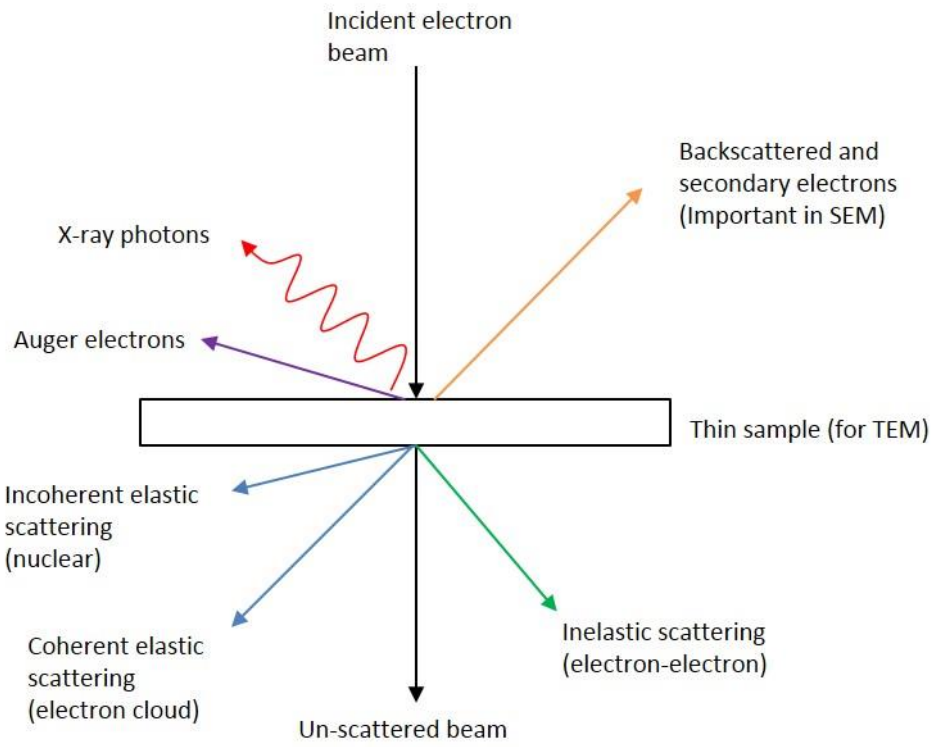

Figure 19: A schematic showing the different types of electron scattering that can occur in TEM (and SEM) imaging. Reproduced from [135].

3.3.3 Lens aberrations

A perfect lens would be able to achieve the resolution dictated by Abbe's formula which for a typical EM operating at 100 kV and a collection angle of 0.1 radians would be 0.02 nm, well into the atomic scale [134]. However, in reality lenses are imperfect and resolution is limited by lens aberrations. The main aberrations in TEM are astigmatic lenses and chromatic and spherical lens aberrations. Astigmatism is a common lens aberration which occurs due to the non-uniform nature of the electromagnetic field within the lens. The focal points of an electron beam passing through perpendicular points in a lens differ. However, most TEMs are equipped with stigmators which can easily correct astigmatism of a lens. Spherical aberrations relate to the imperfect nature of a lens whereby electron waves are bent to a higher degree at the outer edges (Figure 20). This variation means the focal point becomes spread out or blurred and is described as the disc of least confusion; that is, the smallest circle that all the electron beams pass through (Figure 20). The degree of spherical

aberration is defined by Eq. 3.2, where C_s is the spherical aberration coefficient which is usually an inherent value for a given microscope which defines the resolution limit and α is the collection semi-angle. Spherical aberrations can be corrected but this requires additional lenses controlled computationally to be added to the microscope. These are referred to as aberration corrected microscopes and benefit from an improved resolving power [134, 136]. Chromatic aberrations relate to the lenses not coping with the variation in energy of the electrons emitted from the electron gun. Lower energy electrons tend to be bent by a magnetic field to a higher degree. This variation again results in a disc rather than a focused point of converging electron paths and limits resolution (Figure 20). The extent of chromatic aberrations i.e. the diameter of the disc of least confusion (d_c) can be defined by Eq. 3.3, where α is the collection semi-angle, E_0 is the beam energy, ΔE is the energy spread of the beam and C_c is the chromatic aberration coefficient. Some TEMs are fitted with monochromators which act by using an energy selective slit and reduce the spread of electron energies travelling down the column and thereby reduce the effect of this lens aberration.

$$\mathbf{d_s = 2C_s\alpha^3} \qquad \textbf{(3.2)}$$

$$\mathbf{d_c = \frac{2C_c\alpha\Delta E}{E_0}} \qquad \textbf{(3.3)}$$

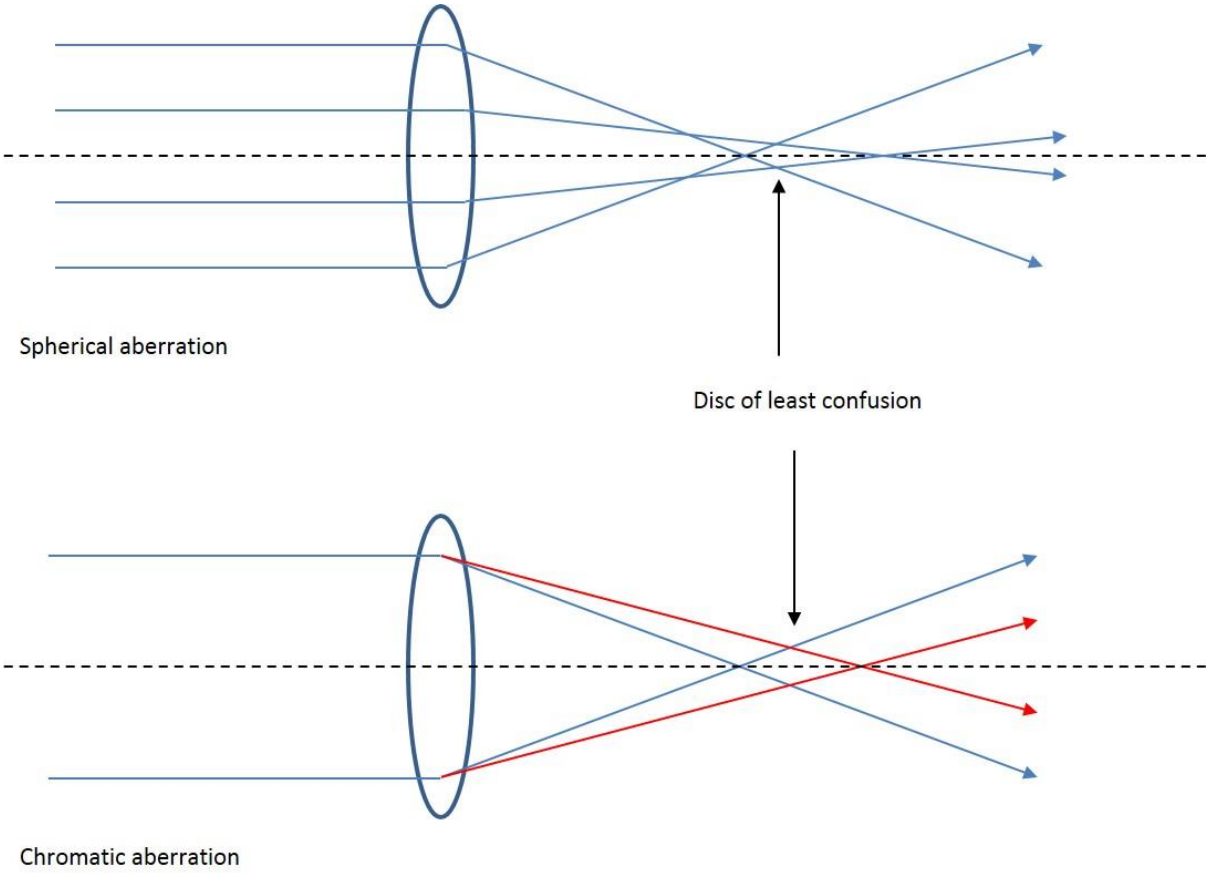

Figure 20: A schematic showing two common lens aberrations in TEM, spherical and chromatic aberrations. Spherical aberrations (top) cause electron waves to be bent more at the periphery of the lens. Chromatic aberrations (bottom) relate to the variation in bending of electrons due to differences in energy whereby lower energy electrons are bent to a larger extent.

3.3.4 Transmission electron microscopy

As the name suggests, in TEM the electron beam passes through the sample. Conventional TEM (CTEM) uses a parallel beam of electrons which passes down the column through a series of condenser lenses and through a condenser aperture (Figure 21). The condenser lenses are electromagnetic lenses composed of a series of copper coils, and by controlling the current flowing through the copper coils the focusing effect of the lens on the electron beam can be altered [134]. Once focused the beam then passes through the sample and interactions take place resulting in either elastic or inelastic scattering as described previously. Imaging can be carried out using bright field (BF) or dark field (DF) modes. BF imaging employs an objective aperture that collects the direct unscattered electrons and scattering

objects appear dark on a bright background. Comparatively DF imaging involves an inversion of contrast (objects appear bright on a dark background) and can be carried out in two ways, either by employing an objective aperture displaced around a diffracted electron beam or by tilting the angle of the incident beam so that diffracted beams are collected in the objective aperture [135].

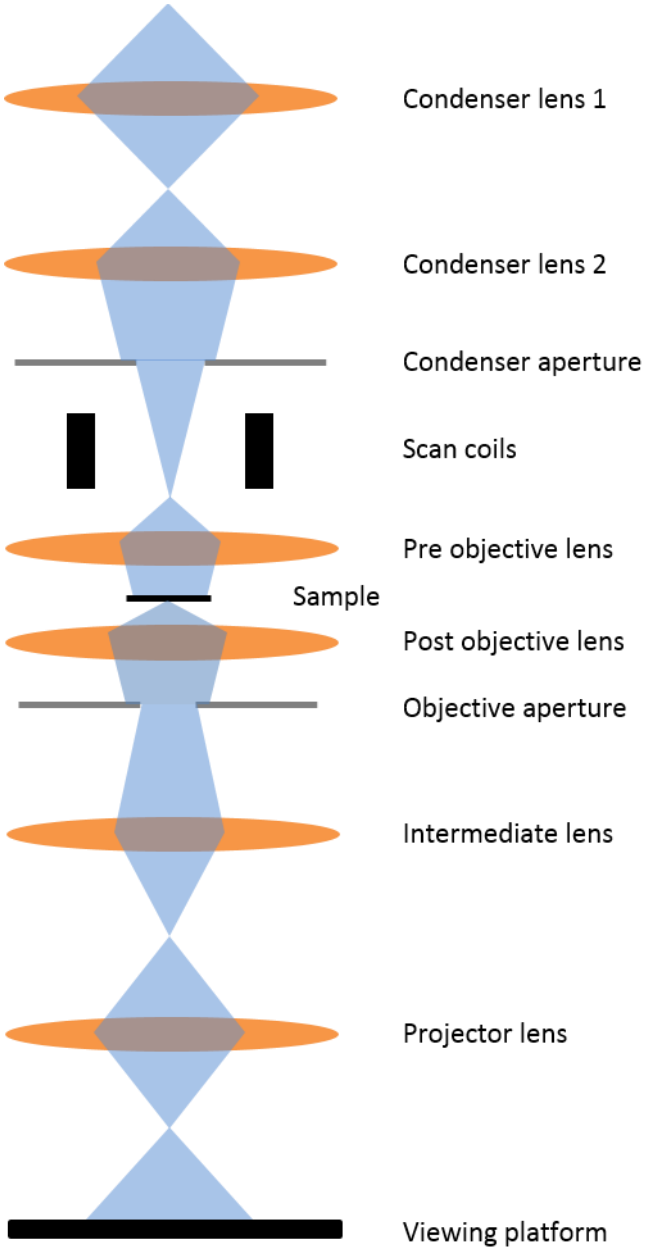

Figure 21: A schematic of a TEM using a twin objective system operating in the BF mode with a parallel beam of illumination.

There are three main contrast mechanisms in TEM imaging:

a. Mass-thickness contrast

This contrast mechanism occurs due to scattering between the electron beam and atoms within the sample. The extent of this scattering is dependent on the mass of the atoms, where heavier atoms scatter electrons more strongly than lighter atoms. In addition thicker or denser regions scatter electrons more strongly or cause multiple scattering to occur. Electrons scattered to higher angles are blocked by the aperture and thus heavier atoms and thicker regions appear darker (Figure 22(A)) [137].

b. Diffraction contrast

For samples with crystallinity, electron diffraction becomes a highly valuable technique. Here it is more appropriate to describe the incident electron beam and transmitted electrons as waves rather than particles. Crystalline samples are highly ordered in a lattice and contain columns and planes of atoms referred to as lattice planes. A specimen of the same mass and thickness can exhibit contrast variations due to the orientation of the crystalline material relative to the electron beam as this results in some regions scattering electrons more strongly than others and appearing darker (Figure 22(B)). The orientation at which diffraction is greatest is defined by the Bragg angle (θ_B) where n = the order of reflection, λ = wavelength and d = the lattice d-spacing (Eq. 3.4). Consequently, the Bragg angle is very small and on the mrad scale for picometre electron wavelengths [138]. Diffraction contrast can be valuable in analysing faults or grain boundaries in crystalline materials [137].

$$\mathbf{n\lambda = 2dsin\theta_B} \qquad \textbf{(3.4)}$$

c. Phase contrast

Phase contrast is sometimes referred to as high resolution (HR)TEM and utilises the interference between more than one diffracted wave and the transmitted beam. It allows direct imaging of the lattice planes within a sample and can therefore provide information about atomic positions [137]. Phase contrast imaging is carried out at high magnifications and usually without an objective aperture, allowing all diffracted waves to be collected and a subsequent interference pattern to be obtained (Figure 22(C)). The extent of under or over focus plays a vital role in phase imaging alongside specimen

thickness and spherical aberrations inherent to the microscope. The Scherzer focus (Δf_{sch}) (Eq. 3.5) defines the optimum defocus condition necessary to allow an additional $\pi/2$ phase shift of the objective lens and equates to the point at which the microscope is operating at the highest performance [139].

$$\mathbf{\Delta f_{Sch} = -1.2(C_s\lambda)^{\frac{1}{2}}} \qquad \textbf{(3.5)}$$

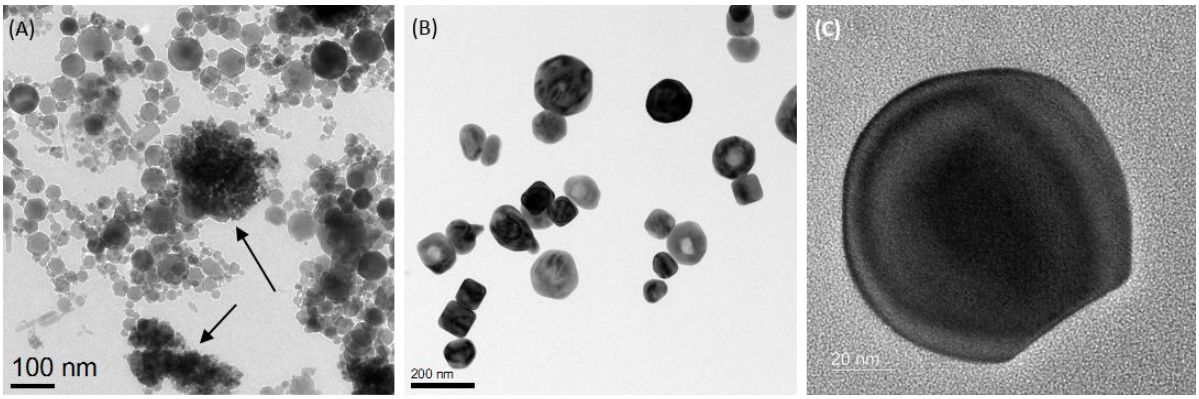

Figure 22: Examples of the three imaging contrast techniques in TEM. (A) A mixture of ZnO, Fe_2O_3 and CeO_2 nanoparticles illustrating mass thickness contrast such that the ceria nanoparticle agglomerates indicated by the black arrows appear darker in comparison to zinc oxide and iron oxide. (B) Diffraction contrast indicated by the variation in contrast between $BaTiO_3$ nanoparticles due to different orientations of the crystals on the support film. (C) Lattice image of TiO_2 orientated along the [111] anatase plane (taken by Dr A. Brown).

For the work carried out during this project two TEMs were used; an FEI Tecnai F20 operating at 200 kV, fitted with a Gatan Orius charge-coupled device (CCD) camera and an Oxford instruments 80 mm^2 X – max EDX detector, and an FEI Titan^3 Themis G2 equipped with a monochromator operating at 300 kV and fitted with 4 EDX silicon drift detectors, a Gatan One-View CMOS camera and a Gatan quantum ER 965 imaging filter.

3.3.5 Scanning transmission electron microscopy

The parallel beam in TEM can be changed to a focused probe which can be scanned across the sample by use of scanning coils within the microscope (Figure 21), this technique is known as STEM. A STEM detector is positioned below the sample and can detect transmitted electrons producing a serially collected image (Figure 23). There are three imaging modes within STEM; BF, annular dark field (ADF) and HAADF. These detectors detect electrons scattered to differing angles, the HAADF detector gathers electrons at angles >50 mrads off axis and was used for the majority of the STEM work carried out in this project. It offers the ability to carry out high resolution Z contrast imaging due to the high collection angles which are dominated by Rutherford scattering and minimise Bragg scattered electrons. The ADF and BF detectors collect electrons scattered to smaller angles with the ADF detector collecting at an angle range of $10<\beta<50$ mrads and the BF detector at <10 mrads. These detectors can be useful for phase contrast imaging and with appropriate care, for the detection of lighter elements, due to the lower scattering angles. Of further importance is the ability to carry out high spatial resolution elemental analysis through both EDX spectroscopy and EELS. [135]

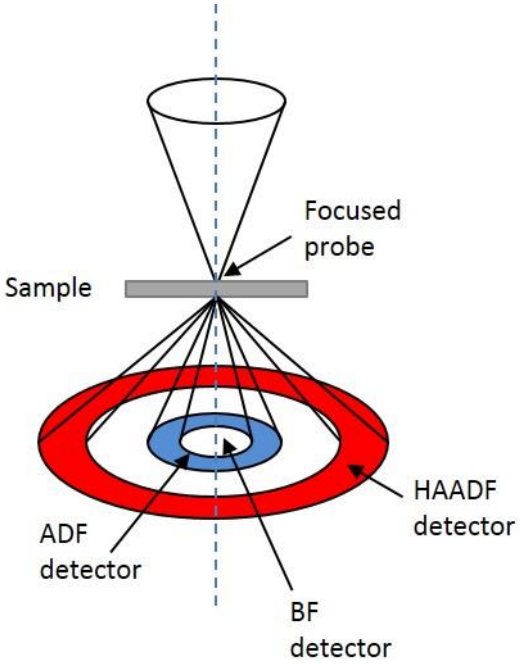

Figure 23: A schematic of a STEM detector for HAADF and ADF imaging. Adapted from [135].

3.3.6 Analytical-STEM

Both EDX spectroscopy and EELS utilise inelastic electron scattering. In EDX spectroscopy the photons or X-rays released as a result of inelastic scattering are detected by EDX detectors positioned above the sample, and each possible transition is identified according to the naming structure set out by Charles Barkla and illustrated in Figure 24 [135]. The associated energy difference of each transition is unique to an atom and therefore the energy of the released X-rays are characteristic of each chemical element. Consequently, EDX spectroscopy provides spatially resolved elemental information from a specimen (Figure 25).

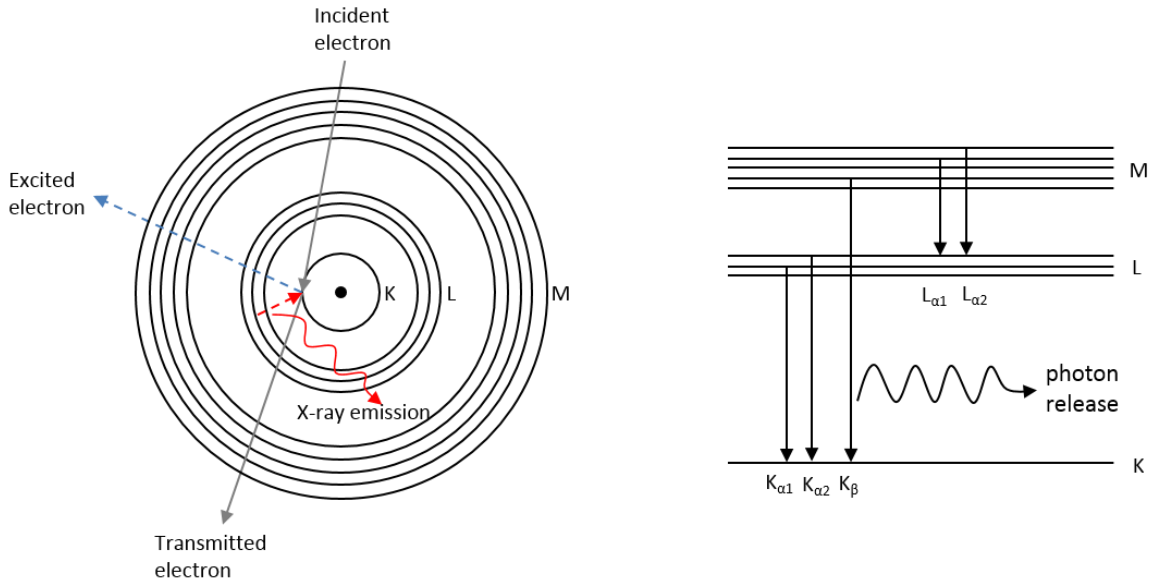

Figure 24: A schematic showing the electron-electron interactions that occur between the electron beam and the electron shell around atoms of the sample in EM imaging. These inelastic interactions cause inner-shell electron excitation, this in turn results in subsequent outer-shell electron relaxation and the release of detectable X-rays.

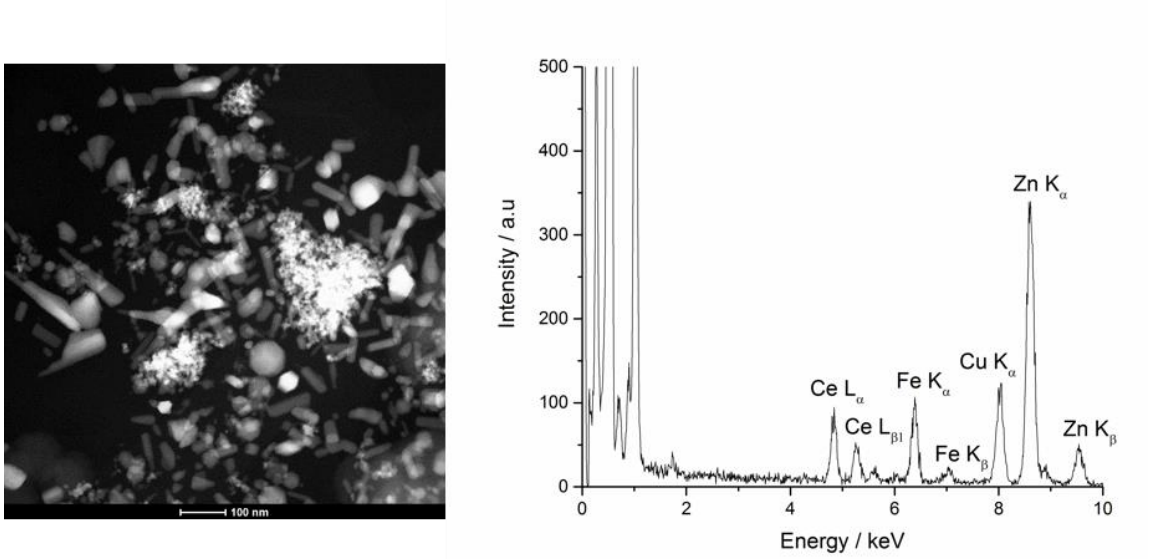

Figure 25: A HAADF STEM image and an EDX spectrum taken from the image area of a specimen prepared from a suspension of ZnO, Fe_2O_3, and CeO_2 nanoparticles dispersed in water.

The second analytical technique is EELS, where a spectrometer and detector sit below the sample and measure the energy loss of the incident electrons. The transmitted electron beam passes through a magnetic prism which bends the electron beam through 90°. This causes the electrons to disperse according to their transmitted energy, with the higher energy electrons i.e. those that have not undergone inelastic scattering, bent to a smaller extent. The dispersed beam then passes through a number of multipole optical elements and is focused onto a CCD detector (Figure 26). It is not possible to collect an entire energy spread spectrum at once, instead the acquisition conditions are optimised such that specific energy ranges pertinent to the sample being investigated are collected. These conditions are achieved by adjusting for example the spectrometer entrance aperture, the CCD channel dispersion and spectrometer drift tube voltage. A dual EELS system was used in this project which enables two spectra of differing energy ranges to be collected at once consecutively. In a thin (< 100 nm) sample the majority of electrons do not undergo any inelastic scattering and hence the zero loss peak (ZLP) i.e. those electrons that have no associated energy loss is by far the strongest peak (Figure 27). The plasmon peak at very low energy loss of ~20-30 eV corresponds to interactions of the beam with the outermost valence electron shells of the atoms and can provide information

regarding the band structure and specimen thickness [140]. For elemental analysis it is the interactions with the inner electron shells known as the core electrons that can give rise to core-loss edges at energies which are characteristic for different elements. In addition through a technique known as electron loss near edge structure (ELNES) the chemical oxidation state of atoms can be determined by probing the empty atomic orbitals positioned just above the Fermi level [141]. EELS is often advantageous over EDX if lower atomic weight elements are present because the cross-sections for detecting these events are larger in EELS [142-144].

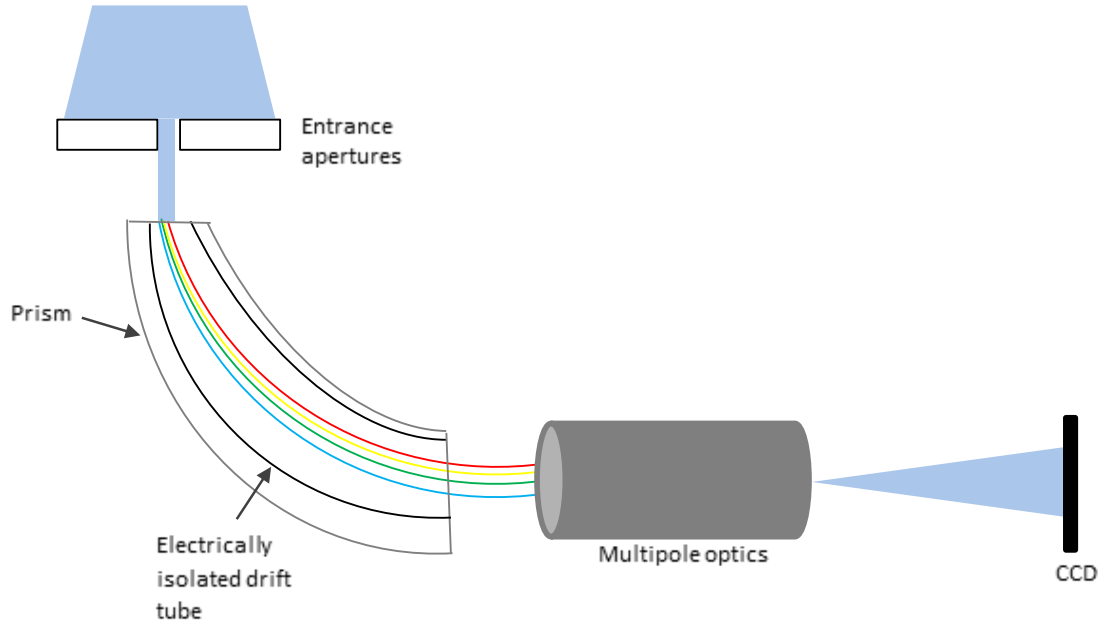

Figure 26: A schematic of an EELS detector system, indicating the prism through which the transmitted beam is bent, multipole optics and the CCD.

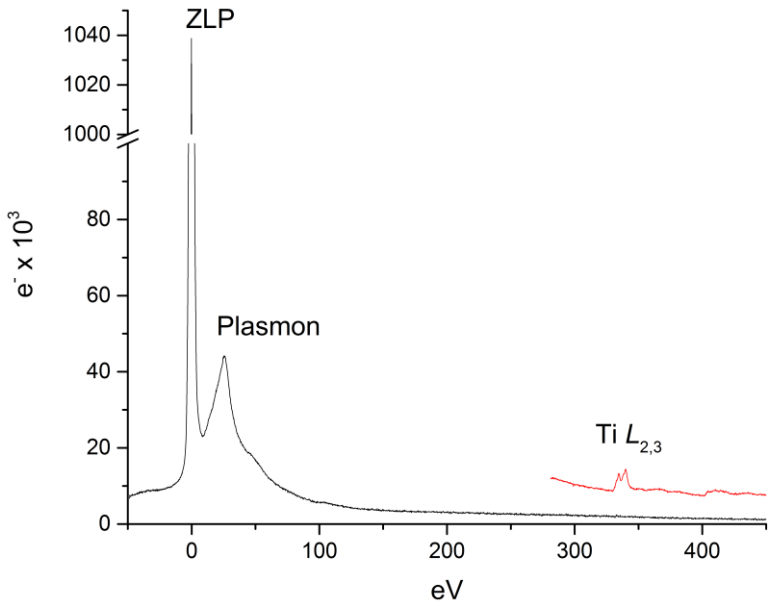

Figure 27: Two EELS spectra obtained from a sample prepared from a $BaTiO_3$ nanoparticle dispersion, showing an example of a zero loss peak, plasmon peak and core loss edge (Ti $L_{2,3}$) (inset).

3.3.7 Automated STEM imaging

In order to generate a protocol through which large, statistically relevant numbers of images could be collected using EM an automated STEM imaging protocol was set up. For this an FEI Helios GA CX dualbeam SEM equipped with a darkfield STEM detector was used. An automated imaging script was written using FEI's iFast Developer software which allowed automated imaging of up to 6 TEM grids. The script was written with an auto focus step to ensure image quality and in order to maximise the area available to image, 200 mesh TEM grids with a continuous carbon support film, were used. Once written the automated imaging script could be set to run over multiple days allowing image datasets of >1000 images per sample to be collected.

3.3.8 Negative staining

Negative staining is a common technique used to enhance contrast when imaging lighter element specimens, typically carbon-based materials such as proteins and polymers [145, 146]. The technique works by applying a heavy metal stain to the grid, which will adhere to areas where no sample is present causing greater contrast between the low molecular weight specimen and grid background

[147]. In this work a 2% uranyl acetate stain was used. The sample was drop cast onto a plasma cleaned TEM grid and dried before a drop of the uranyl acetate stain was placed onto the grid. Through optimisation, staining for 45 seconds was shown to provide the cleanest results. After this time the stain was wicked away with filter paper and the grid left to dry fully before imaging. Figure 28 shows an example of two negatively stained grids prepared by drop-casting either a suspension of Fe_3O_4 nanoparticles coated with PEG or uncoated Fe_3O_4 nanoparticles prior to negative staining. The low contrast polymer coating is clearly visible (Figure 28(A)) after the uranyl acetate stain has been applied whilst no contrast variation was observed for the uncoated sample (Figure 28(B)).

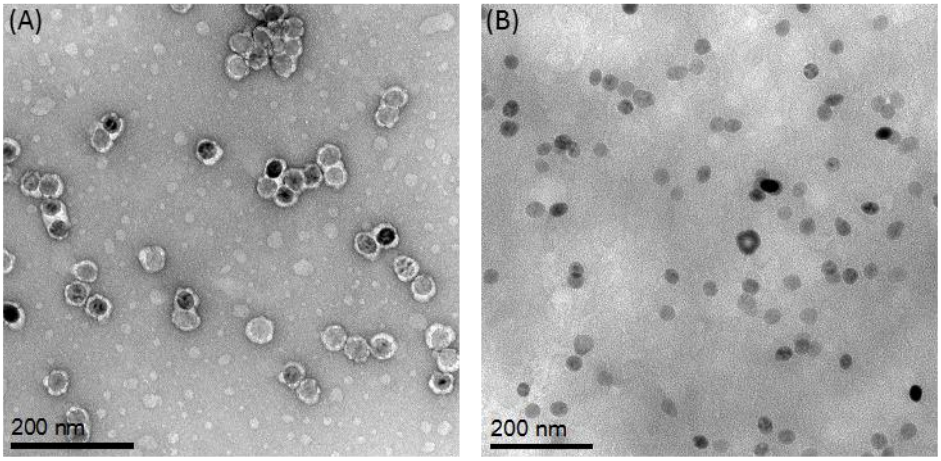

Figure 28: Two samples negatively stained, (A) Fe_3O_4 nanoparticles coated with PEG and (B) Fe_3O_4 nanoparticles uncoated. Negative staining provides contrast for the polymer coating around the nanoparticles in (A) which is otherwise not visible in untreated grids.

3.4 *In situ* electron microscopy

Electrons are strongly scattered by gases and as such cannot penetrate through air. This means in order for electrons to pass through an electron microscope the system must be under ultra-high vacuum. These vacuum requirements mean samples must be dried before loading into the microscope [134]. However, the need to dry soft matter or liquid samples before imaging and analysis means the samples are no longer in the hydrated state, and results can be heavily influenced by drying artefacts [81]. Consequently, a large field of TEM is dedicated to *in situ* techniques which allow imaging in the

native state. Here nanoparticle suspensions were analysed using two *in situ* techniques; cryo-TEM and LCTEM.

3.4.1 Cryogenic-TEM

Cryo-TEM is a powerful tool for the investigation of dispersions and soft matter. Briefly, hydrated samples are rapidly plunge frozen in a cryogen in order to capture the sample in a layer of electron transparent vitreous ice. This process of rapid vitrification ensures the liquid sample is captured in its native state, i.e. without the occurrence of any drying artefacts such as the re-dispersion of materials in the suspending medium. In order to form vitreous ice the temperature must drop below -135^{o}C at a rate faster than 10^{6} ^{o}C/s [94]. For this to be achieved an appropriate cryogen must be used. Although liquid nitrogen is readily available and has a temperature of 77K (well below that required to form vitreous ice) it is a poor cryogen due to its very low heat capacity, resulting in poor vitrification as the sample at room temperature substantially increases the temperature of the surrounding liquid nitrogen and slows the freezing process. In comparison liquid ethane has a much higher heat capacity and therefore acts as a better cryogen and was used for the cryogenic work carried out in this project. An FEI Mark IV Vitrobot© was used for the preparation of the plunge frozen grids. The vitrobot chamber is both temperature and humidity controlled to ensure reduced evaporation of the sample once loaded onto a TEM grid. A temperature of 12^{o}C and a humidity of 100% were set for all sample preparations. A 3.5 µl drop of sample was loaded onto either a Quantifoil or lacey carbon coated grid (EM resolutions). Once loaded the sample was blotted using a blot force setting of 6 to form a thin layer of sample on the grid before being rapidly plunge frozen in liquid ethane. Once frozen the grid was transferred to a Gatan-914 cryo TEM holder and maintained at < -165^{o}C (monitored using a temperature probe) to ensure devitrification of the ice did not take place and the sample could be transferred into the TEM and imaged in the frozen hydrated state [148, 149].

To minimise damage to the vitreous ice during cryo-TEM imaging, a flux of < 10 e/Å^{2}.s was used unless otherwise stated. Considerable cryo-analytical-STEM was carried out using cryo-EDX and cryo-EELS.

This is a novel application of spectroscopy and a thorough report is presented in Chapter 4 which details the conditions required to ensure successful nanoparticle dispersion characterisation can be carried out without significant damage to the vitreous ice. In brief, for all cryo-analytical STEM analysis a probe current between 40-100 pA was used and a nominal probe diameter of 1.4 Å. No sub-pixel scanning was employed. For cryo-EELS analysis either ELNES or spectral imaging (SI) was used. The acquisition conditions for the two techniques needed to be varied such that for ELNES, high signal to background (Hi-Res) conditions were employed with a 2.5 mm spectrometer entrance aperture and no binning and in order to maintain the vitrified ice structure the beam was continually scanned across the entire image area and signal collected from the whole area scanned. For SI, high speed – high signal settings (Hi-SNR) were used such that a 5 mm spectrometer entrance aperture was employed alongside 130 times vertical binning.

An alternative approach for native state analysis has been demonstrated by Hondow *et al.* [102], and was used for some of the work carried out in this project. This procedure utilised the same plunge freezing preparation protocol as described above but incorporated a warming step under vacuum after plunge freezing using a vacuum desiccator. The warming process does not alter the captured position of nanoparticles in a blotted and frozen dispersion and therefore allows dry samples that remain representative of the nanoparticle dispersion to be imaged without the need for more complex *in situ* TEM methods.

3.4.2 Liquid cell-TEM

An alternative to cryo-TEM for native state EM is the use of liquid cell holders [150]. Typically, LCTEM refers to the use of state-of-the-art liquid cell holders, where a liquid is sandwiched between two silicon membrane windows and sealed from the vacuum of the TEM allowing direct imaging of the liquid within the microscope. Here we have used an alternative *static* liquid cell commercially sold as a K-kit provided by Bio-matek. These are single use cells with a micro channel between two silicon nitride membranes that form a central window for LCTEM (Figure 29). Two different micro-channel

gap sizes of 200 nm and 2000 nm were used each with 30 nm silicon nitride windows. The sample was loaded into the K-kit via capillary action for 1 min and then the channel ends sealed using two epoxy glues (Figure 30). The K-kit was then mounted onto a specially designed copper grid with a hole in the middle (Figure 30). The glue was set under vacuum for 1 hour and then left overnight at ambient pressure to dry completely before the assembled K-kit could be loaded into a standard TEM holder and direct imaging in the liquid state could be carried out. In addition an alternative preparation to the K-kit known as thin layer or dry mode exists whereby the micro channel is filled formerly of suspended media but the channel ends are not sealed. This means the liquid dries under vacuum leaving a thin layer adhered to the windows. This drying procedure maintains the position of the nanoparticles in suspension thereby preserving the native state of the suspension, but means any remaining liquid undergoes far less interaction with the electron beam which can reduce H_2 gas bubble formation and other electron beam damage to the sample. In addition the much thinner liquid layer allows greater resolution imaging [151].

EDX spectroscopy could be carried out on the liquid samples loaded in the K-kit. Conditions were optimised to obtain sufficient counts such that when using the 4 EDX silicon drift detector system (FEI Titan) the stage was tilted to $\alpha = -25^{o}$ in order to reduce shadowing effects and only the 3^{rd} EDX detector was used. Signal was further improved by focusing on the lower section of the silicon nitride window if an appropriate sample was present.

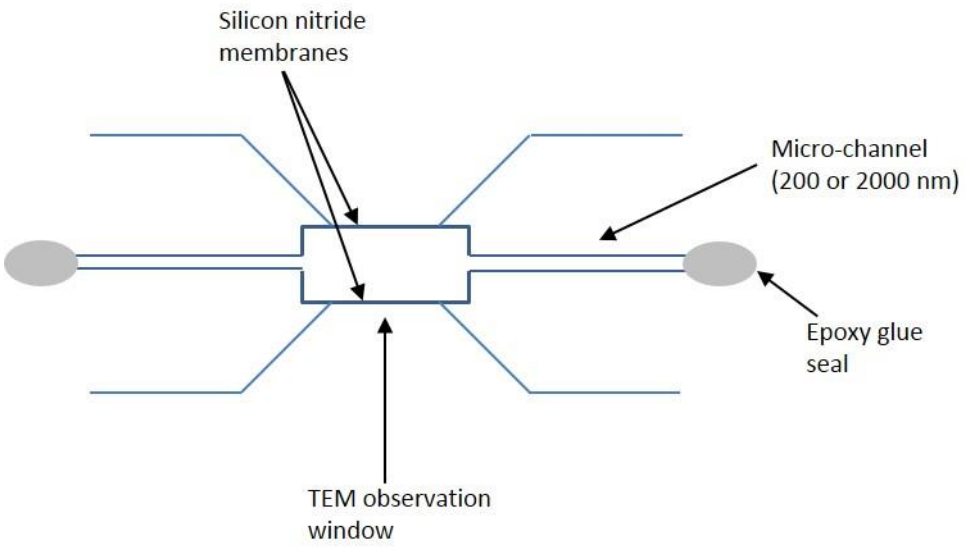

Figure 29: A schematic of a static liquid cell (K-Kit) showing the silicon nitride membrane window, micro-channel and glued ends.

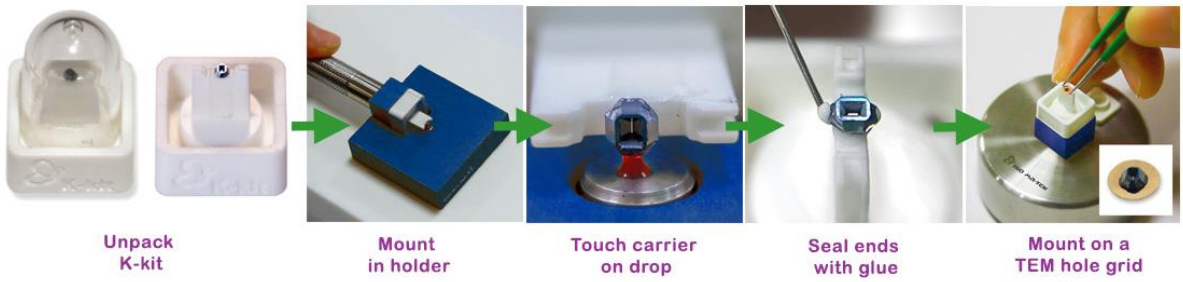

Figure 30: The process of preparing, loading and sealing the K-kit static liquid cell. The liquid sample was loaded via capillary action for one minute before sealing the ends of the channel with epoxy glue and mounting the window onto a custom designed copper TEM grid. Reproduced from [151].

3.4.3 Electron flux and fluence calculations

Beam interactions occur between the electron beam and the sample during TEM imaging and analysis and these tend to be more prominent for *in situ* TEM. All work reported in this project is provided with appropriate reference to the flux and/or fluence used for acquisition. These values have been calculated from the following equations.

For CTEM analysis,

$$\textbf{electron fluence } (\mathbf{e}/\text{Å}^{\mathbf{2}}) = \mathbf{N_e}/\mathbf{A} \qquad \textbf{(3.6)}$$

$$\textbf{electron flux } (\mathbf{e^-/Å^2.s}) = \textbf{fluence/t} \quad \textbf{(3.7)}$$

Where N_e is the sum of electrons in the electron image, taken from Gatan Microscopy Suite software (v.3.0.1), A is the total image area in Å^2 and t is the image acquisition time in seconds. Using the Gatan One-View CCD also allowed pre-set total fluence images to be collected.

For STEM analysis two electron fluxes were used, the localised electron probe flux which is received at each pixel during scanning, defined as F_p (Eq. 3.8) and the more regularly reported averaged flux F_{av} (Eq. 3.9) which is the flux averaged over each pixel in the frame i.e. it takes into account the period of time the pixel is not illuminated. In the following equations I is the probe current in C/s, e=1.602 x 10^{-19} C and is the elementary charge of the electron, A_p is the area of the 1.4 Å diameter scanning probe and A_f is the total frame area.

$$\mathbf{F_p(e^-/Å^2.s) = I/eA_p} \quad \textbf{(3.8)}$$

$$\mathbf{F_{av}(e^-/Å^2.s) = I/e\,A_f} \quad \textbf{(3.9)}$$

For fluence calculations in STEM Eq. 3.10 was used, where t is the dwell time and d the pixel size. This refers to the fluence per pixel and is equivalent to the fluence per frame. In order to calculate total electron fluence for a multi-frame scan Equation 3.10 was multiplied by the total number of frames.

$$\textbf{electron fluence } (\mathbf{e^-/Å^2}) = \mathbf{It/ed^2} \quad \textbf{(3.10)}$$

3.5 Bulk analysis

Bulk analysis was used to provide further characterisation of nanoparticle suspensions and as a comparison to EM analysis, specifically in validating novel automated imaging and analysis techniques.

3.5.1 Dynamic light scattering

A Malvern zetasizer nanoseries ZS was used to carry out DLS for hydrodynamic particle size measurements. Within a dispersion, suspended particles undergo Brownian motion, the velocity of which is dependent upon the particle size. The larger the particle the slower the Brownian motion.

This direct correlation is related mathematically to the hydrodynamic diameter through the Stokes-Einstein equation (Eq. 3.11) where d_H is the hydrodynamic diameter, k_B is the Boltzmann constant, T is absolute temperature, η is viscosity of the suspending media and D is the translational diffusion coefficient. In DLS analysis, a laser is shone through a liquid sample, and a detector positioned at a specified angle to the laser measures the scattered light intensity; for this work a 175^o angle was used (Figure 31). The detected light is then processed through a correlator which measures the light at time t and then t+δt, t+2δt etc where δ is on the nano/micro second scale. Larger particles tend to move more slowly and they don't cut through the laser beam as frequently as faster-moving smaller particles. This means there is a difference in the correlation versus time plot of different sized particles where larger particles will show a correlation plot that drops off more slowly. Using the correlation function this information can be transformed in order to obtain the particle diffusion coefficient and consequently using the Stokes-Einstein equation a particle size distribution plot can be obtained. The Raleigh approximation states that the intensity of scattered light is proportional to d^6 where d is the particle diameter, hence larger particles dominate a DLS intensity distribution plot. Using Mie theory, volume and number size distributions can also be calculated from an intensity plot which can dispel to some extent the bias toward larger particles. Where comparisons between EM and DLS data have been carried out here, number and/or volume size distributions were preferentially used [152, 153].

$$\mathbf{d_H = \frac{K_B T}{3\pi\eta D}} \qquad \textbf{(3.11)}$$

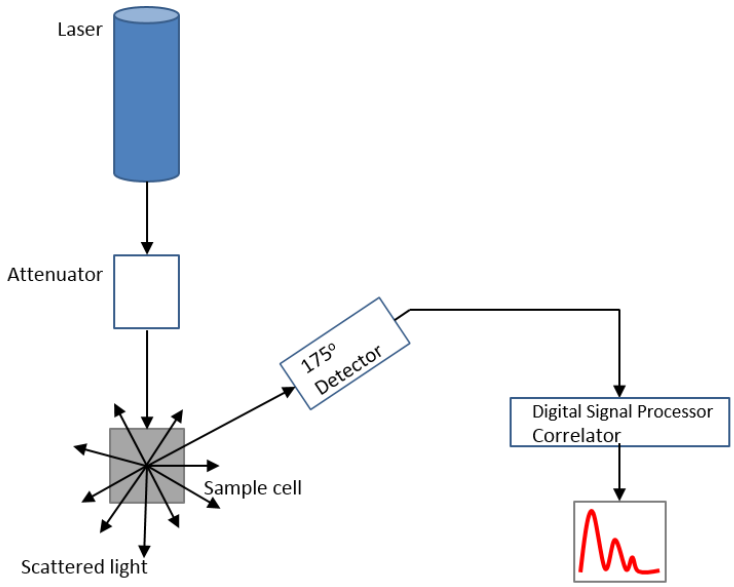

Figure 31: A schematic of a Zetasizer used to carry out DLS measurements to obtain size distributions of particles in suspension.

3.5.2 Zeta potential

The surface of nanoparticles can often be charged and as a result when dispersed in solution, ions in the solution of opposite charge to the nanoparticle surface are attracted to the nanoparticle via electrostatic forces and form a strongly bound layer around the nanoparticles, known as the Stern layer. More weakly bound ions then form a diffuse layer around the Stern layer and the two layers combined are known as the electrical double layer. The zeta potential is the electrostatic potential at the boundary of this double layer and the surrounding media and an understanding of this property for nanoparticles is useful for assessing colloidal stability since higher magnitude potentials can provide significant electrostatic repulsion of neighbouring particles (Figure 32).

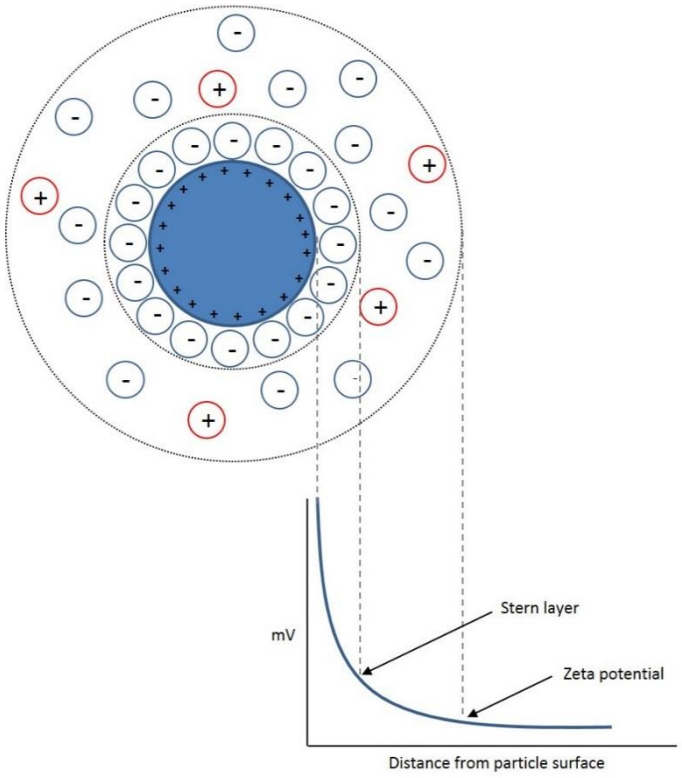

Figure 32: A schematic illustrating the double layer theory of charged nanoparticles in suspension. The Stern layer forms of strongly bound ions around the nanoparticle and then a diffuse layer forms made up of more weakly associated ions. The Zeta potential is the electrostatic potential at the edge of the diffuse layer.

Zeta potential measurements were taken using the Malvern Zetasizer nanoseries ZS. A dispersion was loaded into a DTS1070 folded capillary zeta cell and placed in the instrument. The instrument works by applying an electric field to the sample which causes the charged particles to move. The electrophoretic mobility is the ratio between the nanoparticle velocity and the applied electric field. This is measured by monitoring the frequency shifts in the laser light caused by the moving nanoparticles under an electric field using a Doppler interferometer. The zeta potential (ζ) can be calculated using the Henry equation (Eq. 3.12) relating electrophoretic mobility (μ_e) with the dielectric constant (ε), absolute zero-shear viscosity of the medium (η), and the Henry function f(kα) which includes the radius of the particle (α) and the Debye length (*k*). [154, 155]

$$\mu_e = \frac{2\varepsilon\zeta f(k\alpha)}{3\eta} \quad \textbf{(3.12)}$$

All zeta potential measurements were carried out in water. Efforts were made to take measurements in biological fluids using monomodal output modes with lower voltages to try and counter the high conductivity of these media. However, inconsistent data for a number of nanoparticle systems led to the belief this was not possible to do accurately with the instrumentation available.

3.6 Gold nanoparticle cell-uptake studies

The final results chapter focuses on work carried out at the University of Swansea's Medical School within the In Vitro Toxicological Group under the guidance of Dr Steve Evans. Two gold nanoparticle systems were used, both were coated with PEG (MW 5000) terminated with either an amine or methyl functional group and are henceforth referred to as Au-NH_2 and Au-OMe. Both nanoparticles had a primary particle size of 30 nm and a stock concentration in water of 2.46 mg/mL. An extensive array of studies were carried out to investigate; protein corona formation, cell uptake, cytotoxicity, genotoxicity and inflammatory effects.

3.6.1 Protein corona analysis

The stock Au-NH_2 and Au-OMe suspensions were bath sonicated for 10 min before diluting to 100 µg/mL in DMEM supplemented with 10% horse serum (HS) pre-warmed to 37^{o}C. The two suspensions were then maintained at 37^{o}C for 1 h whilst on an orbital shaker (SSL1 Stuart) set at 112 rpm to allow a protein corona to form. Both the soft and hard corona were obtained via a procedure of washing steps using PBS. The samples were centrifuged at 18,000 g for 40 min after which the supernatant containing any unabsorbed proteins was carefully removed and discarded. The nanoparticles were then re-dispersed in 0.5 mL of PBS before centrifuging at 18,000 g for 20 min. The supernatant was then removed and retained for soft corona analysis. Three washes in PBS were carried out in total to progressively remove all of the soft corona. The nanoparticles were then re-dispersed a final time in 40 µl of PBS, and this was assigned as the hard corona.

For protein corona analysis SDS-PAGE was used. This procedure was devised by Ulrich K Laemmli [156] and is used for protein separation and analysis. Electrophoresis refers to the movement of charged

particles in response to an electric field. In SDS-PAGE a polyacrylamide gel is used as the matrix for separation and, in principle, protein separation through the gel will depend on charge, size and shape. However, by using SDS, both charge and shape factors can be removed resulting in the movement of the proteins through the gel being largely dependent on size. This is because SDS is a surfactant which denatures proteins causing them to become linear. SDS then binds to these linear proteins giving them an overall negative charge which results in all proteins travelling in the same direction down the gel when an electric field is applied. Since SDS binds to proteins in a constant ratio such that 1.4 g SDS binds to 1 g protein [157] the separation of the proteins is due only to differences in size; smaller proteins travel further down the gel compared to larger proteins. Qualitative analysis can be carried out by running a known standard of proteins (the so-called ladder) alongside unknown samples and comparing the position of the resolved bands in the developed gel. More quantitative analysis can be carried out by extracting the protein bands and undertaking mass spectrometry analysis of these bands [158].

To carry out SDS-PAGE a 4% stacking gel and 10% resolving gel were prepared using the components listed in Table 3. A loading buffer mix was prepared with 270 µl of 3x loading buffer (cell signalling tech #77225) and 30 µl dithiothreitol (DTT) (30x DTT, 1.25 M, cell signalling tech) and 20 µl of this was added to 40 µl of each sample (i.e. wash 1, wash 2, wash 3 and hard corona) for the two nanoparticle suspensions. To denature the proteins all samples were heated for 5 min at 90^{o}C before loading 20 µl of each sample onto the prepared gels alongside 1 µl of the Bio-rad precision plus protein dual colour 161-0374 ladder. The gel was then submerged in running buffer and left to run at 120 V until the protein band had travelled down the gel. Once stopped the gels were then washed and developed using a Pierce Silver stain kit (Thermoscientific #24612) following the procedure set out in Table 4.

Table 3: Protocol for preparing stacking and resolving gels for SDS-PAGE analysis of protein corona

	4% Stacking gel	10% Resolving gel
30% Acrylamide	1.3 mL	10 mL
ddH2O	6 mL	12 mL
1.5 M Tris (pH 8.8)	-	7.5 mL
1 M Tris (pH 6.8)	2.5 mL	-
10 % SDS	100 µL	300 µL
10% APS	50 µL	150 µL
TEMED	10 µL	30 µL

Table 4: Protocol for fixing and developing protein corona gels for protein analysis.

	Procedure	Solution
1.	Wash gel 2 x 5 min	Ultrapure water
2.	Fix gel 2 x 15 min	30% ethanol: 10% acetic acid
3.	Wash gel 2 x 5 min	10% ethanol
4.	Wash gel 2 x 5 min	Ultrapure water
5.	Sensitize gel x 1 min	50 µl sensitizer + 25 mL water
6.	Wash gel 2 x 1 min	Ultrapure water
7.	Stain gel 1 x 30 min	0.5 mL enhancer + 25 mL silver stain
8.	Wash gel 2 x 20 s	Ultrapure water
9.	Develop gel 2 -3 min (until bands appear)	0.5 mL enhancer + 25 mL developer
10.	Stop developing 1 x 10 min	5% acetic acid

3.6.2 Cell uptake studies

The TK6 cell line (human lymphoblast) was used for n=3 repeats of cell uptake studies. From these a number of techniques were used; the cytokinesis-block micronucleus assay (CBMN) to assess cyto and genotoxicity, cell section imaging through TEM and FIB-SEM to assess cell uptake, and enzyme linked immunosorbent assay (ELISA) to assess inflammatory response.

3.6.2.1 Cell culture

Cells were cultured in Gibco RPMI 1640 supplemented with L-glutamine (1%) and HS (10%). A 100,000 cells/mL stock of TK6 cells in CCCM was prepared and 5 mL added to T25 (25 cm^3) flasks per nanoparticle treatment plus one additional flask per treatment for cytotoxicity calculations. These were then incubated for 24 h at 37°C and 5% CO_2. After 24 h a cell count was taken for each cytotoxicity flask before treating all flasks with either Au-NH_2 and Au-OMe nanoparticles at concentrations of 0 µg/mL, 1 µg/mL, 2.5 µg/mL, 5 µg/mL, 10 µg/mL, 25 µg/mL and 50 µg/mL in CCCM. Positive controls of mytomycin C (MMC) (0.01 µM) and LPS were used for the CBMN and ELISA studies respectively. Once treated each flask was incubated for a further 24 h at 37°C and 5% CO_2.

After 24 h the contents of each flask were transferred separately to a clean vial and pelleted via centrifugation for 5 min at 2500 rpm. The supernatant was removed and the cells were washed twice in PBS before being re-dispersed in 5 mL fresh CCCM for the cytotoxicity flasks and fresh media that had been treated with cytochalasin-B (75 mL media + 225 µl cyto-B) for the genotoxicity flasks. The samples were then placed back in the incubator for another 24 h after which the cytotoxicity flasks were cell counted. The remaining genotoxicity flasks were removed, pelleted and washed in 5 mL PBS twice before re-suspending in hypotonic solution (KCl 0.56%) and centrifuging immediately at 800 rpm for 10 min. The cells were then re-suspended and incubated for 10 mins in fix 1 (methanol:acetic acid: 0.9% NaCl (5:16)) before centrifuging at 800 rpm for 10 min and re-suspending in fix 2 (methanol:acetic acid (5:1)) and incubating for 10 min. The cells were washed a further 3 times in fix 2 and left overnight at 4°C. The final stage was preparation of slides. The cells were re-suspended in 1 mL of fix 2 and 100 µl pipetted onto a clean slide before leaving vertically to dry. Slides were then stained with 30 µL of Vectashield mounting medium with 4',6-diamidino-2-phenylindole (DAPI) before applying a coverslip and incubating in the dark for 10 min. The cells were then scored using an automated method on a MicroNucFL10BN sjmodif classifier.

In this procedure, for cytotoxicity analysis the relative population doubling (RPD) calculation was used (Eq. 3.13 and 3.14). A smaller RPD indicated a greater cytotoxic response.

$$\mathbf{RPD} = \frac{\mathbf{Number\ of\ population\ doublings\ in\ treated\ cells}}{\mathbf{Number\ of\ population\ doublings\ in\ untreated\ cells}} \mathbf{x\ 100} \qquad \mathbf{(3.13)}$$

$$\mathbf{population\ doubling} = \frac{\left[\log\left(\frac{\mathbf{post-treatment\ cell\ number}}{\mathbf{intial\ cell\ number}}\right)\right]}{\log(2)} \qquad \mathbf{(3.14)}$$

For genotoxicity analysis the use of cyto-B inhibits cell division but allows nuclear division to take place, resulting in the formation of bi-nucleated cells [159]. This permits the production of markers of genotoxicity such as micro-nuclei (Mn), nucleoplasmic bridges (NPB) and nuclear buds (NBUDS). Figure 33, taken from [159], shows typical light microscopy images of cells in different states that can be counted for CBMN assay scoring. For this work, an automated procedure was used which just counted the prevalence of Mn in bi-nucleated cells to provide genotoxicity data,

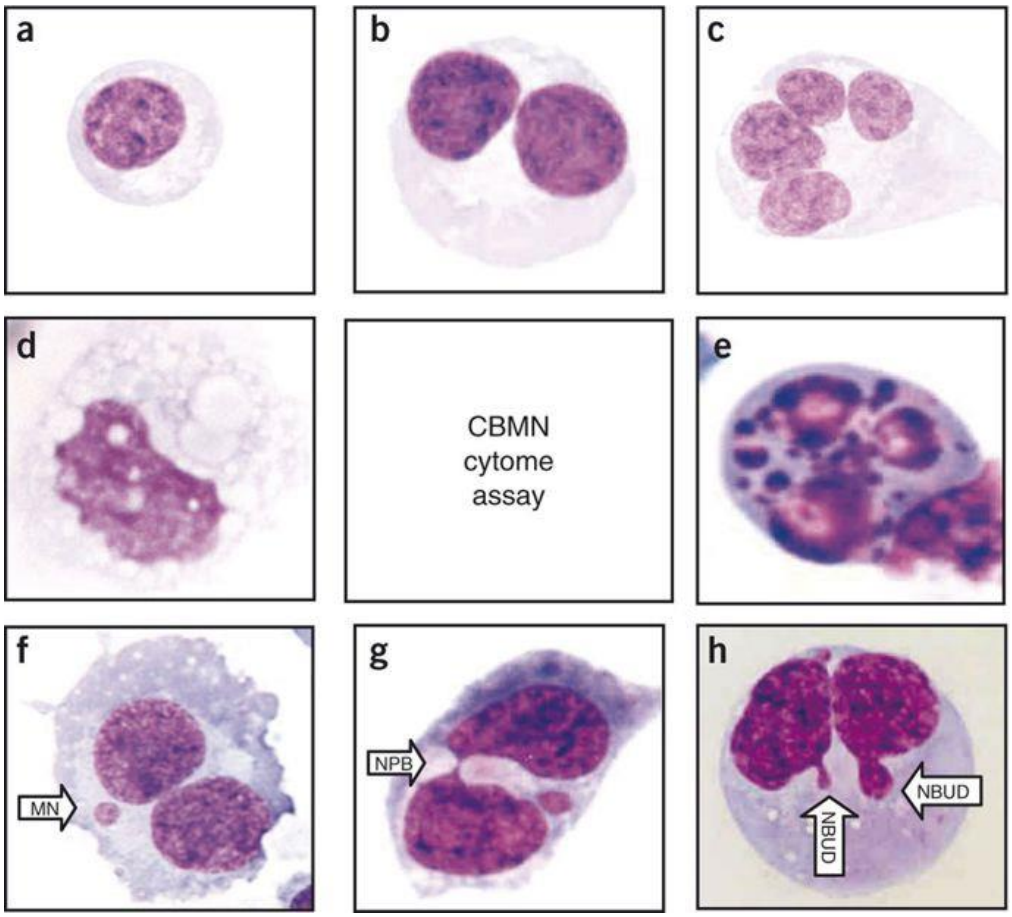

Figure 33: Taken from [159] this figure shows the different types of cells to be counted when carrying out the CBMN assay. (a) mono-nucleated cell, (b) bi-nucleated cell, (c) multi-nucleated cell, (d) early

necrotic cell, (e) late apoptotic cell, (f) bi-nucleated cell containing a Mn, (g) Bi-nucleated cell containing a NPB and (h) bi-nucleated cell containing NBUDs.

3.6.2.2 Enzyme linked immunosorbent assay

To investigate the inflammatory response of the TK6 cells to gold nanoparticles, a Human Interleukin-6 (IL-6) DuoSet ELISA kit was used. This assay is designed to quantify the amount of IL-6 present in probed samples. IL-6 can be expressed in a range of cells and is known to be important in driving acute inflammation. Therefore it can act as a marker for cellular injury and/or infection [160]. After 24 h incubation with gold nanoparticles the cells were pelleted as previously described and 1 mL of supernatant was retained for ELISA analysis. There are a number of different types of ELISA [161, 162], but the most robust is the sandwich assay and as such a solid-phase sandwich assay was used in this work. A 96 well plate is prepared such that each well is pre-coated with a capture antibody that is target-specific, in this case to IL-6. Standards, controls and samples are then added to each well and any target present will bind to the capture antibody. A washing procedure is used to remove any unbound components before a detector antibody, again specific to the target antigen, is added on top (i.e. forming the sandwich). A secondary antibody conjugated with an enzyme is then introduced which binds to the detector antibody. Once bound the conjugated enzyme can act as a target for a substrate solution which reacts with the enzyme-antibody-target complex to produce a measurable signal. The intensity of the signal is proportional to the amount of target compound (here IL-6) in the original sample. Therefore this technique provides a simple semi-quantitative pathway to observe levels of antigens that are markers for a range of specific cellular pathways and processes.

Guidance in carrying out this procedure was provided by Dr Kirsty Meldrum of Swansea University's In Vitro Toxicology Group and the plate was prepared following the kit protocol. To prepare standards for the calibration plot, a maximum standard of 600 pg/mL IL-6 was prepared and a seven point standard curve was used by carrying out a 2-fold serial dilution. A final standard of DI water was used as the blank. To prepare the plate for sample loading, 50 μg/mL of capture antibody was added to

each well before sealing and leaving overnight. The plate was aspirated and then washed with wash buffer three times. Following this 50 µL of reagent diluent was used to block the plate for 1 h at room temperature. The plate was then washed again following the same aspiration and wash procedure before 50 µl of standards, samples and controls were added to the wells, and the plate left for 2 h at room temperature. A third wash step was then used before adding the detection antibody in reagent diluent and incubating for a further 2 h. After a further wash step 50 µl of enzyme linked streptavidin was added to each well and the plate incubated away from direct sunlight for 20 min. A final wash step was carried out before adding 50 µl of substrate solution and the plate incubated for a further 20 min. Finally a stop solution of 2 N sulphuric acid was added after sufficient colour had developed. The optical density of each well was determined immediately using a microplate reader set to 450 nm, and the level of IL-6 in each sample could then be calculated using standard calibration curves. The specific details of the solutions used were: reagent Diluent - 1% BSA in PBS, wash buffer - 0.05% Tween in PBS (250 µL Tween 20 in 500 mL PBS) stored at 4˚C and a substrate solution - 1:1 mixture of H_2O_2 and tetramethylbenzidine.

3.6.2.3 Preparation of cell sections for examination by electron microscopy

In order to carry out TEM imaging of cells treated with the gold nanoparticles a procedure of resin embedding and sectioning was carried out. The initial process fixes and stains the cells before ultra-thin resin sections are cut and mounted onto a TEM grid prior to imaging. After the cells had been treated with nanoparticles and left to incubate for 24 h they were pelleted and washed in pre-warmed PBS. The pellet was then re-suspended in 100 mM phosphate buffered/2.5% EM grade glutaraldehyde for 15 min at 37^{o}C to fix the cells. This suspension was then transferred to a 1.5 mL Eppendorf tube before removing the fixative and re-suspending in fresh 2.5% glutaraldehyde fix at 4^{o}C overnight. The cells were then washed and suspended in fresh maintenance solution and stained with 1% osmium tetraoxide to fix the lipids in the cell and stain lipid-rich membranes before being left on a rocker in a cold room for 1.5 h. Cells were then pelleted for the final time before following the dehydration

protocol set out in Table 5 where 0.5 mL of each solution was added and removed without disturbing the pellet.

Table 5: Staining process for resin embedding cell sections

Solution	Time
10% ethanol	10 min
70% ethanol	30 min
100% ethanol	20 min
100% ethanol	20 min
Propylene oxide	10 min
Propylene oxide	10 min
50:50 resin:propylene oxide	90 min

The cells were then placed in 100% resin and left overnight in the fridge. Fresh resin was then applied and the samples left in an oven at 60°C to set completely (24 h). Sectioning was carried out by Dr Steve Evans using a Leica M80 EM UC7 ultramicrotome. This allows very thin sections of cells to be cut using a diamond knife. The ultra-thin slices (typically <100 nm thick) are collected in a liquid filled channel before mounting onto a TEM grid [134].

3.6.2.4 Electron microscopy of cell sections

Imaging of the cell sections was carried out using the FEI Titan Themis^3 after coating the grid with an ultra-thin amorphous carbon coating. HAADF STEM was used to identify the high contrast nanoparticles within the low contrast cell sections.

In addition to TEM imaging, 3D analysis of the resin block was achieved by using the FEI Helios FIB-SEM to carry out a process known as serial sectioning or 'slice and view'. This technique utilises the ion beam to remove a thin slice (15 nm) from the resin block and then the revealed face is imaged with the electron beam and the process is repeated until a desired volume has been imaged. A total of 603 images were collected for the slice and view datasets reported in this research. For the ion milling process a 30 kV ion beam was used corresponding to a 9.3 nA current. The area milled was

40.8 x 27.6 x 25 µm (x, y, depth). For imaging, back scattered electrons were detected using a 5 kV electron beam and a 0.8 nA current. The pixel dwell time was 10 µs and image size 6144 x 4096 pixels. Image resolution was x = 13 nm, y = 17 nm and z = 15 nm. Once collected the images were processed using the software Imaris 9.5.0. This provided 3D reconstructions of the image slices and quantitative analysis of the total number of nanoparticles within individual whole cells. To carry out this analysis thresholding was used by applying a surface to the 3D reconstruction. A manual absolute intensity threshold was used with surface smoothing to 20 nm. Once the threshold was applied specific values and statistics could be obtained for each particle.

3.7 Data analysis

For data analysis OriginPro (v. 2016 [163]) software was used unless stated otherwise. All statistical analysis was carried out using this software. For statistical analysis the student t-test was used, either paired or un-paired and results were considered significant (*) when $p<0.05$.

For thermodynamic modelling (see Chapter 5 sections 5.1.3 and 5.1.4) HYDRA-MEDUSA and HSC Chemistry (v 5.1) softwares were used. This was carried out by Dr Sergio Sanchez-Segado (Department of Chemical and Environmental Engineering, Technical University of Cartagena).

Summary

This chapter has provided details of a range of nanoparticle systems used for the work carried out in this project. Specifically an overview of TEM and STEM and their importance in carrying out characterisation of nanoparticle dispersions is detailed. In addition details of the bulk analysis techniques that have been used in conjunction with EM to ensure statistical relevance and provide surface charge information has been given. All specific S/TEM conditions are provided whenever necessary in the following results chapters.

Chapter 4

4. DEVELOPMENT OF CRYOGENIC ANALYTICAL STEM TECHNIQUES

This chapter details the development and optimisation of cryo-analytical STEM to carry out full and accurate characterisation of a model nanoparticle suspension captured in the frozen hydrated state. Conditions for successful elemental analysis using both cryo-STEM-EDX and cryo-STEM-EELS are described in detail. In addition, benefits of STEM over CTEM are identified suggesting the damage rate of vitreous ice per unit of electron fluence is reduced in STEM. Certain parameters have then been investigated in STEM to ascertain the optimal collection conditions for spectroscopy. Finally, comparisons between cryogenic and static liquid cell techniques are described, illustrating the potential benefits of using cryo conditions to reduce or delay beam-sample interaction.

The work detailed in section 4.1 and 4.2 has been published in Ilett *et al.* Micron 2019 [120].

4.1 Nanoparticle dispersion characterisation

A model nanoparticle system containing ZnO, Fe_2O_3, CeO_2 and Au-Ag core-shell nanoparticles dispersed in water was used to develop and confirm the applicability of carrying out novel cryo-analytical S/TEM to accurately identify and characterise frozen, hydrated nanoparticle dispersions.

4.1.1 Phase contrast Cryo-TEM

Initial characterisation of the model suspension captured in the frozen, hydrated state was carried out using CTEM for imaging and lattice imaging under cryo conditions. This was performed under low dose conditions using an electron flux of < 20 $e^-/Å^2.s$ to prevent significant damage to the vitreous ice. Lattice information can be used to identify phases within a sample [164]. In order to obtain lattice information the fast Fourier Transform (FFT) of a specific area in an image was obtained which provided the power spectrum or 'diffraction' spot array from the crystalline nanoparticles within that specific area (Figure 34). From this the presence of CeO_2 within the frozen suspension was confirmed by the diffraction spots/rings that corresponded to d-spacings of 3.1 Å, 2.7 Å and 1.9 Å which index to the (111), (002) and (022) lattice planes of CeO_2 respectively (Figure 34(A,B)). However, it was not possible to definitively identify the other components within the model dispersion due to the overlap of common d-spacings of ZnO and Fe_2O_3 crystals. This is indicated in Figure 34(C,D) where a diffraction spot corresponding to a d-spacing of 2.5 Å (blue ring in Figure 34) could indicate the presence of either the (101) lattice plane in ZnO or the (311) lattice plane in Fe_2O_3. For better resolution lattice imaging high magnifications were required, and in order to limit the electron flux to prevent devitrification of the ice in cryo-TEM, the electron beam was spread. However, this resulted in noisy imaging which limited the contrast of the diffraction spots in the FFT (Figure 34(D)). Consequently, for this reason and the overlap of d-spacings for lattice planes, it was not possible to identify each separate component of the model nanoparticle suspension using phase contrast CTEM alone and therefore an alternative analytical approach was needed. What follows are the full details of the development and application of cryo-analytical-STEM techniques to fully characterise the model suspension.

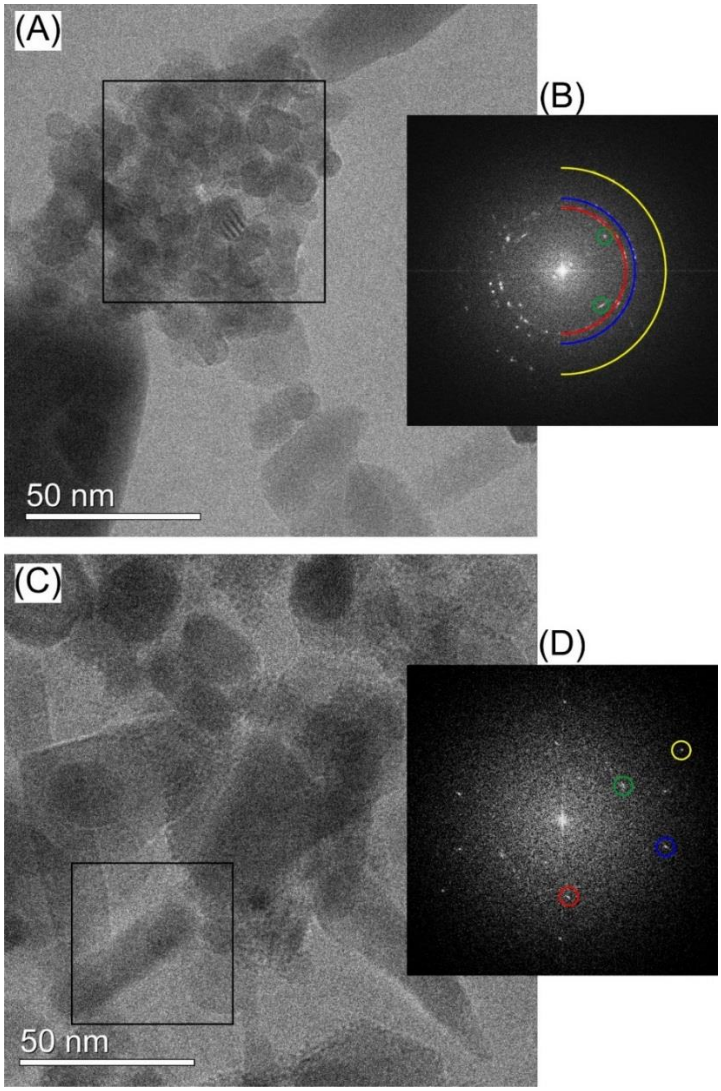

Figure 34: Cryo-CTEM images of a model nanoparticle dispersion in water containing ZnO, Fe_2O_3, CeO_2 and Au-Ag core-shell nanoparticles, captured in vitreous ice. FFTs (B) and (D) were obtained from the boxed regions in (A) and (C) respectively and show the diffraction spots identified. The spots in FFT (B) correspond to the (111) (red), (002) (blue) and (022) (yellow) lattice planes of ceria and the (201) (green) lattice plane in Fe_2O_3. The FFT in (D) could be assigned to Fe_2O_3 (e.g. (201) green and (211) red) or either Fe_2O_3 or ZnO (e.g. Fe_2O_3 (311) or ZnO (101) (blue) and Fe_2O_3 (410) or ZnO (102) (yellow)). Reproduced from Ilett *et al.* [120].

4.1.2 Cryo-STEM-EDX

Using cryo-analytical-STEM provides a pathway for accurate spatial resolution of elements within a sample allowing the characterisation of a nanoparticle dispersion within the frozen, hydrated state.

However, in order to achieve this, any analysis needs to be carried out without significant damage to the vitreous ice, since melting or devitrification will result in the artificial movement of nanoparticles within the sample.

EDX mapping and analysis was carried out on the model nanoparticle suspension. The EDX map and spectrum shown in Figure 35(A-F) was achieved using a pixel size of 3 nm, a pixel dwell time of 23 µs and a 100 pA probe current. These conditions resulted in a probe flux (F_p) of 40 x 10^7 $e^-/Å^2$.s and an average flux per pixel (F_{av}) of 3 $e^-/Å^2$.s, and a total accumulated electron fluence of 1300 $e^-/Å^2$ after 82 frames. No significant damage to the vitreous ice was seen during the scan and X-ray signals for Fe (K_α), Zn (K_α) and Ce (L_α) were collected confirming the presence of the ZnO, Fe_2O_3 and CeO_2 nanoparticles in the model dispersion. In order to successfully identify and map the Au-Ag core-shell nanoparticles within the specimen it was necessary to increase the magnification and hence reduce the pixel size. The second EDX spectrum and map in Figure 35 (G-I) was taken using a pixel size of 0.93 nm resulting in a significant increase to the total accumulated electron fluence of the scan up to 9100 $e^-/Å^2$. However, the vitreous ice still remained intact for the duration of the scan and no movement or disintegration of the nanoparticles was observed. Under these conditions both the gold core and silver shell of the nanoparticles could be identified and mapped. Therefore, all four nanoparticles within the model suspension were successfully identified and accurately mapped in their frozen or native suspension state using cryo-STEM-EDX.

The use of Cryo-STEM-EDX is still quite novel and the work shown here uses a model system of dense nanoparticles that are themselves beam stable. Yet, for the technique to become widely used, information regarding the applicability to more beam sensitive samples is required. Wolf *et al.* [115] showed that cryo-STEM-EDX can have potential uses within biological samples when looking at 'phosphorus detection in vitrified bacteria'. However they used an electron flux of 16 x 10^4 $e^-/Å^2$.s which is significantly higher than the electron flux used here. Indeed, they do note significant damage to the sample after EDX analysis whereas here when using a smaller F_{av}, EDX analysis was achieved

without detectable beam damage to the vitreous ice in the sample. Nonetheless it is worth noting again that in this current work a system of electron dense stable nanoparticles was used, rather than organic materials such as bacterial cells which are more electron beam sensitive [165]. More recently Leitjen *et al.* [118] used a range of cryo-analytical techniques including cryo-STEM-EDX to investigate the oxygen content of photovoltaics. More in line with what has been shown here they demonstrated that cryo-STEM-EDX of meaningful signal to noise could be achieved using total accumulated fluences of just 405 $e^-/Å^2$. However, they limit the pixel size to 17.12 nm which for a large proportion of ultra-fine nanoparticle research would not be a viable resolution.

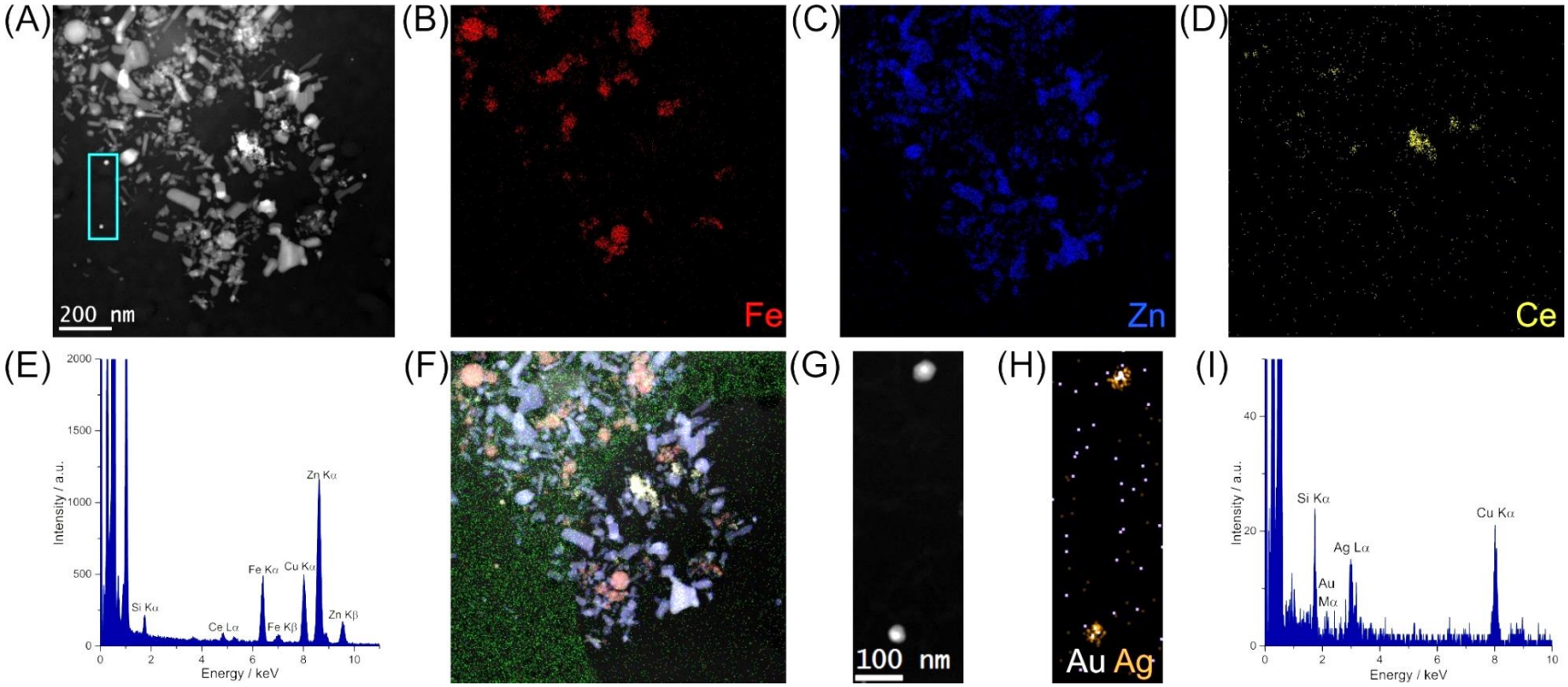

Figure 35: Cryo-STEM-EDX analysis of a model nanoparticle system collected using a 100 pA probe current for 472 s (1300 $e^-/Å^2$) and showing the presence of CeO_2, Fe_2O_3, ZnO and Au-Ag core-shell nanoparticles. (A) HAADF STEM image showing the area used for EDX analysis. Elemental X-ray mapping of (B) Fe Kα; (C) Zn Kα and (D) Ce Lα is shown alongside the EDX spectrum (E) from the whole image area in (A). Combined EDX maps of Fe Kα (red), Zn Kα (blue), Ce Lα (yellow) and C Kα (green) are shown in (F). To confirm the presence of Ag-Au nanoparticles a second cryo-EDX dataset was collected from the blue boxed region in (A); (G) HAADF STEM image; (H) Ag L (orange) and Au Mα (white) EDX maps and (I) EDX spectrum from the area. The Mα Au signal was used rather than the Lα to avoid the interference of the Zn Kβ signal. Reproduced from Ilett *et al.* [120].

4.1.3 Cryo-STEM-EELS

Having successfully shown that all constituents of the model nanoparticle system could be identified and characterised by cryo-STEM-EDX further method development was carried out to optimise and perform cryo-EELS on the same model suspension. EELS can have advantages over EDX for the analysis of lower atomic number elements and also identifying elements which have overlapping EDX signals and hence are not distinct. Initial work looked to optimise the camera length for use in STEM-EELS, an important parameter as the camera length dictates the collection angle and so, in turn, the signal to background of the spectra. Ideally a collection angle large enough to allow a significant proportion of electrons to be recorded without collecting a substantial proportion of background signal is required to ensure a good signal to background ratio. It is typically stated that the optimum collection angle at a particular ionisation or core-edge is roughly 3 times the characteristic scattering angle (θ_E) of the element of interest [138]. This can be estimated using Eq. 4.1, where E_{edge} is the energy loss value of the elemental edge and E_0 is the incident beam energy, in this case 300 keV. Accordingly, the characteristic scattering angles for the Fe, Ce and Zn edges are ~ 3.6, 4.5 and 4.8 mrad which suggest a camera length of 91 or 115 mm would be appropriate as these correspond to collection angles of 5.6 and 4.5 mrad respectively when using a 2.5 mm spectrometer entrance aperture. However, counter-intuitively four shorter camera lengths were experimentally identified as optimal; 29.5, 37, 46 and 58 mm (Figure 36). This could be due to the effective collection angle (β^*) being a convolution of the convergence (α) and collection (β) angles in STEM [typically approximated as $\beta^*=\sqrt{(\alpha^2+\beta^2)}$], so at the lower ideal ($3\theta_E$) collection angles the STEM convergence angle (8.2 mrad) dominates resulting in many core-edge energy loss electrons falling outside the collected beam.

$$\boldsymbol{\theta_E = \frac{E_{edge}}{2E_0}} \qquad \textbf{(4.1)}$$

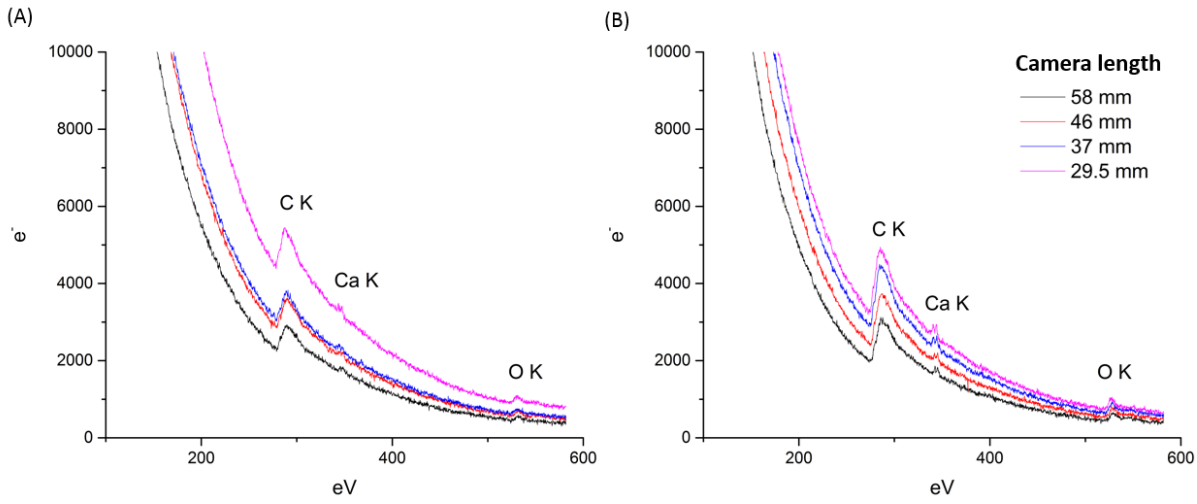

(C)	Si:B - 6 s	Si:B -10 s
58 mm	1.25	1.54
46 mm	1.25	1.57
37 mm	1.26	1.52
29.5 mm	1.22	1.52

Figure 36: EEL spectra showing the absolute intensity of the carbon *K*-edge (from the TEM support film) collected at four different camera lengths without background subtraction after a 6 s (A) and 10 s (B) exposure. The signal to background ratio (Si:B) was calculated for each camera length from the C K edge by dividing the peak maxima (signal) by the peak minima (background) and the values are shown in (C). These did not vary significantly between the four camera lengths but did improve with increased exposure time.

For conventional drop-cast and air-dried samples STEM-EELS is carried out using SI where an EEL spectrum is taken at each pixel of a scanned area. However, for this method of analysis pixel dwell times can be up to 10s of seconds. As such, for a typical SI acquisition using a dwell time of 30 seconds, a pixel size of 1 nm and a probe current of 100 pA the total electron fluence would be on the order of 10^8 $e^-/Å^2$ which is considerable and would lead to significant damage if not destruction of vitreous ice, and any beam sensitive materials. Therefore standard acquisition conditions need to be adapted in order to successfully carry out cryo-STEM-EELS without melting the vitreous ice and two different modes of acquisition were adopted.

Firstly, to carry out ELNES analysis the electron beam was continually scanned across an image area using a dwell time of 5 µs and a single EEL spectrum was collected to obtain a clear edge signal, averaged over the whole image area. No vertical binning of the detector was used and a small 2.5 mm aperture was used to maximise energy resolution. An example of a spectrum obtained using this acquisition is provided in Figure 37, where a total electron fluence of 2000 $e^-/Å^2$ was required to collect the averaged spectrum from the HAADF STEM image shown alongside. From this analysis, signals corresponding to the Fe $L_{2,3}$ edges; Ce $M_{4,5}$ edges and the Zn L_3 edge were identified and these confirmed the presence of Fe_2O_3, ZnO and CeO_2 nanoparticles in the model suspension. In this example (Figure 37) the energy resolution was not high enough to carry out true ELNES where the signal to noise (S/N) was insufficient to separate the Fe^{3+} and Fe^{2+} components of the Fe L_3 peak. However, Freeman *et al.* [166] have shown that cryo-ELNES can be achieved, albeit with the use of a monochromator and higher electron beam current.

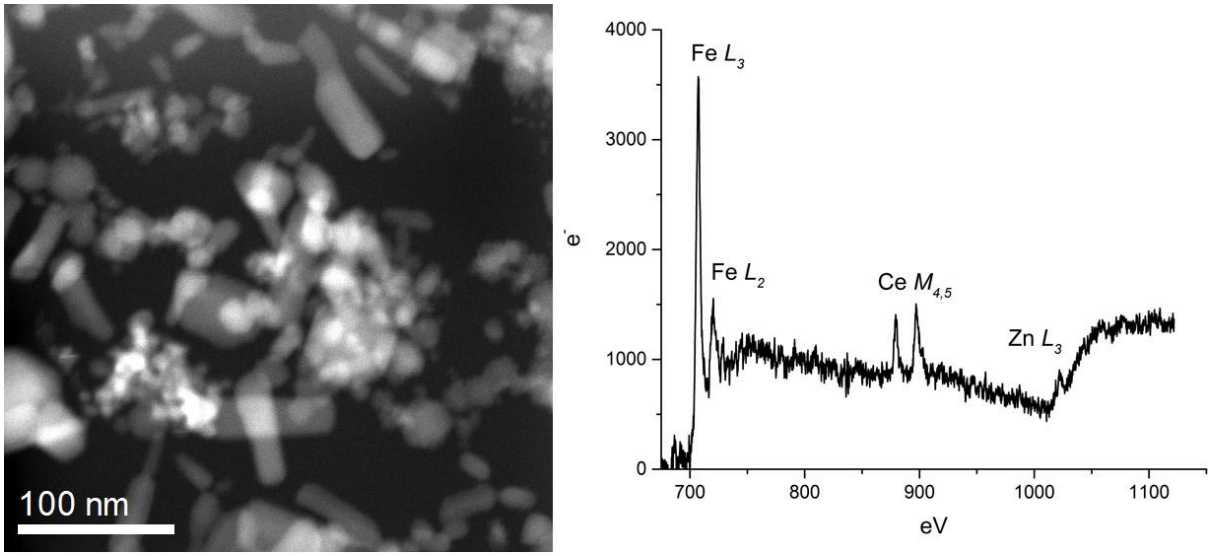

Figure 37: Cryo-STEM-EELS of a model nanoparticle suspension containing ZnO, Fe_2O_3, CeO_2 and Au-Ag core-shell nanoparticles. The Cryo-HAADF STEM image corresponds to the area analysed. The background subtracted cryo-EEL spectrum was obtained using a 0.25 eV/ch dispersion, 2.5 mm entrance aperture, 660 eV HL drift tube with a 60 s exposure and 5 µs dwell time at 225kx magnification. The total electron fluence was 2000 $e^-/Å^2$. The Fe $L_{2,3}$ white line edge at 708 eV

confirmed the presence of Fe_2O_3 nanoparticles, the Ce $M_{4,5}$ edges at 883–901 eV confirmed the presence of CeO_2 nanoparticles and the Zn L_3 edge at 1020 eV confirmed the presence of ZnO nanoparticles. No Au or Ag edges were obtained. Reproduced from Ilett *et al.* [120].

Secondly, in order to achieve and map spatial resolution of elements within a scanned area of a dispersion the acquisition conditions were altered and subsequently optimised such that STEM SI could be carried out on cryo samples (Figure 38). Hi-speed acquisition parameters were used to widen the spectrometer aperture from 2.5 mm to 5 mm and 130x vertical binning of the detector was employed to enhance the signal. It is noticeable that core-edge fine structure (ELNES) is lost when using these Hi-speed conditions, evidenced by comparing the EEL spectra in Figure 37 and Figure 38. However, sufficient signal was still collected to identify the three core-edges for Fe, Ce and Zn allowing dynamic mapping of these elements, producing the coloured SI map in Figure 38 where blue correpsonds to the Fe in the Fe_2O_3 nanoparticles, red to Ce in the CeO_2 nanoparticles and green to Zn in the ZnO nanoparticles. To achieve the data in Figure 38, a total electron fluence of just 2500 $e^-/Å^2$ was required, and no significant damage to the vitreous ice was observed. Similar to the data obtained from cryo-STEM-EDX ceria nanoparticles appeared to be present as larger agglomerates rather than isolated particles, whilst Fe_2O_3 and ZnO were highly concentrated and present throughout the suspension.

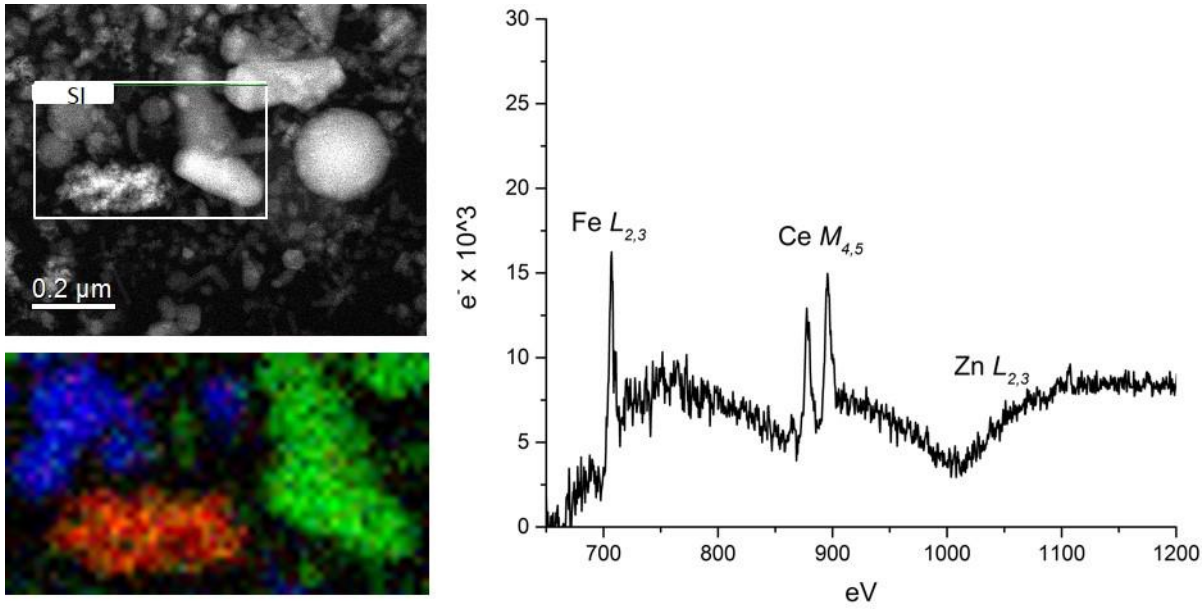

Figure 38: EELS-SI using dynamic mapping of a model nanoparticle suspension containing ZnO, Fe_2O_3, CeO_2 and Au-Ag core-shell nanoparticles. Signals for Fe ($L_{2,3}$) (blue), Zn (L_3) (green) and Ce ($M_{4,5}$) (red) were all detected. High speed settings were used in order to obtain the required spatial information whilst limiting the total electron fluence to 2500 $e^-/Å^2$.

Previously, work that has employed cryo-EELS predominantly looked only at the low loss region [116, 117, 167]. Probing this low loss region usually requires small electron fluences to obtain adequate signal since more electrons travelling through the sample undergo low electron energy loss, and so the signal tends to be many orders of magnitude higher than the core loss signals. The advances made here in carrying out successful high energy loss cryo-EELS indicate the possibility of elemental chemical shift measurement and mapping in ice and indeed since this work was published in [120], a more recent report on cryo-EELS even refers to the investigation of critical dose by looking at changes in intensity of core loss edges [118].

4.2 TEM v STEM under cryogenic conditions

Whilst carrying out cryo-analytical-S/TEM on the model nanoparticle dispersion it was noted that damage to the vitreous ice appeared more obvious at lower electron fluences when using CTEM rather than STEM. Where damage was observed it was visualised as bubbling in the ice and was presumably

due to H_2 formation during the radiolysis of water. As such, work was carried out to see whether there was a significant difference in the damage rates observed when using CTEM compared to STEM, and if certain acquisition conditions influence the observed damage rates.

Using the One-View camera, images of specific total electron fluences could be captured in CTEM. Starting at low electron fluences and increasing, it was seen that exposure to total electron fluences beyond 400 $e^-/Å^2$ could cause movement of nanoparticles within an imaged area of the suspension. This agrees with previous work that reports bubbling in vitreous ice can occur after exposure to total electron fluences of 100 $e^-/Å^2$ and beyond 400-500 $e^-/Å^2$ significant damage to the ice is observed [168]. This movement of nanoparticles also means the state of the dispersion has altered. Further images using higher total electron fluences could not be captured due to excessive movement of nanoparticles impeding the drift correction technology of the One-View camera. In comparison under STEM conditions a range of images were taken corresponding to total electron fluences ranging from 100 $e^-/Å^2$ up to 8000 $e^-/Å^2$. As a qualitative measure of ice damage, the extent of bubbling in the ice was monitored. Only slight bubbling of the vitreous ice was seen after exposure to a total electron fluence of up to 1000 $e^-/Å^2$. STEM scans/images taken using total electron fluences of between 1500 and 4000 $e^-/Å^2$ could be achieved with only minor damage to the ice being observed that did not cause significant melting or any movement of the encapsulated nanoparticles (Figure 39). Beyond 4000 $e^-/Å^2$ more obvious bubbling of the ice was seen, although movement of the nanoparticles was only observed at 8000 $e^-/Å^2$. It is likely that by using HAADF STEM, Z contrast imaging will mask some of the damage to the vitreous ice as the high atomic weight of the nanoparticles increases their contrast, suppressing the visibility of the matrix ice (Figure 39(D)). Ultimately, qualitatively, STEM appeared to have measurable benefits over CTEM in delaying vitreous ice damage.

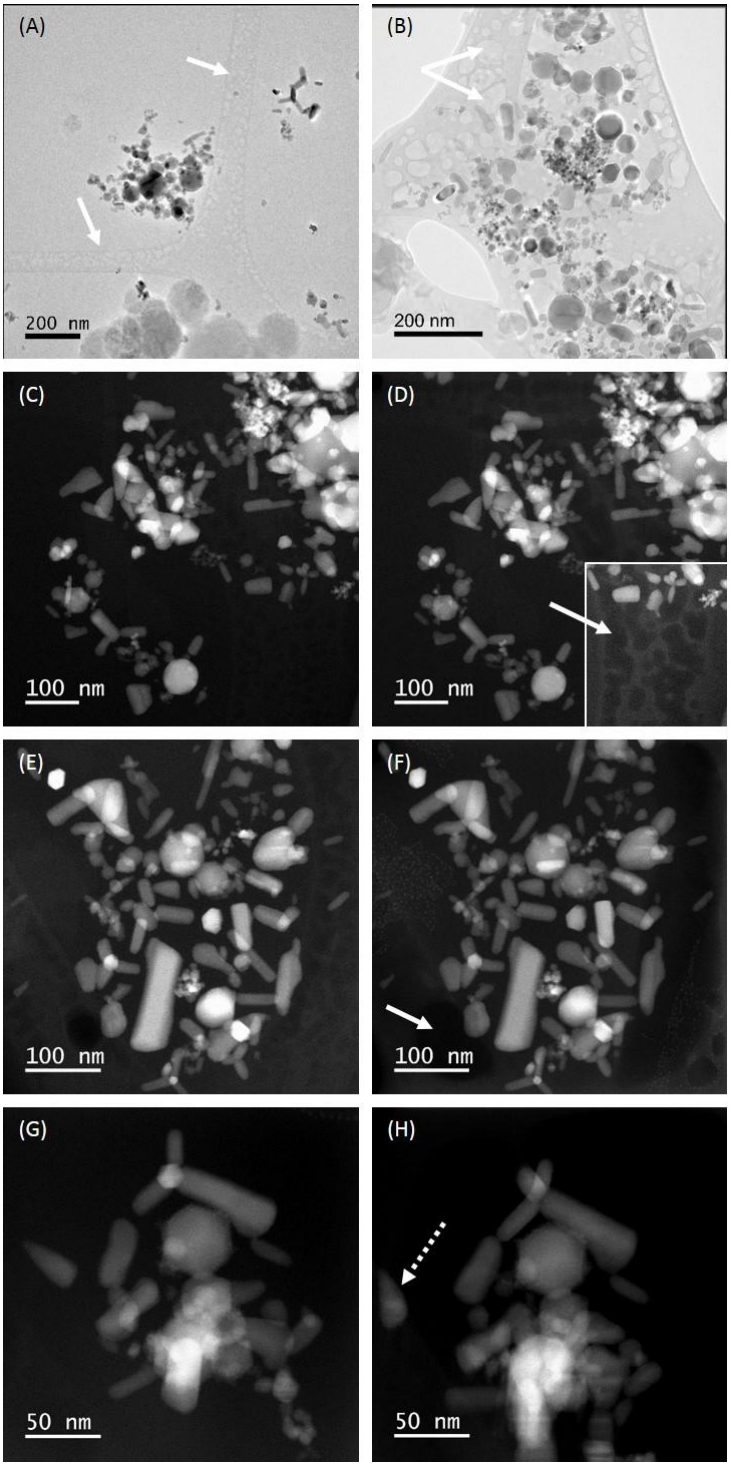

Figure 39: Qualitative assessment of the damage to the vitreous ice after exposure to increasing electron fluence in CTEM and STEM. For CTEM, some damage was seen as bubbles forming in the region of the carbon film after 100 $e^-/Å^2$ (A), whilst more significant damage to the ice was observed after 400 $e^-/Å^2$ (B). In comparison HAADF STEM images taken before (fluence 300 $e^-/Å^2$) (C) and after (D) exposing the sample to a further fluence of 1000 $e^-/Å^2$ showed some destruction to the ice (inset

in (D) altering the contrast shows more clearly the bubbling observed in the vitreous ice indicated by the white arrow). Higher total accumulated fluences could be used in HAADF STEM with (E and F) showing images before and after exposure to 4000 $e^-/Å^2$. After exposure to 8000 $e^-/Å^2$ (H) damage and movement of nanoparticles was observed. Adapted from Ilett *et al*. [120].

Vitreous ice damage is caused by the radiolysis of water which occurs upon exposure to the electron beam. During the radiolysis of water, radiolysis products consisting of hydrated electrons (e_h) and $OH^\bullet$, $H^\bullet$ and $H_2^\bullet$ radicals are produced. Once formed these damage products can undergo further reactions and produce secondary damage products such as H_2O_2, H_3O^+ and $H_2O^\bullet$ [169]. These species are highly reactive and can diffuse in solution to then react with each other or the surrounding hydrated sample. Since it is these secondary damage products that react with the vitreous ice and/or frozen sample to alter it, the radiolysis of water is said to be a diffusion-limited process [110]. This becomes important when trying to explain why damage may be more significant in CTEM compared to STEM. In his paper 'Radiation damage to organic and inorganic specimens in the TEM', Egerton [170] describes diffusion limited processes as having a sublinear relationship between dose rate and damage rate such that damage rate plateaus at higher dose rates (Figure 40(A)). For low dose cryo-CTEM an electron flux of < 10 $e^-/Å^2.s$ was used. This would correspond to operating at a lower dose rate, equivalent to the steep linear portion of the curve, as labelled in Figure 40(A). In comparison, the probe flux used in STEM was on the order of 10^8 $e^-/Å^2.s$ (for a probe diameter of 1.4 Å and a 60 pA probe current) which is significantly higher, and even when taking into account the beam broadening that occurs through a thicker ice sample (100 nm) the F_p (10^6 $e^-/Å^2.s$) is still orders of magnitude higher than in CTEM and would correspond to operating at the region at which the damage rate has likely plateaued (Figure 40(A)). Therefore the damage per unit fluence (i.e. the gradient of the curve) would be lower in STEM than CTEM and this agrees with the observations in Figure 39.

In addition, it is possible that certain healing processes could occur in STEM when pixels are no longer irradiated by the electron beam. Out diffusion of reactive damage products would be lower in STEM

than CTEM, where illumination is only of an isolated pixel rather than the whole sample area. This limited diffusion could lead to rapid recombination of reactive damage products (e.g. $H^{\bullet}$ and $OH^{\bullet}$ to H_2O) once a pixel is no longer illuminated [171]. Furthermore, delocalised damage does occur some distance remote from the STEM probe position (Figure 40 (B,C)). Egerton has determined that the distance of delocalised damage can be estimated if the primary electron excitation energy for the sample is known [172]. For water radiolysis this is 7.4 eV [173] which corresponds to an estimate of the maximum delocalised damage distance when using a 300 kV accelerating voltage of between 2 and 6 nm. Therefore, for ice or water any pixel size smaller than (at a minimum) 2 nm would result in oversampling where pixels undergo damage when neighbouring pixels are illuminated. It is suggested that in order to minimise non-direct damage of vitreous ice and therefore any redistribution of nanoparticles in a sample, a pixel size of > 2 nm should be used where possible. This would ensure the distance of delocalised damage would be equal to or smaller than the pixel size and therefore would prevent sampling of already damaged pixels (oversampling) in a manner analogous to leapfrog scanning [174]. It is likely that in some instances where higher resolution imaging is necessary, sub-pixel scanning and subsequent image modelling would be required.

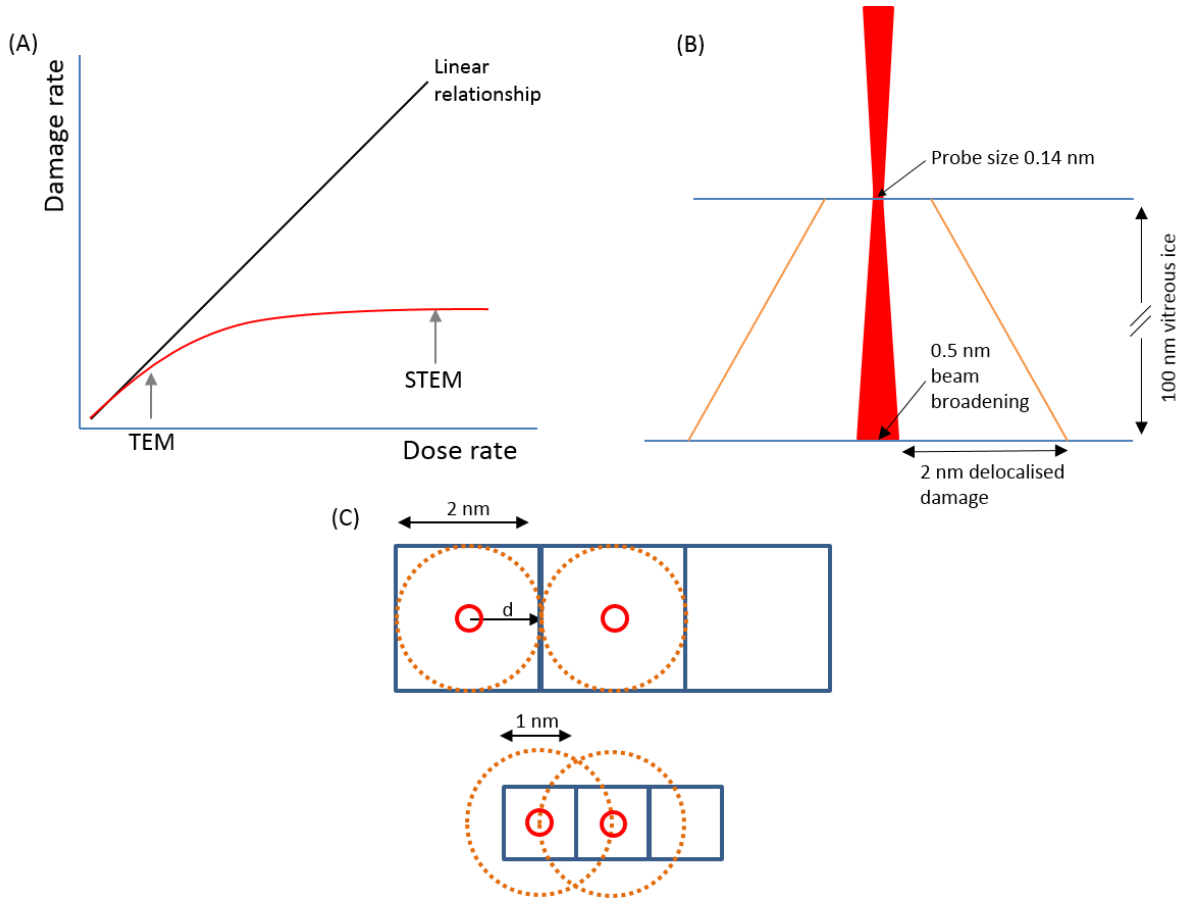

Figure 40: (A) A schematic (Egerton, 2019) postulating the relationship between dose rate and damage rate. The diffusion limited damage in ice corresponds to a power law relationship with exponent <1, between damage rate and dose rate (red curve in schematic). This suggests that lower flux CTEM operates at the linear portion of this curve. In comparison STEM operates at a higher flux per pixel i.e. probe flux (Fp), and hence damage per unit fluence is lower. (B) A schematic (not to scale) showing the estimated beam broadening that will occur in STEM through 100 nm of vitreous ice, and the calculated minimum delocalised damage region (shown in orange) around the probe. (C) An alternative view of (B) showing multiple pixels with the STEM probe size and estimated delocalised damage areas (d) illustrated. Reducing the pixel size would result in the delocalised damage extending beyond the imaging pixel and oversampling would occur. Reproduced from Ilett *et al.* [120].

4.3 Optimising STEM conditions

After establishing that there was potential promise in using STEM to delay vitreous ice damage when compared to CTEM, a quantitative approach to measure ice damage was developed. Changes in ice thickness were monitored using EELS SI to estimate absolute thickness of irradiated areas using the ratio of the elastic (ZLP) and inelastic (remaining energy losses) parts of the energy loss spectrum. Collection and convergence semi-angles of 8.2 and 21.0 mrads respectively were used and a mean atomic number of 3.3 for water. Data was collected in order to verify the predictions from Figure 40 and identify whether original ice thickness, probe current and pixel size influence damage to the vitreous ice. In essence a reduction in the ice thickness driven by H_2 gas formation and release was used as a marker for damage.

4.3.1 Ice thickness sample variation

Throughout the course of multiple cryo experiments it was noted that there was a degree of variation in the original ice thickness of the samples. This was most likely due to variations during sample preparation such as differences in the humidity on each separate day, along with variation in the speed and quality of transfer, potential differences in the blotting process and sampling position on the grid. Ice of different initial thickness does indeed thin at different rates (Figure 41). There is a notable decrease in damage rate for a sample of original thickness, 540 nm compared to a sample with original thickness of 220 nm. The gradient of the line is significantly lower for the 540 nm sample compared to the 220 nm sample, dropping from 0.004 to 0.002 ($Å^2/e^-$) respectively (Figure 41). However, this difference probably stems from the measurements being taken as damage per unit area rather than per unit volume. If alternatively damage per unit volume was measured where for example, a 5000 $e^-/Å^2$ fluence equated to ~0.96 $e^-/Å^3$ for the 220 nm thick sample but only ~0.39 $e^-/Å^3$ for the 540 nm thick sample (calculated assuming a 1.4 Å diameter cylinder is exposed by the focused probe), then it becomes obvious that exposing the samples to the same electron fluence per unit area equates to exposing the thinner sample to an electron fluence per unit volume that is ~2.5 times greater than

that of the thicker sample. This then approximately agrees with the observed 2 times increase in the damage rate seen for the 220 nm sample (Figure 41).

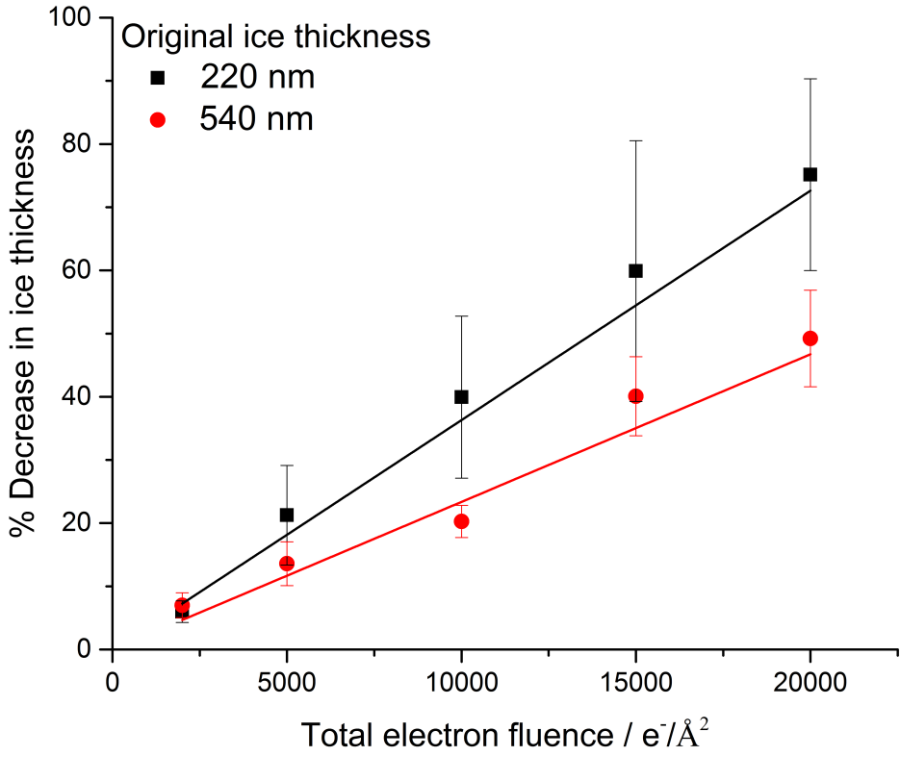

Figure 41: Percentage decrease in ice thickness as a function of the total electron fluence for two varying original ice thicknesses; a 540 nm 'thick' sample (red, circle) and a 220 nm 'thin' sample (black, square). A significant difference was seen in the damage rate, with the thinner sample damaging more quickly ($p<0.05$). However, expressing these measurements per unit volume of irradiated ice rather than per unit area suggests similar damage rates overall. Errors are reported as the standard deviation from n=3 measurements and the linear fit is pinned through (0,0).

4.3.2 Influence of probe current on damage rate

Work was carried out to analyse whether the probe current and therefore F_p had any effect on the damage rate of the vitreous ice under STEM conditions. By ensuring the pixel size and dwell time were kept constant (1 nm, 20 µs) three different probe currents of 60 pA, 100 pA and 280 pA were compared (Figure 42). To obtain the data presented, ice thickness measurements were taken from n=3 areas and the error presented as the standard deviation of the three repeats. Figure 40(A) suggests that altering

the probe current would have little effect on the observed damage since the three probe currents relate to F_p values of 3 x 10^8 $e^-/Å^2$.s, 4 x 10^8 $e^-/Å^2$.s and 1 x 10^9 $e^-/Å^2$.s for 60 pA, 100 pA and 280 pA respectively and therefore, it is likely that for each probe current the microscope is operating at the region where damage rate v dose rate plateaus. This was confirmed through ice thickness measurements which indicated that the decrease in ice thickness was similar within error for each probe current at each total electron fluence (Figure 42). However, running a statistical analysis to compare the three data sets illustrates there was a small significant ($p<0.05$) difference between the datasets for 60 pA and 280 pA, and therefore it was suggested that for any cryo-STEM work where possible the probe current should be kept below 100 pA.

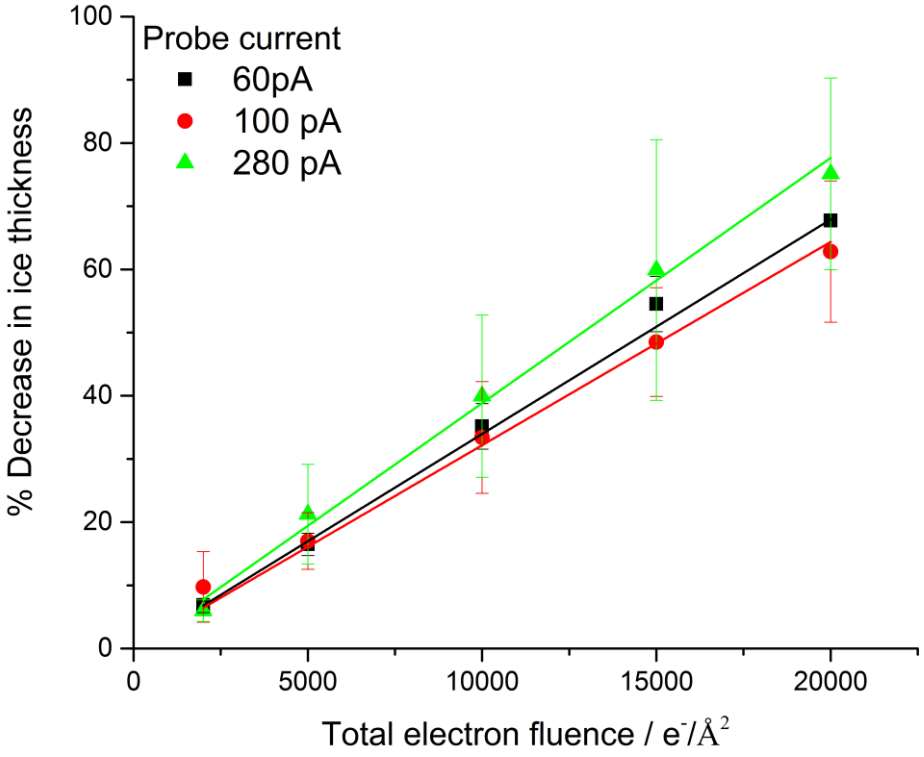

Figure 42: Percentage decrease in ice thickness as a function of total electron fluence for three different probe currents; 60 pA (black, square), 100 pA (red, circle) and 280 pA (green, triangle). The damage rate was relatively similar for each probe current within error. However, a statistically significant difference was observed between 60 pA and 280 pA ($p<0.05$). The errors are given as the standard deviation of n=3 measurements and the linear fit is pinned to (0,0).

4.3.3 Influence of pixel size on damage rate

Finally an investigation into how the pixel size can influence vitreous ice damage was carried out. Three pixel sizes of 0.1 nm, 1 nm and 10 nm were used and for each experiment the probe current was kept at 60 pA and the dwell time at 20 µs. Again, from Figure 40 it would be predicted that there would be an increase in damage with decreasing pixel size due to the implications of delocalised damage, and the occurrence of oversampling at the smaller pixel sizes (< 2 nm). This was confirmed through the measurements taken which demonstrated an increase in ice damage after exposure to the same total electron fluence when smaller pixel sizes were used (Figure 43). Note that for the larger pixel size of 10 nm only small total electron fluence data could be collected due to the number of scans required to achieve certain total electron fleunces with the pre-set dwell time and probe current. For example to achieve a 5000 $e^-/Å^2$ total accumulated fluence, 6677 frames would be required which would equate to 9 h collection time for a 512 x 512 pixel image which was not feasible. Therefore, a log-log plot was used to determine that there appeared to be a power law relationship between electron fluence and ice damage, indicated by the linear fit to the re-plotted data. A power law relationship between damage and fluence has previously been reported by Pan *et al.* [175] and its occurrence was attributed to the power law dependence of surface diffusion. Here surface diffusion of the secondary radiolytic products may well dominate in thin ice. Fitting the data allowed predictions to be made regarding ice damage at higher total electron fluences when using a 10 nm pixel size (Figure 43 – blue line).

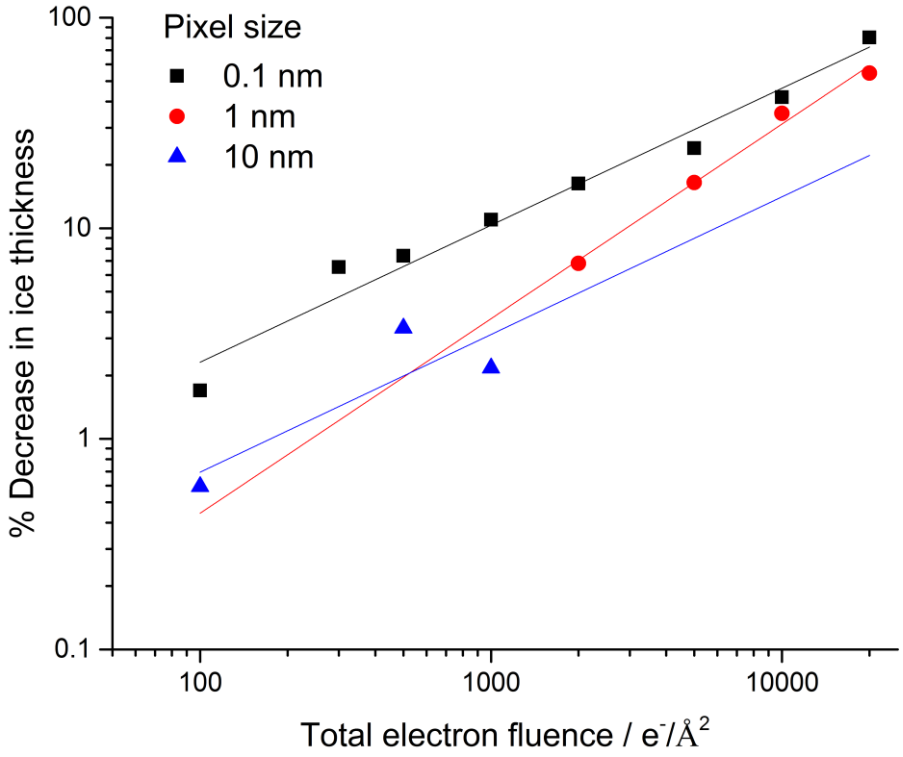

Figure 43: Percentage decrease in ice thickness as a function of total electron fluence for three different pixel sizes; 0.1 nm (black, square), 1 nm (red, circle) and 10 nm (blue, triangle). A log-log plot was used to obtain a linear fit, indicating a power law relationship between ice damage and electron fluence. Greater damage was observed when using smaller pixel sizes. Data is plotted as the mean of n=3 experiments.

4.4 CTEM conditions

An investigation into whether quantitative measurements of ice damage could also be conducted for CTEM was carried out. Results were inconsistent and not reproducible. Initial attempts to replicate ice thickness measurements using the ratio of the elastic to inelastic parts of the EEL spectrum did not show any significant thinning of the ice despite exposure to electron fluences beyond what had previously been shown to cause significant bubbling in the ice (Figure 44). In instances where bubbling was observed it tended to occur preferentially in the regions overlapping the carbon support film on the TEM grid. This has been noted previously by Chen *et al.* [176] who suggested that the structural discontinuity that occurs at the interface between ice and the carbon support film could act as

nucleation points for the formation of gas bubbles. In addition the conductive nature of the carbon coating could promote the conduction of damage products away more easily, preventing recombination back to H_2O. Figure 44 shows that in some areas where bubbling was observed, damage to vitreous ice over the carbon film occurred at a total fluence of between 0 – 500 $e^-/Å^2$, and bubbling within a hole occurred at 2000 $e^-/Å^2$. The bubbling indicated by the white box in Figure 44 resulted in the movement of nanoparticles within the vitreous ice, disrupting the original position of the nanoparticles in suspension, something that was not observed for the same total electron fluence using STEM (e.g. Figure 39). The discrepancies in ice damage between samples or even different areas within the same sample could be explained by the mechanism through which bubbling occurs. Bubbling of ice is a marker of damage and occurs due to the production of gaseous H_2 but only occurs when there is some sample present within the ice that is available to react with the radiolytic damage products to produce this molecular H_2. In the case of pure vitreous ice the onset of bubbling would be expected to be delayed to higher doses if not eliminated due to the rapid recombination of $H^\bullet$ and $OH^\bullet$ radicals back to H_2O [177-179]. Therefore areas of vitreous ice on the support grid with little to no sample captured would not be anticipated to show significant damage even under large total electron fluences [179].

In addition to bubbling it was also noted that in some cases crystallisation of the vitreous ice occurred upon beam exposure. Again, this crystallisation led to the artificial movement of nanoparticles captured in the ice, changing the original dispersion in suspension. Nonetheless, this observation, in similarity to ice bubbling, was not consistently reproducible for specified total electron fluences between samples or areas within the same sample. It was observed that crystallisation preferentially occurred in areas where there were already elements of crystalline ice present, probably due to these crystalline regions acting as heterogeneous nucleation sites for further crystallisation (Figure 45(B)). Samples with better quality amorphous ice (i.e. fewer crystals and frost) did not tend to show crystallisation upon exposure to the same total accumulated electron fluences (Figure 45(C)). Crystallisation should only occur if the localised temperature rises above the vitrification temperature

(-135^{o}C). Previous work by Karuppasamy *et al.* [180] demonstrated the crystallisation of vitreous ice in cryo-TEM, and by using 'lumped model calculations' they estimated the likely temperature changes under the electron beam and concluded that crystallisation would only occur when higher electron fluxes were used (>50 $e^{-}/Å^{2}.s$) and/or when there was poor thermal contact between the grid and the cryo holder [181].

From these investigations it was not possible to obtain a single critical dose for vitreous ice damage in CTEM. However, the work highlighted that common differences in ice quality, ice thickness and amount of sample in the area being imaged, can have significant effects on the observed damage to the vitreous ice. These differences are driven primarily through differences that occur during sample preparation such as changes in humidity, the quality of liquid ethane and the speed of transfer to the cryo holder etc. However, the indication was, that when damage did occur in CTEM it caused significant movement of nanoparticles away from the original suspension positions and occurred after the sample was exposed to electron fluences that were 4x lower than was necessary to observe the same nanoparticle movement in STEM.

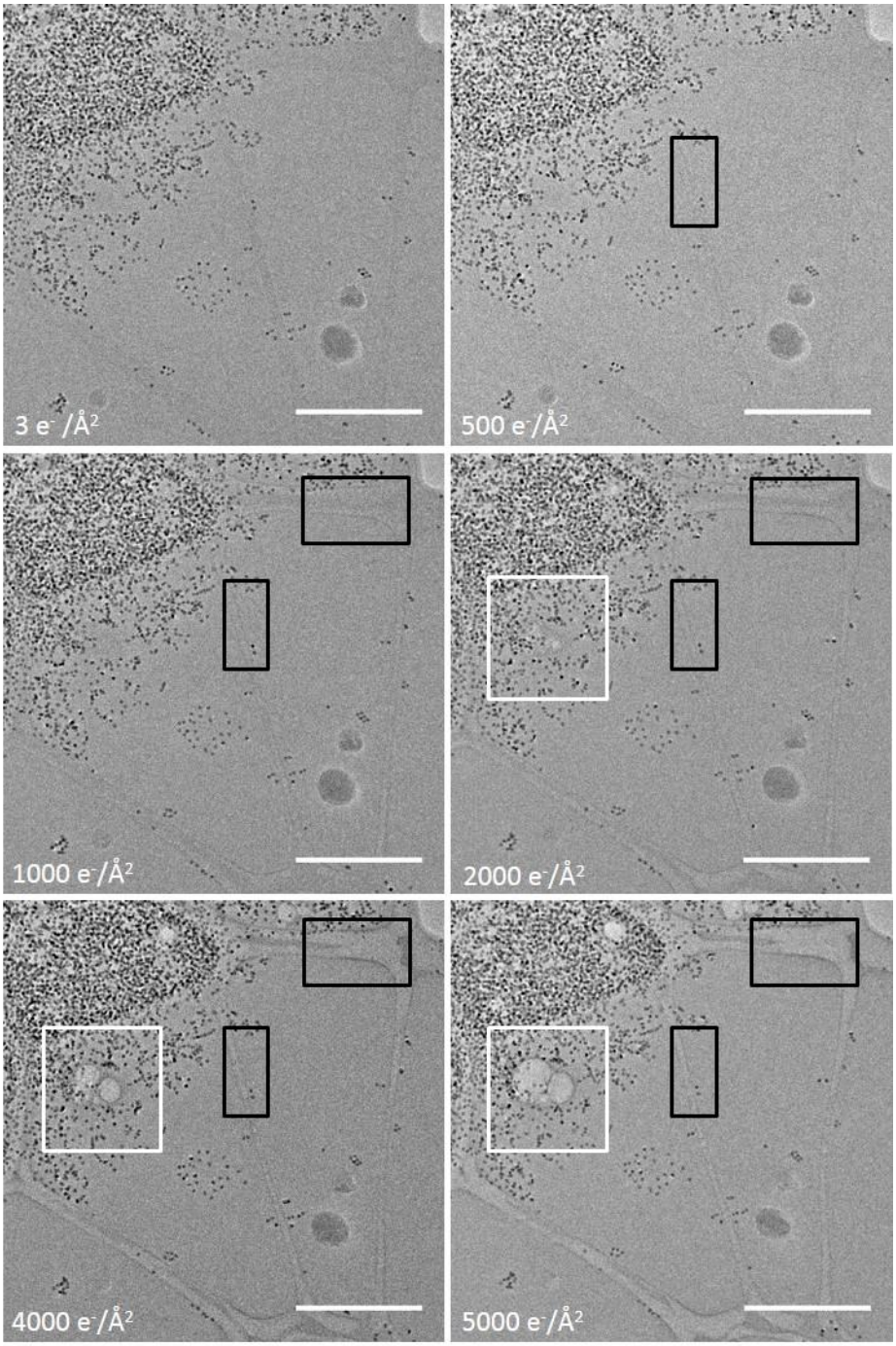

Figure 44: Cryo-CTEM images indicating bubbling in vitreous ice as a function of electron fluence. Damage occurred preferentially at the site of the carbon film indicated by the black boxes at 500 $e^-/Å^2$. Further damage is seen within the holes after exposure to 2000 $e^-/Å^2$ indicated by the white boxes. Scale bar indicates 1000 nm.

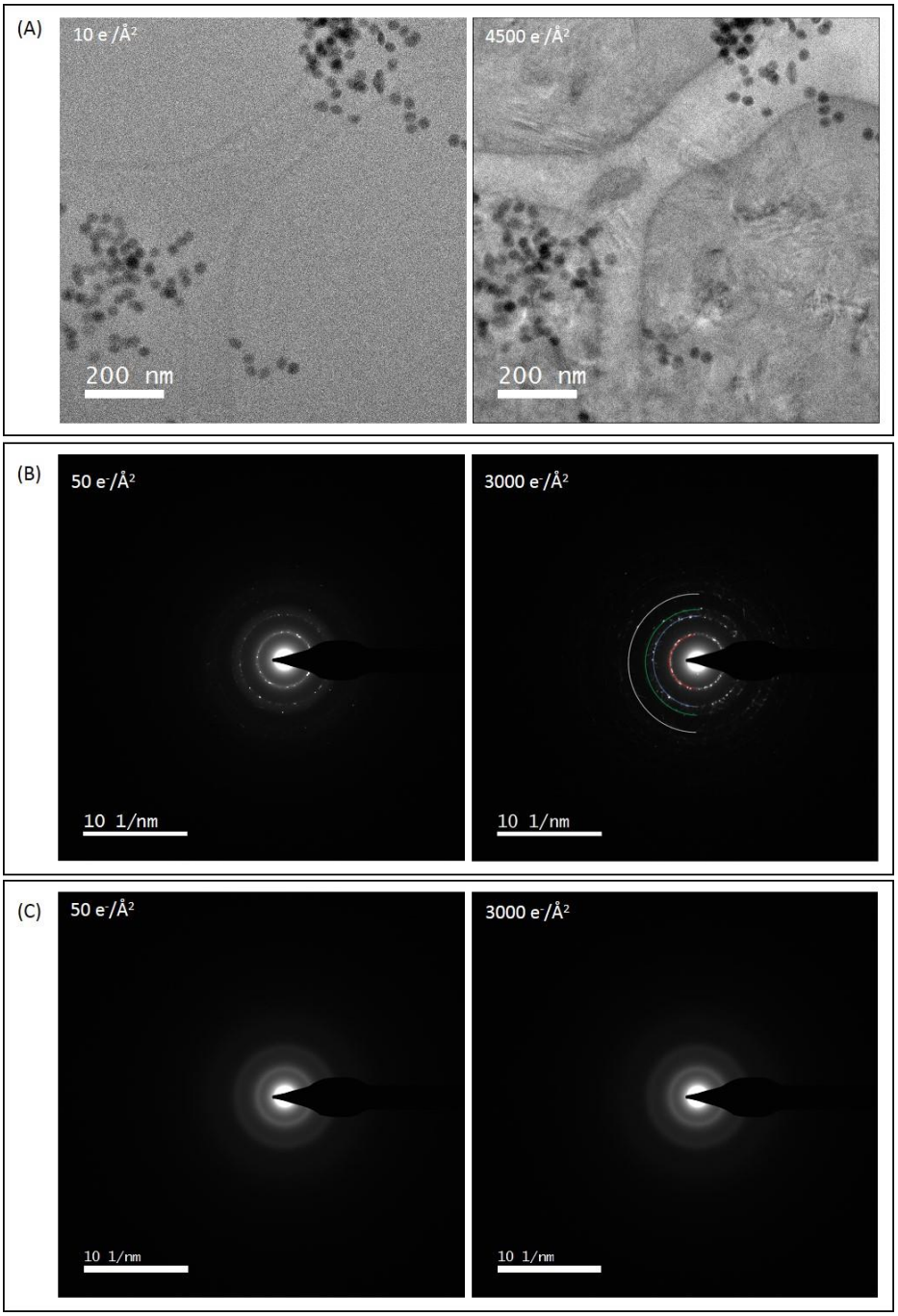

Figure 45: Three datasets showing the variation in crystallisation in cryo-CTEM. (A) Cryo-TEM image showing clear crystallisation occurred from a region of amorphous vitreous ice after exposure to 4500 $e^-/Å^2$. (B) Further evidence of ice crystallisation in a region with some degree of original crystallinity; brighter diffraction spots were observed after exposure to 3000 $e^-/Å^2$. The diffraction pattern suggested cubic ice formed with the (111) (red), (220) (blue), (311) (green) and (400) (white)

lattice planes identified. (C) A final dataset showing no evidence of crystallisation of the vitreous ice after exposure to 3000 $e^-/Å^2$. For all datasets a 50 $e^-/Å^2$.s probe flux was used.

4.5 Liquid cell TEM

Recently, there has been a rapid increase in research using and developing liquid cell technologies for *in situ* TEM [182]. This technique has obvious benefits for highly accurate characterisation of suspensions as no pre-sample preparation processes are involved and samples can be imaged directly when dispersed in solution. However, as the technique becomes more prevalent, an understanding of the complex chemistry that can occur in a sample during electron beam irradiation is necessary [183]. Here using a static liquid cell, commercially sold as a K-kit, characterisation of the same model nanoparticle system that was used for cryo-analytical-STEM has been carried out to determine whether: a) the same degree of accuracy of elemental analysis could be carried out on suspensions in solution compared to suspensions captured in a layer of vitreous ice, b) whether the same nanoparticle dispersion state was observed in the static liquid cell and c) whether there was a significant difference in beam interactions within the liquid cell compared to frozen vitreous samples.

Initial optimisation of STEM-EDX was carried out using a K-kit prepared for dry mode analysis, i.e. the suspending media was removed leaving some nanoparticles still adhered to the windows of the K-kit. This reduced beam interaction complications (in the presence of liquid) and permitted a higher probe current to be used allowing optimal collection parameters to be ascertained (see Chapter 3, section 3.4.2). Once optimised STEM-EDX analysis was carried out on the model suspension in the liquid state (i.e. in wet mode). Successful EDX spectroscopy identified each element within the suspension and the positions of the elements were mapped as before for cryo analysis in order to investigate the dispersion of each nanoparticle type. X-ray elemental maps of Fe (K_α), Ce (L_α) and Zn (L_α) are shown in Figure 46 and qualitative assessment of a number of areas within the sample showed no obvious difference in the dispersion of the different nanoparticles when captured in the frozen hydrated state compared to direct analysis in solution. Due to size of the nanoparticle clusters a large channel gap

size of 2000 µm was used to maximise the amount of sample in the liquid cell and this meant EELS was not possible.

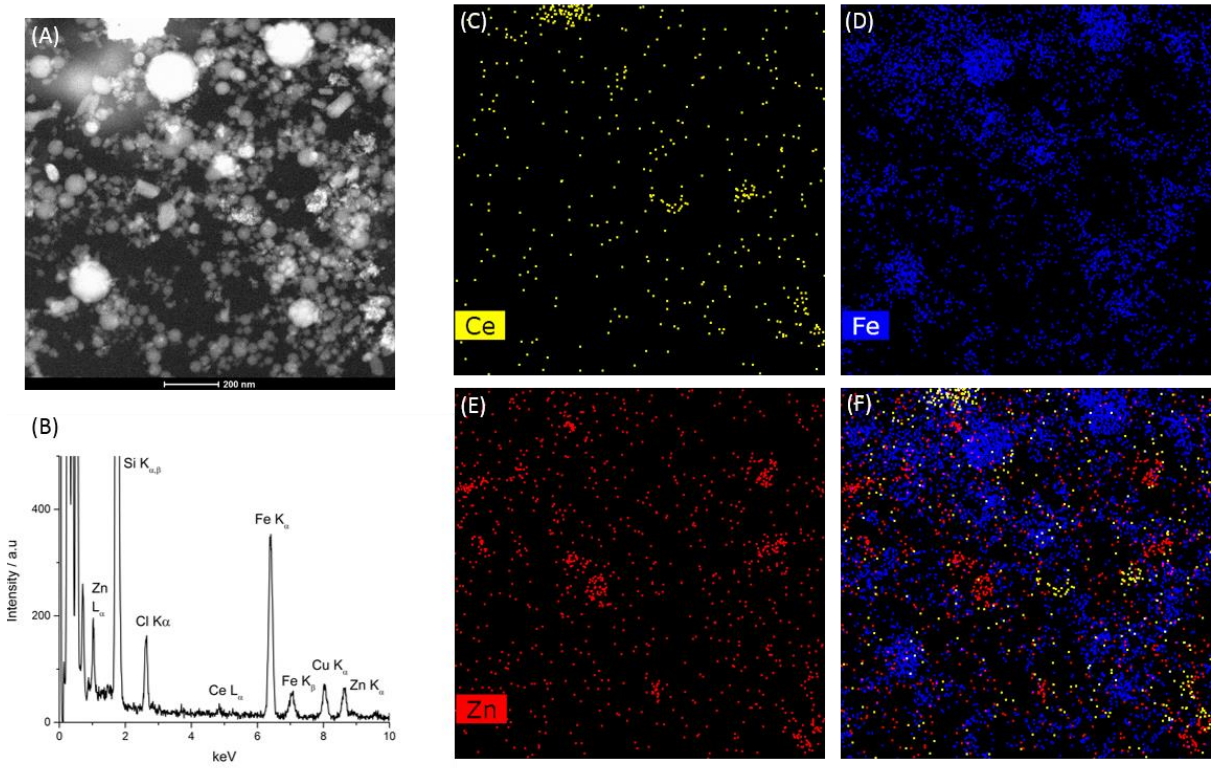

Figure 46: STEM-EDX of a model nanoparticle suspension containing ZnO, Fe_2O_3, CeO_2 and Au-Ag core-shell nanoparticles, in a static liquid cell. (A) A HAADF STEM image of the model nanoparticle suspension from which the corresponding EDX maps and spectrum were obtained. From the EDX spectrum (B) mapping of Ce L_α (C), Fe K_α (D) and Zn L_α (E) X-rays is shown. A combined elemental map is provided in (F).

During EDX analysis there was evidence of some dissolution of nanoparticles during beam irradiation, most obviously the ZnO nanoparticles (Figure 47). It is known that upon exposure to the electron beam the pH of water contained within a liquid cell can be reduced due to the formation of H_3O^+ ions during the radiolysis of water [169]. Since the solubility of ZnO increases in more acidic environments [184] the dissolution of ZnO nanoparticles after exposure to the electron beam may occur and this was apparently the case here (Figure 47). Further investigation of beam damage driving nanoparticle dissolution was carried out on a dispersion of iron oxide nanoparticles (Fe_3O_4-PEG) in water. The

sample was exposed to increasing total electron fluence with images taken after each illumination (Figure 48). There was clear evidence that significant dissolution occurred after just 60 $e^-/Å^2$ with a measurable decrease in nanoparticle diameter, and after 200 $e^-/Å^2$ all original nanoparticles within the window had dissolved. Although here this artefact is detrimental to the analysis of nanoparticle suspensions, there could well be potential applications of this effect in mimicking low pH environments that are typically found within some intercellular compartments (e.g. in endosomes and lysosomes), and are known to stimulate the dissolution of some nanoparticles, causing (nano)toxicity. Therefore, beam induced radiolysis could be useful for the *in situ* study of inflammatory responses of biological cells to some nanoparticles. However, a thorough understanding of dose effects beyond just lowering of the pH would of course be required in order to do this.

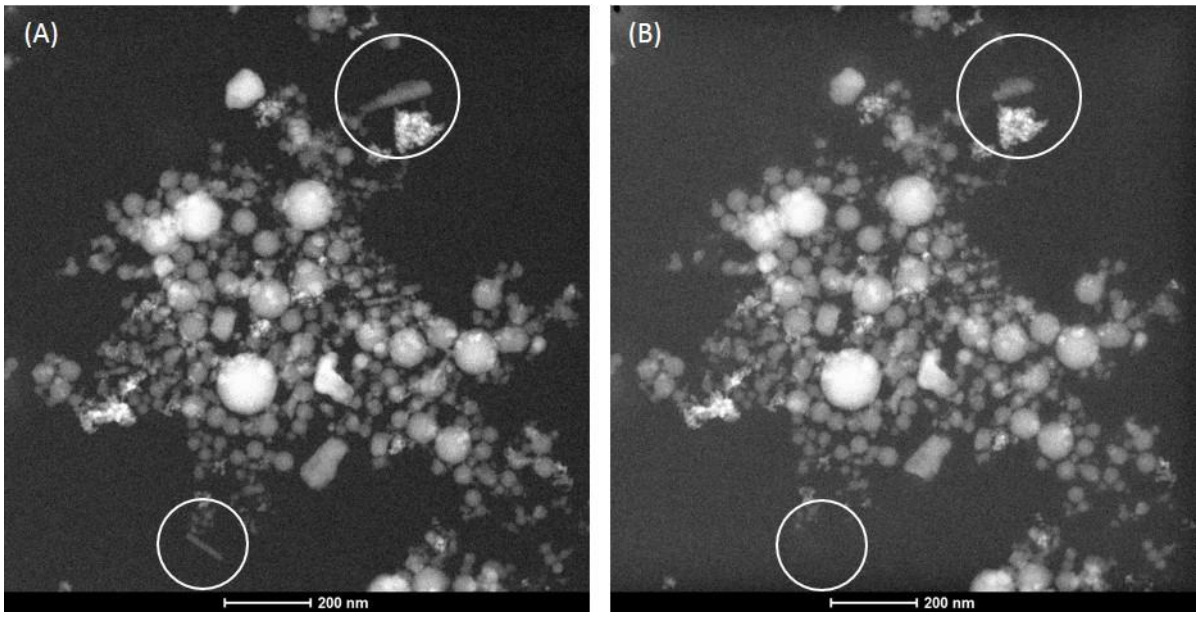

Figure 47: Evidence of nanoparticle dissolution in the static liquid cell. HAADF STEM images of the model multi-type nanoparticle suspension in liquid taken after exposure to an initial electron fluence of 30 $e^-/Å^2$ (A) and after exposure to a further 300 $e^-/Å^2$ (B). Examples of the dissolution of ZnO nanoparticles is indicated by the circled regions.

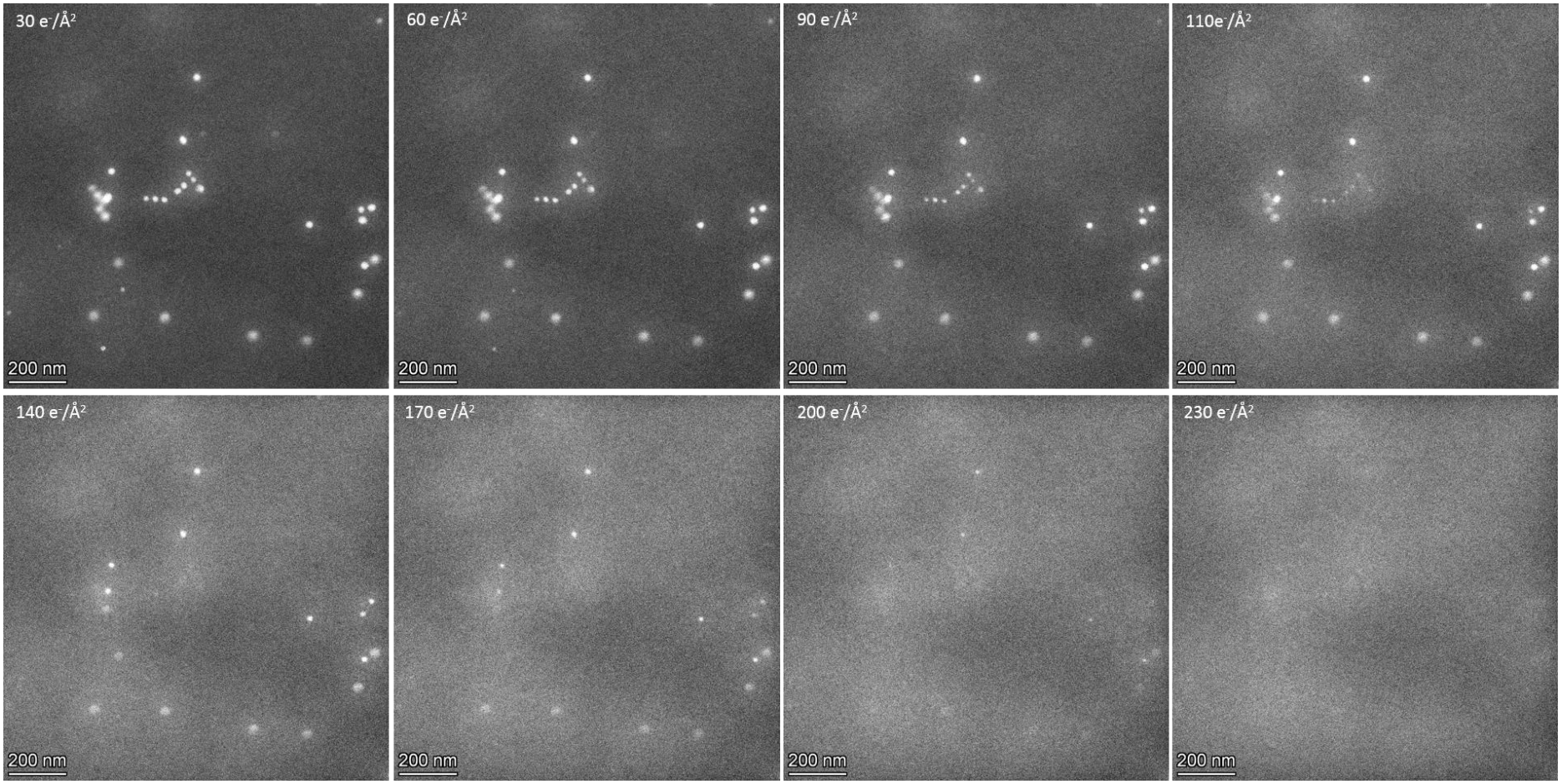

Figure 48: HAADF STEM images of Fe_3O_4-PEG nanoparticles dispersed in water and loaded in a static liquid cell. There was evidence of significant dissolution of the nanoparticles after exposure to increasing total electron fluence. No movement of the nanoparticles was observed suggesting the nanoparticles were adhered to the upper and/or lower silicon nitride window surfaces.

For each example system, the same sample was characterised using cryo conditions when captured in a layer of vitreous ice (data not shown for Fe_3O_4-PEG suspension). In the case of both sample systems the nanoparticles remained stable under the electron beam in cryo conditions. There are a number of possible reasons for this; the significantly lower temperatures of vitreous ice compared to liquid water will dramatically reduce reaction rates involved in the radiolysis of water and the subsequent reactions of secondary damage products [185, 186]. Consequently, the rate of radiation damage will be slower for frozen samples in cryo-TEM compared to liquid samples in LCTEM. Additionally, the diffusion rate in vitreous ice held at -137°C (i.e. below the glass transition temperature) will be significantly slower than in solution [187]. Since the radiolysis of water is diffusion limited then these slower diffusion rates of the damage products will cause a reduction in the observed damage. Evidence of this has been shown previously by a number of papers referring to the damage products in cryo conditions as being 'frozen' and therefore preventing further secondary damage reactions to occur [168, 188].

The overall suggestion here is that in some instances cryogenic *in situ* techniques may be more suitable than liquid cell techniques for the characterisation of nanoparticle suspensions (notably where nanoparticles of interest are sensitive to changes in pH). No obvious difference in the signal to noise of the characterisation data was seen in the two techniques yet beam induced effects were significantly reduced for the frozen hydrated sample.

Summary

This chapter has detailed the precise conditions for successful cryo-STEM-EDX and EELS analysis to characterise a model nanoparticle suspension that contained four different nanoparticle types. Each component was successfully identified and mapped within a suspension. Moreover a significant difference in the destruction of vitreous ice illuminated by the electron beam was shown between CTEM and STEM, where it was observed that STEM was advantageous in reducing the damage per

unit electron fluence of the vitreous ice. An investigation into factors affecting ice damage in STEM identified that thicker ice damages more slowly per unit area, probe current has limited impact on damage rates as expected for inverse damage and the existence of delocalised damage means pixel size can greatly affect damage rates. Comparative studies in CTEM showed a degree of variation, but indicated bubbling and crystallisation can occur at lower fluences than in STEM causing artificial movement of nanoparticles away from the original position. Finally, the characterisation of the model suspension using a static liquid cell was carried out which indicated certain limitations of LCTEM whereby the beam induced reduction in pH can drive dissolution of iron and zinc oxide nanoparticles, which does not occur when using cryo-EM. Ultimately, the development and optimisation of analytical cryo-STEM techniques should allow these techniques to be powerful tools for nanoparticle dispersion characterisation of more complex 'real' systems as will be presented in the following chapter.

Chapter 5

5. CHARACTERISATION OF NANOPARTICLES IN COMPLEX BIOLOGICAL MEDIA VIA *IN SITU* AND AUTOMATED STEM TECHNIQUES

Having successfully developed and fully optimised cryo-analytical-STEM to carry out accurate nanoparticle characterisation of a model nanoparticle suspension, the next step was to apply this technique to more relevant systems to begin to understand the interactions at the bio-nano interface. In this chapter cryo-analytical-STEM is used to probe the solid-liquid interface of a number of different nanoparticle systems dispersed in CCM.

The second section of this chapter details a novel method developed to carry out automated STEM imaging and analysis to investigate the dispersion state of nanoparticles in a number of biological media. The automated data analysis protocol was validated using a simple system of silica nanoparticles in water, and following validation was used on several nanoparticle systems to

investigate the agglomerate size and consequently dispersion behaviour of these nanoparticles in biological media.

Work in this chapter has been published in the following peer reviewed journals:

-Section 5.1.2 in Ilett *et al.* Journal of Physics:Conference Series 2017 [189]

-Sections 5.1.1 and 5.1.3-5.1.5 in Ilett *et al.* Scientific Reports 2020 [90]

-Sections 5.2.3-5.2.7 in Ilett *et al.* Journal of Microscopy 2019 [190]

5.1 Nanoparticles dispersed in cell culture media

For any *in vitro* study, nanoparticles are routinely dispersed in CCM for delivery to cells. Therefore, it is of significant value to understand how nanoparticles interact with the many components present in CCM in order to predict and evaluate any potential therapeutic benefit and/or toxicological impact *in vivo*. CCM typically comprises of vitamins, amino acids and salts, alongside commonly added protein supplements to aid in cell growth and therefore the complex nature of the media can alter the way in which nanoparticles may behave. It is well documented that when nanoparticles come into contact with biological fluids containing proteins a protein corona forms [53]. A protein corona is a coating formed of two layers; the hard corona which contains proteins with a high affinity association to the nanoparticle surface and the soft corona which contains proteins with a lower affinity association. Moreover, biological fluids tend to have a high ion content and therefore electrostatic interactions between these ions and the nanoparticle surface can occur [31, 37]. To begin to probe these solid-liquid interactions a number of different nanoparticle systems were dispersed in CCM, either DMEM or RPMI with or without the addition of 10% FBS, and full characterisation of the behaviour of the nanoparticles upon dispersion was performed.

5.1.1 Interactions at the bio-nano interface

Six different nanoparticles were each individually dispersed in DMEM with 10% FBS at 100 µg/mL via bath ultra-sonication. These were, gold coated with PSS (Au-PSS), barium titante ($BaTiO_3$), zinc oxide

(ZnO), titanium dioxide (TiO_2), iron (III) oxide (Fe_2O_3) and barium titanate coated with poly-l-lysine ($BaTiO_3$-PLL). Once dispersed, TEM grids were prepared via drop casting and air drying the suspension. Upon imaging the TEM grids it was obvious that a coating had established around each different type of nanoparticle (Figure 49(A-F)). EDX analysis was carried out on the coating and it appeared to contain a number of ionic constituents present in the CCM (Na, Cl, Ca, P, Mg) (Figure 49(H)). The zeta potentials (measured in water) of each nanoparticle were different suggesting the coating formation was independent of surface charge of the nanoparticle (Figure 49(G)). However, since drying artefacts are known to occur when using drop-casting TEM grid preparation [189, 191], *in situ* native state characterisation was carried out using the cryo-analytical-STEM techniques established in the previous chapter to confirm the presence and composition of the coating.

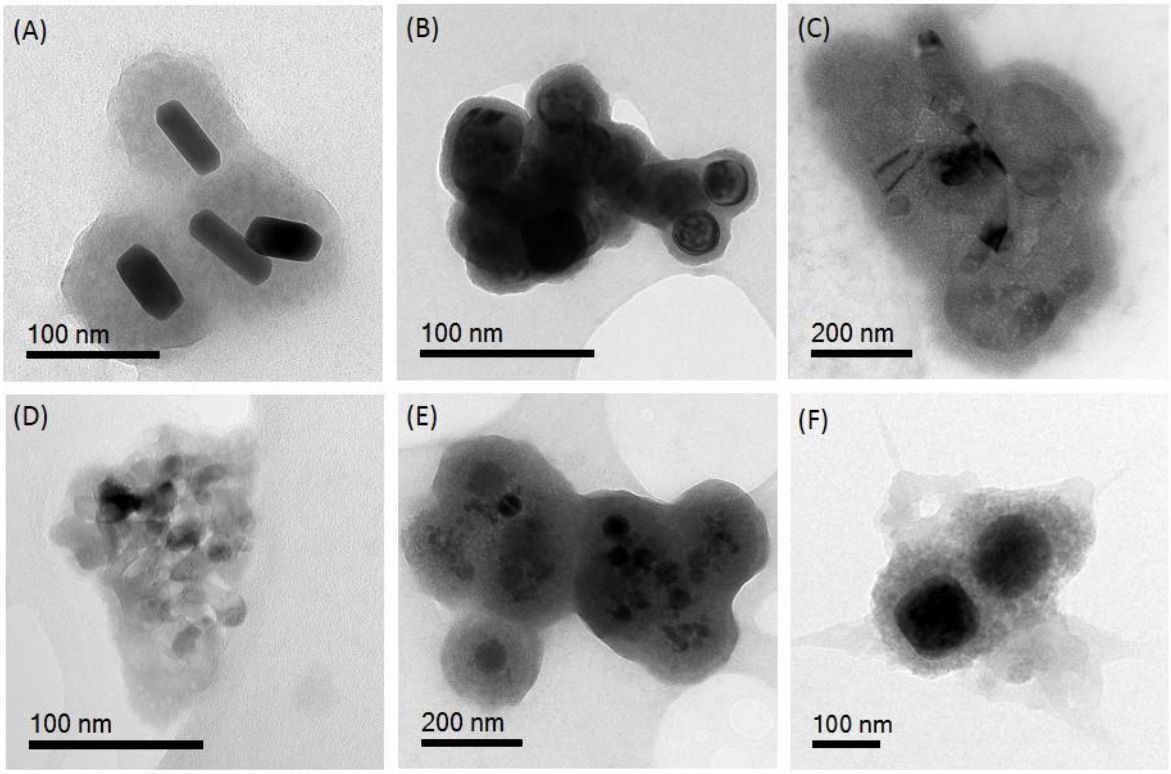

(G)

	Zeta potential / mV
Au-PSS	- 42 ± 0.6
$BaTiO_3$	- 24 ± 0.8
ZnO	+ 7.5 ± 0.6
TiO_2	+ 11 ± 0.6
Fe_2O_3	+ 21 ± 0.3
$BaTiO_3$-PLL	+ 48 ± 0.3

(H)

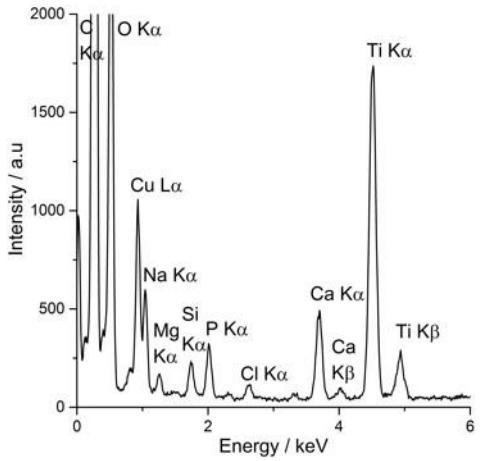

Figure 49: TEM images of six nanoparticle systems dispersed in CCM prepared by drop-casting and air drying. (A) Au-PSS, (B) $BaTiO_3$, (C) ZnO, (D) TiO_2, (E) Fe_2O_3 and (F) $BaTiO_3$-PLL. Each system showed a coating formed around the nanoparticle after suspending in cell culture. (G) Table indicating the variation in zeta potential of the different nanoparticles (all measurements taken in water). EDX analysis of the coating around TiO_2 (H) indicated several elements were present in the coating (Na, P, Ca, Cl and Mg). Reproduced from Ilett *et al.* [90].

5.1.2 Drop cast v cryo analytical STEM

It was found that there were significant differences in the composition of the coating when analysed *in situ* using cryo conditions rather than dried samples. A suspension of $BaTiO_3$-PLL nanoparticles in CCCM was either prepared for TEM via drop casting and air drying or by plunge freezing and cryo-transfer. When comparing the EDX maps from analytical-STEM of these two samples a significant difference in the elemental composition of the coating was observed for the two preparation techniques (Figure 50). For the drop cast sample (Figure 50(A)) the EDX maps indicated a number of elements present in CCM spatially resolved to the position of the coating (Ca, P, Cl, Na, K, Mg). In contrast under cryo conditions the EDX maps showed that only Ca and P spatially resolved to the position of the coating and the other elements of Na, Cl, Mg and K remained dispersed in the ice. This suggested that during air drying, artefacts occurred such that additional components in the CCM accumulated around the nanoparticles, whilst when suspended in solution it was actually a calcium-phosphorous-rich corona that formed around the nanoparticles. A previous report by Xu *et al.* [78] detailed the formation of a similar coating that they referred to as a 'nano-bio-complex' around CuO and ZnO nanoparticles dispersed in CCM. They postulated that K^+, Ca^{2+}, Na^+, P^{4-} and Cl^- ions formed a complex around the nanoparticles. However, they looked only at air dried samples and therefore considering the work shown here, it is likely that the results were also influenced by drying artefacts and *in situ* EM techniques would be necessary to confirm their findings.

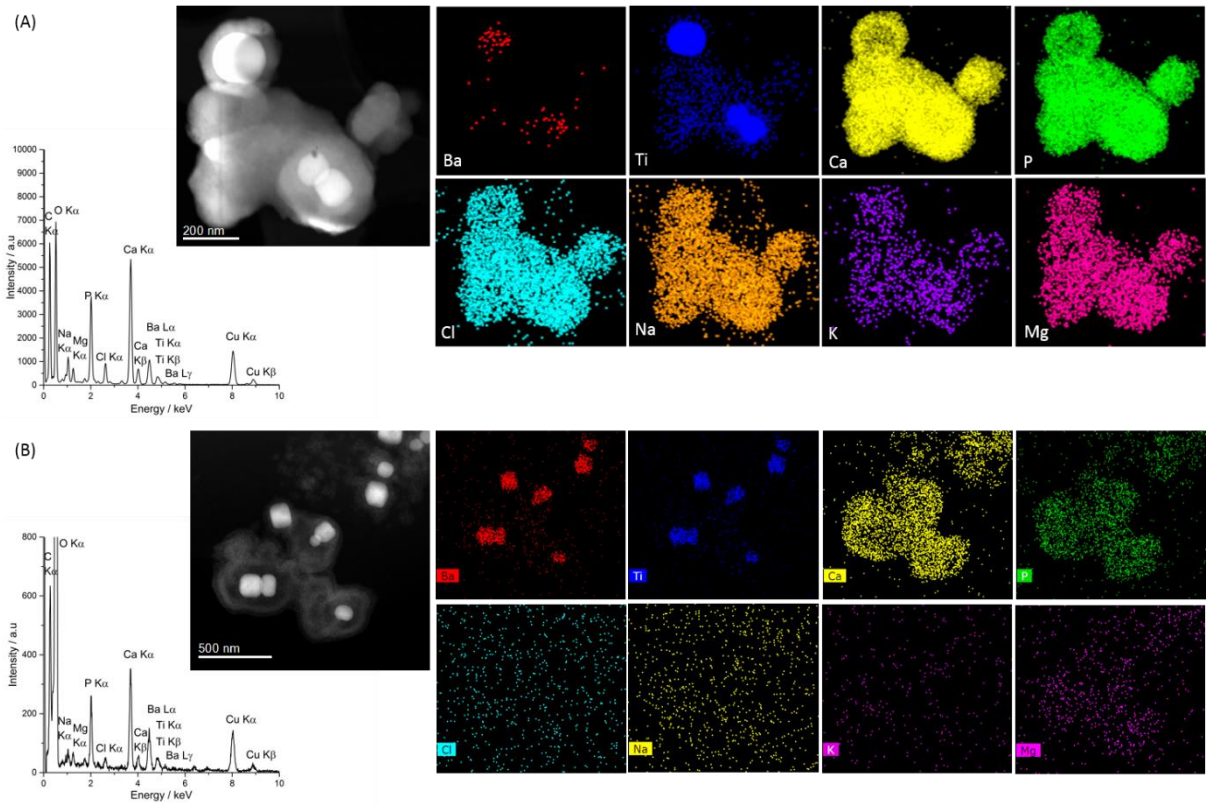

Figure 50: A comparison between $BaTiO_3$-PLL nanoparticles dispersed in CCCM and characterised after drop cast preparation (A) or under cryo conditions (B). Drying artefacts were seen to occur using conventional drop cast techniques where a number of elements spatially resolved to the position of the coating. However when characterising the system in the frozen hydrated state only Ca and P spatially resolved to the position of the coating and the other components of the media were present only in solution. EDX maps were obtained from signals for Ba Lα (red), Ti Kα (blue), Ca Kα (yellow), P Kα (green), Cl Kα (turquoise), Na Kα (orange), K Kα (purple) and Mg Kα (pink). Adapted from Ilett *et al.* [90].

5.1.3 Sample preparation artefacts

Having confirmed that the coating was Ca and P rich, the next step was to try to understand the mechanisms involved in the coating formation. From initial observations the Ca and P rich coating appeared to establish only when extended (>10 min) bath sonication was used to fully disperse the nanoparticles in CCM. Further investigation found that the coating could establish in between 30 – 60 minutes. This suggested that the coating could be linked to the sonication process. To confirm or

otherwise that this was the case, the pH of CCM was monitored during bath ultrasonication, incubation in a water bath (at 40°C) and incubation at room temperature over a period of 24 h, all at atmospheric CO_2 conditions. For both bath ultrasonication and incubation in the water bath a rise in temperature to 40°C or more within 10 minutes was observed. In addition a significant increase in pH from 7-7.25 to over 8 occurred over the course of ~150 minutes. Comparatively the pH rise of the sample incubated at room temperature was far slower, taking hours to reach a value close to 8.0 (Figure 51). Furthermore to confirm that the length of incubation was not the critical factor in coating formation a sample of $BaTiO_3$ nanoparticles in CCM was incubated at room temperature for 3 h and no coating was observed (Figure 52). However it would be predicted that a coating would form after 24 h room temperature incubation where a pH rise comparative to that seen at the higher temperature bath sonication/water bath incubation was reached.

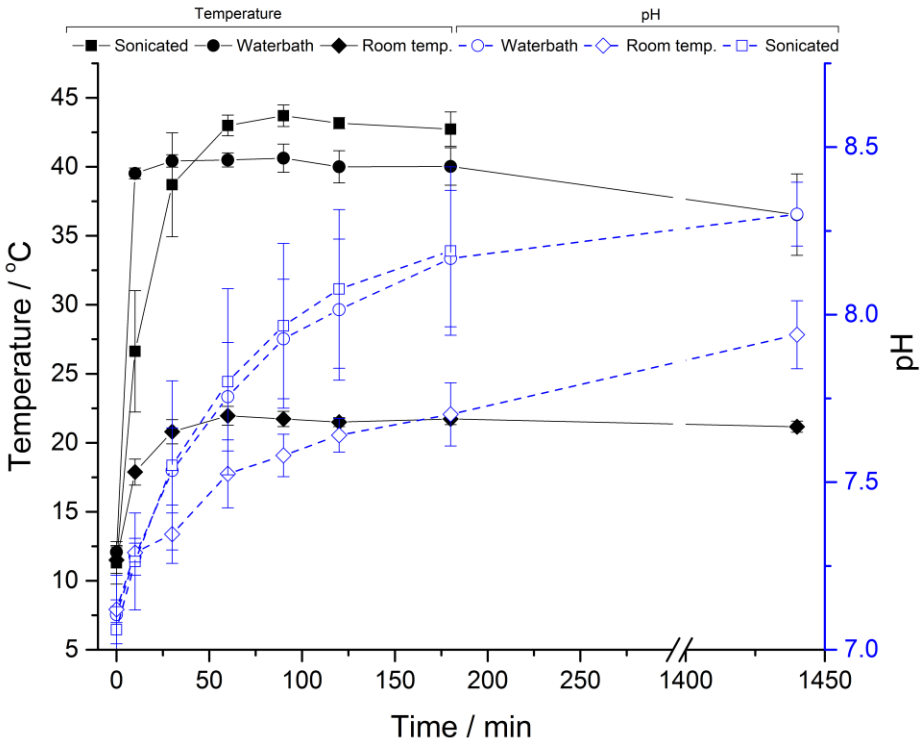

Figure 51: pH (dashed line) and temperature (solid line) measurements of CCM either bath sonicated, incubated in a water bath at 40°C or incubated at room temperature in atmospheric CO_2 levels. For bath sonication, measurements were taken over a period of 3 h; whilst for incubation at

40°C in a water bath and at room temperature, measurements were taken over a period of 24 h. The increase in pH of the CCM was much quicker when at the elevated temperatures of the water bath and bath sonicator reaching >8 after 3 h. In comparison the increase in pH at room temperature was much slower, only reaching ~8 after 24 h incubation. Reproduced from Ilett *et al.* [90].

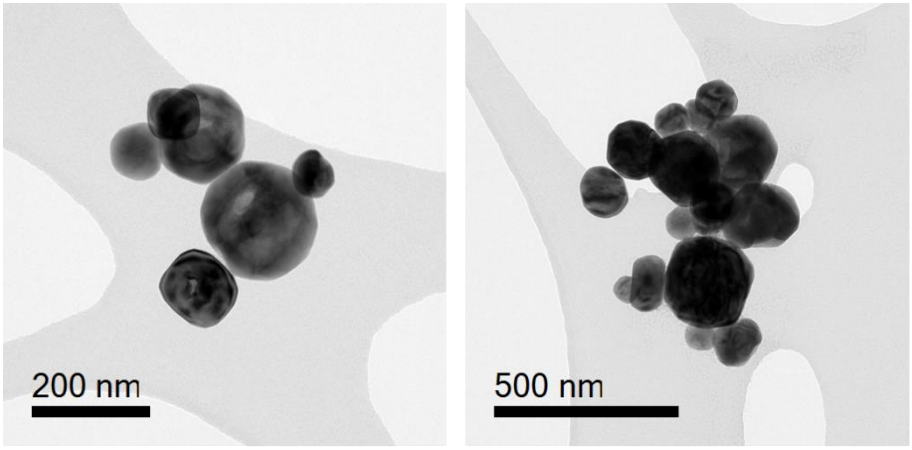

Figure 52: $BaTiO_3$ nanoparticles dispersed in CCM and incubated at room temperature for 3 h. No calcium phosphate coating was observed which confirmed that pH and temperature were the critical factors in coating formation. Reproduced from Ilett *et al.* [90].

It was confirmed that the presence of FBS did not affect whether a coating established, with the coating observed in both cases in agreement with the results in [79]. This suggests that any involvement of proteins in the coating formation is minimal and not crucial. Furthermore, the coating was seen to form on three different size/shape ZnO nanoparticles (Figure 53) when sonicated in CCCM. Both these observations suggested that the coating formation was an artefact of sample preparation.

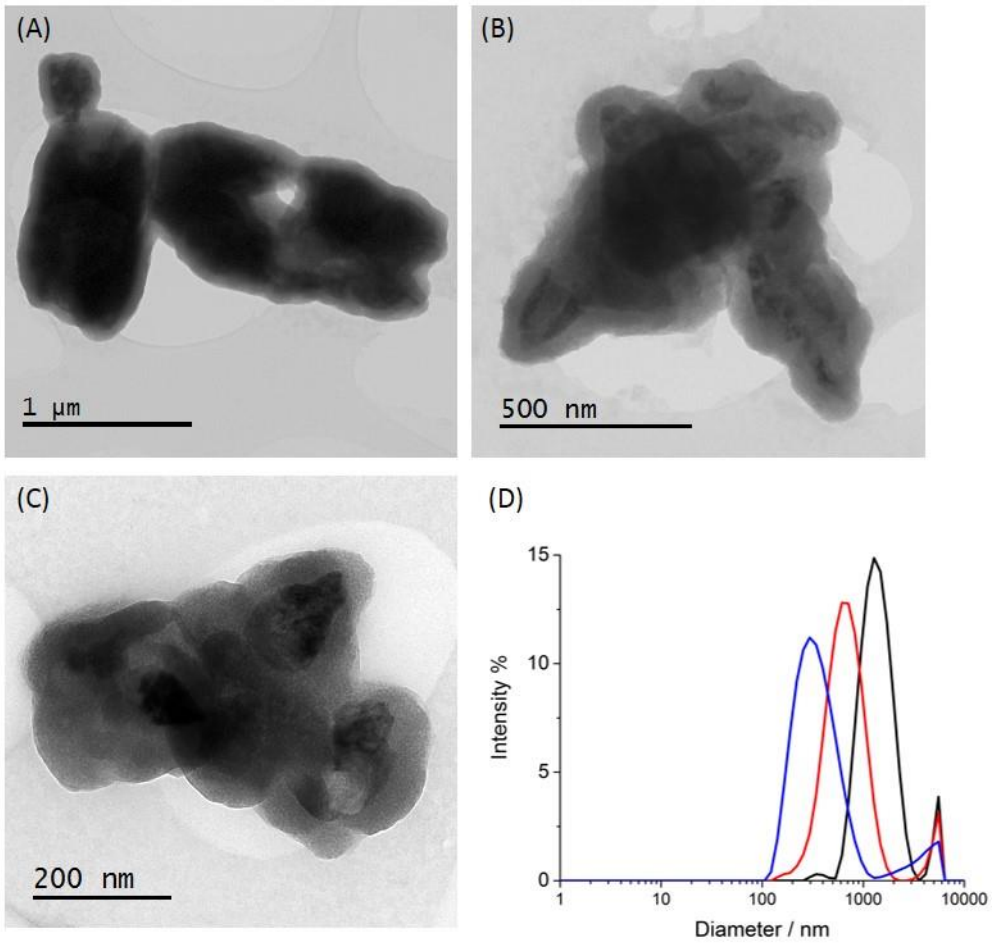

Figure 53: Three ZnO nanoparticles of different shape and size dispersed in CCCM and drop cast onto a TEM grid and dried. The DLS plot in (D) indicates the increase in size where the blue line corresponds to the particles imaged in (C), the red line to the particles imaged in (B) and the black line to the particles imaged in (A). The hydrodynamic radii were 295 ± 11 nm, 615 ± 36 nm and 1281 ± 141 nm with the range given as the standard deviation of n=3 measurements. The calcium phosphorus rich coating established on all three nanoparticles confirming that coating formation was independent of size and shape. Reproduced from Ilett *et al.* [90].

CCM is a complex system with delicate chemistry designed to regulate conditions such that the media remains optimised for healthy cell growth. Typically CCM is a carbonate buffered system, but these buffers are only effective at maintaining physiological pH (~7.4) under specific conditions, usually 37°C and 5% CO_2 levels. However, suspension preparation here, and in most materials research laboratories, was carried out using atmospheric conditions where the CO_2 level is far lower (~1%).

Therefore it is hypothesised that in accordance with Le Chatelier's principle the reduced CO_2 level would promote the recombination of HCO_3^- and H^+ to favour the production of CO_2 (Eq. 5.1). This would in turn lead to a reduction in the level of H^+ and subsequently drive pH to more alkaline values as observed here (Figure 51), and temperature increases the rate at which this pH change occurs. This is important since according to one of the main distributors of CCM the precipitation of Ca by phosphate ions will become a problem when the pH level becomes more basic than 7.6 [192].

$$\mathbf{H_2O + CO_2 \leftrightarrow H_2CO_3 \leftrightarrow H^+ + HCO_3^-} \qquad \textbf{(5.1)}$$

Furthermore, the increase in temperature that is associated with bath ultrasonication due to excessive heating of the bulk liquid through ultrasonic waves will further favour the precipitation of calcium phosphate since calcium phosphate dissolution is an exothermic process, thus solubility decreases with increasing temperature [193]. Accordingly, it was concluded that the Ca and P rich coating seen here was an artefact of sample preparation whereby a significant increase in pH and temperature induced during bath sonication promoted the precipitation of calcium by phosphate ions.

The concept that calcium can be precipitated from the media by phosphate ions at high enough pH was investigated further using the modelling software HYDRA-MEDUSA (carried out by Dr Sergio Sanchez-Segado) to look at the ionic equilibrium of the DMEM media in the pH range 5.0 to 8.0. This was useful in confirming that Ca was indeed precipitated by PO_4^{3-} at increasing pH levels. Looking in detail at Figure 54, in the pH range 5 to 6.5, the concentration of Ca^{2+} and $H_2PO_4^-$ remained constant but at pH values > 6.5 a decrease in the concentration of the Ca^{2+} and $H_2PO_4^-$ ions was observed due to precipitation of $Ca_5(PO_4)_3OH(s)$ (hydroxyapatite (HA)), which was verified when the concentration of the precipitate remained almost constant above pH 7.15. However, this exact pH value of precipitation is not in agreement with the work shown here or the known fact that at physiological pH Ca and P remain in solution in CCM. Since one of the limitations of the HYDRA-MEDUSA software is that it can only account for the inorganic ions in a solution to calculate the equilibrium conditions this suggests that the organic compounds (amino acids and vitamins) that are also present in CCM must also influence the precipitation process. Indeed there are reports on this in the literature where *in*

vitro studies have shown that amino acids can promote HA precipitation through their binding to surfaces and attracting Ca^{2+} and PO_4^{3-} ions, increasing local supersaturation levels [194]. In addition Tavafoghi *et al.* [195], studied the effect of the amino acids L-arginine and L-glutamic acid. They observed that in solutions without amino acids dissolved; HA precipitation was instantaneous as predicted with the software HYDRA-MEDUSA. In solutions containing only one of the amino acids, the precipitation was delayed by 11 and 18 hours for glutamic acid and arginine respectively, and for solutions containing both amino acids the precipitation was delayed for 4 hours. It is known that glutamic acid and arginine form complexes with Ca^{2+} and PO_4^{3-} which results in an inhibition of the precipitation as a consequence of the decrease in the concentration of free ions [196]. On the other hand, when both amino acids are dissolved in the same solution the tendency to interact between each other is higher than their individual interactions with either Ca^{2+} or PO_4^{3-} [195]. This is worth noting considering that there are differences in the formulation of common CCM. For the case here where DMEM was used primarily, this contains only L-arginine. However, RPMI normally contains a mixture of both L-glutamic acid and L-arginine. Therefore, it could be suggested that the precipitation of Ca by PO_4^{3-} may potentially occur at variable time points between different biological media and this requires further investigation beyond the scope of this project.

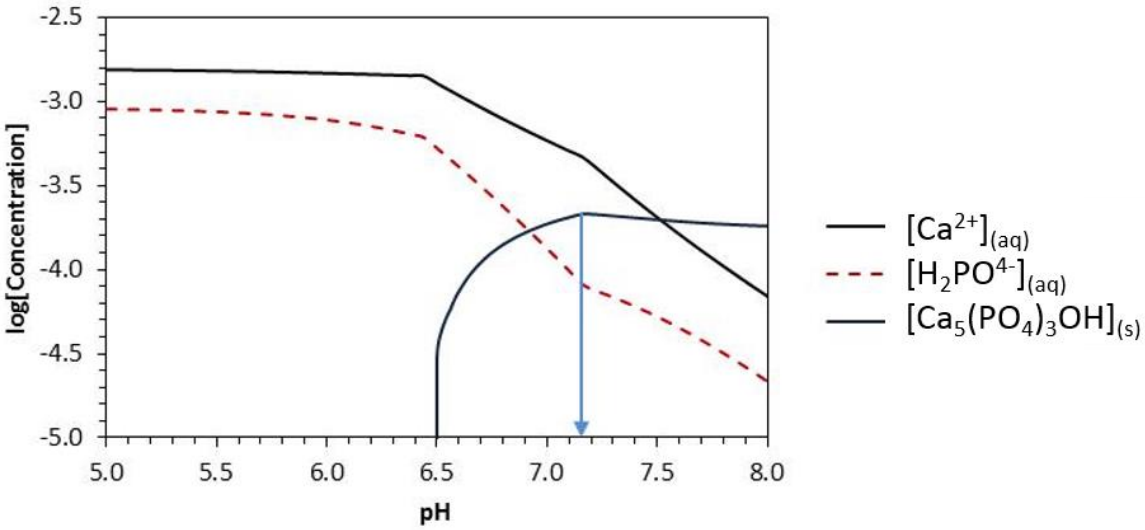

Figure 54: Ionic equilibrium data for DMEM at 25°C obtained from HYDRA-MEDUSA software. Precipitation of Ca by phosphate is predicted to occur at pH 6.5 but this does not consider the organic species present in the media (vitamins, amino acids and proteins) which can delay precipitation.

In addition to the work by Xu *et al.* two further papers have been published by Riberio *et al.* detailing the formation of a Ca and P rich coating around TiO_2 nanoparticles [79, 197]. These works claim that this coating was due to significant interactions occurring at the bio-nano interface of the nanoparticles and is indicative of a significant change in the biological identity of the nanoparticles *in vivo*. However, from the evidence provided here it is reasonable to suggest that the cited coating by Riberio *et al.* could be an artefact of sample preparation. The papers suggest that the samples were prepared under atmospheric conditions and therefore possible changes in the pH would have been favoured at the lower CO_2 levels which could have induced the precipitation of calcium phosphate around the nanoparticles. Furthermore, this work also detailed cell uptake studies of the TiO_2 nanoparticles, yet the results from this aspect of the study did not indicate any Ca and P accumulation around the nanoparticles taken up into the cells. It is possible that these cell uptake studies were carried out separate to the STEM characterisation studies and in a laboratory where appropriate conditions could be maintained to prevent any extreme changes in the pH or temperature of the media. This is of

significance considering incorrect conclusions concerning bio-camouflage and ease of cell uptake may have been reported as a consequence of misinterpretation of the interactions at the bio-nano interface.

A final investigation was carried out looking at the potential of using probe sonication rather than bath sonication. Recently, there has been a move toward standardisation of protocols used for nanoparticle dispersion preparation in order to reduce the level of variation between facilities [198, 199]. These protocols tend to prioritise the use of probe sonication. A sample of $BaTiO_3$ in CCCM was probe sonicated for <15 min and upon dispersion characterisation, no obvious calcium phosphorus coating was seen. This can be explained by the shorter timescales used for probe sonication as compared to bath sonication, thereby reducing the time available for a significant change in pH to occur. It is also standard procedure to place samples in a cooling water bath to prevent excessive temperature rise, therefore further reducing the drive toward calcium phosphate precipitation. Consequently, probe sonication could be a possible advantageous alternative for nanoparticle dispersion preparation. However, the higher power compared to bath sonication carries an increased risk of detrimentally causing physical or chemical changes to the inherent properties of the nanoparticles or media within a suspension and therefore it should be used with caution [200].

5.1.4 What form of calcium phosphate?

Selected area electron diffraction indicated that the coating was amorphous. EDX and EELS quantification were used and benchmarked against calcium phosphate standards (Table 6). From EDX quantification the average Ca to P ratio in the coating was 1.39 ± 0.30 and from EELS quantification it was 1.63 ± 0.46, where the reported error is taken as the standard deviation from n>3 measurements (Table 7). These results were not conclusive since octacalcium phosphate ($Ca_8H_2(PO_4)_6.5H_2O$), tri basic calcium phosphate ($Ca_3(PO_4)_2$) and HA ($Ca_5(PO_4)_3OH$) have Ca to P ratios of 1.33, 1.5 and 1.67 respectively which would all fit with the reported quantification within error.

Table 6: EDX and EELS quantification of the Ca to P ratio of standards; tribasic calcium phosphate and hydroxyapatite. Errors were calculated as the standard deviation of n>3 measurements.

	EDX	EELS	Expected
Tribasic calcium phosphate	1.42 ± 0.03	1.48 ± 0.23	1.5
Hydroxyapatite	1.60 ± 0.04	1.77 ± 0.14	1.67

Table 7: Ca to P ratios obtained through EDX and EELS quantification. There was some suggestion that there could be a degree of difference in the composition of the coating between two different media, although this was not significant. Errors are given as the standard deviation of n>3 measurements.

	EDX analysis			**EELS analysis**
	$BaTiO_3$ in DMEM	$BaTiO_3$-PLL in DMEM	$BaTiO_3$-PLL in RPMI	$BaTiO_3$ in DMEM
Sample 1 (avg)	1.06	1.50	1.21	1.73
Sample 2 (avg)	1.18	1.26	1.11	1.43
Sample 3	1.94	-	1.22	-
Average	1.39 ± 0.30	1.38 ± 0.47	1.21 ± 0.06	1.63 ± 0.46

To investigate the most likely form of calcium phosphate to precipitate out of solution thermodynamic modelling was carried out using HSC Chemistry (v 5.1 [201]). Again the thermodynamic modelling was conducted on a system modelled only on the ions present in CCM and not the additional organic constituents. This showed that the favoured calcium phosphate precipitates from a system modelled on the ions present in DMEM were $Ca(OH)_2*Ca_3(PO_4)_2$ and $Ca_5(PO_4)_3OH$ (HA) (Table 8). Of the two $Ca(OH)_2*Ca_3(PO_4)_2$ had the lowest ΔG value, however precipitation kinetics do not depend entirely on ΔG and were this the largest phase of coating the Ca to P ratio would have been 2, which does not agree with the EDX and EELS data (Table 7). Therefore, using both experimental and modelled results it was concluded that the most likely form of the coating was an amorphous calcium phosphate with HA stoichiometry.

Table 8: Thermodynamic modelling carried out using HSC Chemistry (v 5.1) software. Highlighted in red are the three most likely forms of calcium phosphate precipitate to form from a system modelled on the ions present in CCM.

	T / °C	ΔH / kJ	ΔS / J/K	ΔG / kJ
$Ca^{(+2a)} + PO_4^{(-3a)} + H_2O(l) = CaHPO_4 + OH^{(-a)}$	25.00	68.898	308.171	-22.983
$Ca^{(+2a)} + PO_4^{(-3a)} + 3H_2O(l) = CaHPO_4*2H_2O + OH^{(-a)}$	25.00	230.408	365.315	121.489
$Ca^{(+2a)} + PO_4^{(-3a)} + 3H_2O(l) = CaHPO_4*2H_2O + OH^{(-a)}$	25.00	33.781	246.428	-39.691
$4Ca^{(+2a)} + 2PO_4^{(-3a)} + 2H_2O(l) = Ca(OH)_2*Ca_3(PO_4)_2 + 2H^{(+a)}$	25.00	-8205.711	611.363	-8387.989
$Ca^{(+2a)} + 2H_2O(l) = Ca(OH)_2 + 2H(+a)$	25.00	128.843	-0.016	128.848
$3Ca^{(+2a)} + 2PO_4^{(-3a)} = Ca_3(PO_4)_2$	25.00	77.249	847.391	-175.401
$2Ca^{(+2a)} + 2PO_4^{(-3a)} + 2H^{(+a)} = Ca_2P_2O_7 + H_2O(l)$	25.00	30.338	814.100	-212.386
$5Ca^{(+2a)} + 3PO_4^{(-3a)} + H_2O(l) = Ca_5(PO_4)_3OH + H^{(+a)}$	25.00	132.846	1265.751	-244.538
$10Ca^{(+2a)} + 6PO_4^{(-3a)} + 2H_2O(l) = *3Ca_3(PO_4)_2*Ca(OH)_2 + 2H^{(+a)}$	25.00	269.884	2531.494	-484.881

5.1.5 Recommendations for sample preparation without artefact inducement

The unintentional formation of a calcium phosphate coating around nanoparticles dispersed in CCM could have significant implications on the interpretation of cell uptake and toxicological studies. A significant amount of research has been carried out looking at designing nanoparticles to either promote or deter protein binding for improved use in medicine [202, 203]. However calcium can act as a bridging agent for the adsorption of negatively charged species such as BSA (often a large component of protein coronas) onto nanoparticles with a negatively charged surface, which could potentially promote unwanted protein binding [204]. Furthermore, calcium phosphate coated surfaces can alter specific protein adsorption which could again disrupt the behaviour of the nanoparticles in biological studies [205]. Moreover, the surface design of some nanoparticles is intended to improve colloidal stability and the formation of a layer of calcium phosphate on the nanoparticle surface could then alter or disrupt the dispersion of the nanoparticles. At the very least a protein corona will be altered if calcium phosphate competes for binding at surfaces of nanoparticles and this may affect the biological function of the nanoparticles. This would however only be the case

if all the nanoparticles for cellular delivery were inappropriately prepared rather than just those for STEM investigation.

To address the work shown here that suggested sample preparation can cause significant artefacts in terms of forcing artificial calcium and phosphorus rich coatings, an alternative approach was used such that any extended sonication to fully disperse the nanoparticles was carried out initially in water before diluting in CCM without further sonication. Using this procedure ensured that the pH of CCM did not vary dramatically away from 7.4 and nor was the temperature increased significantly, both factors which would deter calcium phosphate precipitation. Upon utilising this preparation procedure when dispersing $BaTiO_3$-PLL nanoparticles in CCCM, no calcium phosphate coating was observed around the nanoparticles (Figure 55). Consequently, in order to ensure no artefacts occur during the preparation of nanoparticles in biological media the following suggestions are recommended:

- When using CCM for specimen preparation the pH should be monitored to ensure no significant changes are occurring, and work should be carried out under as close to physiological conditions as possible. For example, if prolonged sonication is required for nanoparticle dispersion, this should be carried out in water before diluting to appropriate concentrations in the required biological media.
- Cryo-S/TEM analysis should be used in preference to dry samples to eliminate any drying artefacts.
- In research collaborations where research is undertaken in multiple locations, clear and precise communication between all research facilities should be prioritised to ensure exact procedures are replicated in all locations.

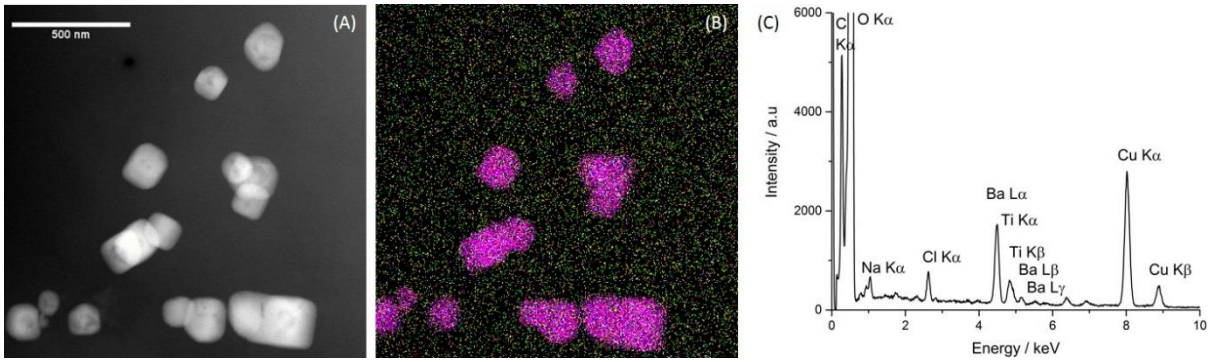

Figure 55: Cryo-analytical-STEM characterisation of $BaTiO_3$-PLL nanoparticles in CCCM prepared without artificial adjustments to pH or temperature. EDX analysis indicates following the recommended sample preparation prevents the formation of the calcium and phosphorus rich coating. The combined elemental map in (B) maps the X-ray signals of Ba (red), Ti (blue), Na (green) and Cl (yellow) of the HAADF STEM image (A) and the spectra in (C) is from the whole image area. Reproduced from Ilett *et al.* [90].

5.2 Nanoparticle dispersion states

Colloidal stability is another important factor in the behaviour and subsequent application of nanoparticles in medicine. It refers to how well nanoparticles remain monodispersed within a suspension. The dispersion state of nanoparticles is particularly important since any change in agglomeration state will effectively change the size and therefore the dose of nanoparticles that cells are exposed to either *in vivo* or *in vitro*. Investigating nanoparticle dispersion by using bulk DLS techniques is a simple and effective protocol, however it can be complicated by the more complex nature of biological media. Therefore, initial investigation of nanoparticle dispersion in a number of biological media was carried out using DLS (section 5.2.1 and 5.2.2) before developing EM techniques to carry out the dispersion analysis of the same suspensions and compare the results (section 5.2.8).

5.2.1 Nanoparticles in lysosomal buffers

Lysosomal buffers [206] were used to mimic the likely environments in which nanoparticles are stored in cells after uptake by endocytosis. Nanoparticles can be encapsulated in intercellular vesicles known as endosomes and lysosomes [207] which are acidic with a pH of 5.5 and 4.5 respectively. Since pH

can affect surface charge it would be predicted that the dispersion of nanoparticles could alter in these acidic environments.

Au (30 nm spheres) and Fe_3O_4 (30 nm spheres) nanoparticles were dispersed in lysosomal buffers (either pH 5.5 or pH 4.5) and the dispersion state analysed through DLS. The Au nanoparticles were coated with amine-terminated PEG (referred to as Au-NH_2) and the Fe_3O_4 nanoparticles were either; uncoated, coated with a carboxylic acid (–COOH) or coated with PEG (–PEG). Both nanoparticle systems have been linked with potential use in therapeutic medicine [208, 209] and, due to their size and the presence of polymer coatings, would be predicted to undergo cell uptake via encapsulation in endosomes and lysosomes [210].

Initial investigations ascertained that dispersion in CCCM at physiological pH did not affect the dispersion of the Au or Fe_3O_4 nanoparticles, and they remained colloidally stable (Figure 56 and Figure 57). However, suspensions of both the Au and Fe_3O_4 nanoparticles in lysosomal buffers led to significant changes in the dispersion state dependent upon, in the case of the Fe_3O_4 nanoparticles, the surface coating and, in the case of Au-NH_2 nanoparticles, the incubation time. Looking first at Au-NH_2, the nanoparticles remained monodispersed in pH 4.5 and 5.5 lysosomal buffers for the first 24 h. After 48 h there was evidence of some agglomeration which appeared to increase slightly after 72 h (Figure 56(C,D)). The agglomeration appeared to be slightly greater in the pH 5.5 lysosomal buffer compared to pH 4.5. In comparison the Au-NH_2 nanoparticles suspended in DI water and CCCM remained monodisperse with no evidence of agglomeration over a 72 h period. This indicated it was the lower media pH that was driving agglomeration over time. Changes in the zeta potential of the Au-NH_2 nanoparticles must therefore occur over time resulting in reduced colloidal stability of the nanoparticles and the agglomeration observed here.

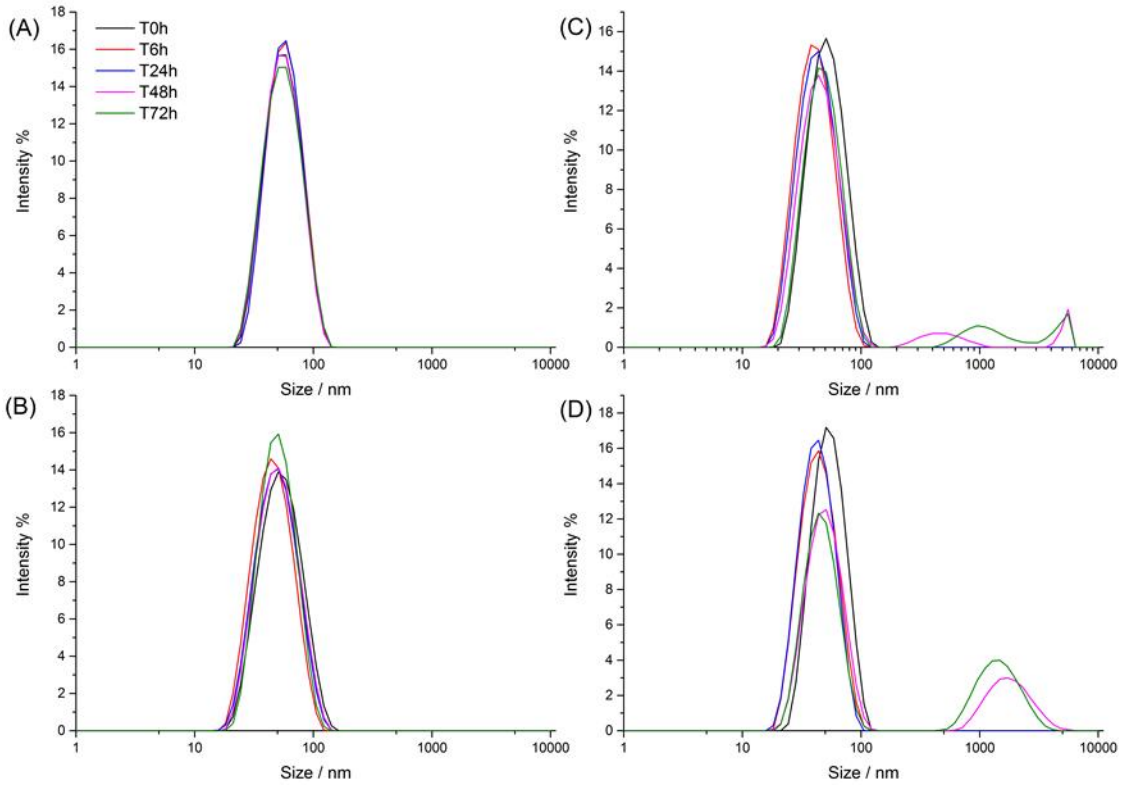

Figure 56: DLS plots for Au-NH_2 nanoparticles dispersed in different media over time. The nanoparticles were dispersed at 100 µg/mL in four different media; (A) H_2O, (B) CCCM, (C) lysosomal buffer pH 4.5 and (D) lysosomal buffer pH 5.5. Nanoparticle agglomeration was only observed after 72 h in both lysosomal buffers. Legend in (A) applies to all plots.

For each Fe_3O_4 nanoparticle system (i.e. uncoated, coated with –COOH or coated with –PEG) the dispersion remained stable in CCCM at pH 7 for up to 4 weeks. This was also the case for the uncoated Fe_3O_4 and Fe_3O_4-PEG nanoparticles in both pH 5 and pH 4.5 lysosomal buffers (Figure 57(A, C)) where the slight discrepancies seen in the data were attributed to measurement errors since there was no clear trend dependent on time or acidity. Comparatively, Fe_3O_4-COOH nanoparticles agglomerated after 7 days in pH 5.5 lysosomal buffer and immediately in a pH 4.5 lysosomal buffer (Figure 57(B)). The greater H^+ content within the acidic lysosomal buffers could reduce the occurrence of Fe_3O_4–COO^- and consequently reduce the electrostatic repulsive interactions between these nanoparticles. This would suggest that in order to prevent excessive agglomeration inside a cell of iron oxide nanoparticles, neutral or positively charged nanoparticles are advantageous.

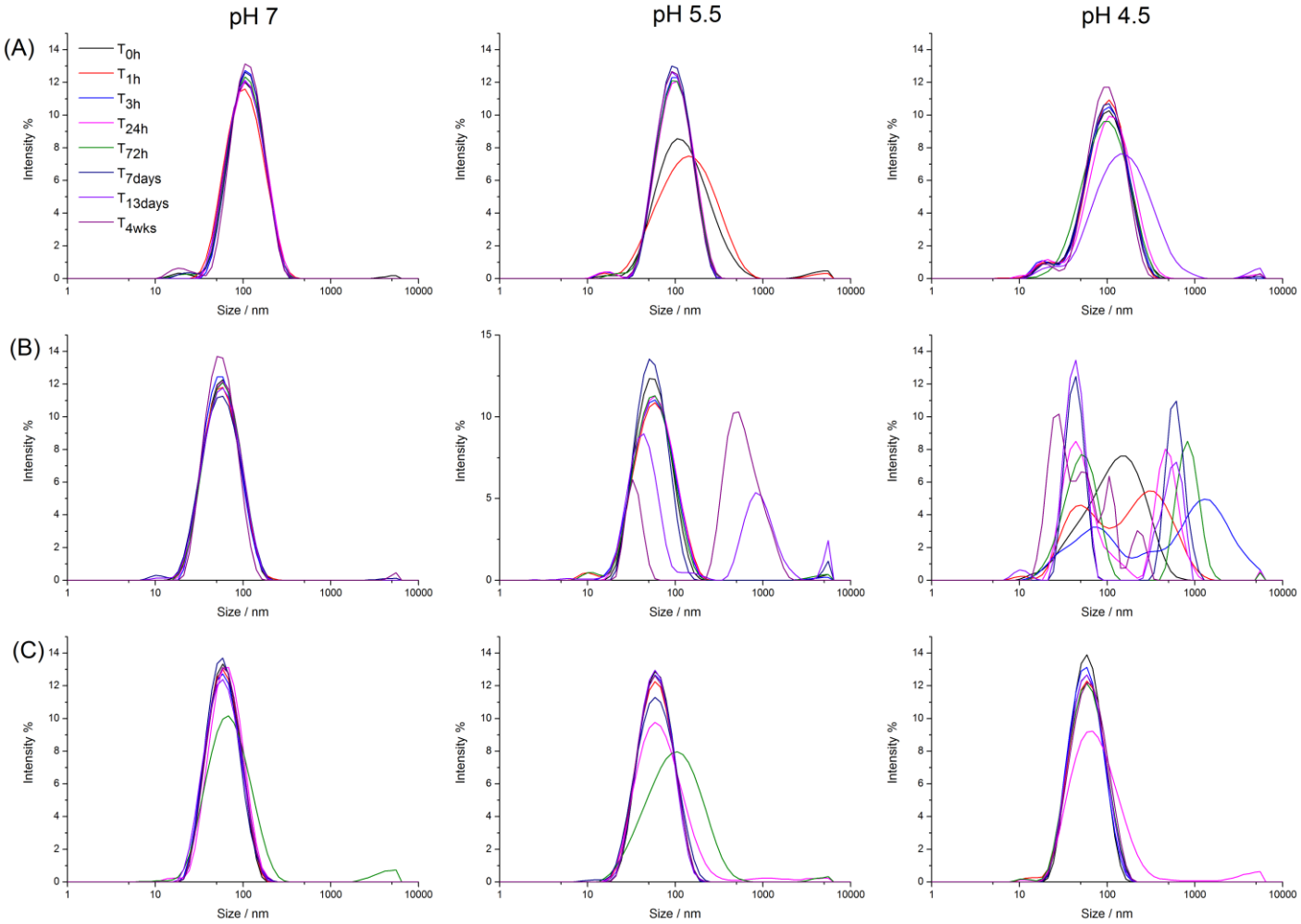

Figure 57: Dispersion states of Fe_3O_4 (A), Fe_3O_4-COOH (B) and Fe_3O_4-PEG (C) nanoparticles dispersed in lysosomal buffers at pH 7, pH 5.5 and pH 4.5. Significant agglomeration and colloidal instability was observed for Fe_3O_4-COOH nanoparticles in low pH buffers. The legend in (A) applies to all plots.

5.2.2 Nanoparticles in simulated body fluid

Another biological dispersant is SBF; a salt solution designed to mimic the concentration of salts within the blood plasma but which, unlike CCCM, does not contain any proteins, vitamins or amino acids. Monitoring how nanoparticles behave in SBF can be a useful tool in identifying potential shielding effects in high ionic strength media and also whether protein interactions play a role in stabilising dispersions. Au-NH_2 and Au-OMe nanoparticles were dispersed in SBF and DI water and both particles remained monodispersed in each suspending media (Figure 58) indicating both particles are stable in high salt content media. Similarly, Fe_3O_4-COOH and Fe_3O_4-PEG nanoparticles did not show any change in agglomeration when dispersed in SBF as compared to water (data not shown). However, uncoated Fe_3O_4 nanoparticles dropped out of suspension immediately upon addition to SBF preventing any meaningful DLS data being obtained. For further comparison a third system of uncoated silica nanoparticles (100 nm diameter spheres) was dispersed in DI water, CCCM and SBF (Figure 59). Silica nanoparticles have also been linked with use in therapeutics warranting an understanding of their behaviour in biological fluids [211, 212]. Upon dispersion in CCCM the nanoparticles remained monodispersed with a small signal at ~7 nm relating to the serum proteins contained in CCCM, specifically BSA [103]. However significant agglomeration occurred when the particles were dispersed in SBF and this was immediate as measurements were taken directly after sample preparation. To explain this, zeta potential measurements were taken that showed a substantial change from -47.8 ± 1.2 mV in DI water to -13.1 ± 0.6 mV in SBF. Changes in ionic strength of a dispersion media can lead to changes in the electrostatic forces between molecules, where an increase in ionic strength can effectively shield long range electrostatic repulsive forces [32]. It is likely that the high ionic strength of CCM would lead to the same agglomeration of the SiO_2 and Fe_3O_4 nanoparticles, however the presence of proteins within CCCM allowed the formation of a protein corona around the nanoparticles which can provide steric stabilisation. Furthermore, these results suggest that as expected the presence of a polymer coating, independent of the nanoparticle material, significantly enhances colloidal stability in high ionic strength media.

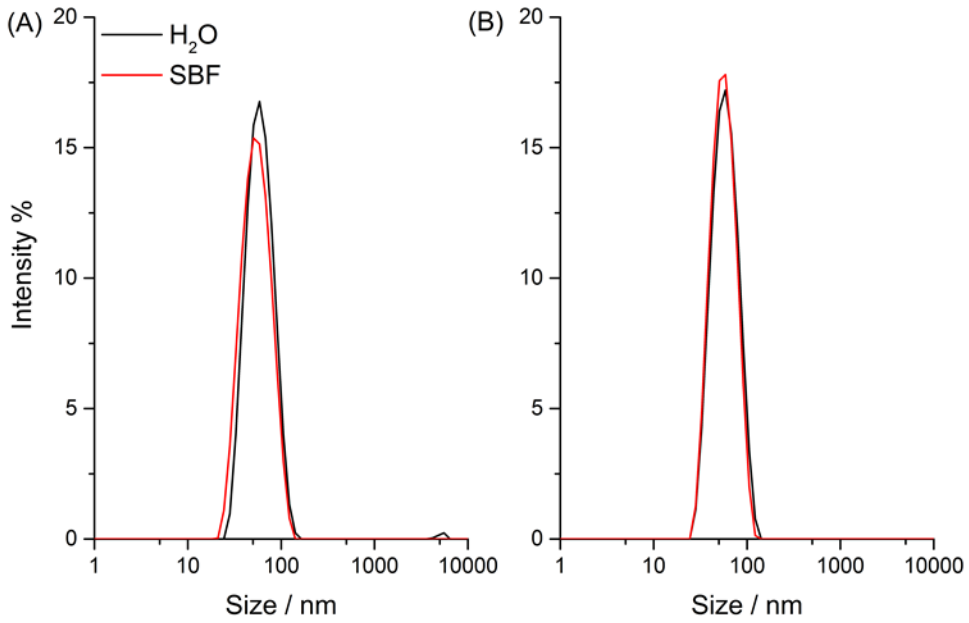

Figure 58: DLS plots of Au-NH_2 (A) and Au-OMe (B) nanoparticles dispersed in H_2O (black) and SBF (red). No change in dispersion state was seen for either nanoparticles when dispersed in the higher ionic strength SBF.

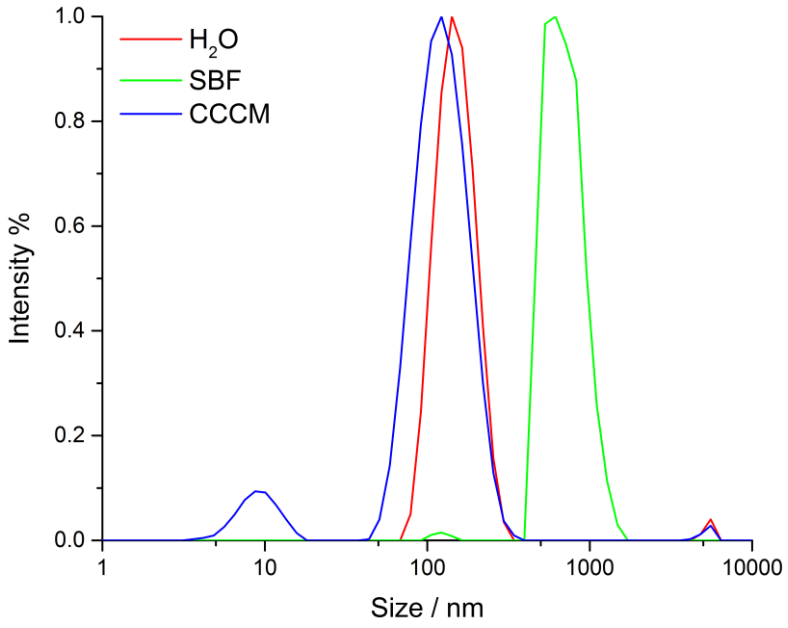

Figure 59: DLS measurement of SiO_2 (100 nm) nanoparticles dispersed in either water (red), SBF (green) or CCCM (blue). Significant agglomeration was observed when dispersed in SBF, compared to no agglomeration when dispersed in water or CCCM.

For these investigations DLS proved an adequate technique to successfully monitor changes in nanoparticle dispersion in different biological media. However, this is not always the case, often when working with more complex biological media DLS can have significant pitfalls. Since it is a light scattering technique it is not able to distinguish between components that are inherently present in the media and the dispersed nanoparticles. For example, the main component of FBS is BSA which has been measured as roughly 7.5 nm as seen in Figure 59 [213]. This can become a significant problem if looking to analyse nanoparticles of a similar size where the nanoparticle signal will be obscured by that from BSA (Figure 60). In addition, all the work presented so far was carried out on dispersions at 100 µg/mL concentration. Typically, in life science, studies implement a range of nanoparticle concentrations which tend to include much lower concentrations. At these lower concentrations the signal from the nanoparticles becomes obscured by signal from the components in the media and therefore any changes in size at lower concentrations which can happen cannot be identified by DLS analysis [103, 214]. In addition, there are cases where the number of nanoparticles in agglomerates of the same hydrodynamic size can be different, something that again is not observable by DLS alone [102]. Consequently, alternative approaches are needed to more accurately characterise nanoparticle dispersion in biological fluids. To that end, the remainder of this chapter reports on the development, validation and subsequent application of an automated imaging and analysis approach that utilises the high spatial resolution capabilities of EM to carry out highly accurate nanoparticle agglomerate analysis.

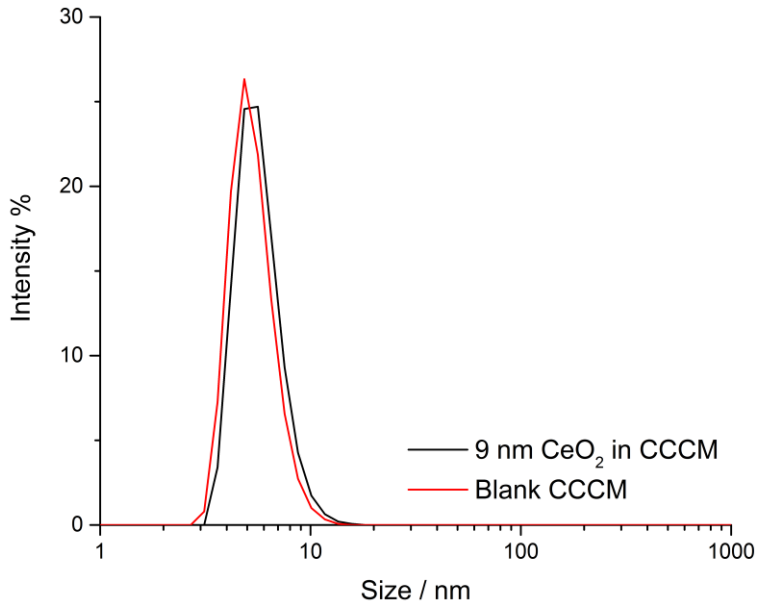

Figure 60: Two DLS plots comparing the size distribution seen when measuring blank CCCM or CCCM with 9 nm ceria nanoparticles dispersed at 5.27 µg/mL. The nanoparticle signal is indistinguishable from the BSA signal in blank CCCM.

5.2.3 Automated imaging set-up

In using EM to carry out dispersion state analysis, sufficiently large datasets of images need to be collected in order to make the measurements statistically relevant. However, to do this manually would be extremely time inefficient. Therefore, an automated imaging process was developed using FEIs iFast developer software for STEM imaging carried out using an FEI Helios GA CX dualbeam FIB-SEM equipped with a darkfield STEM detector. Using the iFast developer software a script was written for automatic imaging including a focusing step prior to image capture to improve the quality of images obtained and account for changes in sample height in different areas of the grid. Including the focus step, the total image capture time was ~50 seconds. Images were taken at a constant magnification row by row in an array formation without any image overlap to ensure agglomerates were not double counted. For larger particles, for example 100 nm SiO_2 nanoparticles a 40 x 40 image array was captured resulting in the collection of 1600 images, each with a field width of 30 µm. This equated to imaging a 1.4 mm^2 region of the specimen (Figure 61(A)). In the case of smaller

nanoparticles where higher magnifications were used and consequently smaller image field widths, multiple image arrays were captured of smaller total image number from the same specimen. The initial starting points of these image arrays were chosen after carrying out an initial screening of the specimen in order to locate reasonable areas (Figure 61(B)). The imaging area was maximised by using larger 200 mesh sized TEM support grids and a maximum of 6 specimens could be loaded in the STEM holder at any one time. Running the automated imaging over multiple days allowed datasets of >1000 images per sample to be collected at once. Finally, since acquisition took place over multiple days, a cryo-sample could not be used, therefore an alternative approach of plunge freezing and then warming back up to room temperature in a manner that did not distort the native dispersion was required. For initial validation and optimisation of the technique, plunge freezing followed by vacuum drying was used, a preparation protocol previously validated by Hondow *et al.* [102]. However, an investigation into a number of warming techniques after plunge freezing is provided in section 5.2.6 which showed a variety of procedures are viable.

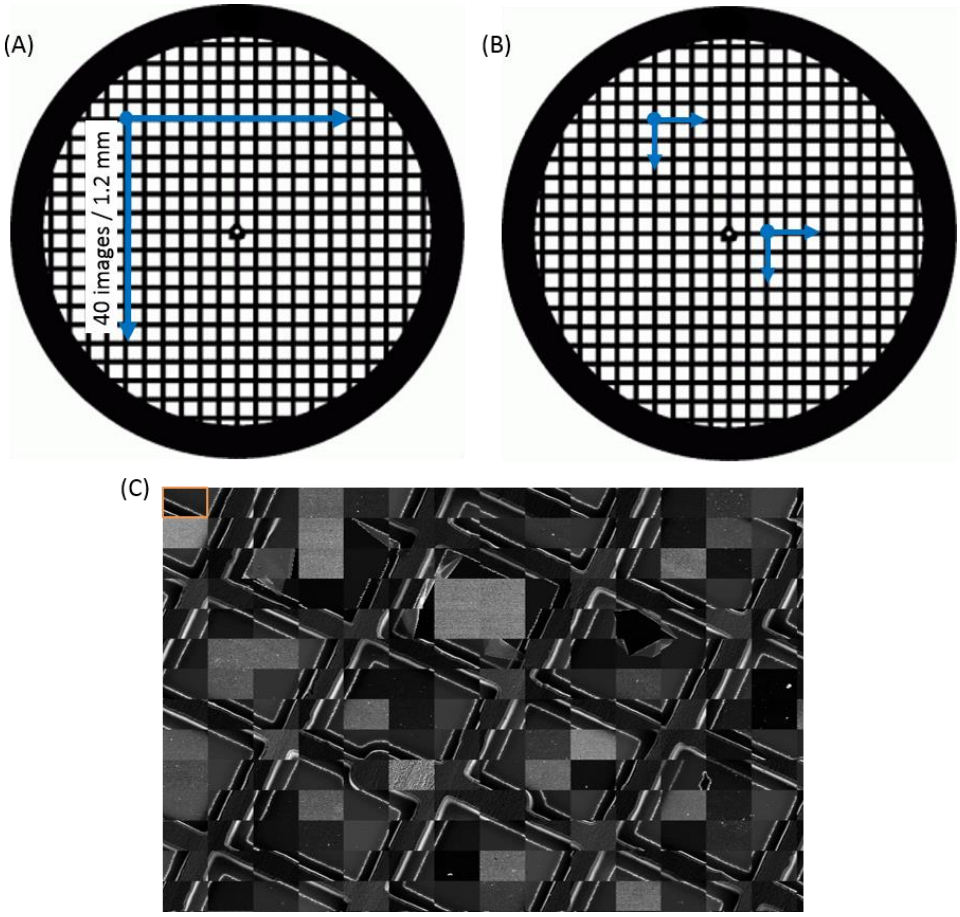

Figure 61: A schematic illustrating the automated imaging process. A 200 mesh TEM support grid with a continuous carbon support film was used. (A) A TEM support grid indicating the large area imaged for SiO_2 nanoparticles. (B) A TEM support grid showing multiple regions imaged for smaller particles. (C) An example of a small 14 x 14 image array, the region outlined in orange (top left) indicates one individual image of 30 µm width. Reproduced from Ilett *et al.* [190].

5.2.4 Automated image analysis design

Manual analysis of very large datasets is extremely time consuming and consequently an automated image analysis protocol was required. Whilst simple thresholding and particle counting can often be successful for HAADF STEM images of nanoparticle systems in water, this approach is not effective on more complex systems (Figure 62). In the case of nanoparticle suspensions in CCM, salts can precipitate on the TEM grid during sample preparation. In such instances simple automated (binary) thresholding could not separate salts from nanoparticles (Figure 62(D)). Therefore, a machine learning

approach was developed to address this. This used two readily available free software codes; CellProfiler (v 2.2.0) [215] and ilastik (v 1.2.3) [216]. This automated analysis protocol was developed by Dr John Wills and Professor Paul Rees of Cambridge and Swansea Universities respectively for analysis of particles in tissue. Here, in collaboration with both, it has been applied to nanoparticle dispersion analysis.

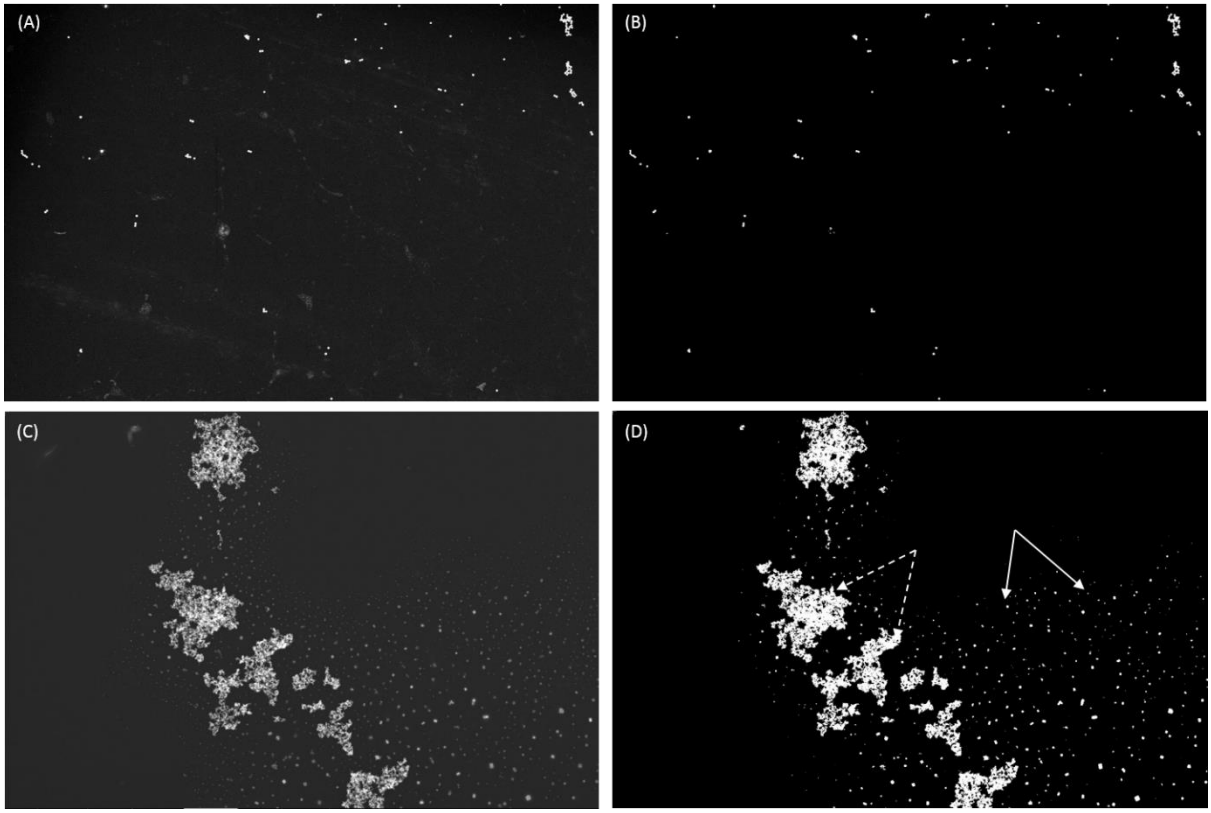

Figure 62: Automated thresholding of HAADF-STEM images taken from samples prepared from nanoparticle suspensions in water and CCCM. (A) Original HAADF STEM image of SiO_2 in water, and (B) after applying simple binary thresholding that indicated successful segmentation of the agglomerates could be achieved. In comparison the original image of Fe_2O_3 nanoparticles suspended in CCCM (C) and after applying simple thresholding (D) that indicated thresholding could not separate salts (solid arrows) from nanoparticles (dashed arrows).

After collecting large image datasets, initial screening was carried out manually to separate in focus and out of focus images. Once accomplished the first analysis protocol was to correct the illumination of each image in order to remove any uneven background contrast levels. This was done using

CellProfiler and the first of two pipelines where every image was loaded into the pipeline and illumination corrected images obtained. The input modules, pipeline 1 and pipeline 2 (referred to later) are summarised in Figure 63. The outputs from the two pipelines are given in Figure 64, Figure 66 and Figure 67.

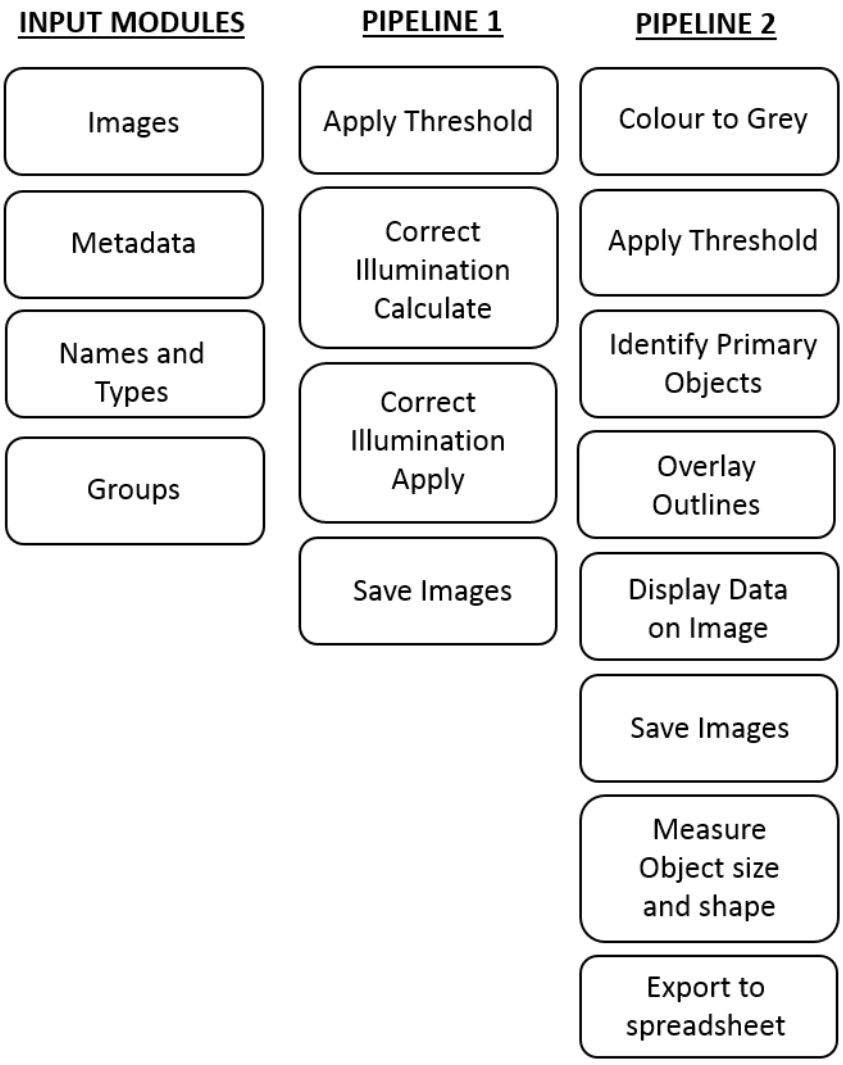

Figure 63: The input modules used for both CellProfiler pipelines in the automated image analysis are given alongside each step in the two CellProfiler pipelines for image illumination correction (pipeline 1) and agglomerate identification and measurement (pipeline 2).

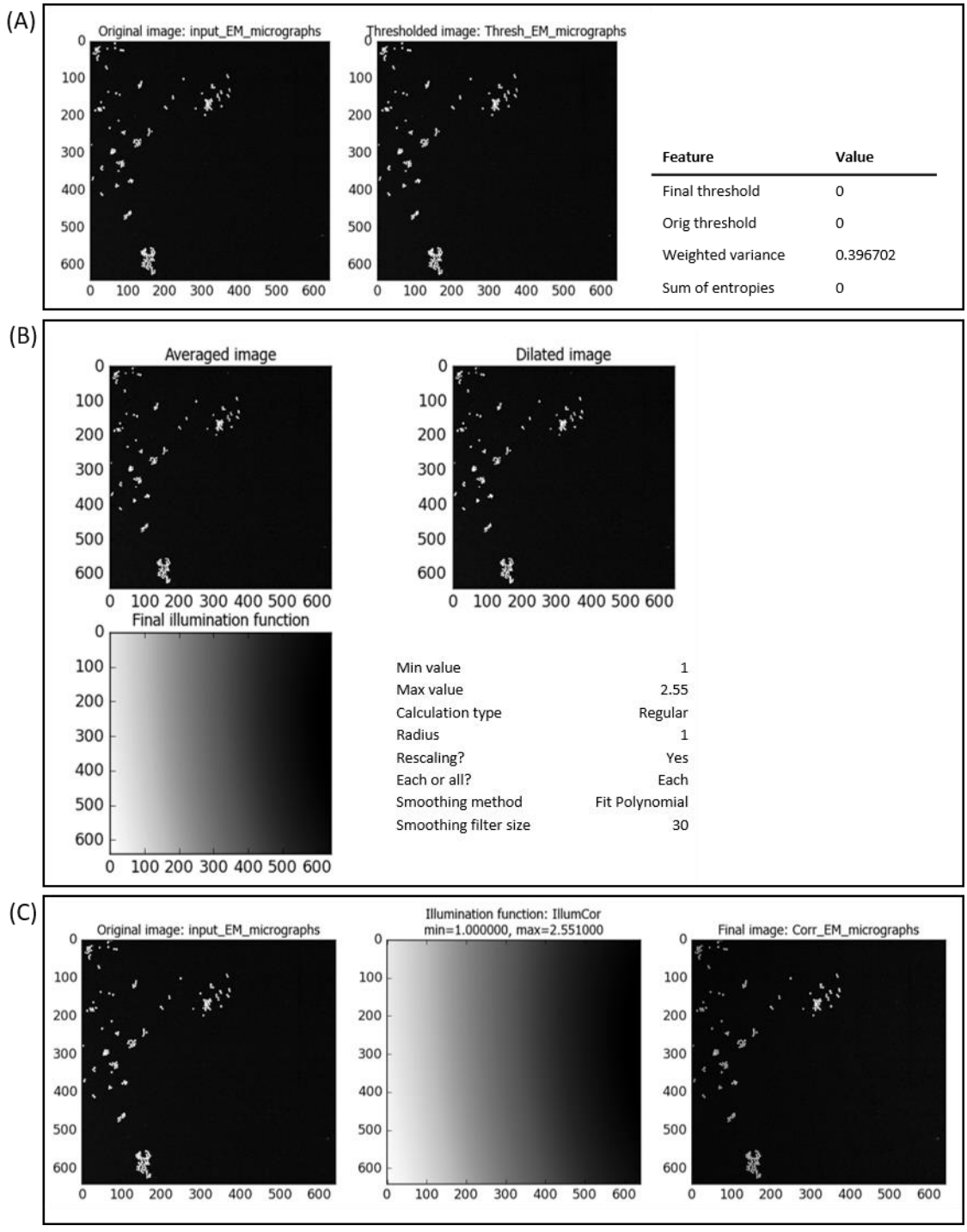

Figure 64: The workflow of the first pipeline used in CellProfiler to correct the illumination of each image. A manual threshold strategy was applied and pixels below the threshold were set to zero (A), the illumination function was then calculated (B) before applying this to each original thresholded image (C).

Once the illumination had been corrected for each image, a randomly selected subset of the images was loaded into the second software, ilastik. This subset was typically <10% of the total number of images in the dataset, although the exact number depended upon the number of images in the dataset being used. The 'pixel classification' workflow was used in ilastik to train the software to identify the agglomerates of nanoparticles within each image. A ground truth was established by manually labelling image pixels into two classes either, agglomerates or background. Note that for the purpose of initial method development and validation, primary particles were included as agglomerates and defined as the minimum agglomerate size. This process is illustrated in Figure 65(A), where the agglomerates were labelled in yellow and the background in blue. The 'live update' option was used to review the predicted pixel classification (Figure 65(B)) and further labels were added until accurate agglomeration identification was achieved. Once this had been carried out on the 'training' images a probability image was obtained for each image which described the probability of each pixel in the image belonging to either the agglomerate or background class (Figure 65(C)).

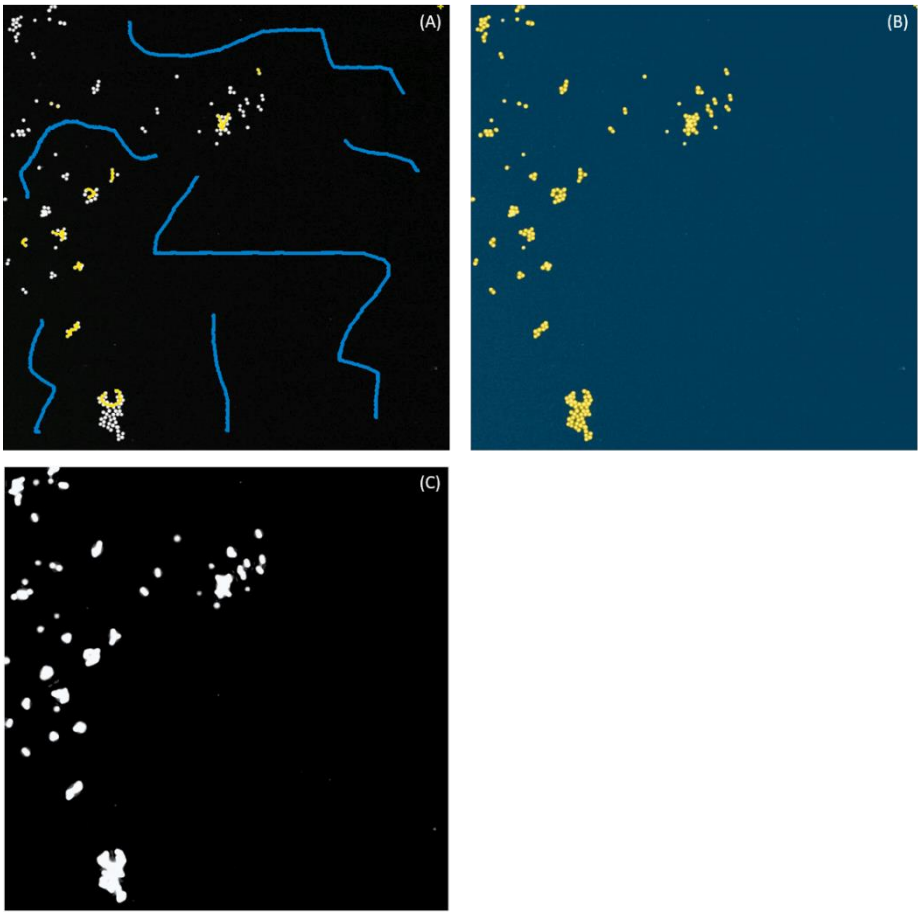

Figure 65: Automated segmentation using ilastik pixel classification. A small subset of test images were used to train the software. (A) Manual labelling of agglomerates in yellow and the background in blue. (B) Using the 'live update' function the predicted identification of agglomerates and background was demonstrated. (C) Once correct segmentation was achieved a probability map for each image was exported.

The final step in the automated imaging analysis was to use pipeline 2 in CellProfiler to extract agglomerate size/shape information. To do this, the original images, the illumination corrected images and the probability images were all loaded into CellProfiler. Pipeline 2 had the same input modules as pipeline 1 and the pipeline steps were provided in Figure 63. The outputs of the pipeline are shown in Figure 66 and Figure 67.

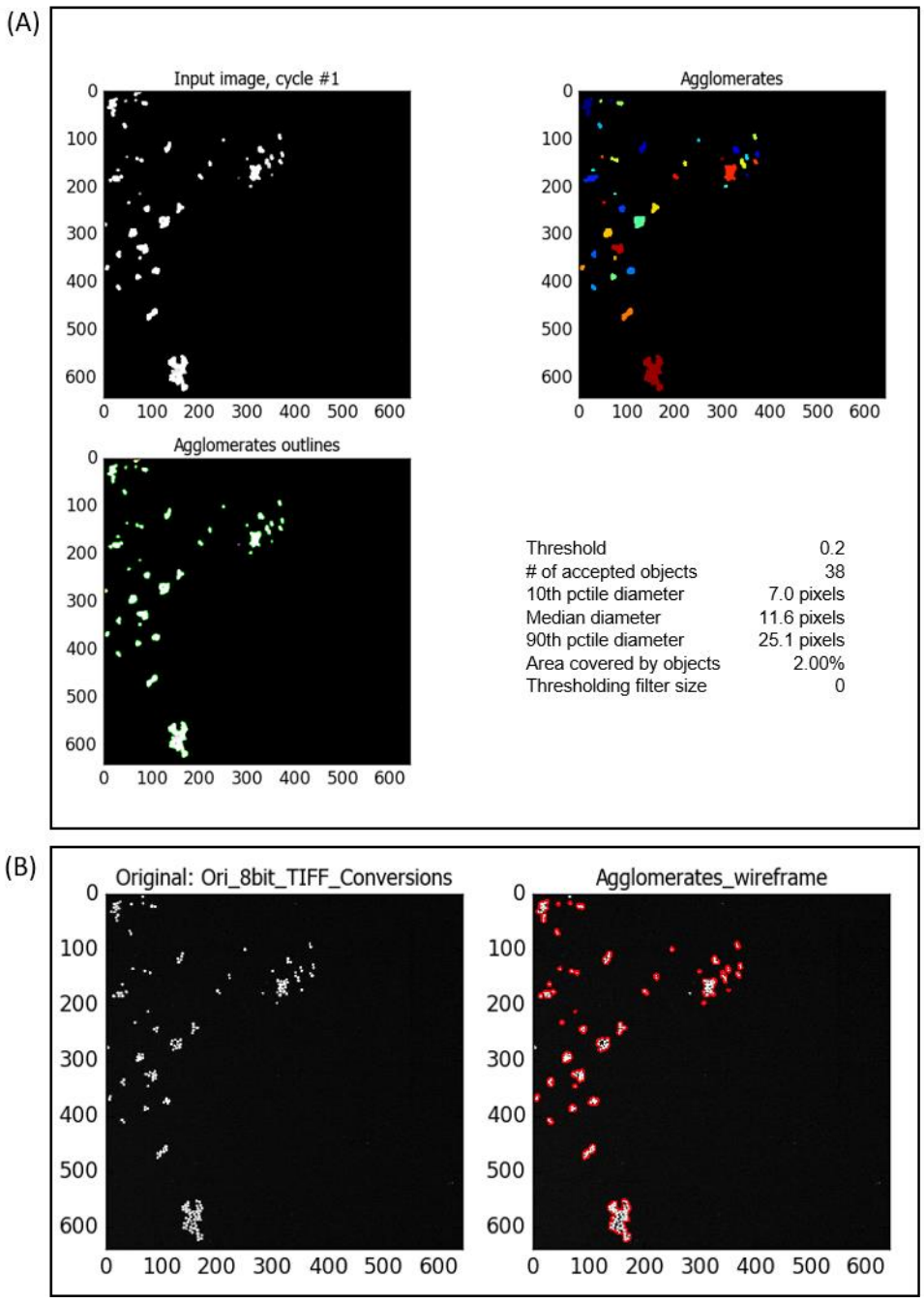

Figure 66: CellProfiler – pipline two outputs. (A) Primary objects were identified and any agglomerates touching the outer border of the image were disregarded. (B) Each object was marked by overlaying outlines on each primary object.

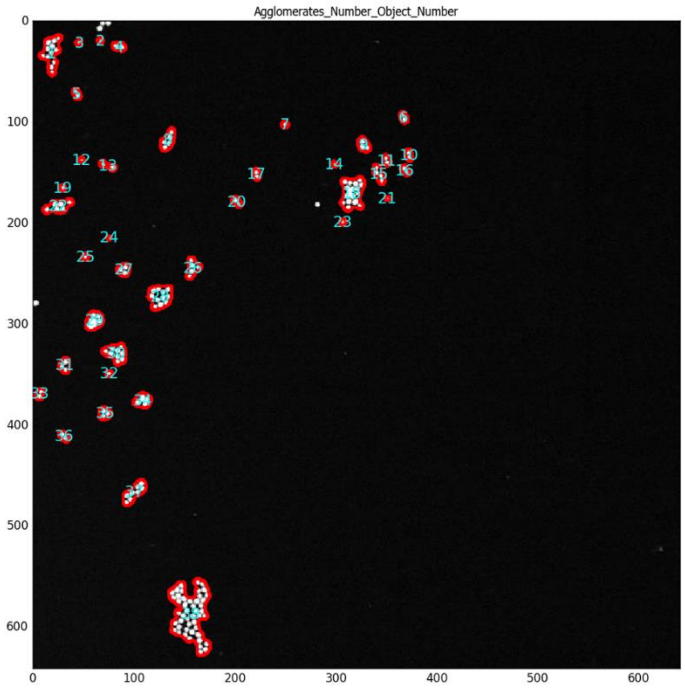

Object	Feature	Mean	Median	STD
Agglomerates	Eccentricity	0.63	0.71	0.22
Agglomerates	MajorAxisLength	18.33	14.12	13.22
Agglomerates	MinorAxisLength	11.93	9.34	6.78
Agglomerates	Orientation	5.81	4.73	54.89
Agglomerates	Compactness	1.14	1.08	0.19
Agglomerates	Area	211.21	104	321.63
Agglomerates	Center_X	154.05	97.5	123.23
Agglomerates	Center_Y	209.47	171.5	130.44
Agglomerates	Extent	0.72	0.74	0.08
Agglomerates	Perimeter	53.79	37.92	45.1
Agglomerates	Solidity	0.91	0.92	0.05
Agglomerates	FormFactor	0.81	0.87	0.16
Agglomerates	EulerNumber	1	1	0
Agglomerates	MaximumRadius	5.44	4.74	2.23
Agglomerates	MeanRadius	2.37	2.15	0.76
Agglomerates	MedianRadius	2.15	2	0.72
Agglomerates	MinFeretDiameter	11.3	8.49	7.1
Agglomerates	MaxFeretDiameter	17.67	13.32	13.32

Figure 67: Every identified agglomerate was numbered on each image and size and shape information was exported as an excel spreadsheet for each numbered object.

5.2.5 Validation

In order to assess the accuracy of the developed automated imaging and analysis process, a simple suspension of SiO_2 nanoparticles (100 nm diameter spheres) dispersed in DI water was used to carry out a comparison between automated and manual analysis. DLS analysis showed the sample was monodispersed with a polydispersity index (PDI) of 0.2 (Figure 68). Firstly, using only a small dataset of 10 dark field STEM images of the monodispersed silica prepared via plunge freezing and vacuum drying, manual segmentation was carried out on each image. In total 420 objects were identified (Figure 69). In comparison, automated segmentation using ilastik of the same 10 images identified 425 objects. This showed very close agreement between manual and automated segmentation with only a 1% difference in identification. It is likely the slight discrepancy would have been due to damaged areas on the grid being erroneously classified as agglomerates by automated analysis. Indeed in order

to quantitatively assess the accuracy of the segmentation a comparison was carried out between manually segmented images and the automated segmented images from ilastik using the Jaccard index [217] with 2 fields of view and an accuracy of 81 ± 12% was achieved across 63 agglomerate objects scored, which was deemed sufficiently accurate at this stage. Secondly, validation of the measurements obtained from the second pipeline used in CellProfiler was carried out using the same dataset. Manual size analysis was carried out using Gatan Microscopy Suite® (v 3.0.1) to measure the Feret diameter of each nanoparticle agglomerate. When compared initially to the data obtained through automated analysis it was found that there was a consistent overestimation of the agglomerate size by the automated analysis where the mean size was 210 ± 8 nm from automated analysis and only 170 ± 9 nm from manual analysis. It was concluded that this was likely due to artefacts in the image where small focal variations existed which caused, in some cases, contrast differences to extend beyond the outer pixel of the agglomerates. This was a result of recording low magnification images for the size of nanoparticles being assessed in order to maximise the amount of sample imaged. In order to combat this, an erosion step was added to the second CellProfiler pipeline after which there was improved agreement between the automated and manual size measurements confirmed using a two-sample t-test which indicated there was no significant difference between the two datasets ($p>0.05$) (Figure 69).

The analysis showed the suspension was largely monodispersed since the average agglomerate size (150 ± 8 nm) was comparable to the primary single particle size (100 nm), and this agreed with the DLS data of the same dispersion.

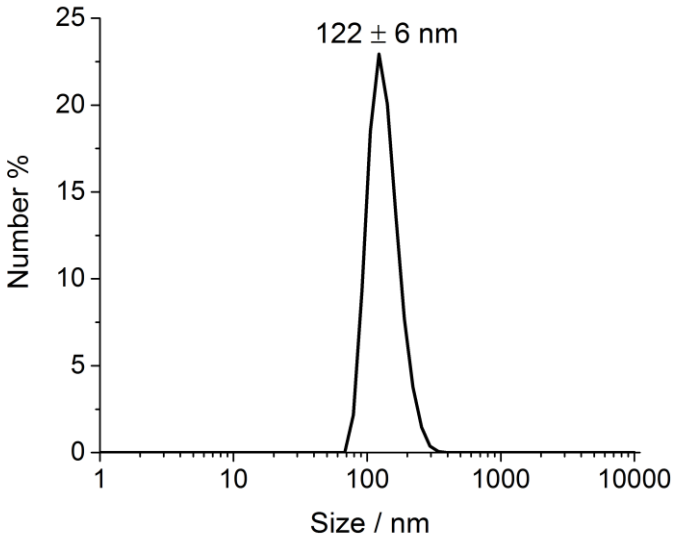

Figure 68: A DLS plot for monodispersed SiO_2 in water (100 µg/mL). Z average was 122 ± 6 nm and the PDI was 0.2.

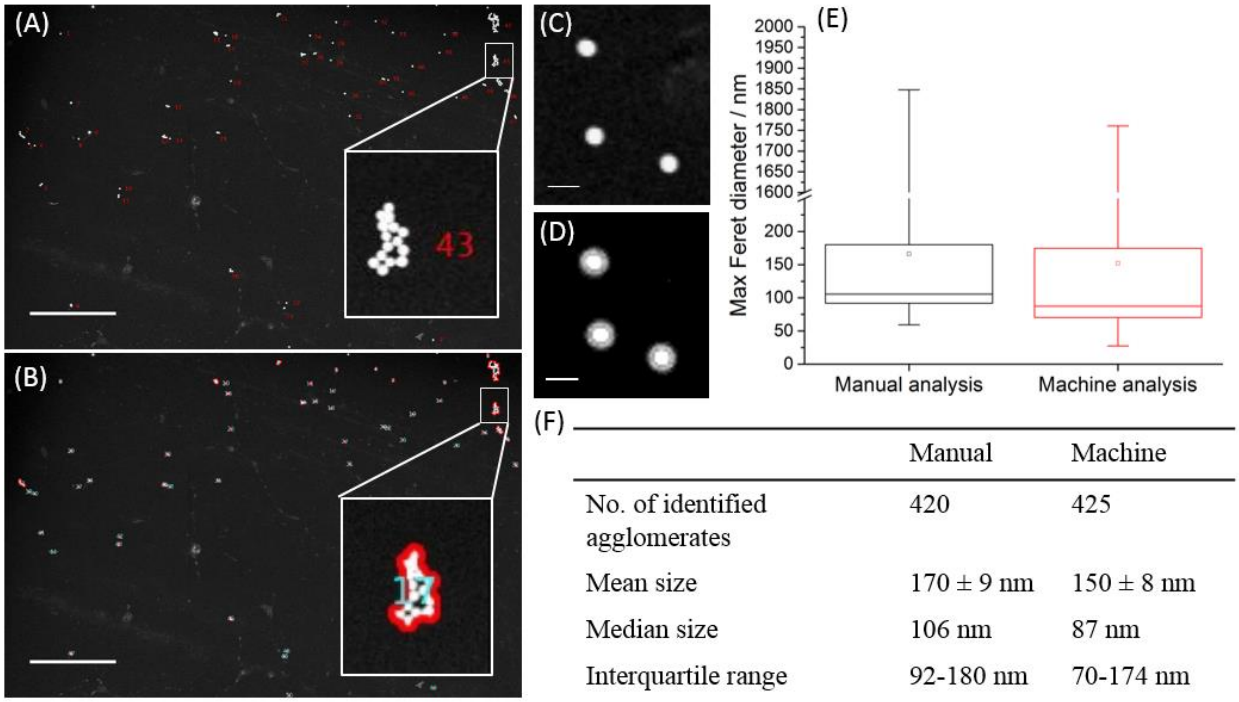

(F)

	Manual	Machine
No. of identified agglomerates	420	425
Mean size	170 ± 9 nm	150 ± 8 nm
Median size	106 nm	87 nm
Interquartile range	92-180 nm	70-174 nm

Figure 69: (A) Dark field STEM image of silica nanoparticles dispersed in water with manual identification of each nanoparticle agglomerate. This was compared to the machine segmentation of the same STEM image (B). The insets in both STEM images show an enlarged region (white box)

indicating more clearly a specific nanoparticle agglomerate. The white scale bar indicates a distance of 5 µm. (D) Example of the focal halo that can erroneously be included in image segmentation in an exported probability image from ilastik, (and has been eliminated by an erosion step in the processing) (C) shows the same area of the original, image (the white scale bars represent a distance of 200 nm). (E) A comparison between the Feret diameter measured manually and by machine analysis is shown using a box and whisker plot, presenting the interquartile range (the box), the median (-) the mean (▫) and the overall range of the data. There was no significant difference between the two datasets ($p>0.05$). (F) A summary of the measurement data of the Feret diameters shown in the box and whisker plot indicating that there was good agreement between the manual and machine learning approaches. The standard error of the mean is reported for uncertainty values. Reproduced from Ilett *et al.* [190].

5.2.6 Validating native state representative sample preparation techniques

Having validated a novel automated imaging and analysis protocol this provided the pathway to carry out an investigation into determining the most appropriate warming techniques of frozen samples for EM analysis which maintain the native position of the nanoparticles in dispersion but allow dry state analysis to be carried out. Hondow *et al.* [102] previously validated that plunge freezing followed by vacuum drying either in the TEM or using a vacuum desiccator maintains the native position of the nanoparticles in suspension on the TEM grid. However, there are a further two techniques of interest which are yet to be validated. These are; plunge freezing followed by either freeze drying or controlled sublimation using a quorum cryo chamber (10 min at 90°C).

Two suspensions of SiO_2 in water were used, one of which was monodispersed and the other which was acidified to force nanoparticle agglomeration. Four TEM grids of each sample were prepared by; conventional drop-casting and air drying, plunge freezing followed by warming under vacuum, plunge freezing followed by freeze drying and plunge freezing followed by controlled cryo sublimation. For all plunge frozen grids the sample was blotted prior to drying. The automated imaging process was

carried out on each sample to collect statistically large datasets. Once collected the validated automated imaging analysis protocol was used to compare the dispersion representation between the different grids and also with DLS measurements (Figure 70).

Examining the size distributions for both the monodispersed and agglomerated SiO_2 suspensions, all sample preparation procedures led to similar agglomerate size distributions (Figure 70). To a degree it could be argued that for both suspensions the size distributions extended to larger agglomerate sizes for the drop-cast samples. This was more obvious for the monodispersed sample, which would be expected since drying artefacts tend to lead to the formation of large clusters of nanoparticles on the grid and these would be more noticeable against the primary particle size in the monodispersed sample rather than against the larger agglomerates in the agglomerated sample. For all the plunge frozen and warmed samples there was agreement between the size distributions. This indicated that warming via freeze drying and controlled sublimation, in similarity to warming via vacuum drying, are appropriate warming procedures that maintain the original position of the nanoparticle dispersion.

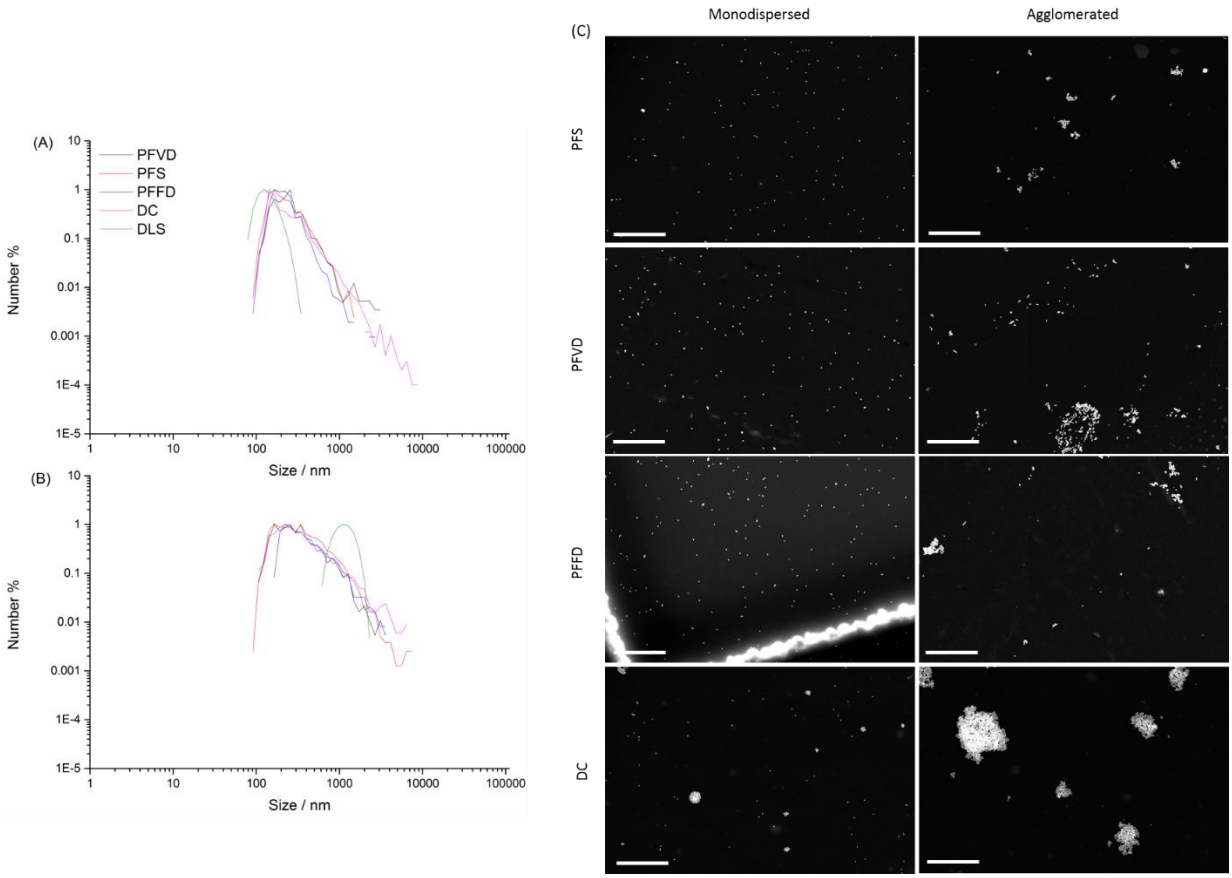

Figure 70: Log size distributions of a monodisperse (A) and agglomerated (B) system of SiO_2 nanoparticles in water. Automated size analysis was carried out on large data sets of samples prepared by plunge freezing vacuum drying (PFVD), controlled sublimation (PFS), plunge freezing followed by freeze drying (PFFD) and drop casting followed by air drying (DC). DLS data is plotted alongside for comparison. All data was normalised to the most frequent size to remove any bias from larger datasets. (C) Examples of HAADF STEM images from each data set indicated that larger agglomerates were observed in the agglomerated system.

From automated analysis there was clear indication of larger agglomerate sizes in the agglomerated system, shown by the higher number of counts in the 1000 – 10000 nm range relative to the monodisperse system (Figure 70). This increased agglomeration was clearly observed in the example HAADF STEM images provided in Figure 70 and agrees with the expected agglomeration via acidification of the system. When comparing the automated EM analysis to the DLS data the size distributions matched closely to the DLS distribution for the monodisperse sample but in the case of

the agglomerated sample the automated analysis indicated size distributions shifted toward smaller hydrodynamic diameters comparative to the size distribution from the DLS data. It is likely that this discrepancy stemmed from the way in which the data was collected in the two techniques. For EM data analysis every particle is counted as an individual object whereas DLS measures scattering light intensity. It is known that the intensity of light scattering is proportional to d^6 where d is the diameter of the particle and hence there is a preferential bias toward larger particles in DLS [218]. This would suggest then, that through automated EM analysis all particles are counted, whilst signal from the smaller particle fractions can be lost in DLS analysis if larger agglomerates are present in the suspension. This shows the potential benefits of using automated EM techniques for size analysis particularly if it is the smaller particle fraction that is of specific interest within a system.

5.2.7 Validating the applicability to more complex systems

The final validation process was to ensure that the automated analysis was appropriate for application to more complex systems. To do this, iron oxide (Fe_2O_3) nanoparticles were dispersed in CCM with and without the addition of FBS and then prepared for STEM imaging by plunge freezing and vacuum drying. DLS data for the two suspensions indicated a significant difference in the agglomeration states of the nanoparticles, where agglomerate size increased dramatically without the addition of FBS (Figure 71). From the automated analysis the same observation was made with the mean agglomerate size increasing from 310 ± 20 nm for the 10% FBS suspension to 640 ± 50 nm for the 0% FBS suspension (Figure 72). The results for the 10% FBS suspension agree well with those from DLS where the mean agglomerate size was 310 ± 20 nm and 260 ± 50 nm for automated and DLS analysis respectively. The increase in size for the 0% FBS suspension was significantly smaller for the automated analysis comparative to the DLS data where the average agglomerate size in the 0% FBS suspension was 1100 ± 220 nm. This discrepancy was thought to be due to the bias of DLS toward larger particles as discussed in the previous section. To verify this hypothesis a volume averaged diameter rather than number averaged diameter for the agglomerates in the 0% FBS suspension was obtained from the EM data and calculated as 1270 ± 220 nm. This agreed far more closely with the Z-average from the DLS

results. However, this discrepancy again illustrates one of the real values of using this automated technique in preference or alongside more traditional light scattering techniques in that by counting each particle individually EM analysis ensures the smaller particle signal is not lost.

The difference in the agglomeration state of the Fe_2O_3 nanoparticles in the presence of 0% or 10% FBS was due to the stabilising effect the serum proteins present in FBS can have [32, 53]. The protein corona that forms around the nanoparticles can act in screening the nanoparticles from the high ionic strength of CCM, preventing any significant reduction in the strength of repulsive electrostatic forces between the nanoparticles [219, 220]. This would result in a reduction in the agglomeration of the Fe_2O_3 nanoparticles as observed here.

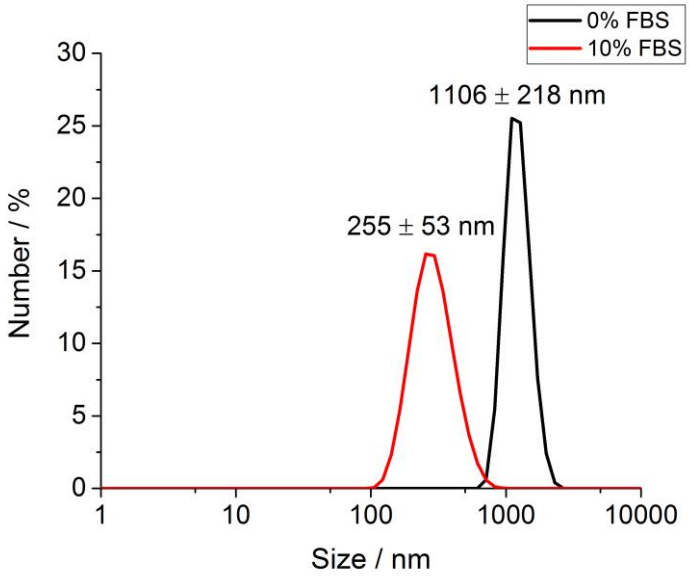

Figure 71: DLS plots of Fe_2O_3 nanoparticles suspended in CCM with (red) and without (black) the addition of FBS. Agglomeration was reduced with the addition of 10% FBS. Errors taken as standard deviation of n=3 measurements.

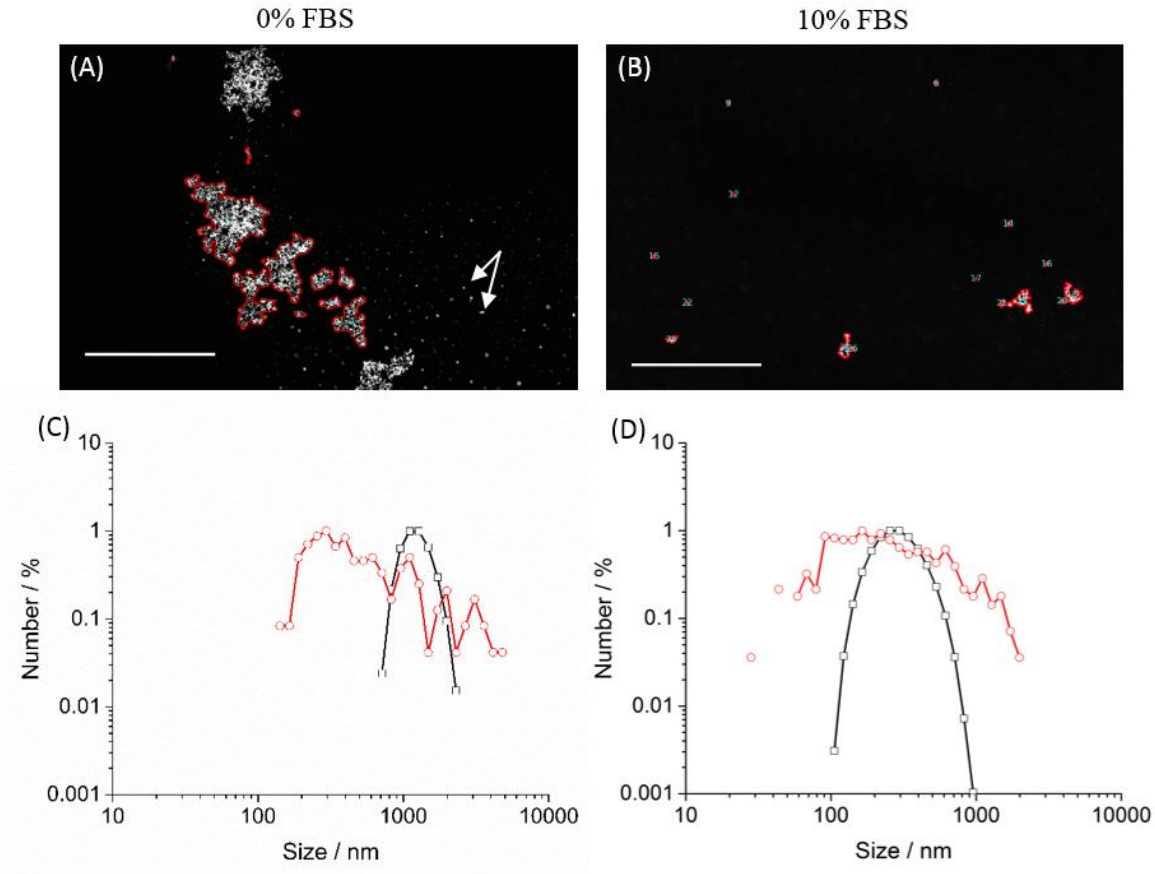

(E)

		Mean size: Number averaged	Mean size: Volume averaged
0% FBS	DLS	1100 ± 220 nm	1290 ± 190 nm
	Machine analysis	640 ± 50 nm	1270 ± 220 nm
10% FBS	DLS	260 ± 50 nm	400 ± 80 nm
	Machine analysis	310 ± 20 nm	560 ±70 nm

Figure 72: Dark field STEM images from TEM grids prepared from iron oxide nanoparticles dispersed in CCM with 0% (A) and 10% (B) FBS. Successful segmentation of nanoparticles from salts (indicated by the white arrows in (A)) was achieved and the white scale bar indicates 5 µm. Number distributions of agglomerate size for EM data analysis by machine learning (red) and for DLS analysis (black) are shown for both systems; 0% FBS (C) and 10% FBS (D). Table (E) presents the mean values from DLS and EM data analysis for both samples calculated using both a number and volume distribution. A larger degree of agglomeration with complex shapes was seen in the 0% FBS

suspension. Good agreement between EM and DLS analysis was seen for the 10% FBS sample, but there was some discrepancy in the 0% FBS sample that may be attributed to overweighting of larger agglomerates in DLS scattering analysis. This was reduced when volume averaged diameters were compared. Reproduced from Ilett *et al.* [190].

This work indicated that the novel automated imaging and analysis approach described is applicable when used on more complex systems. The results also showed that where more traditional image thresholding techniques have difficulty in separating artefacts such as salts present in biological media, here the automated system identified agglomerates without the inclusion of erroneous salts (Figure 72(A)). Furthermore, there are significant advantages of this approach compared to DLS not only in reducing large particle bias but also far more information can be gathered about each agglomerate with up to 20 different size and shape attributes of each nanoparticle agglomerate measured. These include, for example 'form factor' which is a measure of circularity and major and minor axis lengths which are useful when looking at non-circular objects. Such shape information is not achievable through DLS which assumes all particles are spheres. Furthermore, surface area information can also be extracted and is another important factor since it has been linked to playing an important role in nanoparticle toxicity [40].

Ultimately, an automated analysis approach to image classification that was simple, demonstrated to be capable of the task, and most importantly accessible for the non-expert has been developed and validated. The software (ilastik) is open access and has an extremely user-friendly framework which ensures the workflow is widely accessible to all researchers including those without prior knowledge of machine learning. The method utilised sparse labelling to generate a scorable segmentation of image classes which can avoid complications associated with other machine and deep learning approaches where a large amount of precisely labelled data are required as training data in order to be accurate. Furthermore, the probability maps of agglomerate objects sized by this pipeline are compatible with probability maps produced by any machine learning approach and so the process is

transferrable. Finally, a deep learning segmentation algorithm (UNET) will be available in ilastik from spring 2020 should more experienced users wish to extend the capabilities of the workflow.

5.2.8 Application in real systems

The final section of this chapter looks at applying the presented automated protocol to a real system under investigation. For this Fe_3O_4-PEG and Fe_3O_4-COOH nanoparticles were used, these were the same particles initial DLS was carried out on in section 5.2.1. The two nanoparticles were dispersed in water and CCCM at a concentration of 100 µg/mL, and from the original DLS analysis there was a suggestion that agglomerate/particle size decreased upon dispersion in CCCM (Figure 73). This could have been due to components within CCCM screening some attractive electrostatic forces between the particles, although typically the use of polymer coatings does enhance colloidal stability. Therefore, in order to verify this finding, the automated imaging and analysis protocol was used to investigate agglomerate size. From this it was apparent that the dispersion of both Fe_3O_4-PEG and Fe_3O_4-COOH nanoparticles did not change when the particles were suspended in water or CCCM. This discrepancy between the DLS and automated analysis would suggest that the extra components in CCCM, for example BSA (~7 nm), influenced the measured nanoparticle agglomerate size in DLS analysis. From the automated analysis the mean agglomerate sizes were 53 ± 58 nm and 44 ± 26 nm for Fe_3O_4-COOH and 54 ± 38 nm and 45 ± 31 nm for Fe_3O_4-PEG in water and CCCM respectively (Figure 74). However, the size distributions clearly indicated two peaks in both systems. The first of which matched very accurately to the primary particle size (30 nm); 33 nm and 38 nm for Fe_3O_4-PEG and Fe_3O_4-COOH respectively. This suggested that the dispersion was mainly monodispersed but with the presence of some larger agglomerates. Such fine detail was not provided from the DLS analysis and could potentially influence any observed behaviour in biological studies such as cellular uptake. For example, size can play a role in defining whether a nanoparticle is taken up into a cell with larger nanoparticles sometimes showing slower uptake [221]. Therefore, the dose of primary particle nanoparticles would not be as high since some nanoparticles exist as agglomerates. The next stage

would be to run the same automated analysis on samples of varying concentration to ascertain whether there are any changes in dispersion state.

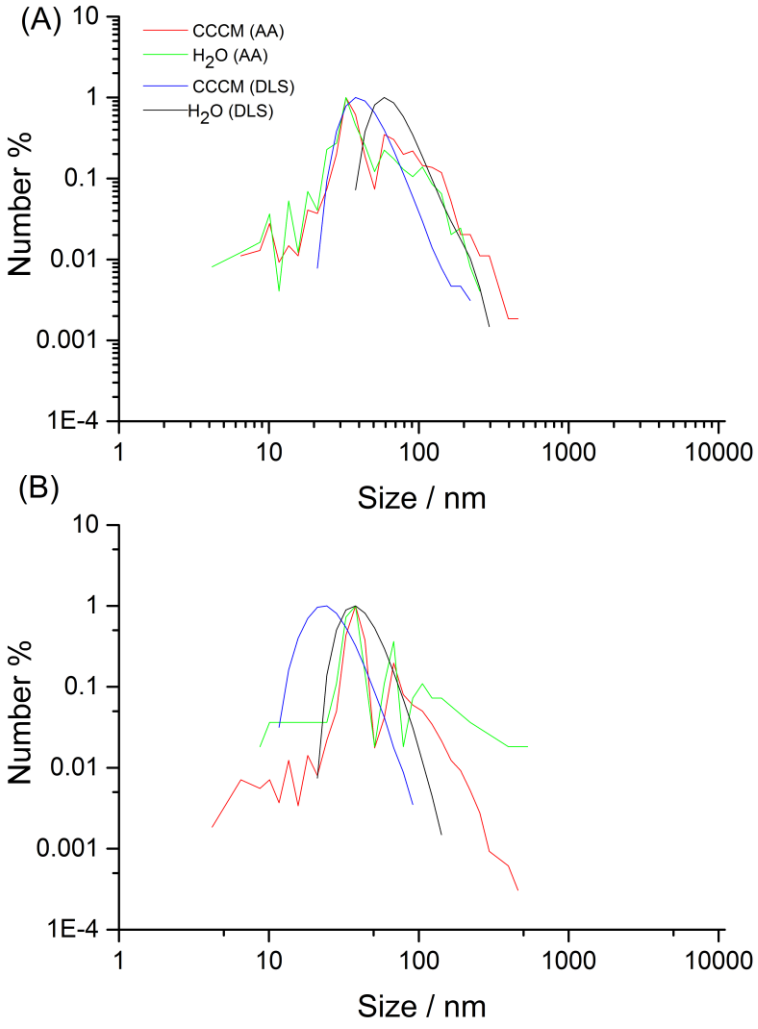

Figure 73: Automated EM analysis (AA) of (A) Fe_3O_4-PEG and (B) Fe_3O_4-COOH nanoparticles dispersed in water and CCCM at a concentration of 100 µg/mL. By automated EM imaging and analysis, no difference was observed between the dispersion state of the nanoparticles, despite the DLS analysis suggesting otherwise. DLS can be influenced by components inherently present in the media which could have led to the discrepancies seen.

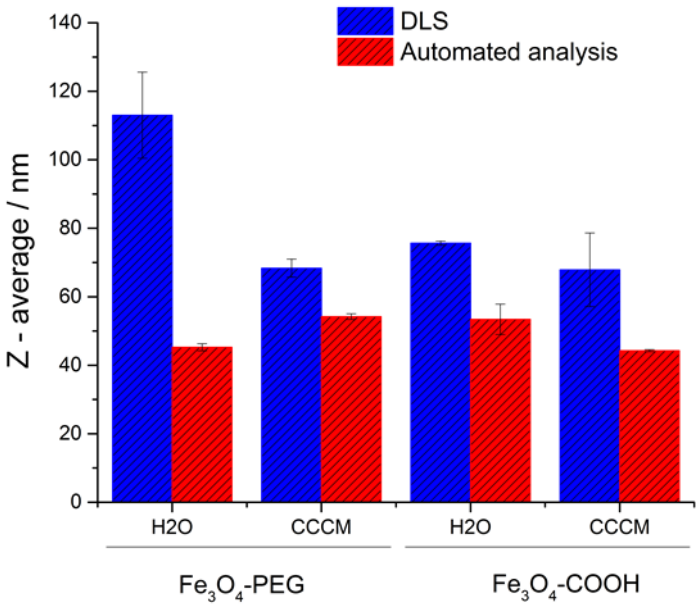

Figure 74: Mean agglomerate sizes for Fe_3O_4-PEG and Fe_3O_4-COOH nanoparticles dispersed in water and CCCM at 50 µg/mL. DLS data (blue) is compared to automated EM analysis (red). Discrepancies within DLS data for Fe_3O_4-PEG dispersions in CCCM and DI H_2O were removed when automated EM analysis was used. Standard error mean was used as the plotted error.

This automated analysis removed the confounding factors associated with DLS when using more complex media and indicated that the dispersion of Fe_3O_4-PEG and Fe_3O_4-COOH nanoparticles did not change as a result of the different particle coating or a change in suspending media from water to CCCM. However, there is an argument that there should be an indication of an increase in the primary particle size when the nanoparticles were dispersed in CCCM since it would be predicted that a protein corona would form around the particles [222]. However, this corona is not visible in HAADF STEM and therefore was not included in the automated image analysis measurements. This was not detrimental in this investigation since it was an indication of a change in agglomerate size that was being investigated. However, a fuller understanding including any size changes due to protein corona formation would be valuable. To that end the following chapter looks in part at the problems associated with imaging low contrast light element proteins and whether EM techniques have the potential to image some of these protein coronas around nanoparticles.

Summary

This chapter has provided evidence of interactions at the bio-nano interface that can be artificially induced when preparing nanoparticle suspensions in CCCM. Changes in pH and temperature of incubating culture media were identified as key factors in the development of a calcium-phosphorus-rich coating around a number of nanoparticle systems. Cryo-analytical STEM was used to assess and understand this coating formation, and ultimately show how to prevent such sample preparation artefacts from occurring. In demonstrating the success of using cryo-analytical STEM in characterising known nanoparticle dispersions in more complex biological media, further implications of this work could be in addressing current concerns regarding how to measure and understand unknown micro/nanoparticle pollutants present in the environment [223].

Following this, an investigation into understanding the dispersion states of nanoparticles in more complex systems was carried out. DLS was used initially to show the variation in dispersion of several nanoparticles in different biological fluids. However, DLS can be limited by interfering signals from components within biological media which can reduce its effectiveness for dispersion analysis of nanoparticles in biological suspensions. Therefore, an automated EM procedure was developed and validated which provides a pathway for agglomerate analysis, utilising simple automated image analysis through two freeware codes, CellProfiler and ilastik making it accessible to a range of researchers.

Chapter 6

6. CELLULAR UPTAKE OF NANOPARTICLES AND INVESTIGATION OF THE PROTEIN CORONA

This chapter details two important studies looking at the interactions between nanoparticles and cells, and nanoparticle surfaces and proteins.

First an extensive cellular uptake study detailing the uptake and effect of two gold nanoparticles coated with PEG and terminated with either amine (Au-NH_2) or methyl (Au-OMe), by blood TK6 cells is provided. Immunogenic response to the nanoparticles was measured and cellular response was monitored by two assays examining cytotoxicity and genotoxicity. Cellular uptake was confirmed by resin embedding and carrying out TEM analysis on ultra-thin sections and 3D analysis using a FIB-SEM.

The second section of the chapter presents work focused on investigating the protein corona. The traditional bulk technique of SDS-PAGE was used to examine the protein corona around the Au-NH_2 and Au-OMe nanoparticles. Further work is then presented on preliminary attempts to image and characterise the protein corona using EM methods.

6.1 Exposing cells to gold nanoparticles

Cell uptake studies were set up as described in Chapter 3, section 3.6. The reason gold nanoparticles were chosen is due to a vast number of studies linking gold nanoparticles with potential in medicine, for example; drug delivery [224], medical imaging [225, 226] and cancer therapy [227]. Consequently, furthering our understanding of how gold nanoparticles interact with certain cells and/or proteins is important in continuing the development of nanomedicines. So far, most medical applications that gold nanoparticles have been linked with require the nanoparticles to be administered via the blood stream, therefore an understanding of how these nanoparticles interact with certain blood cells is vital. Accordingly, the human lymphoblastoid TK6 cell line was selected to carry out the cell uptake and toxicity studies, since TK6 cells are immune blood cells [228]. This cell line is commonly used for a number of assays since it typically undergoes high cell proliferation and is relatively stable during cell culture [229]. Specifically TK6 cells are suitable for the micronucleus assay regularly used to assess genotoxicity [230].

For medical application gold nanoparticles are rarely used without some form of surface modification to enhance efficacy. For example, for medical imaging, gold nanoparticles can be coated with PEG, a relatively inert polymer that prevents unwanted interactions with biological components and hence enhances blood circulation time [231]. In addition, the specificity of the particles to a target tissue for drug delivery and cancer therapy is often achieved by adding target specific ligands to the nanoparticles surface. These could be target specific antibodies [15], yet this technique can be limited by a short shelf-life and high costs associated with these antibodies. More effective is the use of small organic molecules to impart a biological label on the gold nanoparticle [232]. For this study, TK6 cells were exposed to two types of surface modified Au nanoparticles. These were 30 nm spherical particles coated with 5000 MW PEG either terminated with a NH_2 or OMe functional group. The different terminating groups resulted in a different surface potential for each nanoparticle where the Au-NH_2 nanoparticles had a positive surface potential and the Au-OMe nanoparticles had a neutral surface potential. Differences in surface charge are thought to affect both cell uptake and the cytotoxicity of

nanoparticles. Positive surface potentials can promote cell uptake with a favourable interaction between the nanoparticle and the negatively charged cell membrane [233]. However, such plasma membrane interactions can induce membrane damage and positively charged nanoparticles are often linked with greater cytotoxicity than corresponding neutral or negatively charged particles [234]. The aim of this cell study was to assess cellular uptake, cytotoxicity, genotoxicity and any inflammatory effect induced by both Au nanoparticles on blood TK6 cells and to evaluate whether there was any difference in cellular uptake and/or response between the positive and neutral surface modified Au nanoparticles.

6.1.1 Cellular uptake

Cells were exposed to either Au-NH_2 or Au-OMe at 3 applied doses of 1 µg/mL, 10 µg/mL and 50 µg/mL. The cells were then left for 24 h before being fixed, resin embedded and sectioned for TEM sample preparation (Chapter 3, section 3.6.2). Prepared thin-sections of the 50 µg/mL dosed cells were imaged by both TEM and HAADF STEM and there was evidence that both nanoparticle types underwent cellular uptake (Figure 75 and Figure 76). From qualitative assessment by TEM of cell sections, there was no obvious difference in cell uptake between the two nanoparticle types, however to confirm this a more statistically relevant analysis would be required. For both nanoparticle types uptake was largely seen to have occurred in the cytoplasm with no evidence that nanoparticles entered cell nuclei. Additionally, there was evidence of some nanoparticles encased within single membrane vesicles in the cytoplasm (Figure 75(B) – inset) which suggested those particles were taken up via some form of endocytosis and this is in agreement with previous work published [235]. The nanoparticles were largely seen to be individually dispersed within cells with little evidence of any significant agglomeration taking place. This agreed with DLS data taken from dispersions of the nanoparticles in the CCCM used for the cellular uptake studies, which indicated a monodispersed suspension for both types of nanoparticle (Figure 77).

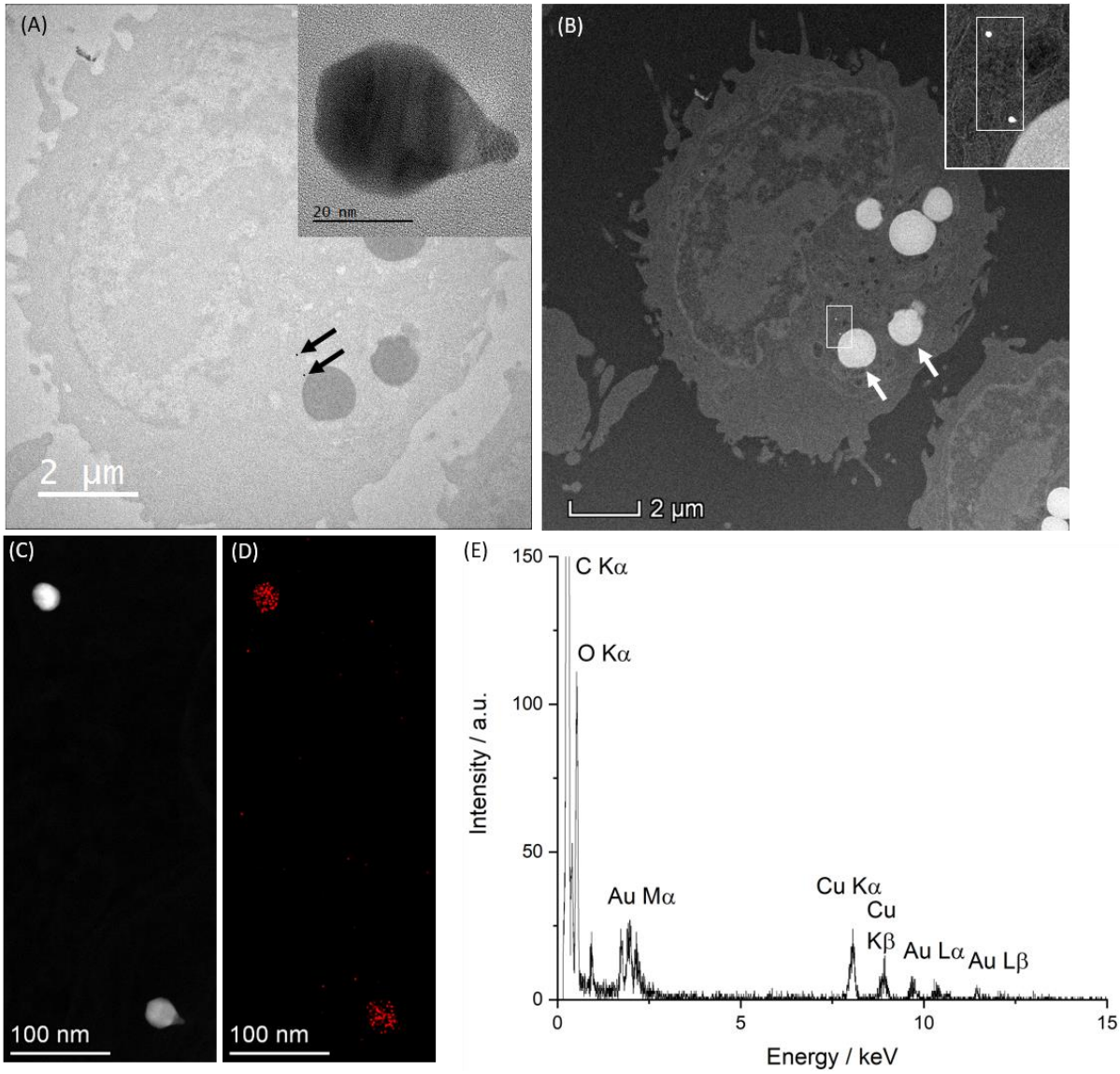

Figure 75: S/TEM imaging and analysis of thin sections prepared from cells treated with Au-NH_2 nanoparticles at 50 µg/mL. (A) A TEM image indicating the presence of two nanoparticles within a cell (black arrows). The inset presents a high magnification image of one of the particles. (B) A HAADF STEM image of the same cell section providing better contrast of the detail within the cell, the lower nanoparticle is encased within a vesicle (inset). The large white circles (white arrow) are lipid droplets which bind the osmium fixative strongly. (C) A higher magnification HAADF STEM image of the two nanoparticles from which EDX analysis was carried out. The X-ray intensity map of the Au Mα signal in red (D) and the EDX spectrum (E) both confirmed the particles were indeed gold nanoparticles.

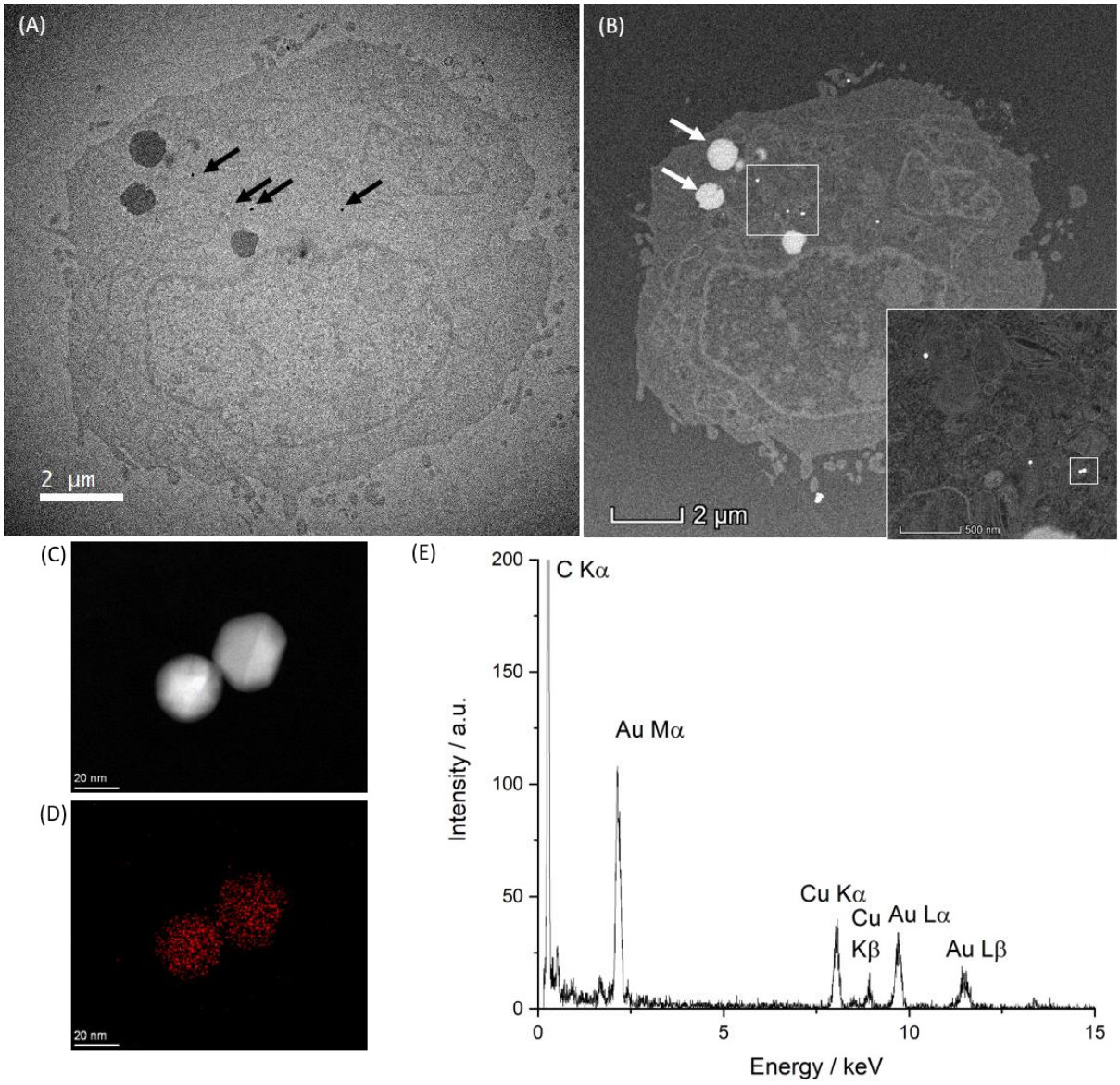

Figure 76: S/TEM imaging and analysis of cellular thin sections prepared from cells treated with 50 µg/mL Au-OMe nanoparticles. (A) A TEM image indicating the presence of Au-OMe nanoparticles within a cell (black arrows). (B) A HAADF STEM image of the same cell section providing better contrast of the detail within the cell. The large white circles (white arrow) are lipid droplets that bind the osmium fixative strongly. (C) A higher magnification HAADF STEM image of two of the nanoparticles analysed by EDX spectroscopy. The X-ray intensity map of the Au Mα signal in red (D) and the EDX spectrum (E) clearly indicated the particles to be gold.

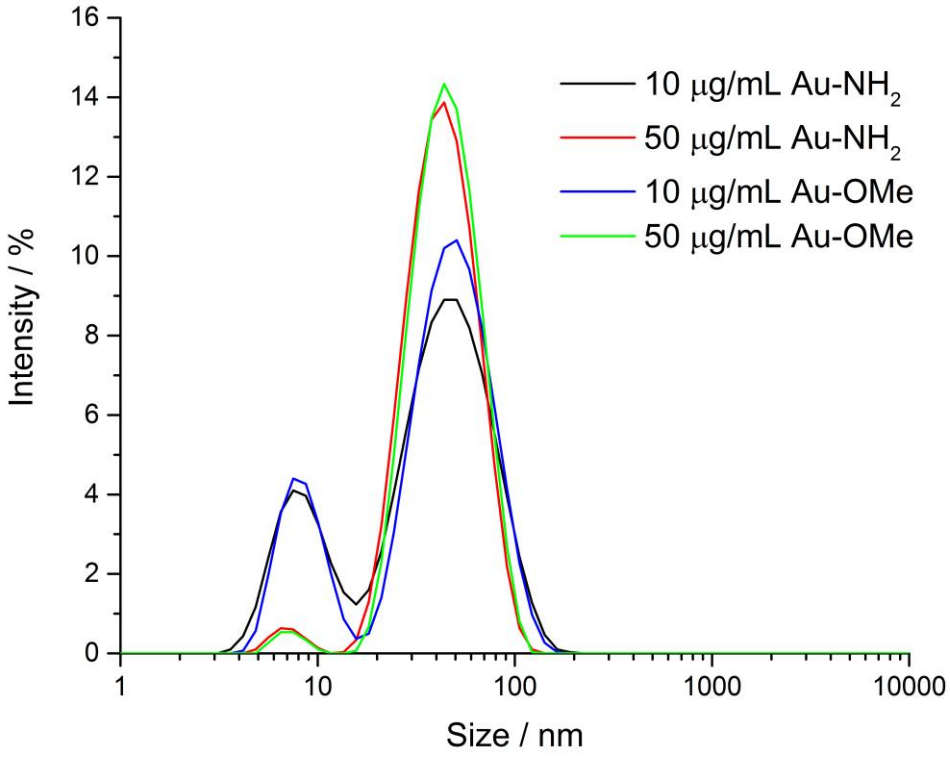

Figure 77: DLS intensity plots of Au-NH_2 and Au-OMe nanoparticles dispersed in CCCM at 10 μg/mL and 50 μg/mL. The scattering peak at ~9 nm is due to the horse serum albumin present in the growth supplement added to the CCM for cell culture.

TEM cell section imaging only allows imaging of a very thin section of a cell. To obtain large volume image analysis of whole cells embedded in a resin block, a process of 'slice and view' was carried out using a Helios Dual Beam FIB-SEM (Chapter 3 section 3.6.2.4). This technique allows serial imaging of the resin block face during ion-beam milling in order to collect image stacks over a volume which can be processed to obtain 3D reconstructions of whole cells. Consequently, information regarding the total number of nanoparticles taken up into an individual cell and also the positions of the nanoparticles within the cells was acquired. 3D reconstructions of cells treated with 50 μg/mL Au-NH_2 nanoparticles and 50 μg/mL Au-OMe are shown in Figure 78 and Figure 79. Imaris software was used to produce these 3D reconstructions and to apply thresholding for quantitative analysis of nanoparticle uptake within individual, whole cells.

Analysis of two cells treated with 50 μg/mL Au-NH_2 showed that uptake varied considerably between cells, where 183 nanoparticles were counted inside one cell compared to just 22 nanoparticles

counted inside another (Figure 78). In comparison, quantitative analysis of Au-OMe nanoparticle uptake showed uptake of 140 nanoparticles in a single individual cell. Consequently, the results indicated similarity to the TEM cell section analysis, that there was no obvious difference between cell uptake of the two different nanoparticle types and that they are taken up individually and in hundreds at the very most. However, the cell numbers measured are very few and further analysis of multiple cells would need to be carried out in order to make any statistical analysis of this observation.

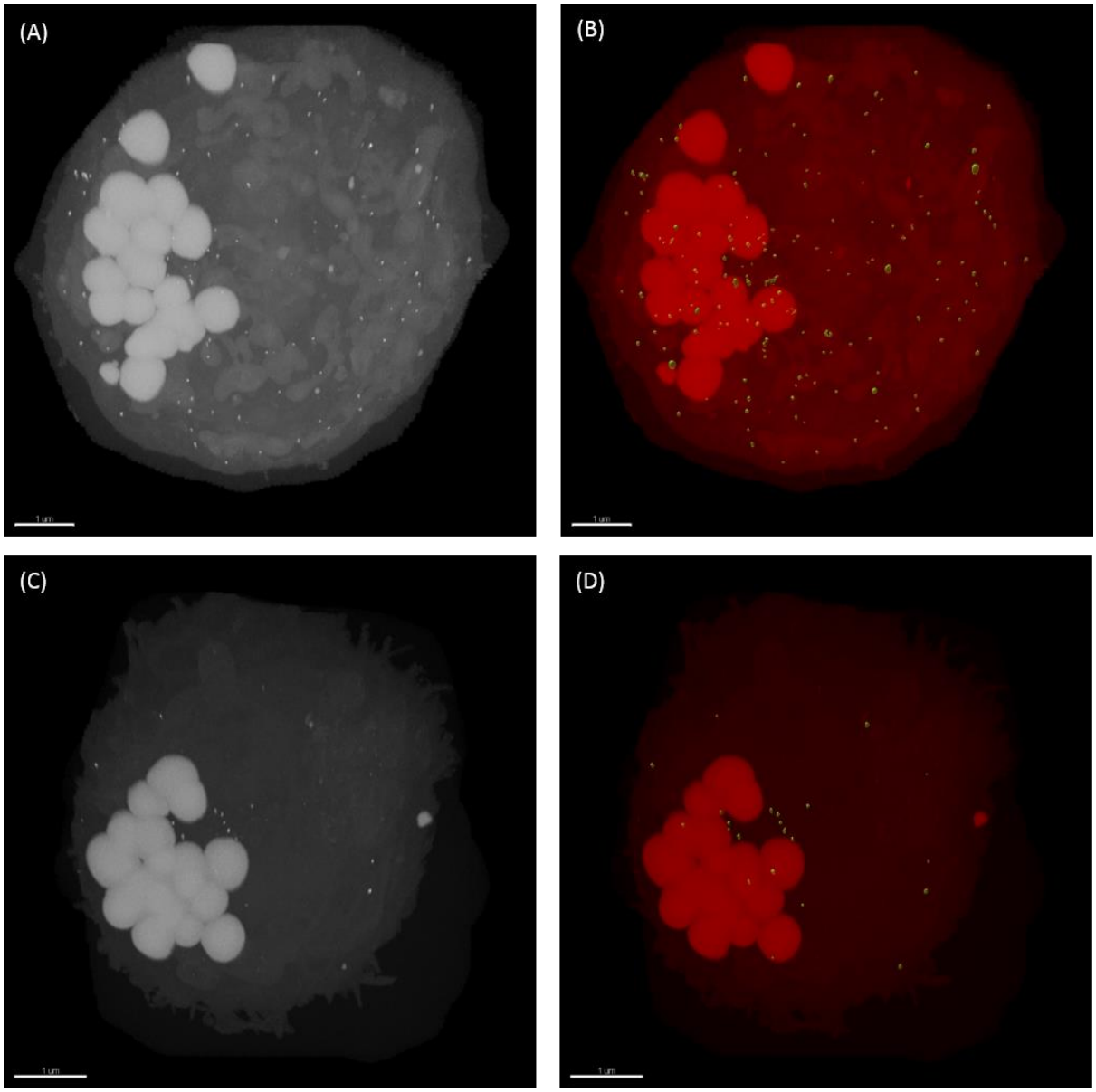

Figure 78: 3D reconstructions produced using Imaris software from image datasets obtained by slice and view imaging of two cells treated with 50 µg/mL Au-NH_2 nanoparticles. The reconstructions illustrate the range of nanoparticle uptake between cells, with (A) showing a cell containing 183 nanoparticles and (C) a cell containing 22 nanoparticles. Images (B) and (D) have been automatically (contrast) thresholded using Imaris software to segment the nanoparticles in green from the components of the cell in red.

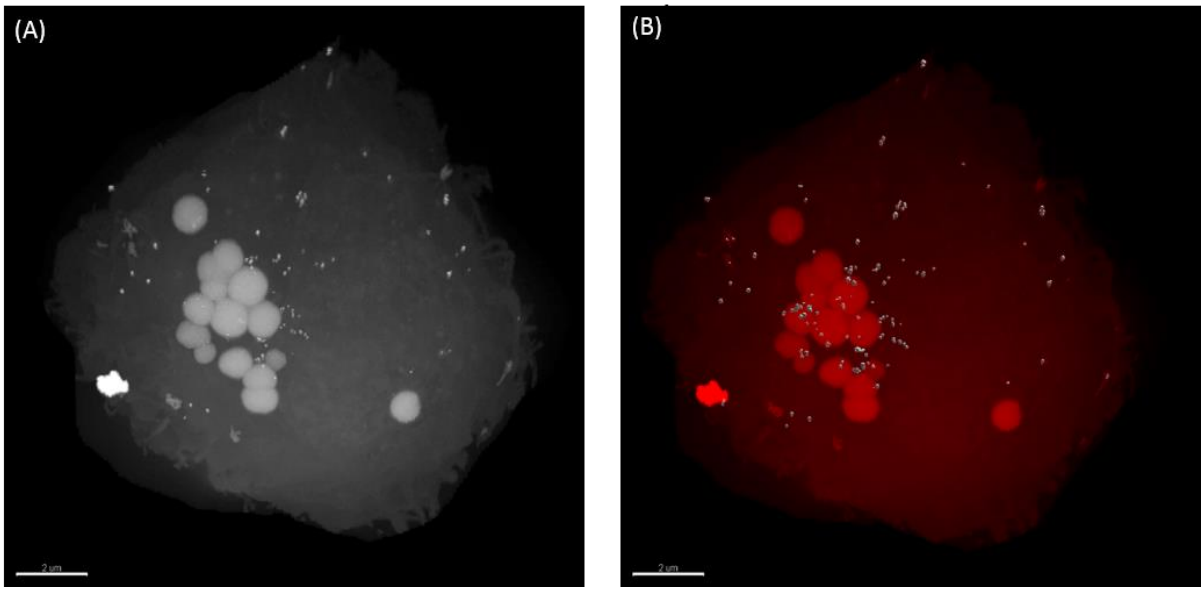

Figure 79: (A) A 3D reconstruction of a whole cell treated with 50 µg/mL Au-OMe nanoparticles produced in Imaris software from image datasets obtained by slice and view imaging. (B) Contrast thresholding was carried out using Imaris software to segment the nanoparticles in green from other cell components in red to count a total of 140 nanoparticles inside the cell.

6.1.2 Genotoxicity and Cytotoxicity

Having established that nanoparticle uptake by the cells had occurred, two assays were used to evaluate the cytotoxicity and genotoxicity of both nanoparticle types. This was done using the RPD cytotoxicity assay which monitors cell survival, and the CBMN assay which monitors the prevalence of micronuclei, a marker of genotoxicity, in binucleated cells, both post nanoparticle exposure and incubation (Figure 80).

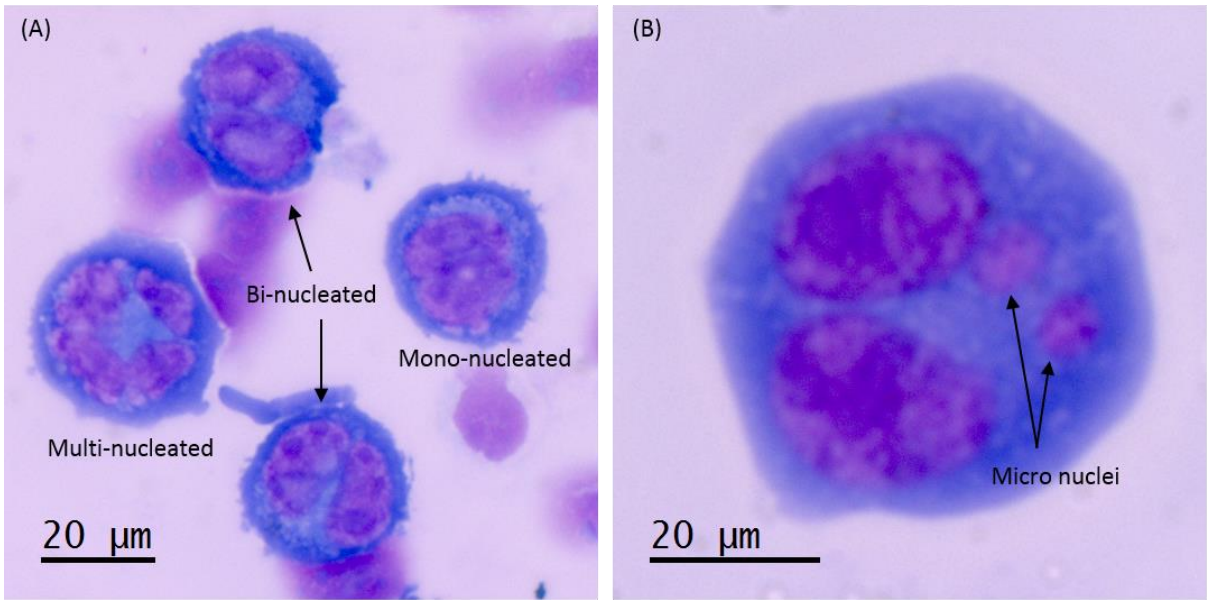

Figure 80: Optical light microscope images of TK6 cells exposed to 1 µg/mL Au-NH_2 nanoparticles for 24 h. (A) shows either bi-nucleated cells which indicate healthy cell division, or mono-nucleated and multi-nucleated cells which can be markers of cell cytotoxicity. (B) shows a bi-nucleated cell containing two micro-nuclei, micro-nuclei are markers of genotoxicity.

For both assays 6 nanoparticle doses were applied; 1 µg/mL, 2.5 µg/mL, 5 µg/mL, 10 µg/mL, 25 µg/mL and 50 µg/mL along with a negative (0 µg/mL) control and the cells incubated for 24 h before preparing samples for the assays (Chapter 3, section 3.6.2). Looking first at the data for the Au-NH_2 nanoparticle treatments (Figure 81), there was a general decrease in % cell survival after exposure and incubation. However, this decrease was only significantly different from the control for the doses of 2.5 µg/mL and 10 µg/mL, and the significance was small. Therefore, the cytotoxicity of the nanoparticles was concluded to be low, never falling below 75% cell survival in any incubation. In the case of the micronucleus assay a more obvious trend of increasing DNA damage with increasing dose was observed, and this was significant compared to the negative control at the highest concentrations of 10, 25 and 50 µg/mL, indicating that as concentration increases so too does the genotoxic action of the nanoparticles.

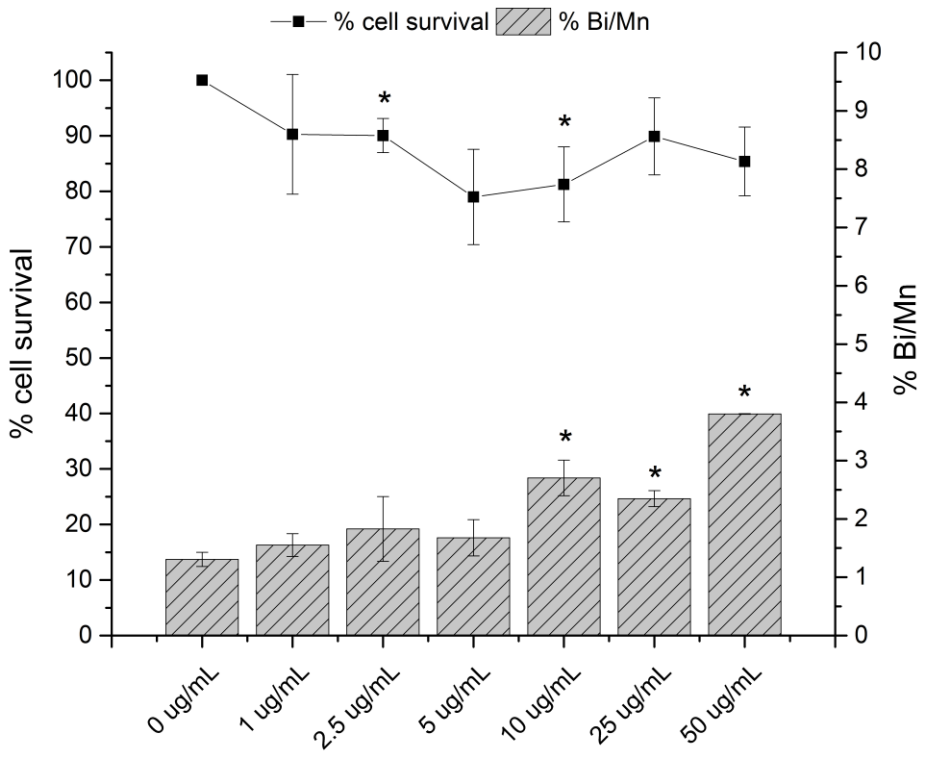

Figure 81: Cell survival and micronucleus presence within bi-nucleated cells for TK6 cells exposed to Au-NH_2. Some degree of toxicity was observed after treatment with nanoparticles (LH y-axis). A significant increase in DNA damage was seen with increasing dose (RH y-axis), where %Bi/Mn is the percent frequency of micronuclei in bi-nucleated cells. Errors are given as the standard deviation of n=3 measurements, with significance obtained by a paired t-test where, * = p<0.05.

For the Au-OMe nanoparticles, the same treatment and results are shown in Figure 82. Larger errors were seen in the cytotoxicity data due to larger variation in the data collected from the three repeats. Accordingly, at no nanoparticle dose treatment was there a significant decrease in cell survival, and the mean cell survival percentage remained the same within error to that observed for the Au-NH_2 nanoparticles, again never dropping below 75%. The genotoxicity data illustrated the same increase in genotoxic action with increasing particle dose/concentration as was observed for the Au-NH_2 nanoparticles and again the % Bi/Mn values obtained at each particle concentration were the same within error as observed for the Au-NH_2 nanoparticle exposures. The results suggested that overall there was little difference in the cellular response to both types of nanoparticles, indicating the suggested similarity in particle uptake obtained by the EM analysis of treated cells could be correct.

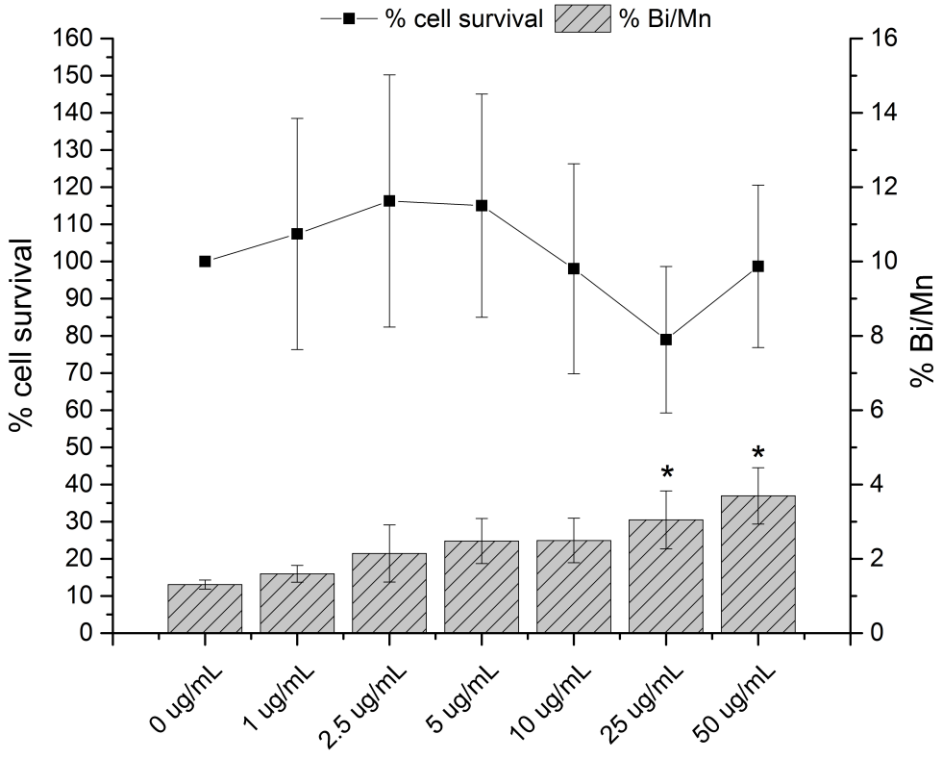

Figure 82: Cell survival and micronuclei presence within bi-nucleated cells for TK6 cells exposed to Au-OMe. No significant cytotoxicity was observed at any dose (LH y-axis), whilst an increase in chromosomal damage was seen with increasing dose (RH y-axis), where %Bi/Mn is the percent frequency of micronuclei in bi-nucleated cells. Errors are given as the standard deviation of n=3 measurements, and statistical significance obtained by a paired t-test, where * = p<0.05.

It is worth noting that significant DNA damage is only seen at the higher nanoparticle dose treatments (>10 μg/mL). Typically, in clinical applications, for example drug delivery, the doses used are lower with some quoting a typical dose of 1-100 nanoparticles per cell, determine by for example mass spectrometry, flow cytometry or UV-vis spectroscopy [236, 237]. Here we note that for the higher 50 μg/mL exposure dose the actual uptake dose is 10 to a few hundred nanoparticles (Figure 75 and Figure 76), so in some cases is higher than the typical uptake dose used in medical application. Therefore, the lower exposure doses (<50 μg/mL) would be more reasonable markers for potential cytotoxicity of the Au nanoparticles. Furthermore, since acute cell survival did not fall below 50% this confirmed that the observed genotoxicity was due to internalised nanoparticle-cellular component

interactions causing specific DNA damage rather than DNA damage as a result of excessive cell death occurring.

In general the bio-toxicity of gold is regarded as low, which agrees with the results observed here. Comparisons with previous studies are complicated by a host of factors that influence cytotoxicity, e.g. size, shape, surface potential and cell type. Typically, positively charged nanoparticles would be expected to be more cytotoxic, yet this was not obvious from the experimental data collected here. This could be due to the dominant PEG coating around both nanoparticle types that can reduce toxicity by reducing interactions with bio-macromolecules, something explored further in section 6.2 [238]. However, in agreement with previous studies, spherical nanoparticles are typically less toxic then other rod-like or ellipse nanoparticles [239] and particles larger than ~10 nm are usually less toxic since they cannot easily pass through the nuclear membrane, limiting DNA interactions and potential genotoxicity [240]. To date publications looking at the toxicity of Au nanoparticles to blood cells is limited. Work published by He *et al.* [241] suggested that there are interactions of Au-PEG nanoparticles with components of blood but did not specifically identify or discuss interactions with TK6 cells. However, this work suggests these coated Au nanoparticles may be suitable for transport within blood and so could have promise as vehicles in medical applications, such as photothermal treatment or drug delivery. However, this would only be the case if the particles were appropriately modified without significant changes in surface chemistry and further work was carried out to explore any interactions between the nanoparticles and other components within the blood.

6.1.3 Inflammation

An IL-6 ELISA was used to investigate the inflammatory response of TK6 cells to the coated Au nanoparticles since the release of IL-6 is a marker of an immunogenic inflammatory response [242]. At no concentration was any significant evidence of IL-6 expression observed for either nanoparticle type (as assessed by paired t test $p>0.05$) and therefore the particles were considered not to cause

any inflammatory response (Figure 83). This again presents both nanoparticle types/coatings as promising transporters in potential therapeutic use.

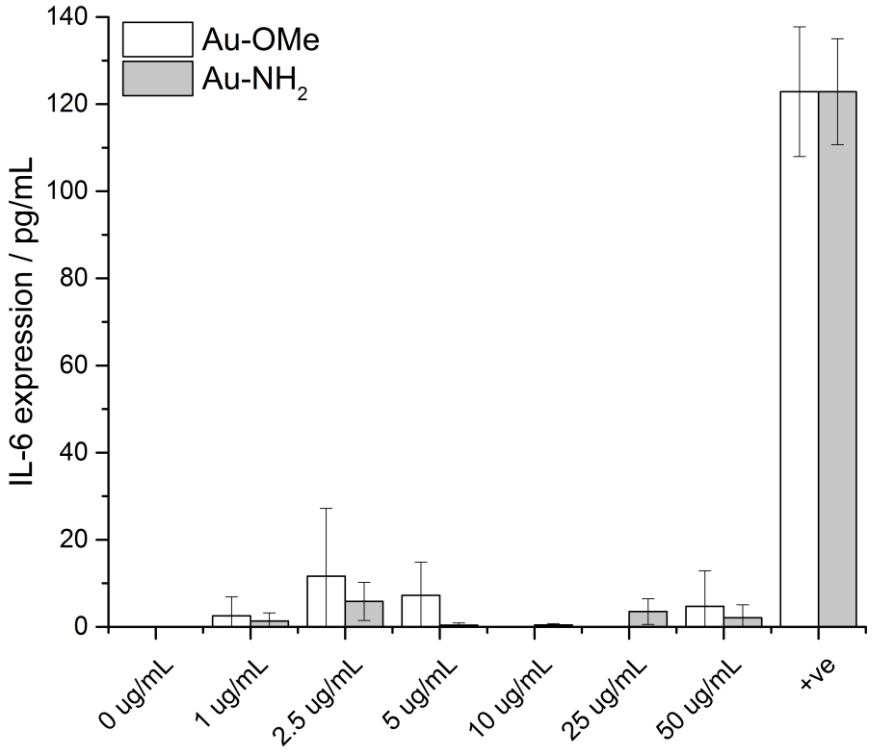

Figure 83: IL-6 ELISA for TK6 cells treated with either Au-NH_2 or Au-OMe nanoparticles. Neither particle type caused any immunogenic response as no significant IL-6 expression was seen at any particle concentration.

To conclude, nanoparticle uptake by exposed TK6 cells *in vitro* of up to a few hundred individual nanoparticles per cell was observed for both nanoparticle types, yet the cytotoxicity and genotoxicity was low particularly at the lower particle concentrations and no immunogenic response to either nanoparticle type was observed. However, this study is one area (acute response to *in vitro* exposure to single cell types) within a wider range of work that extends to *in vivo* studies where inconsistent results are obtained [243]. One reason for this is the added complexity of *in vivo* systems which often means results vary from those obtained *in vitro* [244]. The complexity of the interactions occurring at the bio-nano interface even *in vitro* is still not fully understood, yet these interactions can alter the biological identity of nanoparticles which in turn will dramatically alter how they disperse or how cells

might respond to them. The most widely researched and accepted bio-nano interaction is the formation of a protein corona and the potential for analysis of this by EM will be explored here next.

6.2 Protein corona investigations

Investigation and a full understanding of the protein corona still remains to be wholly established, yet it has been shown that the protein corona has a significant impact on the behaviour of nanoparticles *in vitro* and *in vivo* [7]. The following work details an investigation into the protein corona around both the Au nanoparticle types using SDS-PAGE analysis as a benchmark and then with preliminary attempts to image and characterise the protein corona by EM.

6.2.1 SDS-PAGE

Initial protein corona analysis was carried out using the traditional bulk technique of SDS-PAGE which allows qualitative analysis of proteins within the corona according to protein weight. Both the hard corona and soft corona were investigated (Figure 84) (Chapter 3, section 3.6.1), where the hard corona refers to strongly bound proteins and the soft corona to the outer, more loosely bound proteins. Analysis of the hard corona around both types of nanoparticle indicated the presence of only a small number of protein bands with the two main protein bands at ~75 kDa and ~65 kDa. It is suggested that the band at ~75 kDa indicates the presence of horse transferrin and the band at ~65 kDa indicates the presence of horse serum albumin in the corona, both abundant proteins in the HS growth supplement added to the CCM that the nanoparticles were dispersed in for cell culture [245, 246]. However, to fully identify the proteins further analysis by mass spectrometry would be required. Nevertheless, the results indicate that the composition of the hard corona was similar around the two nanoparticle types which could explain the similarities in cellular uptake and response (both cyto and genotoxic). There were differences in the relative intensity of the bands for the two particle types, with the corona around Au-OMe having a noticeably lower intensity band at 75 kDa. However this would need to be confirmed through a more quantitative analysis.

The reason for the low number of protein bands in the hard corona for both nanoparticle types could have been due to the PEG coating around both nanoparticle types. Traditionally PEG is used as a coating to prevent excessive formation of protein corona around nanoparticles [247, 248] since the hydrophilic nature generates a region of high hydration around the nanoparticle which can preclude interaction with components within the blood [249]. It is thought that this reduction in protein corona formation can increase the circulation time and hence specificity to a target tissue when used in drug delivery [249].

Investigation of the soft corona was carried out by sequential washing of the nanoparticles and analysis of the supernatant. Only in the first wash (W1) were any obvious protein bands present signifying the soft corona was loosely bound to both nanoparticle types and easily removed. In the case of the Au-OMe nanoparticles 8 protein bands were observed compared to only 5 for the Au-NH_2 nanoparticles. This would suggest that whilst the hard corona was very similar for both particle types the composition of the soft corona was different. However, since there was little indication from the *in vitro* studies and EM cell uptake analysis of any significant differences in cellular response to the two nanoparticle types it is suggested that the biological behaviour of the two nanoparticles was predominantly defined by the hard corona, something that has been previously reported in [250]. These results further emphasise the importance of understanding the interactions occurring at the bio-nano interface considering that here two nanoparticle types with significantly different original surface potentials have a similar if not identical biological effect due to surface masking effects by the formation of a comparable hard protein corona around both nanoparticle types.

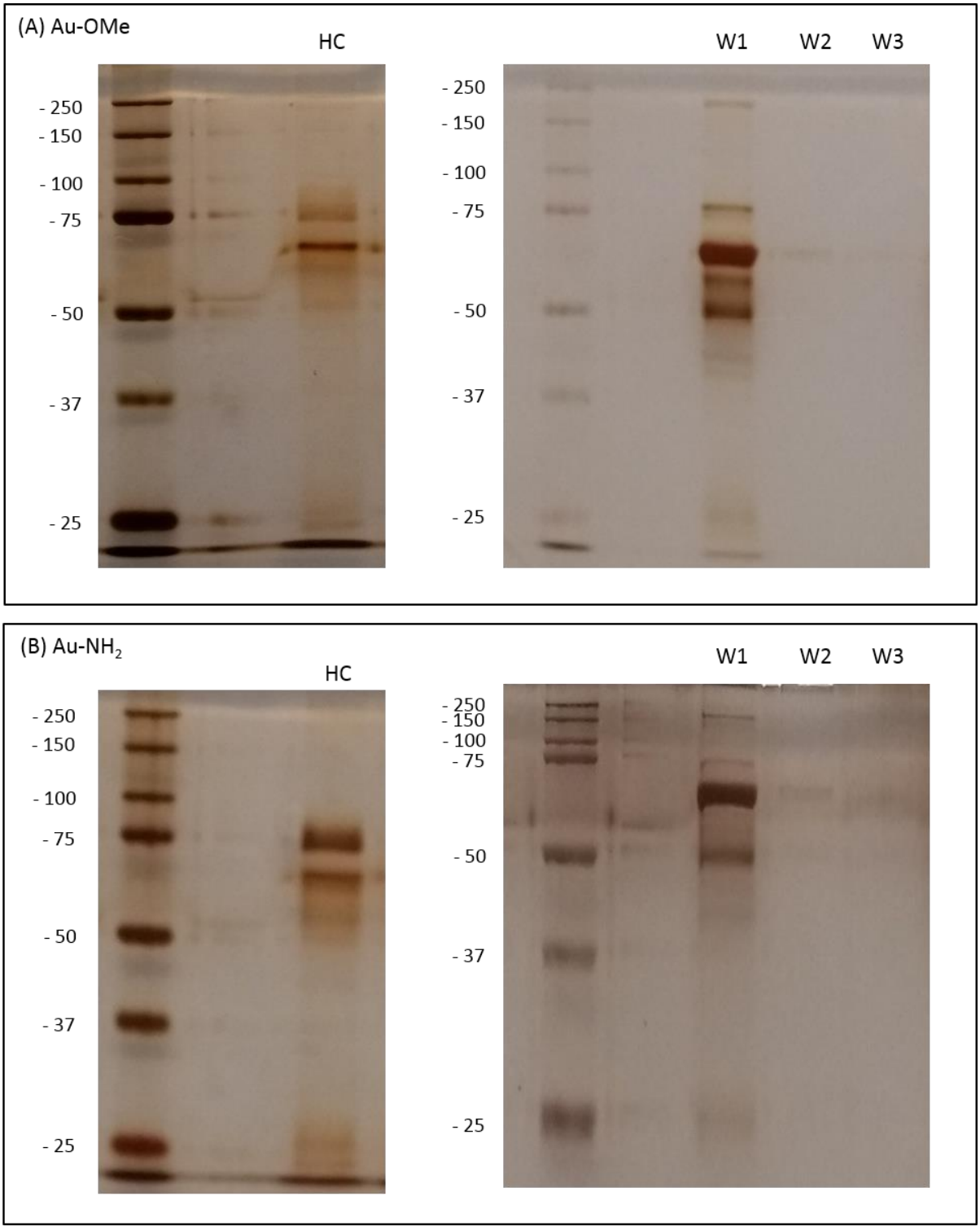

Figure 84: SDS-PAGE of the hard corona (HC) and soft corona around Au-OMe (A) and Au- NH_2 (B) nanoparticles. For soft corona analysis three washes were analysed; wash 1 (W1), wash 2 (W2) and wash 3 (W3). The procedure was repeated three times and in each case the results of each gel were

reproducible. A Bio-rad precision plus protein dual colour reference ladder was used for the protein mass analysis (left hand channel, units are in kDa).

6.2.2 Imaging the protein corona

SDS-PAGE has been the 'gold standard' technique for protein corona analysis for many years. However, it is a bulk analysis technique and therefore can only provide information regarding the proteins present in the bulk solution. The shape, size and importantly homogeneity of any corona is not obtained. Typically schematics illustrating the protein corona around a nanoparticle show a uniform coating around a spherical nanoparticle and this is assumed to be present and identical for every particle in suspension. However, it is possible that there may be some variation in the corona around particles. The spatial resolution imaging achievable by EM would allow such information to be obtained, yet, this is complicated by the low atomic weight and subsequently low contrast of proteins, and their potential to damage and be destroyed under electron irradiation [108].

Initial attempts to image the protein corona were made here utilising negative staining, a technique that can enhance the contrast of low atomic weight soft matter. First, in order to confirm the technique might be viable for protein corona analysis, two systems of Fe_3O_4 nanoparticles were stained and imaged, one un-coated and the other polymer coated (Fe_3O_4-PEG) (Figure 85). In the case of the Fe_3O_4-PEG nanoparticles, negative staining clearly enhanced the contrast of the polymer coating allowing it to be imaged and this illustrated that the particles were uniformly coated (Figure 85(B)). In comparison, and as expected, no coating was seen for the un-coated Fe_3O_4 nanoparticles after application of the same negative staining procedure (Figure 85(A)).

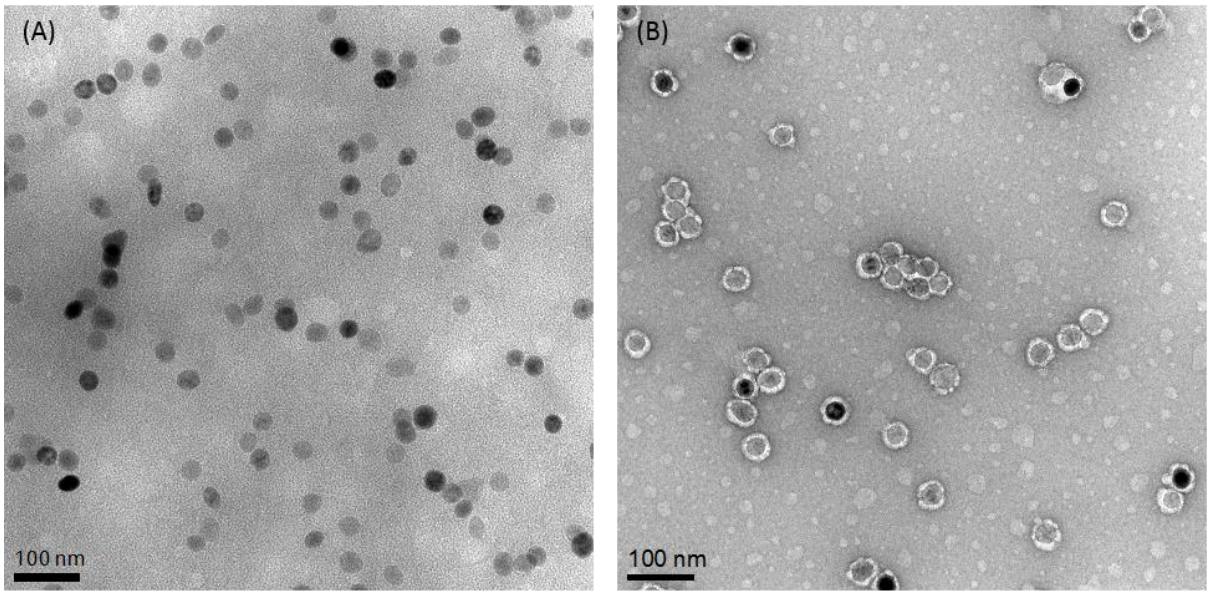

Figure 85: Negatively stained TEM grids of Fe_3O_4 nanoparticles either; (A) uncoated or (B) coated with PEG, and dispersed in water. Negative staining of drop-cast grids with 1% uranyl acetate was carried out for 45 s.

The same negative staining procedure was carried out on a system of SiO_2 nanoparticles dispersed in CCCM (i.e. a protein containing media) where a protein corona was predicted to establish around the nanoparticles. However, regions from the same grid provided very variable data, some particles appeared as normal, some with dark regions around them, and others with the predicted lighter region that would indicate the binding of soft matter (Figure 86). Whether this variability was solely due to pitfalls of the staining technique or actually reflected real and significant differences in the morphology of the protein corona around the SiO_2 nanoparticles could not be determined without further investigation. Therefore alternative EM approaches without any pre-imaging sample treatment were investigated to try and establish the true form of the protein corona.

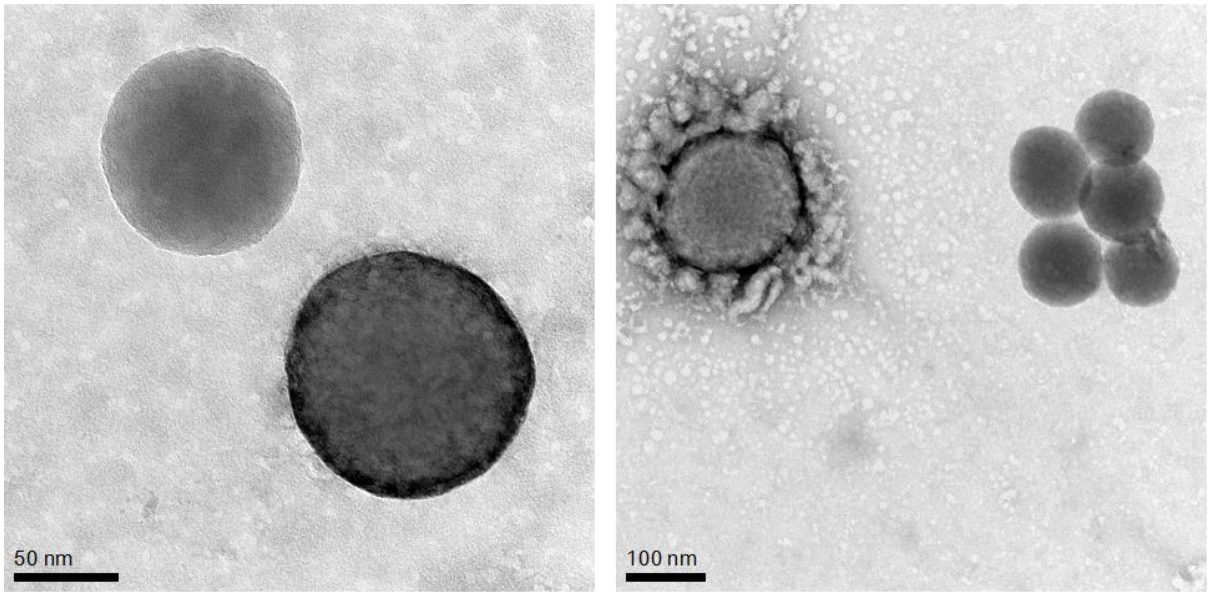

Figure 86: Negatively stained TEM grids of SiO_2 nanoparticles dispersed in CCCM. Negative staining was carried out for 45 s using 1% Agar scientific, non-radioactive alternative stain.

To develop an imaging technique through which low molecular weight elements could be imaged a simple system of Fe_3O_4-PEG dispersed in water was used to first try and image the polymer (PEG) coating. The specimen was prepared for EM imaging using the aforementioned plunge freezing, vacuum drying process described by Hondow *et al.* [102]. HAADF STEM enables Z contrast imaging, yet the high atomic weight of Fe can obscure any contrast from low molecular weight species. To address this issue, annular bright field (ABF)-STEM was used by changing the camera length projecting onto the detector (to 1.15 m) to provide minimum and maximum HAADF collection angles at the BF scattering range of 5 and 30.9 mrad respectively. The reduced collection angle of the annular STEM detector ensured the higher angle (Rutherford) scattered electrons from the dense Fe_3O_4 particles were no longer detected but the lower angle (Bragg) scattered electrons from the polymer coating could be detected. Using this technique, the PEG coating around the Fe_3O_4 nanoparticles was resolved (Figure 87).

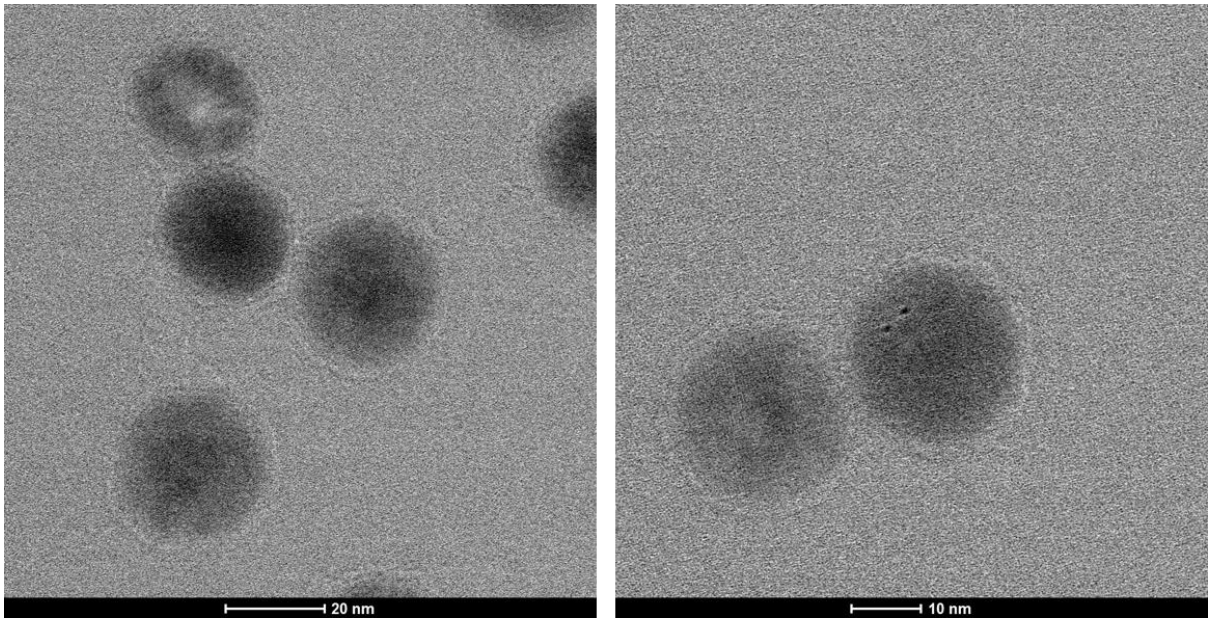

Figure 87: ABF-STEM imaging of a plunge frozen and vacuum dried suspension of Fe_3O_4-PEG nanoparticles in water on a silicon nitride support film. The PEG coating around the Fe_3O_4 nanoparticles was resolved using an annular collection angle of 5 to 30.9 mrad.

In addition to imaging the polymer coating, EDX analysis was also carried out. For most polymers and indeed proteins, the largest elemental component is carbon. Therefore in order to be able to meaningfully analyse the C signal a 50 nm silicon nitride (SiN_X) support grid was used rather than a thin amorphous carbon film supported on a copper grid. EDX analysis of the Fe_3O_4-PEG nanoparticles identified the presence of the C Kα X-ray signal. Mapping this signal showed that there was an obvious C rich coating around the nanoparticles (Figure 88). No obvious signs of contamination were present through the duration of the EDX analysis (at a fluence of 19 x 10^4 $e^-/Å^2$) which suggested the C signal was present from the polymer coating alone. The EDX results suggested the coating was uniform and homogenous around each nanoparticle as per the negative staining results.

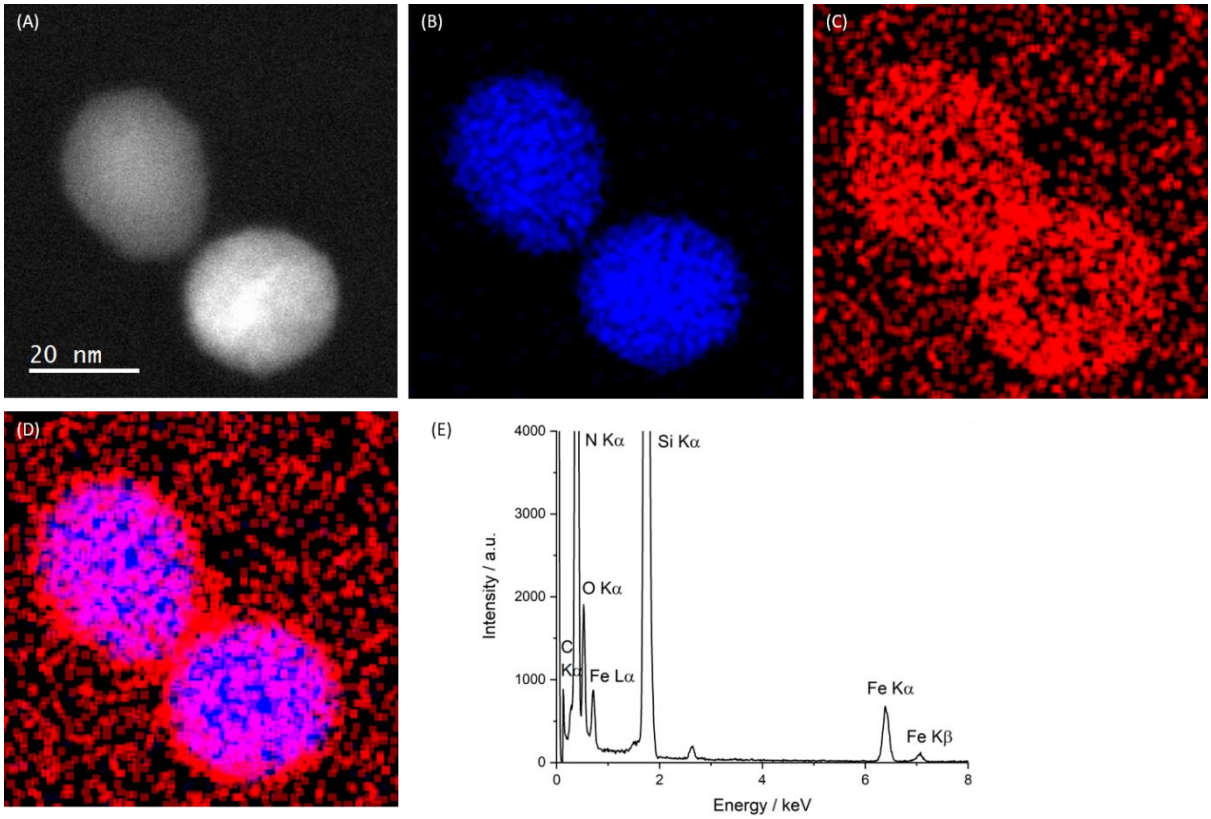

Figure 88: EDX analysis of Fe_3O_4-PEG nanoparticles. (A) HAADF-STEM image of two nanoparticles which does not show an obvious coating around the particles as compared to the ABF-STEM images in Figure 87. EDX mapping of the (B) Fe Kα and (C) C Kα signals observed in the EDX spectrum (E) indicated a carbon rich coating around the nanoparticles. These false colour maps are combined in (D). The total accumulated electron fluence for the EDX map was 19 x 10^4 $e^-/Å^2$.

Having successfully imaged and characterised a low contrast polymer coating around Fe_3O_4 nanoparticles and established the imaging conditions necessary to achieve this, the same techniques were used to try and image and characterise the protein corona around the Au-NH_2 nanoparticles dispersed in CCCM and plunge frozen on SiN_x grids. EDX analysis showed evidence of the presence of C and X-ray mapping the signal indicated it spatially resolved to a coating around the nanoparticles (Figure 89). However, since the Au-NH_2 nanoparticles were already coated with PEG before the predicted formation of a protein corona the presence of the C signal could not be used to confirm or denote successful identification of a protein corona.

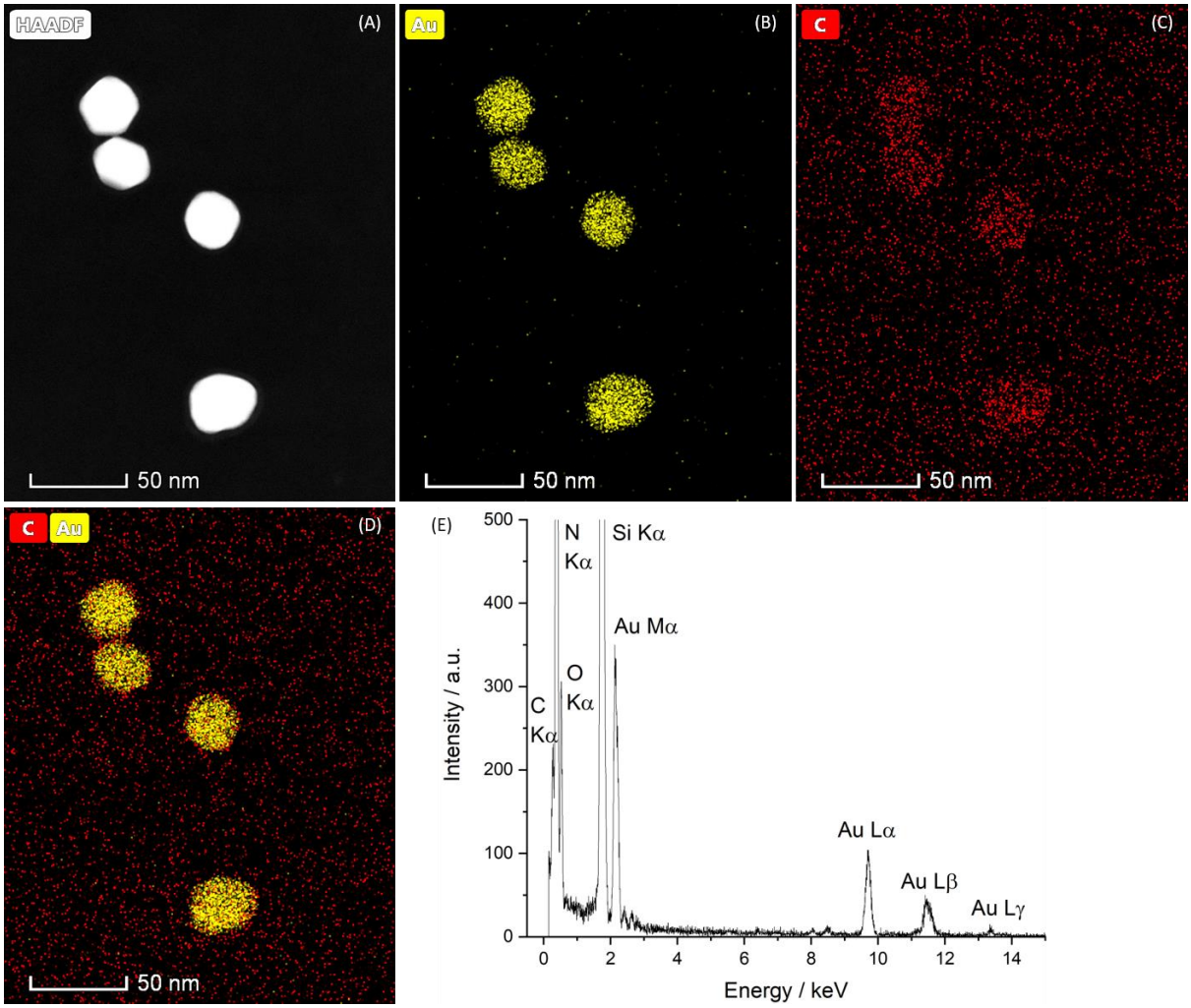

Figure 89: EDX analysis of Au-NH_2 nanoparticles in CCCM plunge frozen and vacuum dried on a SiN_x grid. (A) HAADF-STEM image of the area scanned for EDX analysis. EDX mapping of C Kα X-ray (C) showed a C rich accumulation around the nanoparticles, themselves mapped using the Au Lα X-ray signal (B). A combined EDX map (D) indicated this coating did not extend very far beyond the nanoparticles. The coating could be due to either the PEG coating, the formation of a protein corona or a combination of both. The total accumulated electron fluence of the EDX scan was 24 x 10^3 e^- /Å^2.

To overcome this, an alternative dispersion media was used composed of PBS supplemented with Au (15 nm)-labelled BSA (Au-BSA) (10%). Serum albumin had already been established as being a large component of the hard corona around the Au-NH_2 nanoparticles (section 6.2.1). Therefore it was predicted that BSA would also have a high affinity for the Au-NH_2 nanoparticles, and the smaller 15

nm Au particles would act as a marker of the position of BSA. After dispersing Au-NH_2 nanoparticles in PBS + Au-BSA there was some evidence of BSA accumulation around the nanoparticles (Figure 90). However, analysis of the TEM grid showed significant variation in the position of the smaller Au nanoparticles in relation to the Au-NH_2 particles where in some instances no BSA appeared to be present around the Au-NH_2 (Figure 90(C)). This could be indicative of differences in the protein corona around different nanoparticles in the same suspension, something that would not be apparent from bulk analysis techniques.

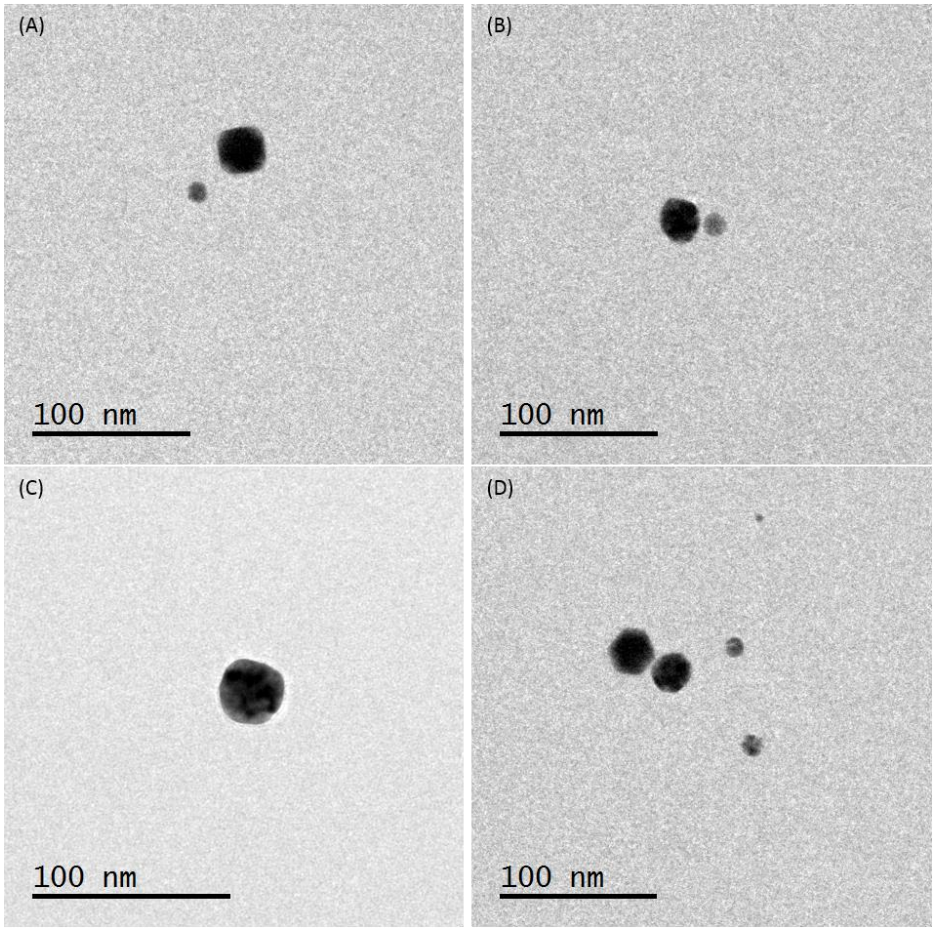

Figure 90: TEM images of Au-NH_2 nanoparticles after incubating in PBS + 15 nm Au-BSA (10%). Variable results were seen with the position and number of 15 nm Au-BSA marker particles around the Au-NH_2 nanoparticles (30 nm) variable.

Further EDX analysis of the Au-NH_2 nanoparticles dispersed in PBS + Au-BSA suggested the presence of a C rich coating around the smaller Au-BSA nanoparticles, although the intensity of the C signal in

the EDX maps was smaller than around the polymer coated Au-NH_2 nanoparticles, perhaps suggestive of the BSA being more diffuse than the polymer coating (Figure 91). However, proteins are electron beam sensitive and the total electron fluence required for the EDX scan in Figure 91 was 15 x 10^4 $e^-/Å^2$. Using such a high total electron fluence could have resulted in beam degradation of the BSA during the course of the EDX analysis which might explain the reduced C signal. Such beam sensitivity complicates EDX characterisation as a longer scan time is required to obtain enough counts to observe any significant elemental signals when using a lower probe current.

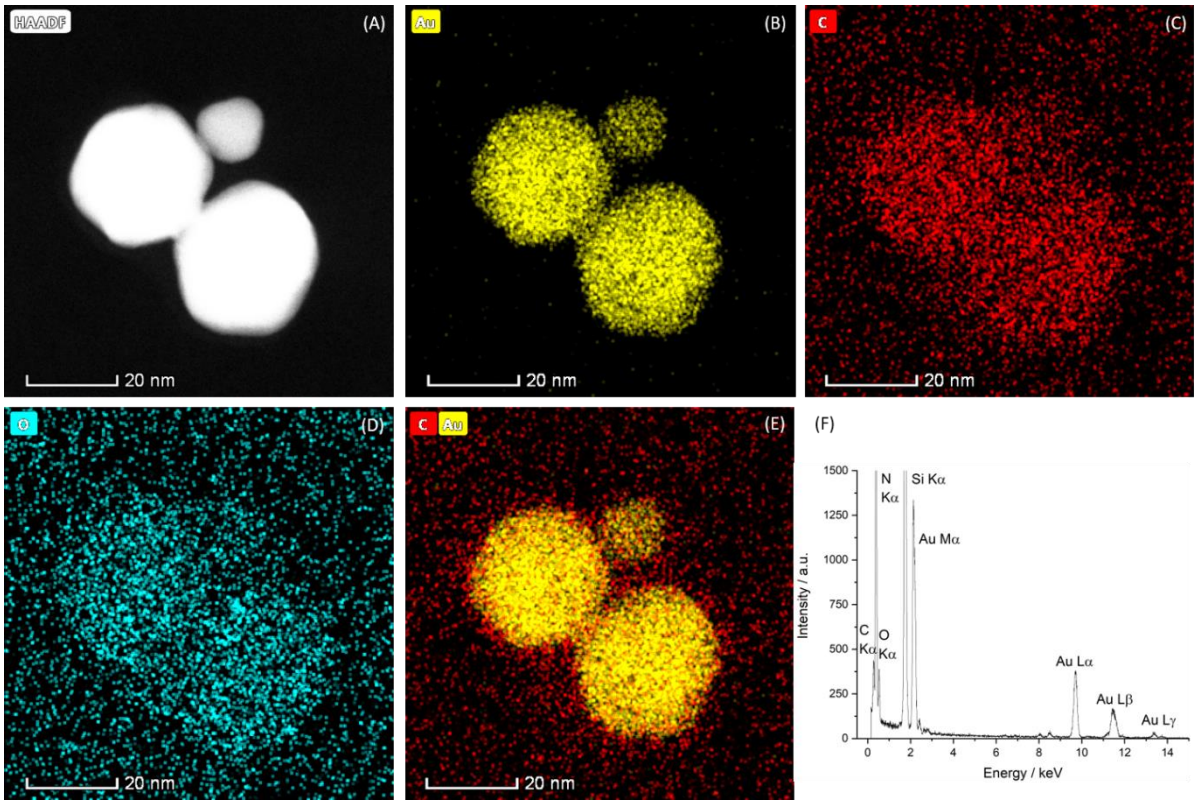

Figure 91: STEM-EDX dataset of Au-NH_2 nanoparticles (30 nm) dispersed in PBS with 10% BSA-Au (15 nm). (A) HAADF STEM image, the larger particles are the Au-NH_2 nanoparticles with the smaller particle the Au-BSA. X-ray maps were obtained for (B) Au Lα X-rays, (C) C Kα X-rays, and (D) O Kα X-rays and the Au and C X-ray maps combined in (E). The EDX spectrum is shown in (F). The total accumulated electron fluence for the EDX scan was 15 x 10^4 $e^-/Å^2$.

Finally, in order to establish whether it might be possible to routinely image the protein corona, ABF-STEM was used to image the BSA protein coating on the 15 nm Au-BSA particles. A camera length of

1.45 m was used relating to minimum and maximum annular collection angles of 4 and 24.5 mrad, incorporating the very outer edge of the zero order BF disc. Under these conditions and using a 10 pA probe current there was some evidence that the BSA coating could be imaged (Figure 92). However, evidence of a coating was not seen on each particle imaged. This could be due to differences in the BSA coating on each particle, yet it was not possible to confirm this by EDX analysis due to excessive contamination during attempts to map the C signal around the Au particles. Consequently, it is difficult to state categorically whether this further demonstrates noticeable differences in the protein coating around individual particles or simply demonstrates the difficulties in imaging a BSA coating. Again, proteins are beam sensitive materials, and although a low probe current was used during imaging, a total electron fluence of 60 $e^-/Å^2$ was still required for image capture which could lead to damage and destruction of the BSA before and/or during imaging. A large number of precipitated salts were also present within the sample (Figure 92), and the Au-BSA particles tended to be found associated with these. This suggested that there was some interaction occurring between a salt precipitate and marker nanoparticles which would support the theory of the BSA being present around the particles and adhering to the surface of the salts. Alternatively, the particles could have acted as a nucleation point, promoting the precipitation of salts from the media and hence explain why they were often found close to the salts. In ABF-STEM imaging there tended to be a gap between the salt and the particle again in support of the presence of a BSA coating on or around the gold markers (Figure 92(A-D)). This was not seen as clearly in the conventional BF TEM images where there is more additional scattering signal from the background support film (Figure 92(E-F)) however the gap could also be an artefact of the ABF-STEM imaging technique. BSA is ~66 kDa and typically biologist's state that resolving proteins below 50 kDa is not possible in cryo-EM [251]. This would suggest that BSA is towards the lower limit of resolution with standard TEM techniques. However, this is referring to resolution for structural analysis rather than detection [252]. BSA is described hydrodynamically as a prolate ellipsoid with dimensions of 140 Å for the major axis and 4 Å for the minor axes [253], this would suggest then that it should be achievable to detect the bulk ~15 nm protein using standard TEM imaging techniques.

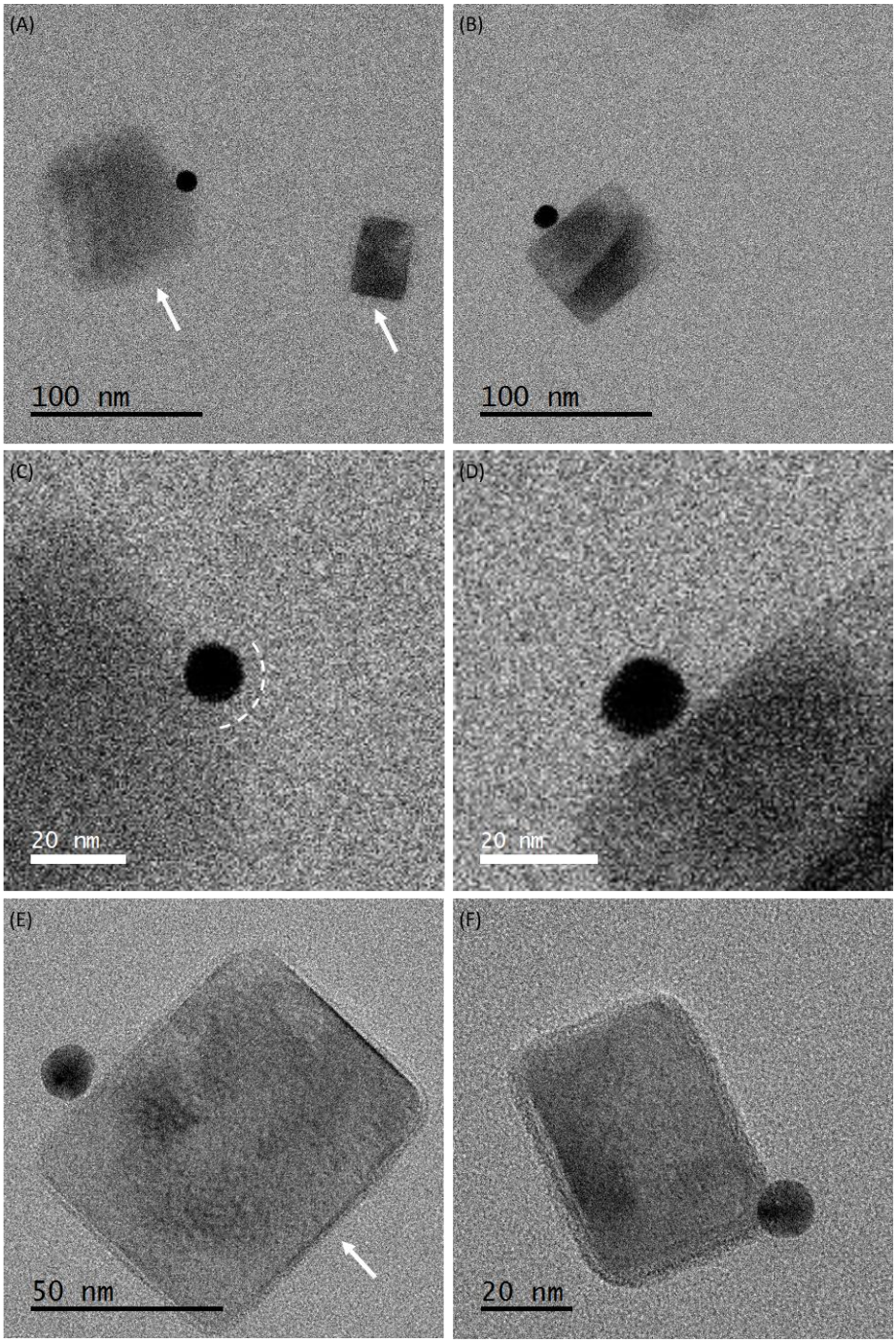

Figure 92: ABF-STEM imaging (A-D) and TEM imaging (E-F) of Au labelled BSA. The Au nanoparticles were found to predominantly associate with salts (white arrows) that had formed in the suspension. A diffuse layer was seen around some Au nanoparticles (C) (dashed line indicating part of the diffuse layer), though this was not seen around every particle imaged (D). The TEM images showed contamination occurred on the sample (layer seen to accumulate around the salts) and there was not always a visible gap between the Au nanoparticle and salt (F).

Current research looking at imaging the protein corona by STEM still remains in the preliminary stages but does suggest that it could be achievable. Kokkinopoulou *et al.* [254] imaged the soft and hard corona around PS nanoparticles using CTEM of negatively stained proteins and observed that the soft corona is a relatively large disperse, non-regular coating around the nanoparticle, extending 70-100 nm beyond the surface of the PS nanoparticles, whilst the hard corona was imaged as a much more tightly bound and regular coating around the particles (Figure 93).

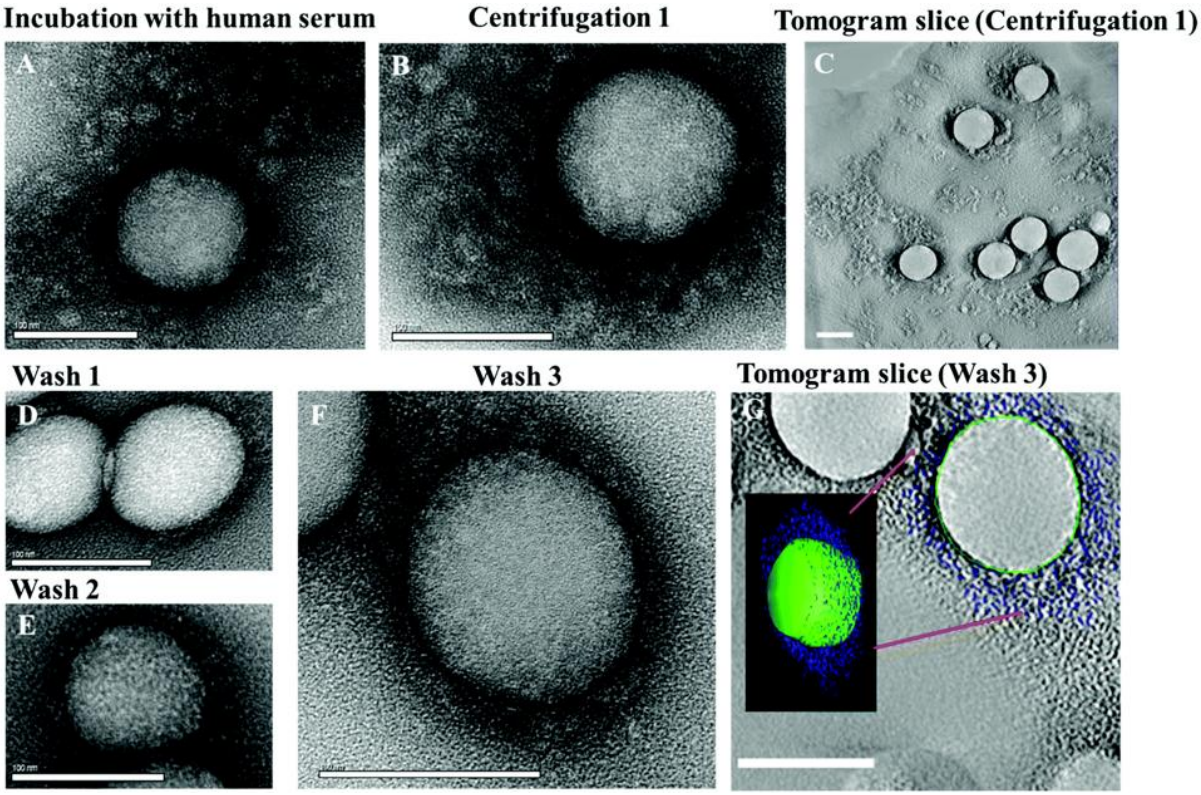

Figure 93: TEM images of the protein corona around un-functionalized PS nanoparticles. (A) The hard and soft corona after incubation of un-functionalized PS nanoparticles in human serum and (B) after centrifugation and removal of the supernatant, but before washing steps. (C) A tomogram slice of an area such as (B), scale bar: 100 nm. The hard corona is shown after the 1st wash (D), the 2nd wash (E) and the 3rd wash (F). An electron tomogram slice of the area presented in (F) is shown in (G) alongside a superimposed 3D reconstruction. Reproduced from [254].

Further work by Zachman *et al.* [119] illustrated the potential of cryo-STEM mapping to observe the solid-liquid interface and dendrites in lithium metal batteries, and although not explicitly

characterising a protein corona, the successful mapping of low molecular weight C would suggest the same procedure should be achievable for a protein corona. However, this work was carried out at lower magnifications than used here and with the use of advanced equipment including cryo-FIB-lift out and a direct electron detector for high resolution low dose EELS, plus additional post processing to increase signal. Thus, it could be that in order to successfully characterise the individual protein corona on nanoparticles, these more advanced EM techniques may be required. Nevertheless, even the early work reported here suggests there may well be a degree of variation in the form of the protein corona around different particles within the same suspension (Figure 86, Figure 90 and Figure 92), illustrating the need for further investigation into implementing EM techniques for high resolution characterisation of the protein corona around nanoparticles in order to advance our understanding of bio-nano interactions.

Summary

This chapter has highlighted the potential for Au-NH_2 and Au-OMe nanoparticles to be dispersed and transported into human lymphoblastoid TK6 cells. This was through clear evidence that despite cellular uptake of both nanoparticle types being observed by EM neither particle type caused any significant cytotoxicity and only at higher particle concentrations was any significant genotoxicity observed. Additionally, neither resulted in the occurrence of any immunogenic response.

The latter work reported in this chapter has indicated the potential for ABF-STEM to image the protein corona around nanoparticles. Early use showed success in imaging polymer coatings around Fe_3O_4 nanoparticles without the use of any contrast enhancing staining. Incorporating STEM-EDX analysis then allowed these polymers to be identified and localised. Finally, there was evidence of some degree of non-uniformity of the protein corona around Au nanoparticles which suggests that the biological identity of every particle within a single suspension may vary considerably. However, this remains preliminary work and further detailed investigation of the protein corona with advanced EM

techniques such as cryo-FIB lift out and transfer, direct electron detection and further image processing are required to confirm this statement.

Chapter 7

7. CONCLUSIONS AND FUTURE WORK

7.1 Summary of findings

The overall aim of this Ph.D. was to establish EM techniques that allowed characterisation of nanoparticles in complex biological media in order to better understand dispersion of the nanoparticles and any interactions at the bio-nano(particle) interface.

In Chapter 4, conditions were optimised and validated for cryo-analytical STEM characterisation of a frozen, aqueous dispersion of a model nanoparticle system. Successful STEM-EDX and STEM-EELS was accomplished to identify all four nanoparticle types within this system without significant damage to the vitreous ice causing unwanted movement of the particles. Two modes of STEM-EELS were optimised such that both elemental detection (EELS) and chemical fingerprinting (ELNES) could be achieved on frozen samples. Further optimisation of STEM conditions identified that operating using a probe current of <100 pA and a pixel size >2 nm was preferable for minimal damage to vitreous ice. Qualitative comparisons between cryo-STEM and cryo-CTEM indicated STEM has advantages in delaying (to higher doses) vitreous ice damage. Egerton [170] postulated that diffusion limited processes, of which water radiolysis is one, have a sublinear relationship between dose rate and

damage rate, which means higher electron flux STEM can operate at a point where damage per unit electron fluence is lower than in CTEM. Furthermore, the results support the suggestion that there could be certain recovery mechanisms occurring in STEM due to short localised illumination rather than prolonged large area illumination as for CTEM. It is proposed that utilising cryo-STEM could at the very least out-run some vitreous ice damage, provided the STEM pixel size is matched to or bigger than the delocalised damage area in order to avoid any over-sampling. This finding could have significant application both in materials and biological sciences for characterising beam sensitive soft matter captured in vitreous ice. Moreover, comparisons between cryo-TEM and LCTEM indicated cryo-TEM can delay and/or prevent some beam induced artefacts. This is due to the out diffusion of the reactive primary and secondary radiolytic products of water radiolysis being significantly reduced in vitreous ice compared to liquid water and, the cryogenic temperatures reducing rates of reactions between damage products and a sample [255]. Consequently, this investigation indicated that at least for non-dynamic investigation of aqueous nanoparticle systems cryo-TEM has advantages over LCTEM.

After developing and optimising cryo-analytical STEM acquisition conditions, Chapter 5 reported the application of these techniques to investigate interactions at the bio-nano interface of nanoparticles dispersed in CCCM. Characterisation of six nanoparticle types dispersed in CCCM using analytical-S/TEM indicated an amorphous coating formed around the surface of all the nanoparticle types. Initial characterisation using STEM-EDX of the suspension prepared for TEM via drop cast – air dried samples suggested the coating was rich in a number of constituents of CCM (Ca, P, Cl, K, Na). However, cryogenic sample preparation followed by cryo-STEM-EDX characterisation indicated the coating was rich only in calcium and phosphorus, highlighting the importance of *in situ* techniques in avoiding drying artefacts and ensuring characterisation of nanoparticles in suspension is representative of the native hydrated state. Further investigation of the calcium-phosphorus-rich corona suggested it was an artefact of bath sonication undertaken in ambient laboratory atmospheric conditions during dispersion preparation (rather than the 5% CO_2 atmospheres typically used for cell culture). An evident

increase in pH and temperature over time during incubation in both a bath sonicator and 40°C water bath in atmospheric conditions was determined as driving the precipitation of Ca by phosphate ions onto the surface of the nanoparticles [192]. Such formation of an artefactual corona around nanoparticles would be detrimental in many cell uptake studies where it might be predicted that the masking of the nanoparticles surface would alter the *in vivo* and/or *in vitro* biological identity of the nanoparticles. Ultimately, recommendations for nanoparticle dispersion preparation when using biological media have been detailed suggesting that where possible any prolonged sonication should be carried out on nanoparticles dispersed in water before dilution in CCM and all experiments should be conducting in as close to physiological conditions as possible.

The latter part of Chapter 5 presented a novel automated EM imaging and analysis protocol for nanoparticle dispersion quantification as a promising alternative to bulk hydrodynamic size distribution measurement techniques (such as DLS) that are often limited by the confounding components within more complex biological media. Automated imaging of TEM support grids was carried out using a Helios FIB-SEM and operating a script written in FEI's iFast developer software, this allowed >1000 images per sample to be captured. These large datasets were then analysed using two free software codes, ilastik and CellProfiler. This process utilised simple machine learning in order to train the ilastik software to identify nanoparticle agglomerates. Accurate image segmentation was achieved such that other components on the grid often present in biological media (e.g. salts) could be separated from nanoparticle agglomerates. Size and shape information for each nanoparticle agglomerate identified by ilastik was obtained using CellProfiler. The image analysis protocol was validated using a simple system of silica nanoparticles monodispersed in water and an agglomerated system of iron oxide nanoparticles in CCM with or without FBS. Significantly, comparisons between size distributions gathered by DLS and by the automated EM analysis indicated that whilst DLS can be biased toward larger particles, EM analysis gathers information on the whole size distribution, and therefore is particularly promising when it is information regarding the smaller nanoparticle agglomerate fraction that is of particular interest. Once validated the protocol was used to assess

whether freeze drying and controlled sublimation were effective warming procedures for plunge frozen TEM grids by comparing with the previously validated vacuum drying preparation route. Both procedures were shown to maintain the original nanoparticle agglomerate size distribution in suspension. Finally, in utilising pre-existing simple machine learning software, the protocol is accessible to a wide range of scientific researchers and therefore should have application in multiple scientific studies.

In the final results chapter, TK6 blood cells were exposed to two types of 30 nm spherical Au nanoparticles coated with 5000 MW PEG and either terminated with a neutral OMe or positive NH_2 functional group (Au-NH_2 and Au-OMe). EM analysis identified that both nanoparticle types were taken up into the cells and preliminary quantitative analysis suggested there was similar uptake efficiency. Cytotoxicity studies identified the particles were relatively non-toxic with cell survival never falling below 75%, and results were comparable for both nanoparticle types. Genotoxic data indicated a clear dependence of genotoxicity on particle exposure dose where genotoxicity increased with increasing dose, and again results were comparable for both nanoparticle types. These data agreed with the general conclusion from previous studies that gold has a relatively low bio-toxicity, particularly when > 2 nm [256]. Further analysis was carried out using SDS-PAGE to examine the protein corona that formed around the functionalised Au nanoparticles dispersed in CCCM. Both nanoparticle types had a hard corona composed primarily of horse serum albumin and horse transferrin. It was concluded that the similarity in the hard corona could explain the similarities in both cell uptake and cyto- and geno-toxicity suggesting the composition of the hard corona rather than the original nanoparticle surface properties is a key determining factor for biological function, agreeing with previous suggestions in the literature [250]. Bulk analysis of the protein corona did identify some variation in the composition of the soft corona around the two nanoparticle types, yet this did not appear to be significantly influential on cell uptake or effect.

Lastly bulk analysis of the protein corona does not permit information regarding size, shape or homogeneity of the corona around different nanoparticles within a single suspension. To address this ABF-STEM was investigated as a potential pathway for direct corona imaging. Initial optimisation was carried out to successfully image a low contrast PEG coating around 30 nm Fe_3O_4 nanoparticles. Once established, ABF-STEM was used to image BSA (a large component of many protein corona) conjugated to 15 nm Au nanoparticles. Some success indicated that it could be possible to identify the corona around nanoparticles and potentially characterise the composition through elemental analysis. Initial results suggest there may be some variation in thickness of the corona around different nanoparticles in a single suspension, but this requires further work for confirmation.

7.2 Final conclusions

- Cryo-analytical-STEM is a powerful, feasible technique for native, hydrated state characterisation of nanoparticles in dispersion.
- Cryo-STEM has advantages over cryo-CTEM in reducing vitreous ice damage per unit of electron fluence.
- Prolonged sonication of nanoparticles suspended in cell culture media under atmospheric conditions during nanoparticle dispersion preparation can induce an artefactual calcium-phosphorus-rich corona around nanoparticles.
- Automated EM imaging and analysis using two freeware codes (CellProfiler and Ilastik) allows accurate nanoparticle agglomerate analysis of nanoparticles dispersed in more complex biological media.
- TK6 blood cells show a similar uptake efficiency, cytotoxicity, genotoxicity and immune response to 30 nm spherical Au nanoparticles coated with 5000 MW PEG and either terminated with positive NH_2 or neutral OMe.
- Sodium dodecyl sulfate-polyacrylamide gel electrophoresis analysis of the protein corona around Au-NH_2 and Au-OMe nanoparticles in complete cell culture media identified a compositionally alike, hard corona around each nanoparticle type.

- ABF-STEM is a potential tool for direct protein corona imaging and initial observations suggest a degree of inter-particle variation in the protein corona around nanoparticles in a single suspension.

7.3 Further work

Finally, in order to continue to build on the work presented in this thesis, a number of further studies are recommended:

Optimise cryo-analytical-STEM for characterisation of more beam sensitive materials. In this work cryo-analytical-STEM was optimised for the characterisation of dense nanoparticles which were relatively stable under the electron beam. Damage to the vitreous ice was the main limitation. However, the next step is to examine the use of cryo-analytical-STEM for characterising more beam sensitive material suspended in vitreous ice, for example polymers and biological samples. It was identified that STEM had advantages over CTEM in delaying beam damage to the vitreous ice, whether or not cryo-STEM could be advantageous in delaying beam damage to other beam sensitive samples such as polymers or biological materials should be the future direction this research takes.

Utilising automated EM imaging and analysis for measurement of more complex nanoparticle dispersions. Having validated and optimised a simple and accessible automated imaging and analysis protocol for nanoparticle agglomerate quantification, future work should look at using this for the routine measurement of more challenging, low concentration nanoparticle dispersions in complex media. This could range from inorganic nanoparticles in biological media such as blood plasma, through to for example nanoplastics in seawater. These studies would allow better information to be gathered regarding nanoparticle dispersion in complex media and hence further progress nanomedical and nanotoxicological studies.

Improve imaging and characterisation of the protein corona. Preliminary studies in the latter section of this thesis identified ABF-STEM as a potential technique for protein corona analysis. Further work is necessary to develop this technique in order to routinely image the protein corona around

nanoparticles. Such studies may well require the use of advanced techniques including the use of direct electron detectors, cryo-FIB-SEM lift out and advanced post processing data analysis. This will allow the size, shape, inter-particle similarity and composition of the protein corona to be assessed and quantified.

Assessing the impact of the protein corona on cell uptake. Ultimately, once imaging has been consistently achieved, studies should be carried out assessing how observable differences in the protein corona between particles either within a single suspension or in multiple suspensions can effect cell uptake and cell function in order to better predict the potential efficacy of designed nanoparticles in medicine and their possible toxicity.

The completion of these further studies would allow cryo-analytical-S/TEM to become a fundamental technique for nanoparticle characterisation in order to achieve progress in the application of nanotechnology within medicine.

REFERENCES

1. Auffan, M., et al., *Towards a definition of inorganic nanoparticles from an environmental, health and safety perspective.* Nature Nanotechnology, 2009. **4**(10): p. 634.
2. Drexler, K.E., C. Peterson, and G. Pergamit, *Unbounding the future: The nanotechnology revolution*, in *Precision Engineering*. 1993, Morrow: New York. p. 306.
3. Hainfeld, J., et al., *Gold nanoparticles: a new X-ray contrast agent.* The British journal of radiology, 2006. **79**(939): p. 248.
4. Mirza, A.Z. and F.A. Siddiqui, *Nanomedicine and drug delivery: a mini review.* International Nano Letters, 2014. **4**(1): p. 94.
5. Hondow, N., A. Brown, and R. Brydson, *Chapter 6 - Nanomaterials: Dispersion, Dissolution and Dose*, in *Frontiers of Nanoscience*, M. Baalousha and J.R. Lead, Editors. 2015, Elsevier. p. 183.
6. Albanese, A. and W.C.W. Chan, *Effect of Gold Nanoparticle Aggregation on Cell Uptake and Toxicity.* ACS Nano, 2011. **5**(7): p. 5478.
7. Cai, K., et al., *Bio-nano interface: The impact of biological environment on nanomaterials and their delivery properties.* Journal of Controlled Release, 2017. **263**: p. 211.
8. Lynch, I. and K.A. Dawson, *Protein-nanoparticle interactions.* Nano Today, 2008. **3**(1–2): p. 40.
9. White, E.R., et al., *Charged Nanoparticle Dynamics in Water Induced by Scanning Transmission Electron Microscopy.* Langmuir, 2012. **28**(8): p. 3695.
10. McComb, D.W., J. Lengyel, and C.B. Carter, *Cryogenic transmission electron microscopy for materials research.* MRS Bulletin, 2019. **44**(12): p. 924.
11. Patra, J.K., et al., *Nano based drug delivery systems: recent developments and future prospects.* Journal of nanobiotechnology, 2018. **16**(1): p. 71.
12. Cormode, D.P., et al., *Nanotechnology in medical imaging: probe design and applications.* Arteriosclerosis, Thrombosis, and Vascular Biology, 2009. **29**(7): p. 992.
13. Rosen, J.E., et al., *Iron oxide nanoparticles for targeted cancer imaging and diagnostics.* Nanomedicine: Nanotechnology, Biology and Medicine, 2012. **8**(3): p. 275.
14. Jin, R., et al., *Superparamagnetic iron oxide nanoparticles for MR imaging and therapy: design considerations and clinical applications.* Current Opinion in Pharmacology, 2014. **18**: p. 18.
15. Popovtzer, R., et al., *Targeted gold nanoparticles enable molecular CT imaging of cancer.* Nano Letters, 2008. **8**(12): p. 4593.
16. Nikoobakht, B. and M.A. El-Sayed, *Preparation and growth mechanism of gold nanorods (NRs) using seed-mediated growth method.* Chemistry of Materials, 2003. **15**(10): p. 1957.
17. Li, G., et al., *A gold nanoparticles enhanced surface plasmon resonance immunosensor for highly sensitive detection of ischemia-modified albumin.* Sensors 2013. **13**(10): p. 12794.
18. Lee, J.H., et al., *Highly sensitive localized surface plasmon resonance immunosensor for label-free detection of HIV-1.* Nanomedicine, 2013. **9**(7): p. 1018.
19. Sonnichsen, C., et al., *A molecular ruler based on plasmon coupling of single gold and silver nanoparticles.* Nature Biotechnology, 2005. **23**(6): p. 741.
20. Popovtzer, R., et al., *Targeted gold nanoparticles enable molecular CT imaging of cancer.* Nano Letters, 2008. **8**(12): p. 4593.

21. Orive, G., et al., *Techniques: New approaches to the delivery of biopharmaceuticals.* Trends in Pharmacological Sciences, 2004. **25**(7): p. 382.

22. Matsumura, Y. and H. Maeda, *A new concept for macromolecular therapeutics in cancer chemotherapy: mechanism of tumoritropic accumulation of proteins and the antitumor agent smancs.* Cancer Research, 1986. **46**(12 Pt 1): p. 6387.

23. Golombek, S.K., et al., *Tumor targeting via EPR: Strategies to enhance patient responses.* Advanced Drug Delivery Reviews, 2018. **130**: p. 17.

24. Zhou, Y., et al., *Crossing the blood-brain barrier with nanoparticles.* Journal of Controlled Release, 2018. **270**: p. 290.

25. Moghimi, S.M., A.C. Hunter, and J.C. Murray, *Long-circulating and target-specific nanoparticles: theory to practice.* Pharmacological Reviews, 2001. **53**(2): p. 283.

26. Esmaeillou, M., et al., *Toxicity of ZnO nanoparticles in healthy adult mice.* Environmental Toxicology and Pharmacology, 2013. **35**(1): p. 67.

27. Barenholz, Y., *Doxil® — The first FDA-approved nano-drug: Lessons learned.* Journal of Controlled Release, 2012. **160**(2): p. 117.

28. Hua, S., *Lipid-based nano-delivery systems for skin delivery of drugs and bioactives.* Frontiers in pharmacology, 2015. **6**: p. 219.

29. Zhang, J. and M. Saltzman, *Engineering biodegradable nanoparticles for drug and gene delivery.* Chemical Engineering Progress, 2013. **109**(3): p. 25.

30. Ventola, C.L., *Progress in Nanomedicine: Approved and Investigational Nanodrugs.* Pharmacy and Therapeutics, 2017. **42**(12): p. 742.

31. Nel, A.E., et al., *Understanding biophysicochemical interactions at the nano-bio interface.* Nature Materials, 2009. **8**(7): p. 543.

32. Treuel, L., et al., *Physicochemical characterization of nanoparticles and their behavior in the biological environment.* Physical Chemistry Chemical Physics, 2014. **16**(29): p. 15053.

33. Allen, L.H. and E. Matijević, *Stability of colloidal silica: I. Effect of simple electrolytes.* Journal of Colloid and Interface Science, 1969. **31**(3): p. 287.

34. Ji, Z., et al., *Dispersion and Stability Optimization of TiO2 Nanoparticles in Cell Culture Media.* Environmental Science & Technology, 2010. **44**(19): p. 7309.

35. Strojan, K., et al., *Dispersion of Nanoparticles in Different Media Importantly Determines the Composition of Their Protein Corona.* PLOS ONE, 2017. **12**(1): p. e0169552.

36. Halamoda-Kenzaoui, B., et al., *Dispersion Behaviour of Silica Nanoparticles in Biological Media and Its Influence on Cellular Uptake.* PLOS ONE, 2015. **10**(10): p. e0141593.

37. Moore, T.L., et al., *Nanoparticle colloidal stability in cell culture media and impact on cellular interactions.* Chemical Society Reviews, 2015. **44**(17): p. 6287.

38. Halamoda-Kenzaoui, B., et al., *The agglomeration state of nanoparticles can influence the mechanism of their cellular internalisation.* Journal of nanobiotechnology, 2017. **15**(1): p. 48.

39. Lee, Y.J., E.Y. Ahn, and Y. Park, *Shape-dependent cytotoxicity and cellular uptake of gold nanoparticles synthesized using green tea extract.* Nanoscale research letters, 2019. **14**(1): p. 129.

40. Oberdörster, G., E. Oberdörster, and J. Oberdörster, *Nanotoxicology: an emerging discipline evolving from studies of ultrafine particles.* Environmental Health Perspectives, 2005. **113**(7): p. 823.

41. Edwards, S.A. and D.R.M. Williams, *Double Layers and Interparticle Forces in Colloid Science and Biology: Analytic Results for the Effect of Ionic Dispersion Forces.* Physical Review Letters, 2004. **92**(24): p. 248303.

42. Boström, M., D.R.M. Williams, and B.W. Ninham, *Specific Ion Effects: Why DLVO Theory Fails for Biology and Colloid Systems.* Physical Review Letters, 2001. **87**(16): p. 168103.

43. Sakura, T., et al., *One-pot preparation of mono-dispersed and physiologically stabilized gold colloid.* Colloid and Polymer Science, 2005. **284**: p. 97.

44. Curtis, C., et al., *Colloidal stability as a determinant of nanoparticle behavior in the brain.* Colloids and Surfaces B: Biointerfaces, 2018. **170**: p. 673.

45. Palacio, J., N.A. Agudelo, and B.L. Lopez, *PEGylation of PLA nanoparticles to improve mucus-penetration and colloidal stability for oral delivery systems.* Current Opinion in Chemical Engineering, 2016. **11**: p. 14.

46. Marins, J.A., et al., *Colloidal Stability of Aqueous Suspensions of Polymer-Coated Iron Oxide Nanorods: Implications for Biomedical Applications.* ACS Applied Nano Materials, 2018. **1**(12): p. 6760.

47. Thorat, N.D., et al., *Enhanced colloidal stability of polymer coated La0.7Sr0.3MnO3 nanoparticles in physiological media for hyperthermia application.* Colloids and Surfaces B: Biointerfaces, 2013. **111**: p. 264.

48. Guerrini, L., R.A. Alvarez-Puebla, and N. Pazos-Perez, *Surface Modifications of Nanoparticles for Stability in Biological Fluids.* Materials, 2018. **11**(7): p. 1154.

49. Zhou, Y. and G.V. Franks, *Flocculation Mechanism Induced by Cationic Polymers Investigated by Light Scattering.* Langmuir, 2006. **22**(16): p. 6775.

50. Wu, L., J. Zhang, and W. Watanabe, *Physical and chemical stability of drug nanoparticles.* Advanced Drug Delivery Reviews, 2011. **63**(6): p. 456.

51. Soenen, S.J.H., et al., *Intracellular Nanoparticle Coating Stability Determines Nanoparticle Diagnostics Efficacy and Cell Functionality.* Small, 2010. **6**(19): p. 2136.

52. Uzman, A., *Molecular biology of the cell (4th ed.)*. 2003, John Wiley & Sons Inc. p. 212.

53. Cedervall, T., et al., *Understanding the nanoparticle–protein corona using methods to quantify exchange rates and affinities of proteins for nanoparticles.* Proceedings of the National Academy of Sciences, 2007. **104**(7): p. 2050.

54. Klein, J., *Probing the interactions of proteins and nanoparticles.* Proceedings of the National Academy of Sciences, 2007. **104**(7): p. 2029.

55. Lundqvist, M., et al., *Nanoparticle size and surface properties determine the protein corona with possible implications for biological impacts.* Proceedings of the National Academy of Sciences of the United States of America, 2008. **105**(38): p. 14265.

56. Cedervall, T., et al., *Detailed Identification of Plasma Proteins Adsorbed on Copolymer Nanoparticles.* Angewandte Chemie International Edition, 2007. **46**(30): p. 5754.

57. Monopoli, M.P., et al., *Physical-Chemical Aspects of Protein Corona: Relevance to in Vitro and in Vivo Biological Impacts of Nanoparticles.* Journal of the American Chemical Society, 2011. **133**(8): p. 2525.

58. Tenzer, S., et al., *Nanoparticle Size Is a Critical Physicochemical Determinant of the Human Blood Plasma Corona: A Comprehensive Quantitative Proteomic Analysis.* ACS Nano, 2011. **5**(9): p. 7155.

59. Buijs, J., et al., *Conformational Stability of Adsorbed Insulin Studied with Mass Spectrometry and Hydrogen Exchange.* Analytical Chemistry, 1999. **71**(15): p. 3219.

60. García-Álvarez, R., et al., *In vivo formation of protein corona on gold nanoparticles. The effect of their size and shape.* Nanoscale, 2018. **10**(3): p. 1256.

61. Lesniak, A., et al., *Nanoparticle Adhesion to the Cell Membrane and Its Effect on Nanoparticle Uptake Efficiency.* Journal of the American Chemical Society, 2013. **135**(4): p. 1438.

62. Cheng, X., et al., *Protein Corona Influences Cellular Uptake of Gold Nanoparticles by Phagocytic and Nonphagocytic Cells in a Size-Dependent Manner.* ACS Applied Materials & Interfaces, 2015. **7**(37): p. 20568.

63. Pozzi, D., et al., *Effect of polyethyleneglycol (PEG) chain length on the bio–nano-interactions between PEGylated lipid nanoparticles and biological fluids: from nanostructure to uptake in cancer cells.* Nanoscale, 2014. **6**(5): p. 2782.

64. Oh, J.Y., et al., *Cloaking nanoparticles with protein corona shield for targeted drug delivery.* Nature Communications, 2018. **9**(1): p. 4548.

65. Simon, J., et al., *Exploiting the biomolecular corona: pre-coating of nanoparticles enables controlled cellular interactions.* Nanoscale, 2018. **10**(22): p. 10731.

66. Yeo, E.L.L., et al., *Protein corona in drug delivery for multimodal cancer therapy in vivo.* Nanoscale, 2018. **10**(5): p. 2461.

67. Xia, B., et al., *Engineered Stealth Porous Silicon Nanoparticles via Surface Encapsulation of Bovine Serum Albumin for Prolonging Blood Circulation in Vivo.* ACS Applied Materials & Interfaces, 2013. **5**(22): p. 11718.

68. Capriotti, A., et al., *Analytical Methods for Characterizing the Nanoparticle–Protein Corona.* Chromatographia, 2014. **77**: p. 755.

69. Caputo, F., et al., *Measuring particle size distribution of nanoparticle enabled medicinal products, the joint view of EUNCL and NCI-NCL. A step by step approach combining orthogonal measurements with increasing complexity.* Journal of Controlled Release, 2019. **299**: p. 31.

70. Malloy, A. and B. Carr, *NanoParticle Tracking Analysis – The Halo™ System.* Particle & Particle Systems Characterization, 2006. **23**(2): p. 197.

71. Filipe, V., A. Hawe, and W. Jiskoot, *Critical evaluation of Nanoparticle Tracking Analysis (NTA) by NanoSight for the measurement of nanoparticles and protein aggregates.* Pharmaceutical Research, 2010. **27**(5): p. 796.

72. Sauvain, J.-J., et al., *Exhaled breath condensate as a matrix for combustion-based nanoparticle exposure and health effect evaluation.* Journal of Aerosol Medicine and Pulmonary Drug Delivery, 2014. **27**: p. 449.

73. Rice, S.B., et al., *Particle size distributions by transmission electron microscopy: an interlaboratory comparison case study.* Metrologia, 2013. **50**(6): p. 663.

74. Souza, T.G.F., V.S.T. Ciminelli, and N.D.S. Mohallem, *A comparison of TEM and DLS methods to characterize size distribution of ceramic nanoparticles.* Journal of Physics: Conference Series, 2016. **733**: p. 012039.

75. Oktay, A.B. and A. Gurses, *Automatic detection, localization and segmentation of nano-particles with deep learning in microscopy images.* Micron, 2019. **120**: p. 113.

76. Walczak, A.P., et al., *Behaviour of silver nanoparticles and silver ions in an in vitro human gastrointestinal digestion model.* Nanotoxicology, 2012. **7**(7): p. 1198.

77. Adachi, K., et al., *In vivo effect of industrial titanium dioxide nanoparticles experimentally exposed to hairless rat skin.* Nanotoxicology, 2010. **4**(3): p. 296.

78. Xu, M., et al., *Formation of Nano-Bio-Complex as Nanomaterials Dispersed in a Biological Solution for Understanding Nanobiological Interactions.* Scientific Reports, 2012. **2**: p. 406.

79. Ribeiro, A.R., et al., *Trojan-Like Internalization of Anatase Titanium Dioxide Nanoparticles by Human Osteoblast Cells.* Scientific Reports, 2016. **6**: p. 23615.

80. Picknett, R.G. and R. Bexon, *The evaporation of sessile or pendant drops in still air.* Journal of Colloid and Interface Science, 1977. **61**(2): p. 336.

81. Deegan, R.D., et al., *Capillary flow as the cause of ring stains from dried liquid drops.* Nature, 1997. **389**(6653): p. 827.

82. Michen, B., et al., *Avoiding drying-artifacts in transmission electron microscopy: Characterizing the size and colloidal state of nanoparticles.* Scientific Reports, 2015. **5**(1): p. 9793.

83. Domingos, R.F., et al., *Characterizing Manufactured Nanoparticles in the Environment: Multimethod Determination of Particle Sizes.* Environmental Science & Technology, 2009. **43**(19): p. 7277.

84. de Jonge, N. and F.M. Ross, *Electron microscopy of specimens in liquid.* Nature Nanotechnology, 2011. **6**(11): p. 695.

85. de Jonge, N., et al., *Electron microscopy of whole cells in liquid with nanometer resolution.* Proceedings of the National Academy of Sciences, 2009. **106**(7): p. 2159.

86. Ievlev, A.V., et al., *Quantitative Description of Crystal Nucleation and Growth from in Situ Liquid Scanning Transmission Electron Microscopy.* ACS Nano, 2015. **9**(12): p. 11784.

87. Evans, J.E., et al., *Controlled Growth of Nanoparticles from Solution with In Situ Liquid Transmission Electron Microscopy.* Nano Letters, 2011. **11**(7): p. 2809.

88. Schneider, N.M., et al., *Electron–Water Interactions and Implications for Liquid Cell Electron Microscopy.* Journal of Physical Chemistry C, 2014. **118**(38): p. 22373.

89. Wei, W., et al., *Observing the Growth of Pb3O4 Nanocrystals by in Situ Liquid Cell Transmission Electron Microscopy.* ACS Applied Materials & Interfaces, 2019. **11**(27): p. 24478.

90. Ilett, M., et al., *Nanoparticle corona artefacts derived from specimen preparation of particle suspensions.* Scientific Reports, 2020. **10**(1): p. 5278.

91. Asghar, M.S.A., et al., *In-situ observation of radiation physics and chemistry of nanostructured cerium oxide in water.* Materials Research Express, 2018. **6**(1): p. 015032.

92. Dobro, M.J., et al., *Chapter Three - Plunge Freezing for Electron Cryomicroscopy*, in *Methods in Enzymology*, G.J. Jensen, Editor. 2010, Academic Press. p. 63.

93. Adrian, M., et al., *Cryo-electron microscopy of viruses.* Nature, 1984. **308**(5954): p. 32.

94. Dubochet, J., et al., *Cryo-electron microscopy of vitrified specimens.* Quarterly Reviews of Biophysics, 2009. **21**(2): p. 129.

95. Attili-Qadri, S., et al., *Oral delivery system prolongs blood circulation of docetaxel nanocapsules via lymphatic absorption.* Proceedings of the National Academy of Sciences, 2013. **110**(43): p. 17498.

96. Hernandez, C., et al., *Cryo-EM Visualization of Lipid and Polymer-Stabilized Perfluorocarbon Gas Nanobubbles - A Step Towards Nanobubble Mediated Drug Delivery.* Scientific Reports, 2017. **7**(1): p. 13517.

97. Zhang, S., et al., *"Single–Single" Amphiphilic Janus Dendrimers Self-Assemble into Uniform Dendrimersomes with Predictable Size.* ACS Nano, 2014. **8**(2): p. 1554.

98. Stewart, P.L., *Cryo-electron microscopy and cryo-electron tomography of nanoparticles.* WIREs Nanomedicine and Nanobiotechnology, 2017. **9**(2): p. e1417.

99. Zachman, M.J., et al., *Cryogenic specimens for nanoscale characterization of solid–liquid interfaces.* MRS Bulletin, 2019. **44**(12): p. 949.

100. Watt, J., D.L. Huber, and P.L. Stewart, *Soft matter and nanomaterials characterization by cryogenic transmission electron microscopy.* MRS Bulletin, 2019. **44**(12): p. 942.

101. Williams, R.E.A., D.W. McComb, and S. Subramaniam, *Cryo-electron microscopy instrumentation and techniques for life sciences and materials science.* MRS Bulletin, 2019. **44**(12): p. 929.

102. Hondow, N., et al., *Quantitative characterization of nanoparticle agglomeration within biological media.* Journal of Nanoparticle Research, 2012. **14**(7): p. 977.

103. Wills, J.W., et al., *Characterizing Nanoparticles in Biological Matrices: Tipping Points in Agglomeration State and Cellular Delivery In Vitro.* ACS Nano, 2017. **11**(12): p. 11986.

104. Patterson, J.P., et al., *CryoTEM as an Advanced Analytical Tool for Materials Chemists.* Accounts of Chemical Research, 2017. **50**(7): p. 1495.

105. Mirabello, G., et al., *Understanding the Formation Mechanism of Magnetic Mesocrystals with (Cryo-)Electron Microscopy.* Chemistry of Materials, 2019. **31**(18): p. 7320.

106. Burrows, N.D. and R.L. Penn, *Cryogenic transmission electron microscopy: aqueous suspensions of nanoscale objects.* Microscopy and Microanalysis, 2013. **19**(6): p. 1542.

107. Dubochet, J., et al., *Electron microscopy of frozen water and aqueous solutions.* Journal of Microscopy, 1982. **128**(3): p. 219.

108. Knapek, E. and J. Dubochet, *Beam damage to organic material is considerably reduced in cryo-electron microscopy.* Journal of Molecular Biology, 1980. **141**(2): p. 147.

109. Egerton, R.F., *Control of radiation damage in the TEM.* Ultramicroscopy, 2013. **127**: p. 100.

110. Le Caër, S., *Water Radiolysis: Influence of Oxide Surfaces on H2 Production under Ionizing Radiation.* Water, 2011. **3**(1): p. 235.

111. Russo, C.J. and R.F. Egerton, *Damage in electron cryomicroscopy: Lessons from biology for materials science.* MRS Bulletin, 2019. **44**(12): p. 935.

112. Oleshko, V.P., et al., *Combined characterization of composite tabular silver halide microcrystals by cryo-EFTEM/EELS and cryo-STEM/EDX techniques.* Microscopy Research and Technique, 1998. **42**(2): p. 108.

113. Oleshko, V.P., et al., *Structural and analytical characterization of Ag(Br,I) nanocrystals by CRYO-AEM techniques.* Nanostructured Materials, 1998. **10**(8): p. 1225.

114. Tester, C.C., et al., *In vitro synthesis and stabilization of amorphous calcium carbonate (ACC) nanoparticles within liposomes.* CrystEngComm, 2011. **13**(12): p. 3975.

115. Wolf, S.G., P. Rez, and M. Elbaum, *Phosphorus detection in vitrified bacteria by cryo-STEM annular dark-field analysis.* Journal of Microscopy, 2015. **260**(2): p. 227.

116. Kim, G., et al., *Diffuse Polymer Interfaces in Lobed Nanoemulsions Preserved in Aqueous Media.* Journal of the American Chemical Society, 2006. **128**(20): p. 6570.

117. Yakovlev, S., et al., *Quantitative nanoscale water mapping in frozen-hydrated skin by low-loss electron energy-loss spectroscopy.* Ultramicroscopy, 2010. **110**(7): p. 866.

118. Leijten, Z.J.W.A., et al., *Low-dose (S)TEM elemental analysis of water and oxygen uptake in beam sensitive materials.* Ultramicroscopy, 2020. **208**: p. 112855.

119. Zachman, M.J., et al., *Cryo-STEM mapping of solid–liquid interfaces and dendrites in lithium-metal batteries.* Nature, 2018. **560**(7718): p. 345.

120. Ilett, M., et al., *Cryo-analytical STEM of frozen, aqueous dispersions of nanoparticles.* Micron, 2019. **120**: p. 35.

121. Eckert, J.O., et al., *Kinetics and Mechanisms of Hydrothermal Synthesis of Barium Titanate.* Journal of the American Ceramic Society, 1996. **79**(11): p. 2929.

122. Matar, O., et al., *Barium Titanate Nanoparticles for Biomarker Applications.* Journal of Physics: Conference Series, 2015. **644**(1): p. 012037.

123. Bamiduro, F., et al., *Hierarchical Growth of ZnO Particles by a Hydrothermal Route.* Journal of the American Ceramic Society, 2014. **97**(5): p. 1619.

124. Roach, L., et al., *Morphological control of seedlessly-synthesized gold nanorods using binary surfactants.* Nanotechnology, 2018. **29**(13): p. 135601.

125. Leonov, A.P., et al., *Detoxification of gold nanorods by treatment with polystyrenesulfonate.* ACS Nano, 2008. **2**(12): p. 2481.

126. Genchi, G.G., et al., *Barium titanate nanoparticles: promising multitasking vectors in nanomedicine.* Nanotechnology, 2016. **27**(23).

127. Xia, T., et al., *Comparison of the mechanism of toxicity of zinc oxide and cerium oxide nanoparticles based on dissolution and oxidative stress properties.* ACS Nano, 2008. **2**(10): p. 2121.

128. Vandebriel, R.J. and W.H. De Jong, *A review of mammalian toxicity of ZnO nanoparticles.* Nanotechnology, science and applications, 2012. **5**: p. 61.

129. Xie, C., et al., *Bacillus subtilis causes dissolution of ceria nanoparticles at the nano–bio interface.* Environmental Science: Nano, 2019. **6**(1): p. 216.

130. Liu, J., et al., *Zinc oxide nanoparticles induce toxic responses in human neuroblastoma SHSY5Y cells in a size-dependent manner.* International journal of nanomedicine, 2017. **12**: p. 8085.

131. Hu, Y.-B., et al., *The endosomal-lysosomal system: from acidification and cargo sorting to neurodegeneration.* Translational neurodegeneration, 2015. **4**: p. 18.

132. Kokubo, T. and H. Takadama, *How useful is SBF in predicting in vivo bone bioactivity?* Biomaterials, 2006. **27**(15): p. 2907.

133. Lambert, L. and T. Mulvey, *Ernst Ruska (1906–1988), Designer Extraordinaire of the Electron Microscope: A Memoir*, in *Advances in Imaging and Electron Physics*, P.W. Hawkes, Editor. 1996, Elsevier. p. 2.

134. Goodhew, P.J., H. John, and B. Richard, *Electron Microscopy and Analysis*. 3rd ed. 2001, London: Taylor&Francis.

135. Williams, D.B. and C.B. Carter, *Transmission Electron Microscopy Part 1 : Basics*. 2nd ed. 2009, New York: Springer Science+Business Media.

136. Hetherington, C., *Aberration correction for TEM.* Materials Today, 2004. **7**(12): p. 50.

137. Brydson, R., A. Brown, and L.G. Benning, *Analytical Transmission Electron Microscopy.* Reviews in Mineralogy & Geochemistry, 2013. **78**: p. 219.

138. R.F.Egerton, *Physical Principles of Electron Microscopy*. 2006, Switzerland: Springer International Publishing.

139. Williams, D.B. and C.B. Carter, *Transmission Electron Microscopy Part 3: Imaging*. 2nd ed. 2009, New York: Springer.

140. Hofer, F., et al., *Fundamentals of electron energy-loss spectroscopy.* IOP Conference Series: Materials Science and Engineering, 2016. **109**: p. 012007.

141. Keast, V.J., et al., *Electron energy-loss near-edge structure – a tool for the investigation of electronic structure on the nanometre scale.* Journal of Microscopy, 2001. **203**(2): p. 135.

142. Leapman, R.D. and J.A. Hunt, *Comparison of detection limits for EELS and EDXS.* Microscopy Microanalysis Microstructures, 1991. **2**(2-3): p. 231.

143. R.F.Egerton, *Electron Energy-Loss Spectroscopy in the Electron Microscope*. 3rd ed. 2011, New York: Springer.

144. Brydson, R., *Electron Energy Loss Spectroscopy*. 1 ed, ed. P. Barlass. 2001, New York: Taylor&Francis. p.1-17.

145. De Carlo, S. and J.R. Harris, *Negative staining and cryo-negative staining of macromolecules and viruses for TEM.* Micron 2011. **42**(2): p. 117.

146. Brenner, S. and R.W. Horne, *A negative staining method for high resolution electron microscopy of viruses.* Biochimica et Biophysica Acta, 1959. **34**: p. 103.

147. Ohi, M., et al., *Negative Staining and Image Classification - Powerful Tools in Modern Electron Microscopy.* Biological procedures online, 2004. **6**: p. 23.

148. Thompson, R.F., et al., *An introduction to sample preparation and imaging by cryo-electron microscopy for structural biology.* Methods, 2016. **100**: p. 3.

149. Cabra, V. and M. Samsó, *Do's and Don'ts of Cryo-electron Microscopy: A Primer on Sample Preparation and High Quality Data Collection for Macromolecular 3D Reconstruction.* Journal of visualized experiments, 2015: p. 52311.

150. de Jonge, N. and F.M. Ross, *Electron microscopy of specimens in liquid.* Nature Nanotechnology, 2011. **6**: p. 695.

151. Bio-Ma-Tek. *K-kit for Liquid TEM:* http://www.bioma-tek.com/bioma-tek/en/goods.php?act=view&no=18. Accessed March 2020].

152. Sakho, E.H.M., et al., *Dynamic Light Scattering (DLS)*, in *Thermal and Rheological Measurement Techniques for Nanomaterials Characterization*. 2017. p. 37.

153. Ramos, A.P., *4 - Dynamic Light Scattering Applied to Nanoparticle Characterization*, in *Nanocharacterization Techniques*, A.L. Da Róz, et al., Editors. 2017, William Andrew Publishing. p. 99.

154. Clogston, J.D. and A.K. Patri, *Zeta Potential Measurement*. Characterization of Nanoparticles Intended for Drug Delivery. , ed. S. McNeil. Vol. 697. 2011: Humana Press. p.63.

155. Doane, T.L., et al., *Nanoparticle ζ -Potentials.* Accounts of Chemical Research, 2012. **45**(3): p. 317.

156. Laemmli, U.K., *Cleavage of structural proteins during the assembly of the head of bacteriophage T4.* Nature, 1970. **227**(5259): p. 680.

157. Smith, B.J., *SDS Polyacrylamide Gel Electrophoresis of Proteins* Proteins. Methods in Molecular Biology, ed. J.M. Walker. Vol. 1. 1984: Humana Press. p.41.

158. Cohen, S.L. and B.T. Chait, *Mass Spectrometry of Whole Proteins Eluted from Sodium Dodecyl Sulfate–Polyacrylamide Gel Electrophoresis Gels.* Analytical Biochemistry, 1997. **247**(2): p. 257.

159. Fenech, M., *Cytokinesis-block micronucleus cytome assay.* Nature Protocols, 2007. **2**: p. 1084.

160. Xing, Z., et al., *IL-6 is an antiinflammatory cytokine required for controlling local or systemic acute inflammatory responses.* The Journal of Clinical Investigation, 1998. **101**(2): p. 311.

161. Aydin, S., *A short history, principles, and types of ELISA, and our laboratory experience with peptide/protein analyses using ELISA.* Peptides, 2015. **72**: p. 4.

162. Kato, K., et al., *Use of Rabbit Antibody IgG Bound onto Plain and Aminoalkylsilyl Glass Surface for the Enzyme-Linked Sandwich Immunoassay.* The Journal of Biochemistry, 1977. **82**(1): p. 261.

163. *Origin(Pro)* 2016, OriginLab corporation: Northampton, MA, USA.

164. Williams, D.B. and C.B. Carter, *Transmission Electron Microscopy Part 2: Diffraction*. 2nd ed. 2009, New York Springer.

165. Talmon, Y., *Electron Beam Radiation Damage to Organic and Biological Cryospecimens. In: Steinbrecht R.A., Zierold K. (eds) Cryotechniques in Biological Electron Mcroscopy*, ed. R.A. Steinbrecht and K. Zierold. Vol. 91. 1987, Berlin, Heidelberg: Springer.

166. Freeman, H.M., et al., *Beam-induced oxidation of mixed-valent Fe (oxyhydr)oxides (green rust) monitored by STEM-EELS.* Micron, 2019. **122**: p. 46.

167. Yakovlev, S. and M. Libera, *Dose-limited spectroscopic imaging of soft materials by low-loss EELS in the scanning transmission electron microscope.* Micron, 2008. **39**(6): p. 734.

168. Moser, T.H., T. Shokuhfar, and J.E. Evans, *Considerations for imaging thick, low contrast, and beam sensitive samples with liquid cell transmission electron microscopy.* Micron, 2019. **117**: p. 8.

169. Schneider, N.M., et al., *Electron–Water Interactions and Implications for Liquid Cell Electron Microscopy.* J. Phys. Chem. C, 2014. **118**(38): p. 22373.

170. Egerton, R.F., *Radiation damage to organic and inorganic specimens in the TEM.* Micron, 2019. **119**: p. 72.

171. VandenBussche, E.J. and D.J. Flannigan, *Reducing Radiation Damage in Soft Matter with Femtosecond-Timed Single-Electron Packets.* Nano Letters, 2019. **19**(9): p. 6687.

172. Egerton, R.F., *Calculation, consequences and measurement of the point spread function for low-loss inelastic scattering.* Microscopy, 2018. **67**(1): p. 52.

173. Uehara, S. and H. Nikjoo, *Monte Carlo Simulation of Water Radiolysis for Low-energy Charged Particles.* Journal of Radiation Research, 2006. **47**(1): p. 69.

174. Egerton, R.F., T. Aoki, and P.A. Crozier, *Taking Advantage of Scattering Delocalization To Reduce Radiation Damage In Vibrational or Valence-Loss EELS and Energy-Filtered TEM Images.* Microscopy and Microanalysis, 2016. **22**(S3): p. 960.

175. Pan, Y.-H., et al., *Electron-beam-induced reduction of Fe3+ in iron phosphate dihydrate, ferrihydrite, haemosiderin and ferritin as revealed by electron energy-loss spectroscopy.* Ultramicroscopy, 2010. **110**(8): p. 1020.

176. Chen, J.Z., et al., *A dose-rate effect in single-particle electron microscopy.* Journal of Structural Biology, 2008. **161**(1): p. 92.

177. Leapman, R.D. and S. Sun, *Cryo-electron energy loss spectroscopy: observations on vitrified hydrated specimens and radiation damage.* Ultramicroscopy, 1995. **59**(1): p. 71.

178. Sousa, A., A. Aitouchen, and M. Libera, *Water mapping in hydrated soft materials.* Ultramicroscopy, 2006. **106**(2): p. 130.

179. Aronova, M.A., A.A. Sousa, and R.D. Leapman, *EELS Characterization of Radiolytic Products in Frozen Samples.* Micron, 2011. **42**(3): p. 252.

180. Karuppasamy, M., et al., *Radiation damage in single-particle cryo-electron microscopy: effects of dose and dose rate.* Journal of synchrotron radiation, 2011. **18**(Pt 3): p. 398.

181. Kuzay, T.M., M. Kazmierczak, and B.J. Hsieh, *X-ray beam/biomaterial thermal interactions in third-generation synchrotron sources.* Acta Crystallographica Section D, 2001. **57**(1): p. 69.

182. Liao, H.-G. and H. Zheng, *Liquid Cell Transmission Electron Microscopy.* Annual Review of Physical Chemistry, 2016. **67**(1): p. 719.

183. Ambrožič, B., et al., *Controlling the radical-induced redox chemistry inside a liquid-cell TEM.* Chemical Science, 2019. **10**(38): p. 8735.

184. Bian, S.-W., et al., *Aggregation and Dissolution of 4 nm ZnO Nanoparticles in Aqueous Environments: Influence of pH, Ionic Strength, Size, and Adsorption of Humic Acid.* Langmuir, 2011. **27**(10): p. 6059.

185. Elliot, A.J. and D.M. Bartels, *The reaction set, rate constants and g-values for the simulation of the radiolysis of light water over the range 20 deg to 350 deg C based on information available in 2008*. Atomic Energy of Canada Ltd; Report number AECL-153-127160-450-001: Canada; 2009. p. 162.

186. Sterniczuk, M. and D.M. Bartels, *Source of Molecular Hydrogen in High-Temperature Water Radiolysis.* The Journal of Physical Chemistry A, 2016. **120**(2): p. 200.

187. Warkentin, M. and R.E. Thorne, *Glass transition in thaumatin crystals revealed through temperature-dependent radiation-sensitivity measurements.* Acta crystallographica. Section D, Biological crystallography, 2010. **66**(Pt 10): p. 1092.

188. Moser, T.H., et al., *The role of electron irradiation history in liquid cell transmission electron microscopy.* Science Advances, 2018. **4**(4): p. eaaq1202.

189. Ilett, M., et al., *Cryo-STEM-EDX spectroscopy for the characterisation of nanoparticles in cell culture media.* Journal of Physics: Conference Series, 2017. **902**(1): p. 012006.

190. Ilett, M., et al., *Application of automated electron microscopy imaging and machine learning to characterise and quantify nanoparticle dispersion in aqueous media.* Journal of Microscopy, 2019.

191. Talmon, Y., *Staining and drying-induced artifacts in electron microscopy of surfactant dispersions.* Journal of Colloid and Interface Science, 1983. **93**(2): p. 366.

192. Conrad, D.R. *Calcium in Cell Culture* https://www.sigmaaldrich.com/life-science/cell-culture/learning-center/media-expert/calcium.html Accessed March 2020].

193. Pan, H.B. and B.W. Darvell, *Calcium Phosphate Solubility: The Need for Re-Evaluation.* Crystal Growth & Design, 2009. **9**(2): p. 639.

194. Tavafoghi, M. and M. Cerruti, *The role of amino acids in hydroxyapatite mineralization.* Journal of the Royal Society, Interface, 2016. **13**(123): p. 20160462.

195. Jahromi, M.T., G. Yao, and M. Cerruti, *The importance of amino acid interactions in the crystallization of hydroxyapatite.* Journal of the Royal Society, Interface, 2012. **10**(80): p. 20120906.

196. Clarke, E.R. and A.E. Martell, *Metal chelates of arginine and related ligands.* Journal of Inorganic and Nuclear Chemistry, 1970. **32**(3): p. 911.

197. Ribeiro, A.R., et al., *Bio-camouflage of anatase nanoparticles explored by in situ high-resolution electron microscopy.* Nanoscale, 2017. **9**(30): p. 10684.

198. Kaur, I., et al., *Dispersion of Nanomaterials in Aqueous Media: Towards Protocol Optimization.* Journal of visualized experiments, 2017(130): p. e56074.

199. Hartmann, N., et al., *Techniques and Protocols for Dispersing Nanoparticle Powders in Aqueous Media - Is there a Rationale for Harmonization?* Journal of toxicology and environmental health. Part B, Critical reviews, 2015. **18**: p. 1.

200. Taurozzi, J.S., V.A. Hackley, and M.R. Wiesner, *Ultrasonic dispersion of nanoparticles for environmental, health and safety assessment – issues and recommendations.* Nanotoxicology, 2011. **5**(4): p. 711.

201. Roine, A., *HSC Chemistry [Software] v 5.1, software available at www.outotec.com/HSC*. 2018, Outotec: Pori.

202. Kane, R.S., P. Deschatelets, and G.M. Whitesides, *Kosmotropes Form the Basis of Protein-Resistant Surfaces.* Langmuir, 2003. **19**(6): p. 2388.

203. Vonarbourg, A., et al., *Parameters influencing the stealthiness of colloidal drug delivery systems.* Biomaterials, 2006. **27**(24): p. 4356.

204. Lima, J., et al., *Interactions between calcium, phosphate, and albumin on the surface of titanium.* Journal of Biomedial Materials Research, 2001. **55**(1): p. 45.

205. Zeng, H., K.K. Chittur, and W.R. Lacefield, *Analysis of bovine serum albumin adsorption on calcium phosphate and titanium surfaces.* Biomaterials, 1999. **20**(4): p. 377.

206. Soenen, S.J.H., et al., *Cytotoxic effects of iron oxide nanoparticles and implications for safety in cell labelling.* Biomaterials, 2011. **32**(1): p. 195.

207. Zhao, J. and M.H. Stenzel, *Entry of nanoparticles into cells: the importance of nanoparticle properties.* Polymer Chemistry, 2018. **9**(3): p. 259.

208. Jokerst, J.V., et al., *Nanoparticle PEGylation for imaging and therapy.* Nanomedicine, 2011. **6**(4): p. 715.

209. Chu, M., et al., *Near-infrared laser light mediated cancer therapy by photothermal effect of Fe3O4 magnetic nanoparticles.* Biomaterials, 2013. **34**(16): p. 4078.

210. Foroozandeh, P. and A.A. Aziz, *Insight into Cellular Uptake and Intracellular Trafficking of Nanoparticles.* Nanoscale research letters, 2018. **13**(1): p. 339.

211. Mamaeva, V., C. Sahlgren, and M. Lindén, *Mesoporous silica nanoparticles in medicine—Recent advances.* Advanced Drug Delivery Reviews, 2013. **65**(5): p. 689.

212. Chen, N.-T., et al., *Theranostic applications of mesoporous silica nanoparticles and their organic/inorganic hybrids.* Journal of Materials Chemistry B, 2013. **1**(25): p. 3128.

213. Sharma, A., P.K. Agarwal, and S. Deep, *Characterization of different conformations of bovine serum albumin and their propensity to aggregate in the presence of N-cetyl-N,N,N-trimethyl ammonium bromide.* Journal of Colloid and Interface Science, 2010. **343**(2): p. 454.

214. Dickson, D., et al., *Dispersion and stability of bare hematite nanoparticles: Effect of dispersion tools, nanoparticle concentration, humic acid and ionic strength.* Science of the Total Environment, 2012. **419**: p. 170.

215. Jones, T.R., et al., *CellProfiler Analyst: data exploration and analysis software for complex image-based screens.* BMC Bioinformatics, 2008. **9**(1): p. 482.

216. Sommer, C., et al., *Ilastik: Interactive learning and segmentation toolkit*, in *IEEE 8th International Symposium on Biomedical Imaging*. 2011. p. 230.

217. Jaccard, P., *Nouvelles Recherches sur la Distribution Florale (Bulletin de la Société Vaudoise des Sciences Naturelles vol 44)*. 1908, Lausanne: Blanchand Ainé.

218. Gebhart, J., *Response of Single-Particle Optical Counters to Particles of irregular shape.* Particle & Particle Systems Characterization, 1991. **8**(1-4): p. 40.

219. Allouni, Z.E., et al., *Agglomeration and sedimentation of TiO2 nanoparticles in cell culture medium.* Colloids and Surfaces B: Biointerfaces, 2009. **68**(1): p. 83.

220. Wang, H., et al., *Formation of a Monolayer Protein Corona around Polystyrene Nanoparticles and Implications for Nanoparticle Agglomeration.* Small, 2019. **15**(22): p. 1900974.

221. Wu, M., et al., *Size-dependent cellular uptake and localization profiles of silver nanoparticles.* International journal of nanomedicine, 2019. **14**: p. 4247.

222. Safi, M., et al., *The effects of aggregation and protein corona on the cellular internalization of iron oxide nanoparticles.* Biomaterials, 2011. **32**(35): p. 9353.

223. Naghdi, M., et al., *Instrumental approach toward understanding nano-pollutants.* Nanotechnology for Environmental Engineering, 2017. **2**(1): p. 3.

224. Farooq, M.U., et al., *Gold Nanoparticles-enabled Efficient Dual Delivery of Anticancer Therapeutics to HeLa Cells.* Scientific Reports, 2018. **8**(1): p. 2907.

225. Rosi, N.L. and C.A. Mirkin, *Nanostructures in Biodiagnostics.* Chemical Reviews, 2005. **105**(4): p. 1547.

226. Murphy, C.J., et al., *Gold Nanoparticles in Biology: Beyond Toxicity to Cellular Imaging.* Accounts of Chemical Research, 2008. **41**(12): p. 1721.

227. Sztandera, K., M. Gorzkiewicz, and B. Klajnert-Maculewicz, *Gold Nanoparticles in Cancer Treatment.* Molecular Pharmaceutics, 2019. **16**(1): p. 1.

228. Murphy, K., *Janeway's immunobiology*. 9th ed. Immunobiology, ed. C. Weaver. 2017, New York, NY: Garland Science,Taylor & Francis Group.

229. Lorge, E., et al., *Standardized cell sources and recommendations for good cell culture practices in genotoxicity testing.* Mutation Research/Genetic Toxicology and Environmental Mutagenesis, 2016. **809**: p. 1.

230. Zhang, L.-S., et al., *A comparative study of TK6 human lymphoblastoid and L5178Y mouse lymphoma cell lines in the in vitro micronucleus test.* Mutation Research Letters, 1995. **347**(3): p. 105.

231. Nune, S.K., et al., *Nanoparticles for biomedical imaging.* Expert opinion on drug delivery, 2009. **6**(11): p. 1175.

232. Weissleder, R., et al., *Cell-specific targeting of nanoparticles by multivalent attachment of small molecules.* Nature Biotechnology, 2005. **23**(11): p. 1418.

233. Fröhlich, E., *The role of surface charge in cellular uptake and cytotoxicity of medical nanoparticles.* International journal of nanomedicine, 2012. **7**: p. 5577.

234. Goodman, C.M., et al., *Toxicity of Gold Nanoparticles Functionalized with Cationic and Anionic Side Chains.* Bioconjugate Chemistry, 2004. **15**(4): p. 897.

235. Brandenberger, C., et al., *Quantitative Evaluation of Cellular Uptake and Trafficking of Plain and Polyethylene Glycol-Coated Gold Nanoparticles.* Small, 2010. **6**(15): p. 1669.

236. Boisselier, E. and D. Astruc, *Gold nanoparticles in nanomedicine: preparations, imaging, diagnostics, therapies and toxicity.* Chemical Society Reviews, 2009. **38**(6): p. 1759.

237. Rischitor, G., et al., *Quantification of the cellular dose and characterization of nanoparticle transport during in vitro testing.* Particle and fibre toxicology, 2016. **13**(1): p. 47.

238. Yu, M., et al., *Dextran and polymer polyethylene glycol (PEG) coating reduce both 5 and 30 nm iron oxide nanoparticle cytotoxicity in 2D and 3D cell culture.* International journal of molecular sciences, 2012. **13**(5): p. 5554.

239. Sukhanova, A., et al., *Dependence of Nanoparticle Toxicity on Their Physical and Chemical Properties.* Nanoscale research letters, 2018. **13**(1): p. 44.

240. Huo, S., et al., *Ultrasmall gold nanoparticles as carriers for nucleus-based gene therapy due to size-dependent nuclear entry.* ACS Nano, 2014. **8**(6): p. 5852.

241. He, Z., et al., *The effects of gold nanoparticles on the human blood functions.* Artificial Cells, Nanomedicine, and Biotechnology, 2018. **46**(sup2): p. 720.

242. McGeough, M.D., et al., *Cutting edge: IL-6 is a marker of inflammation with no direct role in inflammasome-mediated mouse models.* Journal of Immunology, 2012. **189**(6): p. 2707.

243. Donaldson, K., et al., *The limits of testing particle-mediated oxidative stress in vitro in predicting diverse pathologies; relevance for testing of nanoparticles.* Particle and fibre toxicology, 2009. **6**: p. 13.

244. Sayes, C.M., et al., *Comparative pulmonary toxicity assessments of C60 water suspensions in rats: few differences in fullerene toxicity in vivo in contrast to in vitro profiles.* Nano Letters, 2007. **7**(8): p. 2399.

245. Winzen, S., et al., *Complementary analysis of the hard and soft protein corona: sample preparation critically effects corona composition.* Nanoscale, 2015. **7**(7): p. 2992.

246. Yoshinari, K., et al., *A growth-promoting factor for human myeloid leukemia cells from horse serum identified as horse serum transferrin.* Biochimica et Biophysica Acta (BBA) - Molecular Cell Research, 1989. **1010**(1): p. 28.

247. Settanni, G., et al., *Protein corona composition of poly(ethylene glycol)- and poly(phosphoester)-coated nanoparticles correlates strongly with the amino acid composition of the protein surface.* Nanoscale, 2017. **9**(6): p. 2138.

248. Mori, Y., et al., *A new antithrombogenic material with long polyethyleneoxide chains.* Transactions of the American Society Artificial Internal Organs, 1982. **28**: p. 459.

249. Suk, J.S., et al., *PEGylation as a strategy for improving nanoparticle-based drug and gene delivery.* Advanced Drug Delivery Reviews, 2016. **99**(Pt A): p. 28.

250. Lesniak, A., et al., *Serum heat inactivation affects protein corona composition and nanoparticle uptake.* Biomaterials, 2010. **31**(36): p. 9511.

251. Liu, Y., D.T. Huynh, and T.O. Yeates, *A 3.8 Å resolution cryo-EM structure of a small protein bound to an imaging scaffold.* Nature Communications, 2019. **10**(1): p. 1864.

252. Henderson, R., *The potential and limitations of neutrons, electrons and X-rays for atomic resolution microscopy of unstained biological molecules.* Quarterly Reviews of Biophysics, 2009. **28**(2): p. 171.

253. Wright, A.K. and M.R. Thompson, *Hydrodynamic structure of bovine serum albumin determined by transient electric birefringence.* Biophysical Journal, 1975. **15**(2, Part 1): p. 137.

254. Kokkinopoulou, M., et al., *Visualization of the protein corona: towards a biomolecular understanding of nanoparticle-cell-interactions.* Nanoscale, 2017. **9**(25): p. 8858.

255. Egerton, R.F., P. Li, and M. Malac, *Radiation damage in the TEM and SEM.* Micron, 2004. **35**(6): p. 399.

256. Dreaden, E.C., et al., *The golden age: gold nanoparticles for biomedicine.* Chemical Society Reviews, 2012. **41**(7): p. 2740.